SiCN based Anode Materials for Lithium-Ion Batteries

SiCN basierte Anodenmaterialien für Lithium-Ionen-Batterien
Zur Erlangung des akademischen Grades Doktor-Ingenieur (Dr.-Ing.)
genehmigte Dissertation von Dipl.-Ing. Lukas Mirko Reinold aus Wiesbaden
Mai 2016 — Darmstadt — D 17

TECHNISCHE
UNIVERSITÄT
DARMSTADT

FB 11 Material- und Geowissenschaften
Disperse Feststoffe

SiCN based Anode Materials for Lithium-Ion Batteries
SiCN basierte Anodenmaterialien für Lithium-Ionen-Batterien

Genehmigte Dissertation von Dipl.-Ing. Lukas Mirko Reinold aus Wiesbaden

1. Gutachten: Prof. Dr. Prof. h. c. Dr. h. c. Ralf Riedel
2. Gutachten: Prof. Dr. Christina Roth

Tag der Einreichung: 08.10.2015
Tag der Prüfung: 23.12.2015

Darmstadt — D 17

Erklärung zur Dissertation

Hiermit versichere ich, die vorliegende Dissertation ohne Hilfe Dritter nur mit den angegebenen Quellen und Hilfsmitteln angefertigt zu haben. Alle Stellen, die aus Quellen entnommen wurden, sind als solche kenntlich gemacht. Diese Arbeit hat in gleicher oder ähnlicher Form noch keiner Prüfungsbehörde vorgelegen.

Darmstadt, den 24 Mai 2016

(Lukas Mirko Reinold)

Abstract

This thesis deals with the investigation of polymer-derived silicon carbonitride based anode materials for their application in lithium-ion batteries. Carbon-rich silicon carbonitrides are obtained by a pyrolysis of different organosilicon precursors, namely poly(phenylvinylsilylcarbodiimide), poly(phenylvinylsilazane), poly(diphenylsilylcarbodiimide), poly(phenylsilsesquicarbodiimide) and poly(phenylsilsesquiazane). The materials are characterized by means of Raman spectroscopy, elemental analysis, X-ray diffraction and Galvanostatic Cycling with Potential Limitation. Promising results with respect to the capacity, rate capability and cycling stability have been obtained. Namely, silicon carbonitride derived from poly(phenylvinylsilazane) exhibits a 1^{st} cycle specific delithiation capacity as high as 725 $mAh{\cdot}g^{-1}$ and a specific capacity of 624 $mAh{\cdot}g^{-1}$ after prolonged cycling.

Extensive studies on the influence of the pyrolysis temperature between 800 °C and 1300 °C on the electrochemical behavior have been performed on the active materials derived from poly(phenylvinylsilylcarbodiimide) and poly(phenylvinylsilazane). It has been found that the pyrolysis temperature influences the hysteresis, the specific capacity, the rate capability and several aspects related to the stability of the prepared electrodes. Single Particle Measurements have been conducted, giving insight into the intrinsic properties of the materials, namely the charge transfer resistance and the minimum diffusion coefficient. These values are found to depend on the pyrolysis temperature, too. Solid state ^{29}Si, ^{13}C and ^{7}Li Nuclear Magnetic Resonance measurements on poly(phenylvinylsilylcarbodiimide) and poly(phenylvinylsilazane) pyrolyzed at 1100 °C reveal that the free carbon phase acts as major storing site for the lithium ions and that lithium ion motion takes place via a continuum diffusion mechanism described by an activation law.

Moreover, the prospects of silicon carbonitride as stabilizing matrix for prolonged electrochemical cycling of silicon nano powders are addressed. A variety of composites have been prepared differing in the organosilicon precursor, the ratios of compounds, presence/absence of conductive coatings and geometric structure. The highest cycling stability has been achieved for silicon nano particles located in a porous ceramic matrix.

Die vorliegende Arbeit beschäftigt sich mit Anodenmaterialen für die Anwendung in Lithium-Ionen Batterien auf Basis von polymerabgeleitetem Silicumcarbonitrid. Kohlenstoffreiche Siliciumcarbonitride wurden durch eine Pyrolyse von verschiedenen Präkursoren, namentlich poly(phenylvinylsilylcarbodiimid), poly(phenylvinylsilazan), poly(diphenylsilylcarbodiimid), poly(phenylsilsesquicarbodiimid) und poly(phenylsilsesquiazan), erhalten. Die keramischen Materialien wurden mittels Raman Spektroskopie, Elementaranalyse, Röntgenbeugung und Chronopotentiometriemessungen untersucht. Dabei wurden vielversprechende Ergebnisse hinsichtlich der Kapazität, des Leistungsvermögens bei hohen Strömen und der Zyklenstabilität erhalten. Z.B. zeigte poly(phenylvinylsilazan) abgeleitetes Siliciumcarbonitrid im ersten Zyklus eine reversible spezifische Kapazität von 725 mAh·g^{-1}. Auch nach wiederholtem Zyklieren konnte noch eine spezifische Kapazität von 624 mAh·g^{-1} gemessen werden.

Zusätzlich wurden Untersuchungen an poly(phenylvinylsilylcarbodiimid)- und poly(phenylvinylsilazan)abgeleitenden Aktivmaterialien hinsichtlich des Einflusses der Pyrolysetemperatur zwischen 800 °C und 1300 °C auf das elektrochemische Verhalten durchgeführt. Dabei konnte ein Zusammenhang zwischen der Pyrolysetemperatur mit der Hysterese, der spezifischen Kapazität und verschiedenen Aspekten der Stabilität festgestellt werden. Einzelpartikelmessungen gaben Aufschluss über die intrinsischen Eigenschaften der Materialien wie etwa den Durchtrittswiderstand und den minimalen Diffusionkoeffizienten. Auch bei diesen Kennwerten wurde eine Abhängigkeit von der Pyrolysetemperatur nachgewiesen. Die Ergebnisse von Festkörper ^{29}Si, ^{13}C und ^{7}Li Kernspinresonanz-Messungen an Poly(phenylvinylsilylcarbodiimid) und Poly(phenylvinylsilazan) pyrolisiert bei 1100 °C zeigten, dass die freie Kohlenstoffphase als hauptsächlicher Speicher für die Lithiumionen dient, und dass der Transport von Lithiumionen durch einen kontinuierlichen Diffusionsmechanismus erfolgt, der durch ein einfaches Aktivierungsgesetzt beschrieben werden kann.

Schließlich wurden die Erfolgsaussichten von Siliciumcarbonnitrid als stabilisierendes Matrixmaterial für das elektrochemische zyklieren von Siliciumnanopulvern untersucht. Hierfür wurde eine Vielzahl von Kompositen unterschiedlicher Zusammensetzung und unterschiedlichen Aufbaus, mit und ohne leitfähigen Beschichtungen und unter Verwendung unterschiedlicher Präkursoren hergestellt. Die höchste Zyklenstabilität wurde für Siliciumnanopartikel erreicht, die in eine poröse keramische Matrix eingebaut wurden.

Contents

Abbreviations

ATR	attenuated total reflection
BET	Brunauer, Emmett and Teller
BPP model	Bloembergen, Purcell and Pound model
CMC	carboxymethyl cellulose
CNTs	carbon nano tubes
DiPhen	poly(diphenylsilylcarbodiimide)
DMC	dimethyl carbonate
DOC	Depth of Charge
DOD	Depth of Discharge
EC	ethylene carbonate
EERA	European Energy Research Alliance
EMF	electromotive force
FTIR	Fourier Transform Infrared Spectroscopy
FWHM	full width half maximum
GCPL	Galvanostatic Cycling with Potential Limitation
GM35	poly(phenylsilsesquicarbodiimide)
GM65	poly(phenylsilsesquiazane)
HN1	poly(phenylvinylsilylcarbodiimide)
HN3	poly(phenylvinylsilazane)
HOMO	highest occupied molecular orbital
LUMO	lowest unoccupied molecular orbital

MAS	Magic-Angle-Spinning
NMR	Nuclear Magnetic Resonance
NPE	National Platform for Electromobility
PDC	polymer-derived ceramic
PolyR	Polyramic RD-684
PSEDA	polysilylethylenediamine
PVC	poly(vinyl chloride)
RL regime	rigid lattice regime
SAXS	small-angle X-ray scattering
SEI	Solid Electrolyte Interface
SEM	Scanning Electron Microscopy
SET-Plan	Strategic Energy Technology Plan
SiCN	silicon carbonitride
SiOC	silicon oxycarbide
TEM	Transmission Electron Microscopy
TGA	Thermogravimetric analysis

Symbols

a_i	activity
C	capacity
α	asymmetry parameter
τ_c	correlation time
D_{min}	minimum diffusion coefficient
E	potential of working electrode
E_A	activation energy
$E^{\ominus}$	standard electrode potential at an activity of 1
E_{cell}	cell voltage
ϕ	electrical potential
ΔE	electromotive force
$\Delta G_{eq.}$	change in free energy at equilibrium conditions
η	overpotential
F	Faraday constant
$\Delta\varphi$	Galvani potential difference
$\Delta\varphi^{\ominus}$	Galvani potential difference at an activity of 1
j_0	exchange current density
k_b	Boltzmann constant
l	diffusion length
L_a	lateral size of the carbon-nanodomains
λ	wavelength
ω_L	Larmor frequency
μ_i	chemical potential
$\tilde{\mu}_i$	electrochemical potential
$\mu_i^{\ominus}$	chemical potential at unit activity
n	moles of electrons
ν_i	stoichiometric coefficient
R_{ct}	charge transfer resistance
T_1^{-1}	spine-lattice relaxation rate in the laboratory frame

$T_{1\rho}^{-1}$	spine-lattice relaxation rate in the rotating frame
T_2^{-1}	spin-spin relaxation rate
ζ’	cycling stability
T	temperature
ζ	coulombic efficiency

1 Introduction

There is a growing interest of politics, science and industries in technologies for energy storage. The reason for this is the desired Energiewende aiming at replacing fossil and nuclear energies by renewable energies. The generation of energy out of renewable sources reduces the output of greenhouse gases and counters possible problems concerned with limited availability of fossil fuels. However, energy obtained from sun or wind is not necessarily available at a desired time of a day or year. Lithium-ion batteries are a possible candidate for energy storage in both, mobile and stationary applications. The efforts to improve this technology are seen in a series of associations founded to promote research and aiming at transferring the results to real applications. In Germany the National Platform for Electromobility (NPE) was founded in 2010. The task of the NPE is to analyze the development of electro mobility and to give advices to the government on how to achieve the goals of the National Development Plan for Electric Mobility.[1] One ambitious goal of this plan is e.g. to have one million fully electric cars on German roads in 2020. A comparable association at European level is the European Energy Research Alliance (EERA) with the main task being the acceleration of the development of new energy technologies with respect to the European Strategic Energy Technology Plan (SET-Plan).[2]

The history of lithium-ion batteries began already in the 70's with the finding that lithium ions reversible insert into graphite.[3, 4] The commercial breakthrough of lithium-ion batteries was achieved in 1991 when Sony introduced the lithium-ion battery to the market.[5] The lithium-ion battery is a success story since. In 2010 lithium-ion batteries had a market of 7.9 billion dollar and a market share of 26 % in the field of secondary batteries.[6] The commercialization of lithium-ion batteries allowed for strong enhancements in consumer electronics like smartphones and notebooks. Whereas the first electrical vehicles from 1881 were ruled out by the invention of the combustion engine, improved technology and described political and environmental circumstances lead to a comeback of electro mobility. Prominent examples for commercial electric cars are the Tesla Model S with a lot size of 21.000 in 2013 [7] and the BMWi3, which was launched into the market in 2014. Drawbacks of battery driven cars are the high price and low range in comparison with cars driven by combustion engines as well as the availability of charging stations.

Huge efforts are currently made to achieve higher specific and volumetric capacities, higher life times and to increase the safety of lithium-ion batteries. Since the introduction into the market almost no changes have been made in battery chemistry. The progresses during the last two decades were mainly driven by fabrication improvements, e.g. optimization of cell design.[8] The research nowadays deals with all components of the battery, starting with the so called active and inactive materials, the electrolyte, the separator as well as thermal and electrical management. For example a huge variety of materials is currently under investigation aiming at replacing the carbon anode which is mainly used in commercial lithium-ion batteries. Among these alternative materials are metals forming an alloy, conversion electrodes showing outstanding capacities or TiO_2 which exhibits an outstanding cycle life and high safety. Only few of this materials were brought into market so far. One prominent example is the Nexelion of Sony which is using a tin based anode.[5]

This work deals with the development and characterization of active materials that are potential candidates for replacing graphite on the anode side of the cell. A detailed study of silicon carbonitride derived from organosilicon polymers is presented. Besides active materials made solely of this material class, composite materials consisting of silicon carbonitride and nano sized silicon powder are studied as well. For pure silicon carbonitride fundamental questions are in the center of interest. The dependence of chemical composition, the influence of pyrolysis temperature and the determination of the lithium storing sides are addressed. The fabrication of composite materials on the other hand aims at the improvement of the cycling stability of silicon, and thus giving access to its outstanding capacities.

2 Fundamentals and State of the Art

The rising number of publications on the topic of lithium-ion battery research makes it impossible to cover the whole area within this work. To get a rough idea about the amount of papers published on lithium-ion batteries since its introduction to the market in 1991, Figure 2.1, showing the number of publications on the key word "lithium-ion battery", is addressed. The following chapter will therefore concentrate on the fundamentals of lithium-ion batteries and its working principle. Moreover the reader will be introduced into the field of polymer-derived ceramics (PDCs). A detailed summary of the state of the art concerned with anode materials based on PDCs and therefore of interest for this particular work will be addressed in Chapter 2.4. With respect to the composite materials composed of silicon and a silicon carbonitride ceramic, Chapter 2.5 also includes an overview on challenges related to the utilization of silicon as active material in lithium-ion batteries and different approaches to overcome these problems.

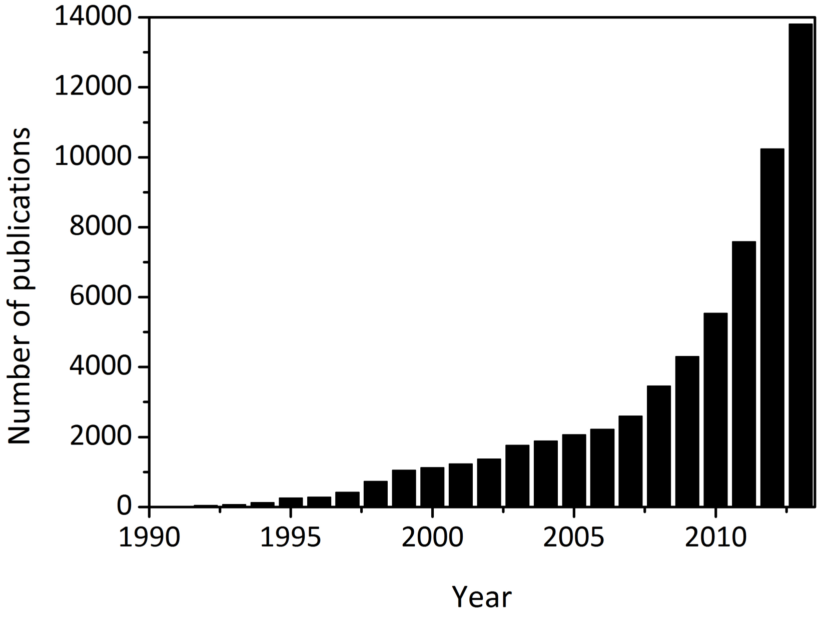

Figure 2.1: Number of publications based on a search with the keyword "lithium-ion battery" in web of knowledge from 1991 till 2013. (Status as of 28th of June 2014)

2.1 Principles of Electrochemistry

The following chapter will introduce some basic electrochemical equations and concepts.[9]

The *electrochemical potential* $\tilde{\mu}_i$ is defined as the work which is necessary to bring 1 M of z-valent ions from a standard state to a specific concentration and electrical potential (see Equation 2.1).

$$\tilde{\mu}_i = \mu_i + z_i F \phi \tag{2.1}$$

It can bee seen from Equation 2.1 that $\tilde{\mu}_i$ depends on the *chemical potential* μ_i as well as an expression for the work being done, with F being the Faraday constant and ϕ being the electrical potential. The chemical potential is defined in Equation 2.2. It depends on the chemical potential at unit activity $\mu_i^{\ominus}$, the temperature T and the activity a_i of the species i.

$$\mu_i = \mu_i^{\ominus} + RT \cdot ln(a_i) \tag{2.2}$$

In electrochemical equilibrium conditions the change in free energy $\Delta G_{eq.}$ must be zero. This is true if the sum of $\tilde{\mu}_i$ times their stoichiometric number ν_i equals zero.

$$\Delta G_{eq.} = \sum_i \nu_i \tilde{\mu}_i = 0 \tag{2.3}$$

Equation 2.1 and 2.3 allow for the calculation of the *Galvani potential difference* $\Delta\varphi$ (inner potential difference between two phases) of a half cell. E.g. $\Delta\varphi$ of a metal electrode (working electrode) in a solution of its ions is given by Equation 2.4 with $\Delta\varphi^{\ominus}$ being the Galvani potential difference between the electrolyte and the electrode at an activity of one.

$$\Delta\varphi = \Delta\varphi^{\ominus} + \frac{RT}{zF} \cdot ln(a_{M^{Z+}}) \tag{2.4}$$

In experimental setups $\Delta\varphi$ is only accessible with respect to a reference electrode with a constant Galvani potential difference $\Delta\varphi$'. The potential of the working electrode is given by the difference in the two Galvani potential differences E and is expressed by the so called *Nernst equation* given in Formula 2.5 with $E^{\ominus}$ being the standard electrode potential at an activity of one.

$$E = E^{\ominus} - \frac{RT}{zF} \cdot ln(a_{M^{Z+}}) \tag{2.5}$$

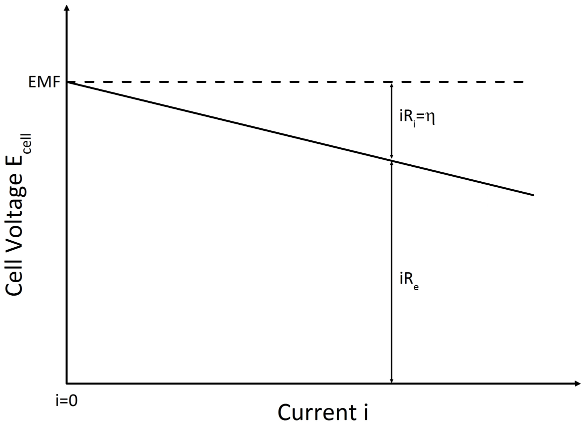

Figure 2.2: Cell voltage in dependence of the load current for a galvanic cell. The cell voltage at i=0 (EMF) decreases with increasing current load. R_i is the internal resistance of the cell and R_e is external resistance, respectively.

The *electromotive force* ΔE (EMF) of a full cell can be obtained by the difference of the potentials on the cathode and the anode as shown in Equation 2.6.

$$\Delta E = E_{cathode} - E_{anode} \tag{2.6}$$

So far, only the condition of electrochemical equilibrium has been discussed in which no current flow is taking place. However, allowing an electrical current to flow trough a cell influences the *cell voltage* E_{cell} as each electrode exhibits a current dependence of its voltage and the internal resistance of the electrolyte leads to an ohmic drop. The deviation of the electrode potential in equilibrium state is called the *overpotential* η and is defined according to Equation 2.7.

$$\eta = E_{cell} - \Delta E \tag{2.7}$$

There are different contributions to the overpotential. At low currents the overpotential is determined by the *electron transfer overpotential,* i.e the limited electron transfer across the phase boundary between electrode and electrolyte. At higher currents the *diffusion overpotential* arising from the slow transport of reactants or the *reaction overpotential* due to the inability of chemical reactions to keep pace with the electron transfer, are the limiting factors. A schematic drawing of the influence of a current flow on the cell voltage is shown in Figure 2.2

The net current j passing the cell is the sum of the anodic current j^- and the cathodic current j^+. From the definitions of j^- and j^+ given in Equation 2.8 and 2.9 the so called Butler-Volmer equation, given in 2.10, can be derived (for the derivation of j^- and j^+ the reader is referred to Reference [9]) with j_0 being the exchange current density, n being the number of moles of electrons and α being the asymmetry parameter.

$$j^- = j_0 \cdot exp\left\{\frac{\alpha n F \eta}{RT}\right\} \tag{2.8}$$

$$j^+ = j_0 exp\left\{\frac{(1-\alpha) n F \eta}{RT}\right\} \tag{2.9}$$

$$j = j_0\left[exp\left\{\frac{(1-\alpha) n F \eta}{RT}\right\} - exp\left\{\frac{\alpha n F \eta}{RT}\right\}\right] \tag{2.10}$$

For small currents the Butler-Volmer equation can be simplified to Equation 2.11. This equation is known as the Tafel equation.

$$j = j_0 exp\left(-\frac{\alpha n F \eta}{RT}\right) \tag{2.11}$$

2.2 Lithium-Ion Battery

In the following the setup and working principle of a lithium-ion battery will be discussed and some specific values characterizing a battery will be introduced.[9, 10]

A battery allows for the conversion of chemical energy into electrical energy via redox reactions. In general batteries can be distinguished into primary and secondary batteries. For secondary batteries it is possible to reverse the conversion of chemical energy into electrical energy. Thus, the battery is recharged and available for current drain again.

A battery usually consists of one or more electrochemical cells which are connected in series or parallel configuration. Basic components of a cell are the electrodes, the current collectors, the electrolyte, the separator and the housing. A schematic drawing of a lithium ion battery is shown in Figure 2.3. In general, the electrode at which oxidation occurs is referred to as anode whereas the electrode at which reduction takes place is named cathode. In consequence this would mean that the electrodes for secondary batteries can not be unambiguously named, as oxidation and reduction occurs on both electrodes depending whether

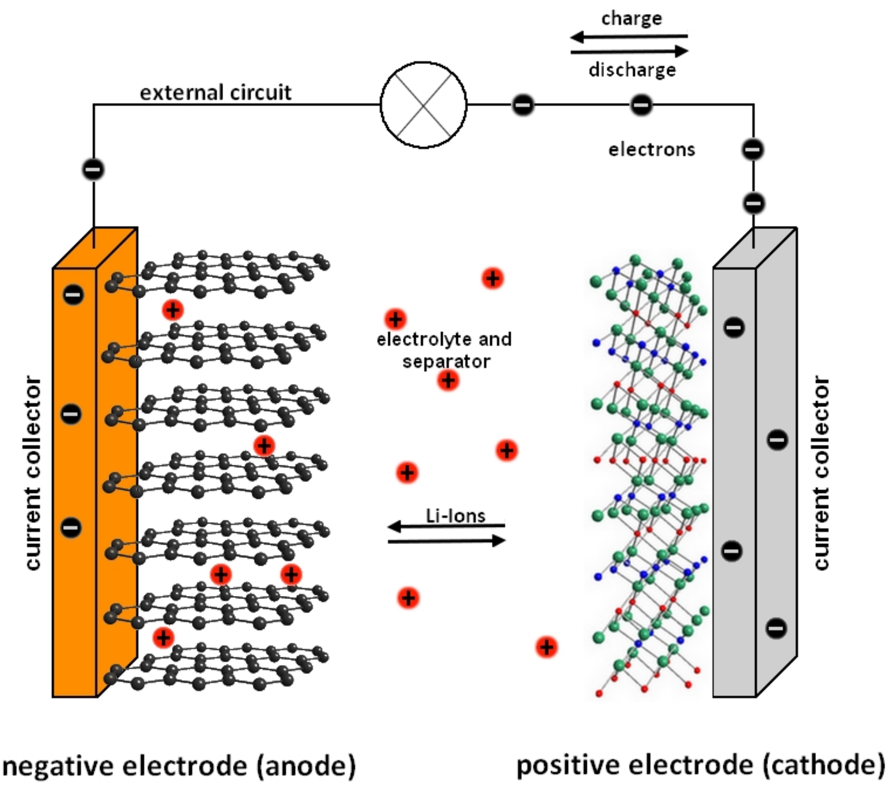

Figure 2.3: Schematic drawing of a lithium-ion battery.

the battery is charged or discharged. Hence, the electrodes are by convention named after there function during discharge, i.e. the more electronegative electrode is called anode (also negative electrode) and the more electropositive electrode is called cathode (also positive electrode).

The positive and negative electrodes are usually composed of an active material for lithium storage and additives, such as a binder and a conducting agent. Typical active materials used nowadays in lithium-ion batteries are graphitic carbons for the negative electrode and lithium cobalt oxide $LiCoO_2$ or lithium iron phosphate $LiFePO_4$ for the positive electrode. During the discharge of the battery, electrons are migrating from the negative electrode to the positive electrode via an external circuit. At the same time lithium ions are migrating through the electrolyte from the negative electrode to the positive electrode. The schematic descriptions of the discharge reactions for a graphite anode and a $LiCoO_2$ cathode in such a cell as well as the overall reaction are given in Equation 2.12 till 2.14.

$$Li_xC_n \longrightarrow nC + xLi^+ + xe^- \tag{2.12}$$

$$Li_{1-x}CoO_2 + xLi^+ + xe^- \longrightarrow LiCoO_2 \tag{2.13}$$

$$Li_{1-x}CoO_2 + Li_xC_n \longrightarrow LiCoO_2 + nC \tag{2.14}$$

There is a wide variety of anode materials being electrochemically active for lithium storage. The mechanisms of lithium storage can differ strongly among these materials. They can be classified into three different categories: i) host materials for the *intercalation* of lithium ions, ii) anode materials which reversibly form an *alloy* with lithium and iii) *conversion* electrodes. The different storing mechanisms and examples for materials are briefly described in the following:

i) **Intercalation**

Intercalation describes the reversible insertion of guest molecules, ions or atoms into a host structure.[11] Graphite is a prominent material which forms intercalation compounds with lithium. During the lithiation lithium ions intercalate between the graphene layers. At the same time the graphitic host material is reduced and the stacking order along c-direction changes from ABAB to AAAA. Graphite can host a maximum of one lithium ion per six carbon atoms, which results in a theoretical capacity of 372 mAh·g^{-1}. Another example for anode materials forming intercalation compounds with lithium is TiO_2 anatase which can store up to 0.5 lithium ions per unit formula which corresponds to a capacity of 200 mAh·g^{-1}.

ii) **Alloying**

An alloy is generally defined as a mixture or solid solution of a metal and another element. The charge and discharge reaction of an electrochemical alloying process with lithium is given in Equation 2.15 with M being one of the following elements: Si, In, Pb, Ga, Ge, Sn, Al, Bi, S. This materials exhibit theoretical capacities up to 3579 mAh·g^{-1} for silicon [12] but usually suffer from the large volume changes during alloying and dealloying.

$$Li_xM \rightleftarrows xLi^+ + xe^- + M \tag{2.15}$$

iii) **Conversion**

Transition metal oxides (e.g. Cu, Fe, Co, Ni) with a rock-salt structure can reversible react with lithium to form lithium oxide and the elemental transition metal as described in Equation 2.16. A drawback of this mechanism is, that an ongoing formation of LiO_2 during charging reduces the conductivity of the active material.

$$M_xO_y + 2yLi \rightleftarrows yLi_2O + xM \tag{2.16}$$

Typical cathode materials which perform intercalation reactions with lithium ions are transition metal oxides with either a layered ($LiMO_2$ M=Ni, Co, Mn and mixtures of them) or spinel ($LiMn_2O_4$, $Li(Co_xNi_yAl_z)O_2$) structure. Transition metal phosphates, like olivine $LiFePO_4$, are also electrochemically active. The intercalation reaction of $LiCoO_2$ has already been shown in Equation 2.12. The amount of lithium which can be provided by $LiCoO_2$ for reversible intercalation and deintercalation is restricted to about half a lithium ion per unit formula. If more than half of the lithium is removed from the structure, irreversible phase transformation occur. If more than x=0.72 is deintercalated, oxygen is released which should be strictly avoided with respect to safety aspects. The available capacity of $LiCoO_2$ is therefore limited to about 150 $mAh \cdot g^{-1}$.[10] The de facto capacity of $LiFePO_4$ amounts approximately 160 $mAh \cdot g^{-1}$ which is close to its theoretical capacity of 170 $mAh \cdot g^{-1}$. The insufficient electronic conductivity of $LiFePO_4$ is usually compensated by conductive coatings.[13]

The cell voltage or *open circuit voltage* V_{OC} is one of the important parameters which describe the performance of a battery. It is determined by the difference in the potentials of the cathode and the anode when no external load is applied and has already been introduced as EMF in Chapter 2.1. During the operation of the cell a non equilibrium state exists and the open circuit voltage is replaced by the *operating voltage*. During discharge the operating voltage is lower than the open circuit voltage due to polarization (ohmic polarization - IR drop, activation polarization and concentration polarization) effects. During charging the operating voltage is larger than the equilibrium potential.

The *capacity* C of a material describes the amount of charge stored (released) during the operation of the battery. As shown in Equation 2.17 it is given by the product of the Faraday constant and the number of moles of electrons n consumed (produced). The gravimetric specific capacity is referred to the mass of the active material (usually in mAh$\cdot g^{-1}$or A$h \cdot Kg^{-1}$) whereas the volumetric specific capacity is referred to the volume of the active material (usually in mAh$\cdot cm^{-3}$ or Ah$\cdot L^{-1}$). Examples for the specific capacity of typical active materials have already been given above.

$$C = n \cdot F \tag{2.17}$$

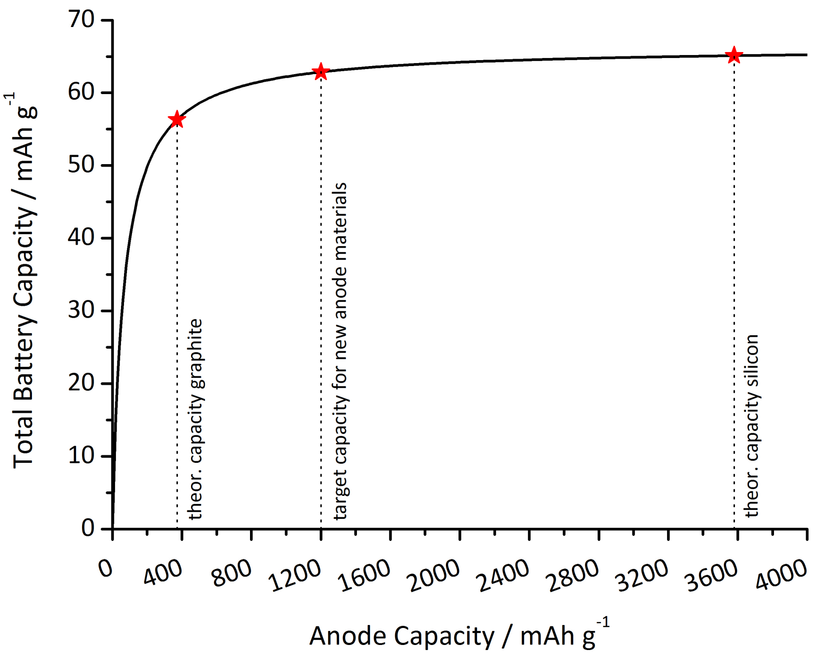

Figure 2.4: Total cell capacity in dependence of the specific anode capacity calculated according to Equation 2.18 assuming $C_{Cathode}$ to be 135 mAh·g^{-1} and Q$_{others}$ to be 130.4 mAh·g^{-1}. The example is based on a Sony 18650G8 cell and is taken from Kasavajjula et al. [14]. The vertical lines correspond to the theoretical capacity of graphite, silicon (at room temperature) and a target capacity of 1200 mAh·g^{-1} for new anode materials.

For the calculation of the capacity of a complete cell C_{total} the inactive components Q_{others} have to be taken into account, too. The capacity is then given by Equation 2.18.

$$C_{total} = \frac{1}{\frac{1}{C_{anode}} + \frac{1}{C_{cathode}} + \frac{1}{Q_{others}}} \tag{2.18}$$

Figure 2.4 is showing a graphical illustration of Equation 2.18 assuming a cathode capacity of 135 mAh·g^{-1} and a Q_{others} of 130.4 mAh·g^{-1} (values are taken from a publication of Kasavajjula et al. [14] and are based on a Sony 18650G8 cell). The total cell capacity shows a saturation with an increase in anode capacity. In conclusion there is no benefit of pushing the anode capacity above a specific capacity of approximately 1200 mAh·g^{-1} without improvement of the other cell components. This again stresses the importance of research on all active and inactive battery components but also allows for some anode materials to limit their Depth of Charge/Discharge or cut off voltages.

The Depth of Charge (DOC) and the Depth of Discharge (DOD) are the fractions of the maximum capacity in percent which can be stored (gained) in (from) the active material. The cut off voltages define the upper and lower potential limit in which the cell is cycled and form the *voltage window*. Usually the electrode potentials, which also equal the fermi levels of the electrodes, define the voltage window. The voltage window is crucial for the choice of the electrolyte used. In case of an electrochemical potential of the anode above the lowest unoccupied molecular orbital (LUMO) the electrolyte will be reduced. An electrochemical potential of the cathode below the highest occupied molecular orbital (HOMO) leads to an oxidation of the electrolyte.[15] Anode materials like metallic lithium, graphite or silicon exhibit a chemical potential which is above the LUMO of nonaqueous electrolytes. Nevertheless, the use of these materials is possible as a passivation layer on the surface of the electrode, the so called Solid Electrolyte Interface (SEI) is formed during the operation of the cell. The SEI inhibits the electron transfer from the anode to the electrolyte. The formation of the SEI usually takes place during the first cycle and leads to irreversible losses, visible in a reduced first cycle *coulombic efficiency* ζ given by Equation 2.19

$$\zeta = \frac{C_{delithiation}}{C_{lithiation}} \cdot 100\,\% \tag{2.19}$$

The *energy* stored in a battery is given by the integral of its potential times the amount of charge q (see Equation 2.20). In analogy to the capacity the energy is either referred to the mass (usually in Wh$\cdot Kg^{-1}$ or mWh$\cdot g^{-1}$) or the volume (usually in Wh$\cdot l^{-1}$ or mWh$\cdot cm^{-3}$). In practice, energy and capacity not only depend on the choice of materials but also on the current density at which lithiation and delithiation occurs. For high current densities the ionic transport of the lithium ions within the electrode or across the electrode-electrolyte phase-boundary is too slow to achieve equilibrium state.[15]

$$Energy = \int E \cdot dq \tag{2.20}$$

The current flowing at a certain potential gives the *power* P of the battery. It is calculated by the product of the current times the potential as shown in Equation 2.21.

$$P = i \cdot E \tag{2.21}$$

One challenge in lithium-ion battery research is to increase the *cycle life* of the cell components. The cycle life specifies the number of charge and discharge cycles N before the capacity falls below a certain percentage of the initial capacity. Usually the end of cycle life is reached when 80 % of the initial capacity is obtained.

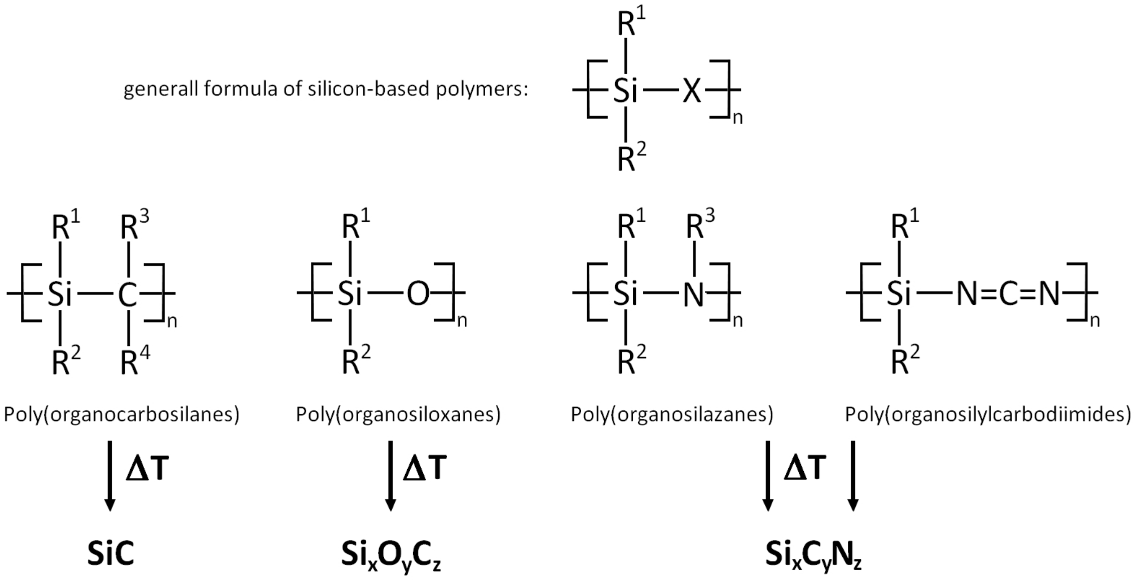

Figure 2.5: General structure of different organosilicon polymers and their chemical composition after pyrolysis.[16]

2.3 Polymer-Derived Ceramics

The synthesis of ceramics via a polymer route allows for the fabrication of ceramics with elemental compositions that are not accessible via the classical powder route. Furthermore, no sintering additives need to be used and the established shaping processes from the polymer industry can be adopted. The fabrication of polymer-derived ceramics (PDCs) usually consists of three major steps:

i) Synthesis of preceramic polymers

ii) Cross-linking of polymers at moderate temperatures

iii) Pyrolysis at elevated temperatures

The third step might be followed by a crystallization step at high temperature. Figure 2.5 shows the general structure of the preceramic organosilicon polymers, the basic classes of silicon-based polymers and the composition of the ceramic after pyrolysis. During the following paragraphs the three major steps involved in the fabrication of PDCs and some of their unique properties as well as their applications will be addressed in more detail.

i) **synthesis of organosilicon polymers:**

The most common starting compounds for preceramic organosilicon polymers are organylchlorosilanes with a chemical structure of R_xSiCl_{4-x} (with x=0-3 and R=functional side group). The formation of organylhalosilanes with side groups like methyl is based on the so called Müller-Rochow-Process, which was independently developed by Müller [17] and Rochow [18] in the early 1940's. As starting compounds for the reaction elemental silicon and haloalkanes are converted into organohalosilanes at temperatures of 250 °C to 320 °C in the presence of a copper catalyst. The reaction equation is given in Formula 2.22 with X being a halogen element and R being e.g. CH_3.

$$Si + RX \xrightarrow{250\,°C-320\,°C,\, Cu-catalyst} R_xSiX_{4-x} \tag{2.22}$$

The Müller-Rochow-Process is still the standard synthesis route for the industrial production of organylhalosilanes. The industrial synthesis of trichlorosilane is realized by the reaction of elemental silicon with hydrogen chloride at temperatures of 300 °C as shown in Equation 2.23. As a side product hydrogen gas is produced. Besides trichlorsilane also dichlorosilane and tetrachlorosilane are obtained via this route, though the formation of tetrachlorosilane is usually realized by a reaction of elemental silicon with chlorine. For the synthesis of monochlorosilane a reaction of tetrachlorosilane and lithium borohydride is used.

$$Si_{(s)} + HCl_{(g)} \longrightarrow HSiCl_3 + H_{2(g)} \tag{2.23}$$

The preparation of linear, high molecular weight *polysilanes* occurs via a modified Wurz coupling of dichlorosilane in the presence of alkali metal in dispersion.[19] The reaction, given in Equation 2.24, is usually performed at elevated temperatures.

$$R^1R^2SiCl_2 + 2Na \longrightarrow (R^1R^2Si)_n + 2NaCl \tag{2.24}$$

The synthesis of *polycarbosilanes* is based on the Kumada rearrangement [20] of polysilanes at elevated temperatures and pressure and involves the formation of radicals by a cleavage of Si-Si bonds. A scheme of the Kumada rearrangement is shown in Figure 2.6

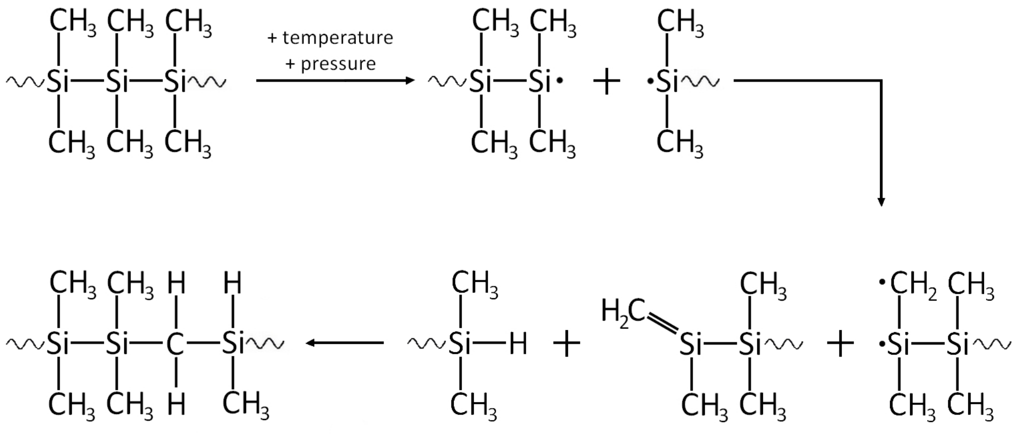

Figure 2.6: Simplified scheme of the synthesis of a polycarbosilane from polysilane via a Kumada rearrangement.

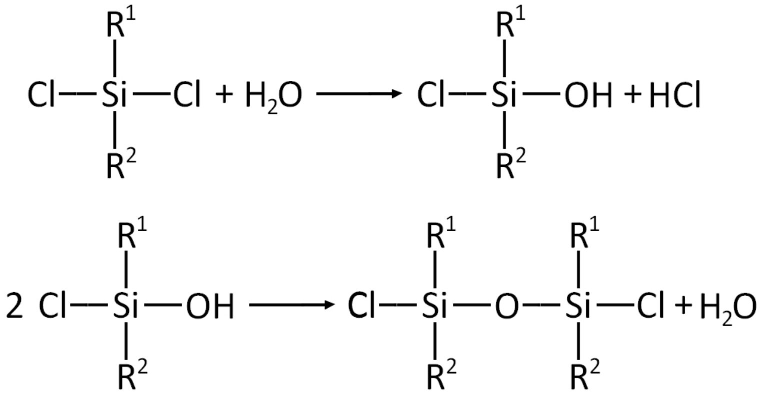

Figure 2.7: Schematic sketch of the hydrolysis reaction of a dichlorosilane (with R^1 and R^2=functional side groups) and the polycondensation reaction.

Polysiloxanes are obtained by a hydrolysis of chlorosilanes. The chlorine atoms are hereby substituted by an OH-group and HCl is formed as a side product. A polycondensation reaction finally results in the formation of polysiloxanes as shown in Figure 2.7.

A reaction of chlorosilanes with ammonia NH_3 or hexamethyldisilazane results in the formation of *polysilazanes*. As a side product the reaction with ammonia leads to the formation of solid ammonium chloride NH_4Cl which is costly to remove from the polysilazane. For the reaction with hexamethyldisilazane the chlorine of the starting silane is bound as trimethylchlorosilane which can be removed by a distillation process.

The synthesis of *polysilycarbodiimides* occurs via silylcarbodiimide monomers. There is a wide variety of possible routes for the synthesis of this monomers. An extensive overview of the different approaches is given in the References [21] and [22]. Among the different routes the easiest is the transamination using silazanes and dicyanodiamide developed by Vostokov et al. [23] shown in Equation 2.25

$$(R_3Si)_2NH + H_2NCN \longrightarrow R_3Si - NCN - SiR_3 + NH_3 \uparrow \tag{2.25}$$

Polysilylcarbodiimides are finally obtained by a reaction of silylcarbodiimides with chlorosilanes and pyridine as a catalyst.[24, 25]

ii) **cross-linking of organosilicon polymers:**

Cross-linking is an important step during the fabrication of PDCs. It inhibits the loss of components with low molecular weight and a fragmentation during pyrolysis and thus increases the ceramic yield. The cross-linking leads to duroplastics and is typically performed in a temperature range of 100 °C till 400 °C. Depending on the preceramic polymer it is also possible to achieve cross-linking reactions by the addition of chemical reagents like catalysts or peroxides [26], free radical initiation techniques and oxygen [27] and e-beam curing [28]. The four most important reactions during the thermal cross-linking of polysilazanes are the *transamination*, the *hydrosilylation*, the *vinyl polymerization* and the *dehydrocoupling* reaction.[16, 26] A scheme of this reactions is given in figure 2.8.

The first cross-linking reaction taking place with increasing temperature is the hydrosilylation reaction at 100 °C till 120 °C. It requires the existence of vinyl groups and

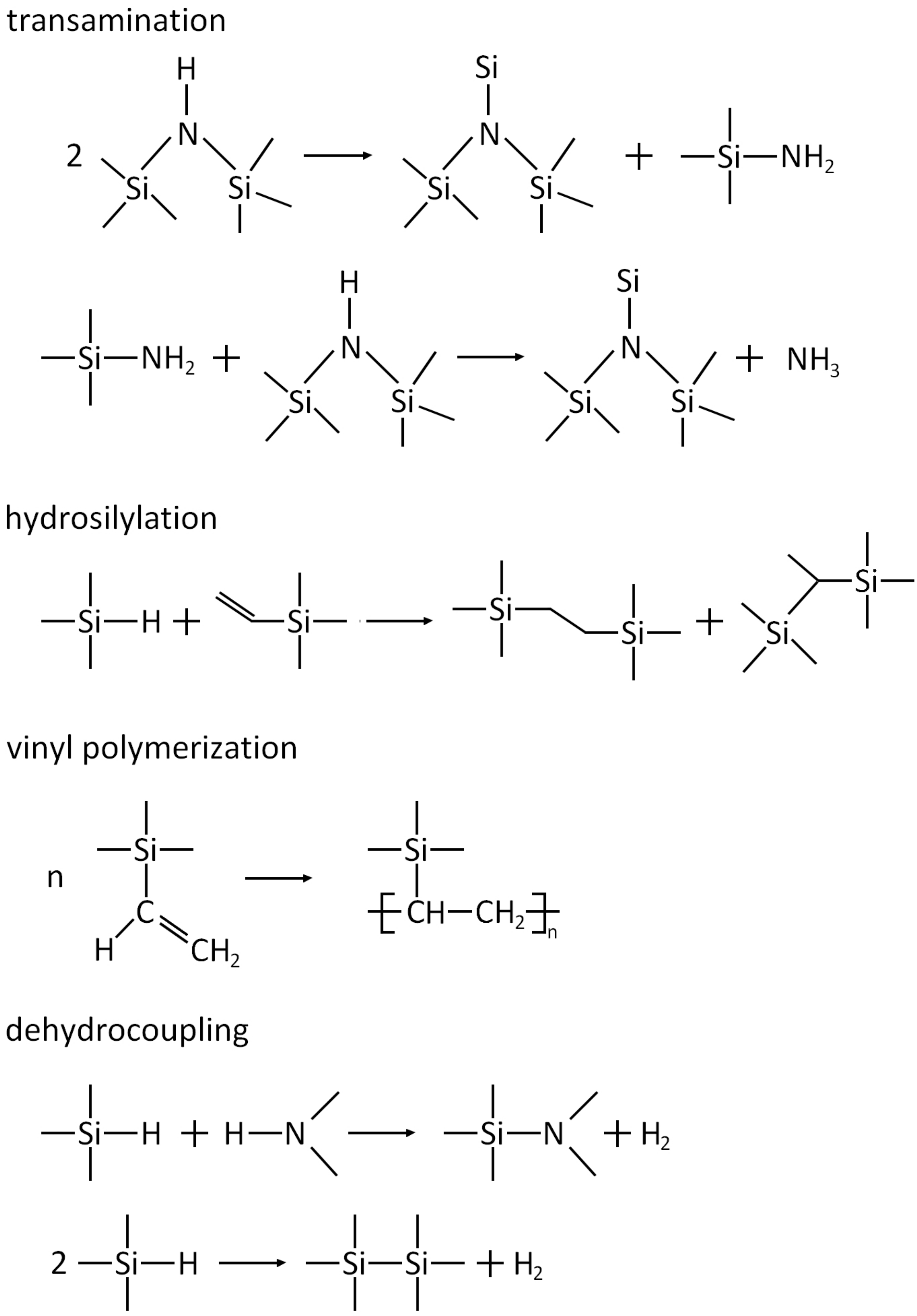

Figure 2.8: Schematic cross-linking reactions of polysilazanes.

Si-H bonds at the polysilazane. Like for the vinyl polymerization no side products are formed during the reaction, i.e no mass loss occurs. Dehydrocoupling starts at about 300 °C and involves the reaction of Si-H bonds with Si-H or N-H bonds and the evolution of hydrogen. Transamination reactions between 200 °C and 400 °C lead to an outgassing of different species like amines, ammonia and silanes, resulting in a decrease of nitrogen and silicon and therefore decrease in the yield of the final ceramic.

iii) **pyrolysis:**

The pyrolysis of the cross-linked polymers at temperatures of about 1000 °C leads to amorphous ceramics whose compositions and microstructures depend on the initial precursor. The polymer to ceramic transformation is usually accompanied by a shrinkage and mass loss as well as the formation of porosity. The pyrolysis of polycarbosilanes leads to amorphous silicon carbide SiC and free carbon.[29] The pyrolysis of polysiloxane results in the formation of silicon oxycarbide (SiOC) and a free carbon phase. The SiOC glass phase consists of various silicon sites ranging from SiC_4 over SiC_3O, SiC_2O_2 $SiCO_3$ to SiO_4. Figure 2.9 shows the microstructure obtained after the pyrolysis of polysilazanes and polysilylcarbodiimides. The pyrolysis for both precursors leads to the formation of amorphous silicon carbonitride (SiCN), however, the microstructures differ strongly. SiCN derived from polysilazane exhibits a mixed bond configuration (tetrahedrally coordinated silicon from SiC_4 via SiC_3N, SiC_2N_2 and $SiCN_3$ to SiN_4) as well as free carbon phase, whereas the pyrolysis of polysilylcarbodiimide results in an amorphous nanocomposite composed of Si_3N_4, SiC and a free carbon phase.[30, 31, 32, 33, 34, 35]

The choice of an appropriate starting precursor and the controlling of the polymer-to-ceramic conversion eventually allows to tailor the properties of the final ceramic. PDCs usually show excellent thermal, chemical and oxidation stability even under harsh conditions which makes them interesting for applications like fibers, glow plugs and coatings for microelectronics. They can also be used in energy storing devices like lithium-ion batteries which will be discussed in Chapter 2.4.

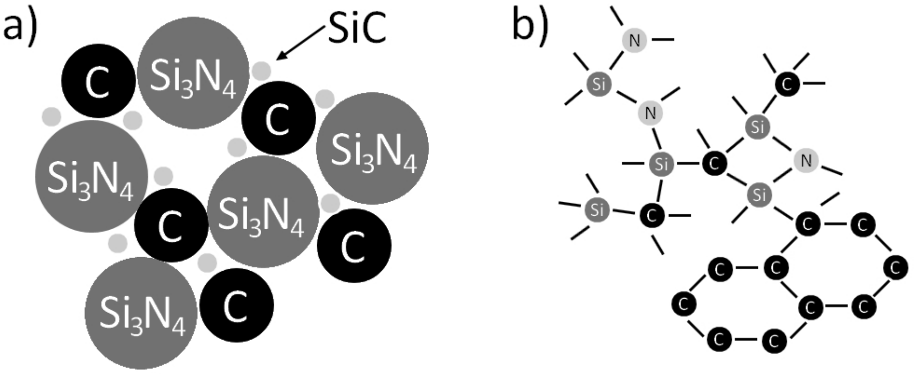

Figure 2.9: Schematic microstructure of SiCN derived from a) polysilylcarbodiimide and b) polysilazane.[30, 31, 36]

2.4 Polymer-Derived Ceramics as Anode Materials

The following section will give a summarized overview on the research on PDC based anode materials published so far with a strong focus on polymer-derived silicon carbonitride and composite materials based on silicon carbonitride.

The application of polysilazane derived silicon carbonitride as an active material in lithium-ion batteries was first patented by Dahn et al. in 1997.[37] Within this patent a single source polysilazane as well as blends of the silazane precursor with pitch have been pyrolyzed at 1000 °C and investigated in terms of their capability to reversibly store lithium ions. First cycle reversible capacities of $450\,\mathrm{mAh\cdot g^{-1}}$ to $560\,\mathrm{mAh\cdot g^{-1}}$ were achieved. For the single source precursor two different heating rates during pyrolysis were chosen, namely $5\,^{\circ}C\cdot\mathrm{min}^{-1}$ and $45\,^{\circ}C\cdot\mathrm{min}^{-1}$. For lower pyrolysis rates the first cycle reversible capacity was increased slightly by $24\,\mathrm{mAh\cdot g^{-1}}$ and the first cycle irreversible capacity was decreased from $517\,\mathrm{mAh\cdot g^{-1}}$ to $301\,\mathrm{mAh\cdot g^{-1}}$. For the investigated blends silazane was mixed with pitch in three different ratios 1:1, 3:1 and 1:3. The blend of the ratio 3:1 showed an increase of $15\,\mathrm{mAh\cdot g^{-1}}$ in the first cycle reversible capacity compared to the single-source attempt with the slow heating rates. A higher amount of pitch lead to a decrease of the capacity below the values obtained for pure silazane-derived ceramics.

Despite the first promising results the next work on SiCN as anode material was not published until 2006 by Kolb et al..[38] Within this work SiCN derived from commercially available polysilazane VL20 was investigated in a temperature range of 1150 °C to 1550 °C. The pyrolyzed ceramics were almost inactive for lithiation and did not exceed a first cycle delithiation capacity of 39 mAh·g^{-1}. Besides pure SiCN ceramics, Kolb et al. also investigated a composite made of cross-linked VL20 and graphite (weight ratio 1:3) in order to suppress exfoliation of the graphite. The mixture was pyrolyzed in a temperature range of 450 °C to 1250 °C. First cycle reversible capacities of up to 474 mAh·g^{-1} were achieved, being the factor 1.3 higher than for the reference graphite electrode prepared. The reference graphite electrode showed a slight capacity fading with prolonged cycling whereas the capacity of the composite even increased with increasing cycle number.

These synergy effects, namely the increased capacity in comparison to the individual components and an enhanced cycling stability of composite materials consisting of graphite embedded into a polymer-derived SiCN matrix, have also been observed by Graczyk-Zajac et al..[39] For this work commercial polysilazane HTT1800 was mixed with graphite SLP50 at a weight ratio of 1:1 and pyrolyzed at three different temperatures, 950 °C, 1100 °C and 1300 °C. Although the composite consisted to large amounts of SiCN derived from HTT1800, which is almost inactive for lithium storage itself, 1st cycle delithiation capacities up to 376 mAh·g^{-1} were measured. In particular the composite pyrolyzed at 1300 °C exhibited enhanced cycling stability and high rate capability in comparison to the the reference graphite electrode. Similar results with respect to the electrochemical performance were also made by Feng et al.[40] for a composite material of SiCN derived from polysilylethylenediamine (PSEDA) and graphite. In contrast to the work of Graczyk-Zajac et al. the precursor was pyrolyzed prior to the mixing with graphite and a heat treatment was performed on the powder mixture with a ceramic to graphite ratio of 9:1 in weight. The same experimental approach was adopted for composites of PSEDA-derived SiCN and 10 wt% of carbon nano tubes (CNTs) [41] instead of graphite, leading to comparable effects. For both PSEDA based composites a fading during the initial 30 cycles took place before the capacity stabilized at 400 mAh·g^{-1} to 450 mAh·g^{-1} and 425 mAh·g^{-1}, respectively, whereas the HTT1800 based composite material exhibited stable delithiation capacities from the beginning.

Besides composite materials of graphite or CNTs in an SiCN matrix also hard carbons derived from potato starch within a SiCN matrix were investigated.[42] Contrary to the composite materials described above no improvement with respect to the capacity was observed. However, a mixture of the polysilazane precursor HTT1800 with the potato starch lead to higher capacities and good rate capabilities. Please note, that it is not valid to talk about this material as a SiCN ceramic anymore due to the high amount of oxygen within these samples originating from the potato starch. Moreover, it stays arguable whether this procedure should be denoted as single-source precursor route or as blending. The authors assume a reaction of the -OH groups of the potato starch with the polysilazane precursor based on their results from thermogravimetric analysis (TGA) and elemental analysis but did not perform any measurements for evaluating the molecular structure.

A similar approach, i.e. the mixing of a polysilazane with a carbon precursor, was studied by Chen et al..[43] Within their work they mixed VL20 with divinylbenzene (DVB) at varying weight ratios prior to the pyrolysis. They claim, that a stepwise heating to first 70 °C and than to 120 °C causes a thermally induced phase separation of cross-linked DVB and cross-linked VL20 due to higher activities of the DVB vinyl groups for polymerization reactions in comparison to the vinyl groups of VL20. The best electrochemical performance was achieved for a VL20 to DVB ratio of 2:3 with stable capacities of 480 $\mathrm{mAh \cdot g^{-1}}$ after 15 cycles.

Studies on single-source derived SiCN materials were performed by Su et al. [44] and Feng [45] using PSEDA and Kaspar et al. [46] and Graczyk-Zajac et al. [47] using polysilylcarbodiimides. Within the work of Su et al. PSEDA was pyrolyzed at temperatures ranging from 600 °C to 1500 °C. The best electrochemical performance was found for ceramics pyrolyzed at temperatures below the crystallization onset of SiC and above the temperature where SiCN is still containing organics. For a pyrolysis temperature of 1000 °C a first cycle discharge capacity of 465 $\mathrm{mAh \cdot g^{-1}}$ was measured, though the material suffered from a constant fading with prolonged cycling and its discharge capacity dropped eventually to 171 $\mathrm{mAh \cdot g^{-1}}$ after 30 cycles. An additional heat treatment at 1000 °C under argon on this particular ceramic lead to improvement on both, capacity and cycling stability.[45]

The work on polysilycarbodiimides was conducted on poly(diphenylsilylcarbodiimide) [46] and poly(phenylvinylsilylcarbodiimide) [47]. The use of this particular precursors lead to high free carbon contents of 57 wt% and 47 wt% in the SiCN ceramics after pyrolysis at 1300 °C. For SiCN derived from poly(diphenylsilylcarbodiimide) reversible capacities up to 392 $\mathrm{mAh \cdot g^{-1}}$ were reported. The best performance for poly(phenylvinylsilylcarbodiimide) derived ceramics was obtained for a pyrolysis temperature of 1300 °C and a high oxygen contamination of more than 10 wt% giving a stable delithiation capacity of 290 $\mathrm{mAh \cdot g^{-1}}$. As already discussed before this material should however not be denoted to as SiCN but rather as a SiCNO ceramic. Within both studies no conducting additive was used for the electrode preparation which possibly lowered the electrochemical performance of these materials.

Ahn et al. reported on the electrochemical behavior of SiCNO ceramics obtained via mixing of silazane and a siloxane (polyureasilazane with 1,3,5,7-tetramethyl-1,3,5,7-tetravinylcyclotertrasiloxane) to tailor the nitrogen to oxygen ratio within the ceramics.[48] Based on their results they concluded that a nitrogen to oxygen ratio below one is required for high capacities, i.e. capacities exceeding the theoretical capacity of graphite multiplied by the fraction of free carbon present in the ceramic. This is explained by the ability of silicon within the mixed bond configuration to reversibly store lithium only if it is bond to oxygen. As silicon is bond to nitrogen the more covalent nature of this bonding does not allow for inducing a dipole into the lithium and thereby reducing the energy barrier. The capability of the mixed bond network of SiOC to accommodate lithium was supported by Liu et al. [49] using ^{29}Si MAS Nuclear Magnetic Resonance (NMR) measurements in combination with X-ray photoelectron spectroscopy (XPS) measurements. Within their studies tetrahedra of SiO_4. SiO_3C, SiO_2C_2 were accounted for reversible lithium storage, whereas $SiOC_3$ and parts of the SiO_4 units are the source of irreversible capacity. The finding that the mixed bond amorphous network plays a major role as lithiation site in PDCs is contradicting to the findings of solid state NMR studies on SiOC ceramics by Fukui et al..[50] Their work presented an experimental proof that the SiOC network is indeed storing lithium ions but only to a minor amount whereas the main part is stored in interstitial places or at the edges of graphene layers of the free carbon phase. In addition micropores provide a minor contribution to the overall stored capacity.

In comparison, much more studies have been published on polymer-derived SiOC anode materials than on polymer-derived SiCN anode materials. The work on polymer-derived silicon oxycarbide as an anode material started in the middle of the 1990’s with Wilson et al. investigating the lithium insertion in pyrolyzed siloxane polymers. Their motivation was to access the high capacities of silicon as an alloying material with Li and at the same time prevent it from fading due to cracking and pulverization.[51] This work already showed the promising properties of PDCs as anode materials, i.e. their high specific capacities of up to 600 $\mathrm{mAh \cdot g^{-1}}$, but also revealed that the first cycle irreversible capacity is a major drawback of this material class. Additionally it was shown, that the capacity of the samples strongly drops when the pyrolysis temperature exceeds the crystallization onset of SiC. Further studies of Wilson et al. [52] on blends of pitch and polysilane and an extensive study of Xing et al.

[53] on polysiloxanes were facing the problem of the high irreversible first cycle capacity. Both studies demonstrated a correlation of the oxygen content to the irreversible capacity, i.e. the higher the oxygen content the higher the irreversible capacity. An increasing amount of oxygen was also found to enlarge the hysteresis of these materials. In addition Xing et al. found that the ceramics of an elemental composition close to the tie-line of C to SiO_2 (ternary composition diagram of Si-O-C) showed promising capacities, however, samples on the tie-line of C-SiC are more promising due to the reduced irreversible losses. Moreover, the samples should exceed a threshold value in the carbon content of 30 at% to achieve a good electrochemical performance.

2.5 Silicon as Active Material in Lithium-Ion Batteries

There is a huge interest in using silicon as anode material because of its ability to reversibly alloy with lithium giving high specific and volumetric capacity. Additionally its potential at 370 mV vs. Li/Li^+ [54] is suitable for high voltage batteries. The electrochemical reaction of silicon with lithium at elevated temperatures of 415 °C occurs via intermediate phases, namely $Li_{12}Si_7$, Li_7Si_3, $Li_{13}Si_4$, $Li_{22}Si_5$.[55] These phases are in accordance with the crystalline phases in the Li-Si phase diagram. If silicon is alloyed up to the lithium richest phase $Li_{22}Si_5$, it exhibits a specific capacity of 4212 $mAh \cdot g^{-1}$ and a volumetric capacity of about 2200 $mAh \cdot cm^{-3}$.

However, at room temperature the electrochemical alloying of silicon is not in agreement with the phase diagram. It was shown by Obrovac and Christensen that crystalline silicon turns amorphous during the first alloying process and crystallizes again to $Li_{15}Si_4$ below 50 mV.[56] This finding was confirmed by in-situ X-ray diffraction studies [57]. During dealloying the crystalline $Li_{15}Si_4$ vanishes subsequently and amorphous Li_xSi is formed. The formation of $Li_{15}Si_4$ corresponds to a specific capacity of 3579 $mAh \cdot g^{-1}$ which is the highest available capacity of silicon at room temperature.

Despite the high capacities silicon has not been used in commercial batteries till now. The alloying process is accompanied by a large volume increase of about 260 %. The volume changes are accompanied by stress which causes a cracking and pulverization of the electrode, so that the electrical contact of active material to the current collector is not provided any longer. In consequence a rapid fading of the capacity with ongoing cycling occurs. Large volume expansions can additionally lead to a cracking of the SEI, hence unprotected active material gets into contact with the electrolyte again and irreversible reactions proceed with ongoing cycling.[58]

It is possible to improve the cycling stability by limiting the lower cut-off potential to above 50 mV.[12, 56] Thereby the phase transformation from amorphous Li_xSi to crystalline $Li_{15}Si_4$ and vice versa is suppressed and isotropic volume changes take place. The limitation in cut-off voltage is at the expense of the capacity, however, the achievable capacities are still sufficient for practical use as has already been discussed in Chapter 2.2. Moreover it has been proposed that the utilization of nanoscaled particles is advantageous for the cycling stability of materials alloying with lithium, e.g. no cracking in silicon nano particles was visible in in-situ Transmission Electron Microscopy (TEM) experiments for particle sizes below a threshold value of about 150 nm.[59]

Different approaches like i) embedding silicon into an active or inactive matrix, ii) chemical bonding of silicon particles to the binder or conducting additive, iii) utilization of nanowires or/and iv) the synthesis of silicon-carbon composites with cavities around the silicon particles have been proposed in order to further improve the cycling stability of silicon. Some of these procedures showed significant benefits on the stability of silicon based electrodes and will be introduced in more detail in the following.

i) **embedding silicon into an active or inactive matrix:**

A common attempt to improve the cycling behavior of silicon is the synthesis of composite materials with silicon dispersed in either an active or inactive matrix. In this context an active matrix refers to a material capable of accommodating lithium itself and therefore attributing to the overall capacity whereas an inactive matrix shows no lithium storage ability. Most of the investigated active matrix materials are carbons. There is a huge variety of experimental approaches to synthesize those composites, e.g. by a carbon coating via a precursor route, ball milling or a deposition route from the gas phase.

The first approach is realized by dispersing silicon nano particles in a carbon precursor, e.g. poly(vinyl chloride) (PVC) [60] or sucrose [61, 62], and conduct a carbonization of the precursor. Electrodes made of nanometer sized silicon particles in a range of 10 nm to 100 nm completely degraded within 15 cycles. A composite material consisting of the same silicon particles embedded in a carbon matrix derived from PVC (56 wt%) showed stable cycling capacities of 1000 $mAh \cdot g^{-1}$ over 20 cycles.[60]

The positive influence of a carbon coating was also found by Yang et al.[61] A silicon reference electrode with particle sizes below 100 nm lost 90 % of its initial capacity within the first five cycles. For the coating the silicon particles were dispersed in sucrose. The carbonization of the sucrose was carried out via a dehydration reaction in the presence of H_2SO_4. Although the so obtained composite material (20 wt% of silicon) still suffered from capacity fading the stability was strongly increased showing a capacity retention of 50 % after 75 cycles. A further improvement of the cycling stability was achieved for this material by ball milling the as-prepared material with graphite.[62] 84.1 % of the first cycle delithiation capacity of 712.8 $mAh{\cdot}g^{-1}$ was retained after 50 cycles.

Kim et al. performed high-energy ball milling for the synthesis of silicon-carbon composites.[63] Ball milling was therefore conducted on a silicon-polystyrene mixture followed by a pyrolysis of the polystyrene precursor. The capacity loss per cycle of the final material with a silicon to carbon ratio of 1:2 and an initial capacity of 850 $mAh{\cdot}g^{-1}$ was reduced to about 1.1 %. Kim et al. also investigated the electrochemical performance of silicon-silicon carbide active materials.[64] The composite material was either obtained by ball milling of silicon with silicon carbide or by reactive ball-milling of silicon and carbon. Both active-inactive composites had an initial capacity of about 370 $mAh{\cdot}g^{-1}$, but the material obtained from the reactive ball-milling route showed a slightly better capacity retention, loosing only about 0.9 % of its capacity per cycle.

Carbon coating can also be achieved by a chemical vapor deposition.[65, 66] Liu et al.[66] used a fluidized-bed type chemical vapor deposition with benzene as carbon source and nitrogen as carrier gas at a deposition temperature of 900 °C to synthesize silicon-carbon composites at a weight ratio of roughly 3:1. For electrochemical testing the capacity was limited. Two fading modes, i) a local loss of electronic contact and ii) the break down of entire electrode structure, were found for silicon reference electrodes. The silicon covered with carbon did only suffer from the second degradation mechanism and capacity retention was extended to 57 cycles at a capacity limit of 1000 $mAh{\cdot}g^{-1}$ whereas the silicon reference electrode rapidly failed after 8 cycles.

ii) **chemical bonding of silicon particles:**

Mazouzi et al. achieved a chemical bonding by an esterfication reaction of the C(O)OH groups of sodium carboxymethyl cellulose (CMC) binder with the SiOH surface groups of silicon.[67] In order to suppress the repulsion between negatively charged SiO^- groups and the ionized carboxylic acid groups of CMC the reaction was performed in a buffered solution of pH 3. During electrochemical testing the lithiation capacity was additionally limited to $1200\,mAh{\cdot}g^{-1}$. Whereas the reference electrode without chemical bonding between silicon and binder failed after 80 cycles the samples prepared in buffered acidic conditions showed a tremendous increase in cycling stability exhibiting more than 700 cycles with $1200\,mAh{\cdot}g^{-1}$.

Chemical bonding of silicon was also investigated by Martin et al..[68] However, the silicon was not bond to the binder but to the surface of graphite. First, p-phenylenediamine was grafted on the graphite. In the following a phenyl bridge was established between the graphite and hydrogen passivated silicon powder. The so prepared material showed an increased capacity retention of 52 % after 50 cycles compared to 38 % for the non-grafted material.

iii) **the synthesis of silicon-carbon composites with cavities around the silicon particles:**

Recently, numerous publications were concerned with the fabrication of porous anode structures to accommodate the large volume changes of silicon. Among them, silicon-carbon composites with a core-shell structure and cavities around the silicon have been investigated.[69, 70, 71, 72] This structure is generally obtained by the formation of a silicon oxide layer on silicon particles. In a further step a carbon coating is applied on the silicon oxide layer. To form the hollow spaces around the silicon particles the silicon oxide layer is finally removed by a treatment with hydrofluoric acid. The so produced active material showed a capacity retention of 86 % after 100 cycles at a discharge capacity of $760\,mAh{\cdot}g^{-1}$.[72]

iv) **silicon nanowires:**

Several publications have proven excellent performances of anodes made from silicon nanowires.[73, 74, 75] The nanowires were directly grown on the current collector making the use of conducting additives and binders redundant. Moreover, the geometry of the nanowires allows for a better accommodation of the volume changes and diffusion paths are small.[73] This leads, in consequence, to a high cycling stability and excellent rate capability. The nanowires can be lithiated up to a capacity of more than 4200 mAh·g^{-1}. This electrochemical characteristic of the nanowires differs from the observations made by Obrovac et al.[56]. Please note, that a capacity of 4200 mAh·g^{-1} is rather in the range of silicon cycled at elevated temperatures of 450 °C. Additionally, no crystallization occurred below a value of 50 mV but the silicon stayed amorphous throughout prolonged cycling.

Recently the dispersion of silicon nano particles in a polymer-derived silicon oxycarbide matrix was reported by Liu et al. [76] and Kaspar et al. [77]. Liu et al. used a sol-gel approach for the composite preparation mixing silicon nano particles with an average size of 60 nm with ethanol, triethoxysilane, diethoxymethylsilane, DVB, polysiloxane, distilled water and chloroplatinic acid. The resulting gel was pyrolyzed at 1100 °C giving an elemental silicon content of roughly 10 wt% and about 21 wt% of free carbon. For the as prepared material a 1st cycle reversible capacity of 1372 mAh·g^{-1} was obtained, being about 400 mAh·g^{-1} higher than for a reference material prepared without silicon nano powder. The capacity droped to 73 % of ts initial value after 30 cycles. Kaspar et al. prepared their composites by mixing polyorganosiloxane Polyramic RD-684 (PolyR) with either crystalline silicon particles (30-50 nm) or amorphous silicon particles (36 nm) followed by a pyrolysis under argon at 1100 °C. After pyrolysis the composites contained 7 wt% (amorphous) and 20 wt% (crystalline) of elemental silicon. 1st cycle reversible capacities of 555 mAh·g^{-1} and 804 mAh·g^{-1} were achieved. Both samples showed an increase in capacity up to 704 mAh·g^{-1} and 965 mAh·g^{-1} during the first few cycles. Whereas the sample with crystalline silicon rapidly broke down after reaching its maximum value due to cracking of the ceramic matrix the capacity of the sample with the amorphous silicon showed an improved stability with a capacity retention of 88 % after 100 cycles (with respect to the maximum obtained value).

For more information on silicon as anode material the reader is referred to review papers like [14] or [78] dealing mainly on nanostructured silicon but also on the effect of SEI formation and inactive electrode materials (substrate/current collector, binder, conducting additive). Aspects of materials that electrochemically alloy with lithium are summarized in a review article by Zhang et al.[79].

3 Experimental

The following chapter presents the experimental details as well as the data handling for the measurements in which a more precise description is necessary. The experimental work is divided into four major parts. First, the fabrication of active materials consisting solely of SiCN is discussed. Afterwards the fabrication of composite materials based on SiCN and the experimental details for the characterization of the obtained ceramic powders are presented. The fourth part describes the preparation of the active materials for electrochemical testing and the electrochemical methods used for this characterization.

The focus of the descriptions is set on the standard procedures for the experiments. If not specified in the text, those procedures were applied. However, sometimes it was necessary to differ from the standard procedures. Any deviations are specified directly within the presentation of the results.

3.1 Fabrication of SiCN Active Materials

For the fabrication of pure silicon carbonitride ceramics, SiCN precursors with varying molecular structures were used. A summary of the investigated samples is given in Table 3.1.

Whereas HTT1800 (Clariant GmbH, Germany) is a commercially available polyorganosilazane, the other precursors have been synthesized in house. The structural formulas and the chemical names of the investigated precursors are shown in Figure 3.1. The ceramics obtained from GM35, GM65, $HN1_a$ and $HN3_a$ and DiPhen were provided by group members. To perform additional experiments another batch of HN1 ($HN1_b$) and HN3 ($HN3_b$) was synthesized. The following two chapters will therefore describe the synthesis of poly(phenylvinylsilylcarbodiimide) (HN1) and poly(phenylvinylsilazane) (HN3) in detail. Moreover, the commercial precursor HTT1800 was chemically modified in order to vary the carbon content of the resulting ceramic after pyrolysis. The procedure of the chemical modification is summarized in Chapter 3.1.3. Finally, the conditions of the polymer to ceramic transformation are given.

Table 3.1: Investigated precursors and their pyrolysis temperature.

Precursor	$T_{Pyrolysis}$ [°C]
HTT1800	1100
$HN1_a$	1100
$HN3_a$	1100
$HN1_b$	800-1300
$HN3_b$	800-1300
GM35	1100
GM65	1100
DiPhen	1100

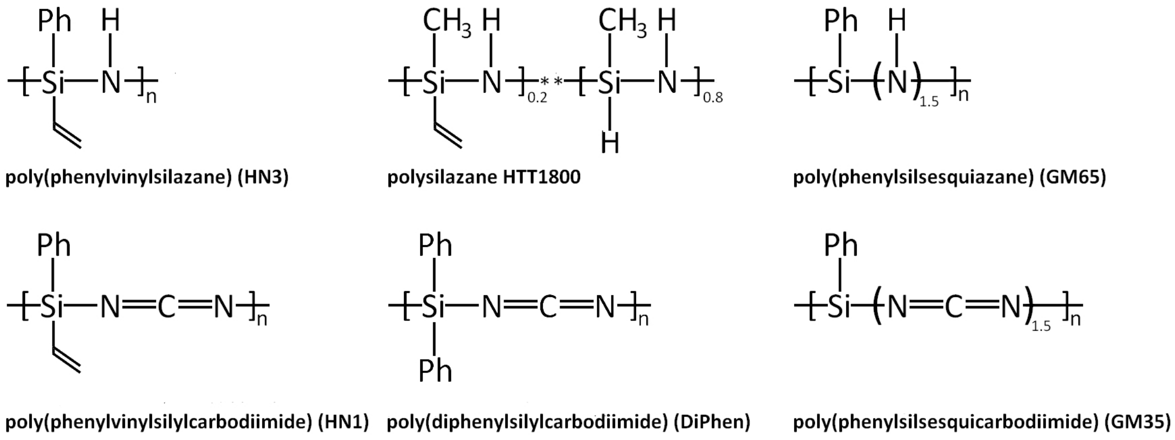

Figure 3.1: Structures and chemical names of organosilicon precursors used.

3.1.1 Synthesis of Poly(phenylvinylsilylcarbodiimide)

The synthesis of poly(phenylvinylsilylcarbodiimide) (HN1) was carried out according to Reference [32].

Bis(trimethylsilyl)carbodiimide was synthesized under argon according to Reference [23]. 177 g of hexamethyldisilazane (ABCR, purity 99.5 %), 42 g of dicyandiamide (Sigma Aldrich, purity 99 %) and 0.2 g of ammonium sulfate as a catalyst were mixed with a stepwise increase of the temperature from 130 °C till 160 °C under reflux until a clear solution was obtained (approximately 15 h). Bis(trimethylsilyl)carbodiimide was separated from the side products of the reaction by a distillation process.

The polycondensation reaction was performed under inert argon atmosphere using Schlenk technique. 0.1477 mol (25 mL) of vinylphenyldichlorosilane and 0.1477 mol (33.35 mL) of bis(trimethylsilyl)carbodiimide were added into a Schlenk flask under constant stirring. Additionally 0.0738 mol (5.94 mL) pyridin were added to catalyze the reaction. The mixture was first heated up in an oil bath to 66 °C for 7 h using a reflux condensor. Approximately 0.4 mL of the mixture were taken out of the flask and mixed with 0.2 mL C_6D_6 for ^1H, ^{13}C dept and ^{29}Si dept NMR probing at 500 MHz. Afterward another heating step was applied at 120 °C for 11 h. NMR probing was performed after 5.5 h and after 11 h. The reaction equation is given in formula 3.1.

$$n(CH_3)_3Si-NCN-Si(CH_3)_3+C_8H_8Cl_2Si\xrightarrow{[Py]}[SiN]_n+2nCH_3SiCl \tag{3.1}$$

The byproduct trimethylchlorosilane and the pyridine were removed by subsequently heating under vacuum. The temperature was stepwise increased from 25 °C to 60 °C to 120 °C till no gas formation was visible anymore.

3.1.2 Synthesis of Poly(phenylvinylsilazane)

The synthesis of poly(phenylvinylsilazane) (HN3) was done via a salt-free polycondensation reaction of 0.1478 mol (30.83 mL) hexamethyldisalazane and 0.1478 mol (25 mL) vinylphenyldichlorosilane. 0.0739 mol (5.93 mL) pyridine were used as a catalyst. Analogous to the synthesis of HN1 all steps very carried out under inert argon atmosphere using

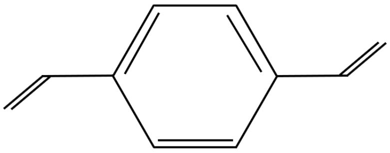

Figure 3.2: Structural formula of p-divinylbenzene.

schlenk technique. The mixed chemicals were kept under reflux for 21 h at 60 °C. The reaction equation is shown in formula 3.2.

$$n(CH_3)_3Si-NH-Si(CH_3)_3+C_8H_8Cl_2Si\xrightarrow{[Py]}[SiN]_n+2nCH_3SiCl \tag{3.2}$$

Afterwards a distillation with a stepwise increasing temperature from 120 °C up to 200 °C was performed followed by applying vacuum at room temperature till no gas evolution was visible anymore.

3.1.3 Chemical Modification of the Polysilazane HTT1800 with Divinylbenzene

The commercial polysilazane HTT1800 was modified with DVB (p-divinylbenzene, 85 %, Sigma-Aldrich, UK). The structural formula of DVB is given in Figure 3.2. The modification occurs via a hydrosilylation reaction (compare Chapter 2.3) of the Si-H groups of the HTT1800 with the vinyl groups of the DVB. All together three different ratios of the vinyl groups of DVB to the Si-H groups of HTT1800 were tested, namely a stoichiometric ratio, an excess of vinyl groups and an excess of Si-H groups, respectively. First, 20 g of HTT1800 were mixed with 8 g (later named HD1), 16 g (HD2) and 32 g (HD3) of DVB. Additionally, 10 ppm platinum catalyst (Pt(0)-1,3-divinyl-1,1,3,3-tetramethyldisiloxane in xylene, Sigma-Aldrich, UK) relative to HTT1800 were added to the mixtures to catalyze the hydrosilylation reaction. The mixture was refluxed at 120 °C for 12 h. All experiments were performed under inert argon atmosphere using Schlenk technique.

3.1.4 Pyrolysis and Powder Preparation

Pyrolysis of the organosilicon polymers up to 1100 °C were carried out in a tube furnace. The polymers were filled into a silica glass crucible which was placed into a silica glass tube. During pyrolysis a constant argon flow was applied. For pyrolysis temperatures of 1300 °C

Table 3.2: Cross linking temperatures, dwelling times for cross linking, and dwelling times at pyrolysis temperature for different precursor.

Precursor	$T_{crosslinking}$ [°C]	$t_{dwell,crosslinking}$ [h]	$t_{dwell,pyrolysis}$ [h]
HTT1800	250	3	3
GM35	-	-	2
GM65	-	-	2
HN1	255	5	2
HN3	269	7	2
DiPhen	-	-	2

samples were first pyrolyzed at 1000 °C and afterward placed into a silicon carbide crucible. Pyrolysis was performed in an alumina tube furnace under constant argon flow. Heating and cooling rates were set to 100 °C·h^{-1}. The dwelling time at the pyrolysis temperature varied in dependence of the used polymer. The dwelling times are listed in Table 3.2. The table also contains cross-linking temperatures and dwelling times for cross-linking.

The resulting ceramics were hand ground after pyrolysis with an agate stone moulder and sieved with a mesh seize of 25 μm or 40 μm.

3.2 Synthesis of Active Composite Materials Containing Elemental Silicon

A variety of different composite materials have been synthesized in order to increase the cycling stability of silicon. A schematic graph of the different composites and their preparation routes is shown in Figure 3.3. An overview of the different composites that have been tested is also given in Table 3.3. The amount of ceramic SiCN matrix after pyrolysis of HTT1800 was determined on the basis of a thermogravimetric analysis (TGA) presented in Reference [39]. The calculation of composites which contain HN1$_b$ and HN3$_b$ were based on the measured mass loss during pyrolysis of the pure materials in Chapter 3.1.4. It was assumed that no reactions during the pyrolysis at 1100 °C between the silicon/carbon and the precursor influence the ceramic yield.

The different approaches during the synthesis of the composites can be divided into three major steps, i) coating of particles with carbon, ii) embedding of silicon or silicon covered with

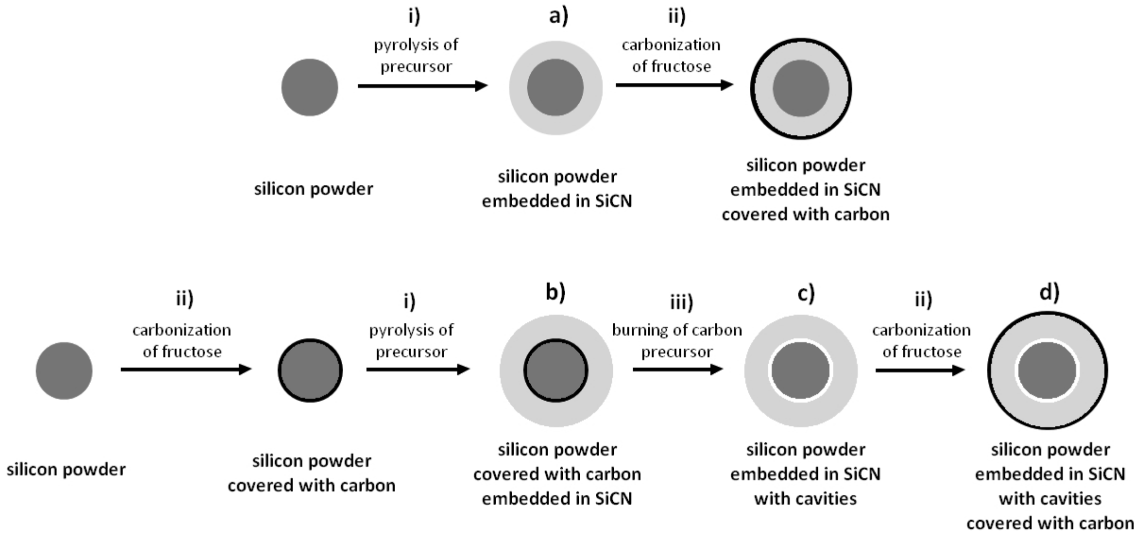

Figure 3.3: Schematic drawing of the synthesized composites and their preparation routes. A detailed list of ratios, temperatures and materials used for the composites a), b), c) and d) is given in Table 3.3. The experimental procedure for the different processing steps i) - iii) is given in the text.

Table 3.3: Overview of the composites tested including the used precursor, the weight ratios of silicon to SiCN and the weight ratios of silicon to carbon coating. The precursors used for the synthesis have already been introduced in Chapter 3.1.

Composites	Precursor	Sample Name	Si:SiCN [wt%] after pyrolysis	Si:Carbon [wt%] after carbonization[2]	$T_{Carbonization}$[1] [°C]	$T_{Carbonization}$[2] [°C]
a	HTT1800	Si:HTT-1:1	1:1	-	-	-
	HTT1800	HTT:Si-1:4	1:4	-	-	-
	HN1$_b$	HN1$_b$:Si-1:1	1:1	-	-	-
	HN1$_b$	HN1$_b$:Si-1:4	1:4	-	-	-
	HN3$_b$	HN3$_b$:Si-1:1	1:1	-	-	-
	HN3$_b$	HN3$_b$:Si-1:4	1:4	-	-	-
b	HTT1800	Si:30F:SiCN	1:4	7:3	600	
	HTT1800	Si:60F:SiCN	1:4	2:3	1100	
c	HTT1800	Si:F:SiCN(30)	1:4	7:3	600	
	HTT1800	Si:F:SiCN(60)	1:4	2:3	1100	
d	HTT1800	Si:F:SiCN(30):30F-900	1:4	7:3	600	900
	HTT1800	Si:F:SiCN(60):30F-900	1:4	2:3	1100	900

[1] Carbonization temperature for the coating of the silicon particles.

[2] Carbonization temperature for the coating of the composite material after the additional heat treatment on air.

carbon in a ceramic matrix and iii) the introduction of cavities around the silicon particles. These steps will be shortly described in the following:

i) D-(-)-Fructose (purity >99 %, Sigma Aldrich) was dissolved in a mixture of ethanol and water (ratio 9:1). The silicon nano powder, the ceramic or the composite was dispersed in the solution of fructose using an ultra-turrax. The solvents were evaporated under vacuum at room temperature for several hours. For carbonization of the fructose the obtained powder was placed into an alumina furnace using a quartz crucible. The carbonization was performed under inert argon atmosphere. Heating and cooling rates were set to 100 °C·h^{-1} and the dwelling time lasted 6 h.

ii) Crystalline nano silicon powder (30 nm-50 nm, Nanostructured & Amorphous Materials Inc., USA) or silicon powder covered with carbon were mixed with different precursors, namely HTT1800, HN1$_b$ and HN3$_b$ in two different weight ratios. For a weight ratio of 1:4 of silicon to ceramic matrix after pyrolysis the silicon was directly dispersed in the liquid precursor using an ultra-turrax (IKA T25 digital ultra-turrax). For a weight ratio of 1:1 after pyrolysis an additional solvent (toluene) was required to allow for mixing of the two components with the ultra-turrax. The pyrolysis of the mixtures was performed according to the programs used for the pure polymers at 1100 °C and have been described in Chapter 3.1.4.

iii) To create free space around the silicon particles the material consisting of silicon nano powder covered with carbon and embedded into a SiCN matrix derived from HTT1800 was heated in air in an alumina furnace at 500 °C for 2 h. The heating and the cooling rates were set to 100 °C·h^{-1}.

Besides the composite materials the pure fructose was also carbonized at temperatures ranging from 300 °C to 1100 °C to obtain reference materials with respect to the yield, the electrical conductivity and the electrochemical behavior.

3.3 Characterization of Active Materials

The following chapters will state precisely on the equipment used for measurements, explain the sample preparation for the different methods applied and describe the evaluation of the data.

3.3.1 Fourier Transform Infrared Spectroscopy

Fourier Transform Infrared Spectroscopy (FTIR) measurements were performed on HTT1800 and HTT1800 modified with DVB to monitor the hydrosilylation reactions. The samples were measured in reflection mode using an attenuated total reflection (ATR) unit. The samples were placed at the ATR unit inside of a glove box to prevent reactions with moisture of the air.

3.3.2 Elemental Analysis

To determine the elemental composition of the pyrolyzed ceramics elemental analysis was performed. Besides silicon, carbon and nitrogen the ceramic samples usually contain oxygen, chlorine and hydrogen. Whereas chlorine and hydrogen are part of the reactants used for the synthesis, oxygen is introduced into the samples during synthesis and pyrolysis. The carbon amount was determined by a combustion analysis with a carbon analyzer Leco C-200, the nitrogen and oxygen content by hot gas extraction with a Leco TC-436 N/O analyzer (Leco Corporation, Michigan, USA). The chlorine and the hydrogen content were measured at the Mikroanalytisches Labor Pascher (Remagen, Germany). The silicon content was not measured but calculated as the difference of the above mentioned elements to 100 %. As some of the ceramics are still sensible to ambient atmosphere, especially when pyrolyzed at low temperatures, the samples were not exposed to air during the measurement. The knowledge of the elemental composition allows to estimate the quantity of free carbon within the samples using formula 3.3 [48] with x, y, z being taken from the empirical formula $SiC_xN_yO_z$ and M_C, M_O, M_N and M_{Si} being the molar mass of the particular elements. For this estimation it is first assumed that oxygen is bonded to silicon as SiO_2 and nitrogen is bonded to silicon as Si_3N_4. The remaining silicon is existing as SiC. Eventually the excess of carbon can be assumed to form the free carbon phase. However, this calculation neglects the influence of hydrogen and chlorine on the phase composition.

$$wt.\%\ free\ C = \frac{\left(x - 1 + \frac{y}{2} + \frac{3z}{4}\right) \cdot M_C}{M_{Si} + x \cdot M_C + y \cdot M_O + z \cdot M_N} \cdot 100 \tag{3.3}$$

3.3.3 X-ray Diffraction

X-ray powder diffraction pattern of the pyrolyzed ceramics and silicon were either obtained in flat-sample transmission geometry on a STOE STAD1 P equipped with monochromatic Mo K_α (λ=0.07093 nm) radiation or the powder samples were measured at a STOE X-ray diffractometer using Ni-filtered Cu K_α (λ=0.15405 nm) radiation. For the measurement at the STOE STADI1 P isoamylacetate was used to fix the powder between two foils of acetate.

For a better readability the 2θ values of all spectra recorded with Cu-K_α radiation have been recalculated to the 2θ values of Mo-K_α radiation using Bragg's law given in Equation 3.4.

$$n\lambda = 2d \cdot sin\theta \tag{3.4}$$

3.3.4 Raman Spectroscopy

The Raman spectra were recorded with a Horiba HR800 micro-Raman spectrometer (Horiba Jobin Yvon, Bensheim, Germany) equipped with an Ar laser (irradiation wavelength 514.5 nm and 488.0 nm) and a He-Ne laser (irradiation wavelength 632.8 nm). The excitation line has its own interference filter (to filter out the plasma emission) and a Raman notch filter (for laser light rejection). The measurements were performed with a grating of 600 and a confocal microscope (magnification 50x, NA 0.5) with a 100 μm aperture, giving a resolution of approximately 2 μm - 4 μm. For the evaluation of the free carbon phase, curve fitting of the Raman bands (OriginPro 9.0 Software) was applied. To follow structural changes within the free carbon phase at different pyrolysis temperatures the bandwidth and intensity of the D- and G-band were identified according to the fitting procedure used by Janakiraman et al. [80], i.e. four lorentzian curves with starting positions at 1200 cm^{-1} (D4-band), 1320 cm^{-1} (D-band), 1500 cm^{-1} (D3-band) and 1600 cm^{-1} (G-band) were set. The overtones are not considered for the evaluation. The intensity ratio of the D and G modes I_D/I_G also enables the evaluation of the carbon nanodomain size by using the formula reported by Ferrari and Robertson [81]:

$$\frac{I_D}{I_G} = C'(\lambda) L_a^2 \tag{3.5}$$

L_a is the size of carbon domains along the six fold ring plane (lateral size), and C′ is a coefficient that depends on the excitation wavelength of the laser. E.g. the value of the coefficient C´ for the wavelength of 514.5 nm of the Ar-ion laser employed is 0.0055 $Å^{-2}$. Formula 3.5 is only valid for stage two of the three-stage model proposed by Ferrari and Robertson [81] and for L_a smaller than 2 nm [82].

3.3.5 Particle Size Distribution Measurements

The particle size distribution of the sieved powders was measured with an Analysette 22 COMPACT (Fritsch, Germany) which is working in a measurement range of 0.3 μm to 300 μm. The measurements were performed in ethanol at constant stirring and ultra sonic treatment.

3.3.6 BET Specific Surface Area

The specific surface area (SSA) and porosity of the samples were determined from the nitrogen adsorption and desorption isotherms with an Autosorb-3B (Quantachrome Instruments, USA) at 77 K using the Brunauer-Emmett-Teller equation and the Barret-Joyner-Halenda method, respectively.

3.3.7 Scanning Electron Microscopy

Scanning Electron Microscopy (SEM) pictures were taken at a Philips XL30 FEG (Philips, Netherlands). All samples were coated with a thin layer of gold using a Quorum Q300T D (Quorum Technologies Ltd, United Kingdom) for 20 s at 30 mA. Imaging was performed at an acceleration voltage of 10 kV with a secondary electron detector. Cycled electrodes needed an additional preparation step prior to the gold coating to remove the salt originating from the electrolyte. The cycled electrodes were washed with dimethyl carbonate DMC (Sigma-Aldrich) after they have been disassembled from the Swagelok® cells and were kept in the glove box for drying.

3.3.8 Thermogravimetric Analysis

Thermogravimetric analysis (TGA) was performed with a STA 449C Jupiter (Netzsch Gerätebau GmbH, Germany) coupled to a FTIR-spectrometer Bruker Tensor27. The TGA was done to monitor the introduction of cavities around silicon particles in the silicon-ceramic composite materials (compare Chapter 3.2) by measuring the mass change as well as the evolution of carbon monoxide and carbon dioxide. The analysis was performed under a constant oxygen gas flow (Air Liquide, purity ≥99.5 %) of 30 ml·L^{-1}. 50 mg of the composite powder were placed into a Al_2O_3 crucible for the measurement. The temperature program was set according to the program used for the heat treatment on the composite materials described in Chapter 3.2, i.e. the sample was heated with 100 °C·h^{-1} up to 400 °C and the dwelling time was set to 3 h. Each 2.26 min FTIR spectra of the outgasing species were recorded in a range from 500 cm^{-1} to 4000 cm^{-1}. The mass change of the sample was recorded with 100 points per minute during the heating ramp and 4 points per minute during the dwelling.

3.4 Characterization Methods Related to the Application of Active Materials as Anode Material in Lithium-Ion Batteries

3.4.1 Electrode Preparation

A homogeneous slurry consisting of 85 wt% active material and varying amounts of Carbon Black Super P® (Timcal Ltd., Switzerland) as conducting additive and polyvinylidenefluoride (PVDF, SOLEF, Germany) dissolved in N-methyl-2-pyrrolidone (NMP, BASF, Germany) as binder was prepared. Typical used ratios of Carbon Black Super P® to PVDF are 1:1 and 2:1. The slurry was printed on the rough side of a copper foil (10 μm thickness, Copper Se-Cu58 (C103), Schlenk Metallfolien, Germany) with a doctor blade. After the printing process the electrodes were dried at temperatures between 40 °C to 80 °C for 24 h. Electrodes of 7 mm or 10 mm in diameter were cut out and dried under vacuum at 80 °C in a Buchi oven for 24 h. Afterward the electrodes were transferred to a glove box (MBraun, Germany) without contact to the ambient air.

3.4.2 Conductivity Measurements

To monitor the influence of the different preparation steps on the electrical conductivity for the composite materials described in Chapter 3.2 4-Point measurements based on the van der Pauw method have been performed on pellets. The pellets were prepared by spreading part of the slurry of the electrode printing on a glass plate for drying at 40 °C for 24 h. After the NMP had been evaporated the material was scratched of the glass plate and ground to a powder. Approximately 100 mg of the as-prepared powder was pressed uniaxial with 30 kN for 5 min.

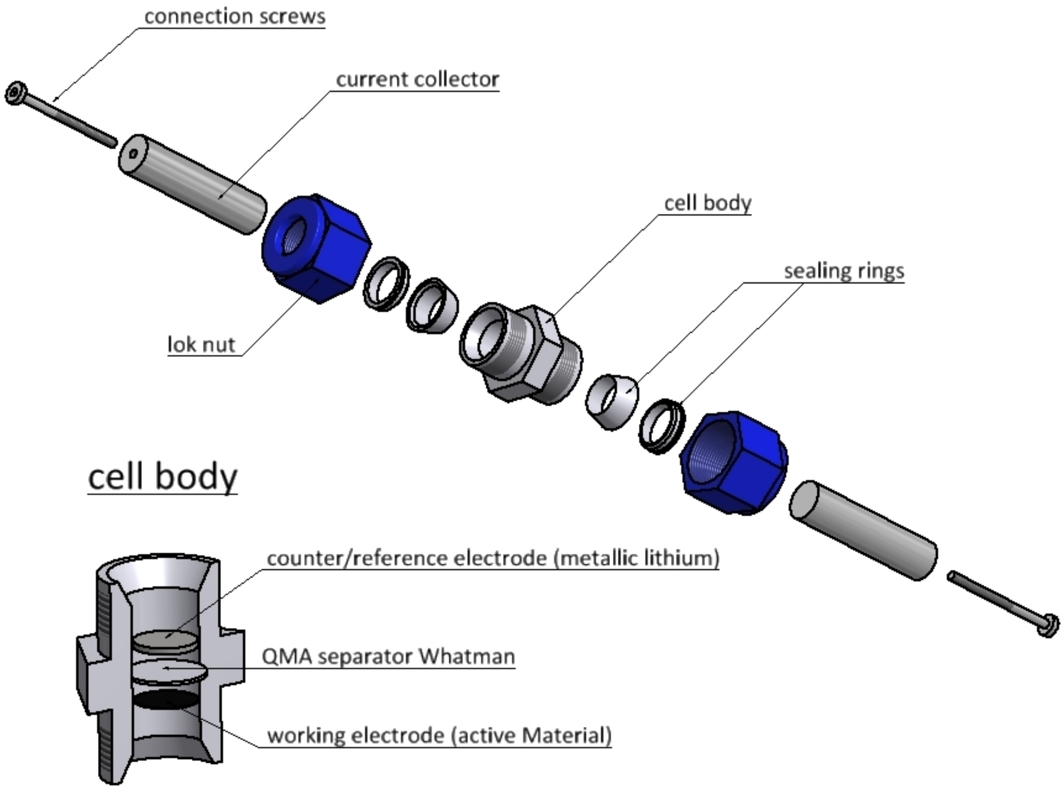

Figure 3.4: Schematic drawing of a Swagelok® cell used for electrochemical testing.

3.4.3 Electrochemical Measurements

Galvanostatic Cycling with Potential Limitation (GCPL) was performed in Swagelok® type half-cell set up with metallic lithium (99.9 % purity, 0.75 mm thickness, Alfa Aesar, Germany) as counter/reference electrode, QMA (Whatman™, United Kingdom) as separator and 180 μL of 1 M $LiPF_6$ in EC:DMC 1:1 wt% (ethylene carbonate:dimethyl carbonate) as electrolyte (LP30, Merck, Germany). A schematic picture of the used Swagelok® cells is shown in Figure 3.4. The testing has been performed with a VMP multipotentiostat (BioLogic Science Instruments, France) at charging (=discharging) rates of C/20, C/10, C/5, C/2 and C/1 calculated with a C/1 current of 372 mA·g^{-1} (taken from the theoretical capacity of graphite of 372 mAh·g^{-1}) for the pure ceramics. The composites which contain silicon have been cycled with a constant rate of C/50 being equal to 71.6 mA·g^{-1} (calculated on the theoretical capacity of silicon at room temperature 3572 mAh·g^{-1}). To prevent confusion the C-rates will be written with small indices, "Si" for silicon and "C" for graphite, referring to the theoretical capacities of commensurating materials used for the calculation of the rate.

3.4.4 Single Particle Measurements

Single Particle Measurements were performed at Kanamura Laboratory, Division of Applied Chemistry, Tokyo Metropolitan University. A schematic setup of the measurement is shown in Figure 3.5. The microelectrode consists of a copper wire with a diameter of 200 μm (The Nilaco Corporation, Japan) and a platinum wire with a diameter of 20 μm (The Nilaco Corporation, Japan) attached to the tip of the copper wire. The combined wires are surrounded by a borosilicate glass capillary (World Precision Instruments, Inc., USA). To prevent electrochemical reactions of the platinum wire during measurement a thin film of copper was electro-deposited on the microelectrode by dipping the head of the electrode into an aqueous solution of 0.6 M $CuSO_4$ and 0.005 M H_2SO_4. A copper plate was used as anode and a current of 50 nA was applied for 120 s using the automatic polarization system HSV-100 (Hokuta Denke, Japan). After the electro-deposition the microelectrode was directly transferred to the glove box (DBO-1KP-STD, MIWA Lock Company, Ltd., Japan), to prevent oxidation of the deposited copper layer. The single particle was contacted under an optical microscope (VHX-200, Keyence, Japan) using a micro manipulator (QuickPro, Micro Support Co., Ltd, Japan). Pictures of the particle were taken at a magnification of 100x and 300x to determine the approximate size of the particle (using lince software). A spherical shape of the particles was assumed. The optical microscope is equipped with a stage to absorb vibrations during measurements. As an electrolyte a 1 M solution of $LiPF_6$ in EC:PC 1:1 in vol % was used (Kishida Chemical Co., Ltd., Japan). A heating plate in combination with a thermo element allowed for varying the electrolyte temperature. For a counter and reference electrode a small piece of metallic lithium foil (Honjo Metal Co., Ltd., Japan) was attached to a nickel wire (The Nilaco Corporation, Japan). Electrochemical testing was performed using a SP-200 potentiostat (BioLogic Science Instruments, France) suitable for low current measurements. Galvanostatic Cycling with Potential Limitation was performed in a voltage range between 3 V and 0.005 V vs. Li/Li^+. First the particle was charged and discharged at 1 nA for several cycles. After the initial cycling, discharge rates were increased with each cycle up to 100 nA. The current for charging was kept constant at 1 nA to ensure a complete lithiation of the particle.

For the evaluation of the measured data from the rate test a Tafel-Plot was plotted. Therefor the logarithm of the discharge current divided by the particle surface was plotted against the voltage at a certain Depth of Discharge (DOD). The equilibrium potential E_{equ} for a DOD

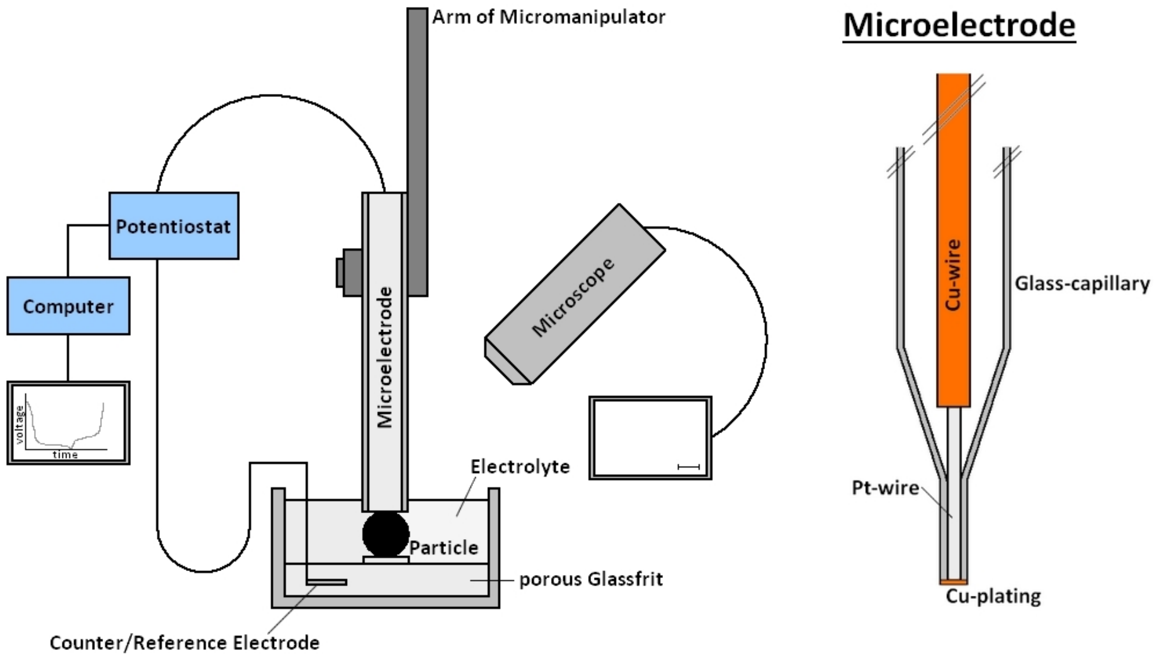

Figure 3.5: Scheme of the Single Particle Measurement setup (left) and schematic setup of the microelectrode (right).

of e.g. 10 % was calculated according to Equation 3.6 taken the midpotential between the potential at 90 % of Depth of Charge (DOC) and 10 % of DOD during the first cycle of the rate test. This assumes that at low currents of 1 nA the measured potentials are close to the equilibrium value.

$$E_{equ} = \frac{E_{90\%DOC} + E_{10\%DOD}}{2} \tag{3.6}$$

The linear sequence of the Tafel-Plot was fitted, assuming a charge transfer coefficient of 0.5. The intercept of the linear sequence with the equilibrium potential gives rise to the exchange current density. The charge transfer resistance R_{ct} can now be calculated with Equation 3.7.[83]

$$R_{ct} = \frac{RT}{F \cdot i_0} \tag{3.7}$$

Moreover, the minimum diffusion coefficient D_{min} can be estimated from the linear segment of the Tafel-Plot using Equation 3.8.

$$D_{min} = \frac{l^2}{6t} \tag{3.8}$$

The radius of the investigated particle is taken as the diffusion length l. The time t required for the lithium ions to diffuse from the surface of the particle to its center is said to be the time necessary for the complete lithiation of the particle at the last data point lying on the linear segment of the Tafel-Plot.

3.4.5 Nuclear Magnetic Resonance Spectroscopy

^{29}Si, ^{13}C and ^{7}Li Nuclear Magnetic Resonance (NMR) measurements samples were performed at HN1$_b$ and HN3$_b$ pyrolyzed at 1100 °C. Pristine (uncycled), lithiated and delithiated samples of the ceramics were measured. The use of printed electrodes was not possible due the high amount of material needed to perform NMR probing. Pressed pellets were used instead to obtain electrodes with roughly 100 mg of mass. First a slurry was prepared according to chapter 3.4.1. The slurry was then spread on a glass plate and dried at 40 °C for 24 h, scratched off and ground. Approximately 100 mg of the as-prepared powder was pressed uniaxial with 30 kN for 5 min to obtain pellets with a diameter of 10 mm and a thickness of roughly 0.8 mm. The pellets were dried under vacuum in a Buchi® Glas Oven at 80 °C for 24 h and transferred into a glove box. Cell assembly was done according to chapter 3.4.3 but an additional polypropylene separator (Celgard 2500) was used to avoid the contamination of the pellets with glass fibers of the QMA separator. Lithiation and delithiation was performed at 3.72 mA·g^{-1} (equivalent to C/100$_C$) at 25 °C and the voltage limits were set to 0.005 V and 3 V vs. Li/Li$^+$. All together six samples were prepared. One sample of each material was only fully lithiated (in the following denoted as HN1$_b$-lith and HN3$_b$-lith) and one sample of each material was lithiated and afterward delithiated up to 3 V (in the following denoted as HN1$_b$-delith and HN3$_b$-delithHN1$_b$). Moreover, one pellet was assembled as described above, but not tested electrochemically to obtain a reference electrode (in the following denoted as HN1$_b$ as prepared and HN3$_b$ as prepared). Afterward the cells were disassembled in the glove box. The pellets were washed with DMC to remove the salt of the electrolyte, dried and ground to a powder for NMR measurements.

The NMR measurements were performed at the Institute for Solid State Research in Dresden (IFW-Dresden) by Seung-Ho Baek using a Tecmag Fourier Transform (FT) pulse spectrometer. A spin-echo sequence ($\pi/2$ - τ - π) was used. The spectra were averaged over 4000 scans with a $\pi/2$ pulse length of 4 μs and a repetition time of 40 s.

^{7}Li NMR spectra and relaxation rates were recorded in a temperature range of 80 K to 420 K to determine the lithium dynamics in the samples. The spine-lattice relaxation rates in the laboratory frame T_1^{-1} and the spin-lattice relaxation rate in the rotating frame $T_{1\rho}^{-1}$ were measured to study the lithium motions on μs and ms timescales, respectively. For the T_1^{-1} measurements the saturation recovery method was employed and T_1 was obtained by fitting the relaxation of the nuclear magnetization M(t) to a single exponential function shown in Formula 3.9 with δ being the fitting parameter.

$$1 - \frac{M(t)}{M(\infty)} = \delta \cdot exp\left(\frac{-t}{T_1}\right) \tag{3.9}$$

4 Results and Discussion

The chapter "Results and Discussion" is divided into three major parts. The first part focuses on the characterization of different pure silicon carbonitride ceramics followed by a strong focus based on the samples HN1 and HN3 in the second part. These parts of the thesis have been partly published ([84, 85, 86]) but are described here in a much broader context. The third part is summarizing the studies on composite materials of SiCN with silicon. These composites are comprised of the precursors and SiCN materials investigated in the first part.

4.1 Silicon Carbonitride

In the following chapter the investigation on various polymer-derived SiCN ceramics is presented. All ceramics have been obtained at a pyrolysis temperature of 1100 °C with a dwelling time of 2 h. The only differences in sample preparation have been done with respect to the cross-linking as already mentioned in Chapter 3.1.4. The ceramics are characterized by means of elemental analysis, X-ray diffraction and Raman spectroscopy. Finally, their electrochemical performance is compared. The results are discussed in the context of literature reports available on the topic of SiCN, which have already been summarized in Chapter 2.4. Furthermore, publications on the subject of SiOC and carbonaceous anode materials are used for description and discussion.

4.1.1 Elemental Analysis

Table 4.1.1 summarizes the results of the elemental analysis of the investigated SiCN ceramics derived from six different precursors, namely the commercially available HTT 1800, and synthesized $HN1_a$, $HN3_a$, GM35, GM65 and DiPhen. All these samples have been pyrolyzed at 1100 °C. Additionally to the investigated samples, Table 4.1.1 contains elemental compositions of SiCN ceramics investigated by other research groups with respect to their electrochemical properties.

The free carbon content ranges from 7.5 wt% for SiCN derived from HTT1800 up to 57.1 wt% for SiCN derived from $HN1_a$. SiCN derived from HTT1800 is considered as a carbon-poor polymer-derived silicon carbonitride ceramic whereas the other samples are classified as carbon-rich polymer-derived silicon carbonitride ceramics. Colombo et al. [16] defined ceramics to be carbon-rich if they exceed a threshold of 20 wt% of carbon while those ceramics with less than 20 wt% of carbon are defined as carbon-poor. For SiCN derived from GM35 and PSEDA with an additional heat treatment it is not possible to estimate the free carbon content according to Formula 3.3. For GM35 this is due to the high amount of nitrogen present in the sample. The amount of silicon can not completely consume the nitrogen in the form of Si_3N_4. However, solid state ^{13}C Magic-Angle-Spinning (MAS) NMR measurements by Widgeon et al. on this material revealed the existence of the free carbon phase.[87] It was shown that the excess of nitrogen for this particular system is located at the interfaces of the carbon nanodomains to the Si_3N_4 nano-domains. For PSEDA with an additional heat treatment the elemental composition implies rather the existence of a free silicon phase than of a free carbon phase, as the complete carbon is formally bonded to silicon as SiC.

The presence of chlorine in the samples is attributed to the end groups of the synthesized polymers as well as residuals of the reactions byproduct trimethylchlorosilane (compare reaction equation given in Chapter 3.1). Even though the syntheses have been carried out under inert argon atmosphere all samples contain oxygen. Moreover a considerable amount of hydrogen remains in the pyrolyzed ceramics. The amount of chlorine in the samples derived from PSEDA and Dahn1-Dahn4 was not given in the literature, but it is likely that they contain it due to the use of dichlorosilanes [88] and trichlorosilanes for the synthesis.

Table 4.1.1 also contains the values of the atomic ratios between nitrogen and oxygen. The values are in the range of 6.1 for $HN3_a$ to 36.7 for HTT1800 and therefore significantly higher than 1. The nitrogen to oxygen ratio might have an impact on the electrochemical performance of the samples (compare Chapter 2.4) and will be addressed in more detail in Chapter 4.1.4.

The elemental composition of all ceramics is also displayed in the composition diagram of Figure 4.1 for visualizing the data from Table 4.1.1. Please note that the silicon which is formally bonded as SiO_2 is not considered for the shown compositions. The samples derived from the precursors GM65, HN1, HN3 and DiPhen, as well as the samples synthesized by Dahn et al. [37] are all located close to the tie-line between C and Si_3N_4. The carbon-poor SiCN ceramics HTT1800 and PSEDA untreated are located in the same 3 field-region of Si_3N_4, SiC and C but shifted much closer to the SiC-Si_3N_4 tie-line. GM35 is located in the three-field-region of SiC, Si_3N_4 and nitrogen whereas heat treated PSEDA is located in the

Table 4.1: Results of elemental analysis for silicon carbonitride ceramics derived from different precursors. The free carbon content was estimated according to Equation 3.3.

Precursor	Si [wt.%]	C [wt.%]	N [wt.%]	O [wt.%]	H [wt.%]	Cl [wt.%]	Free C [wt.%]	Sum-formula	Ratio N/O
HTT1800[1]	58.40	17.39	23.48	0.73	-	-	7.5	$SiC_{0.70}N_{0.81}O_{0.02}$	36.7
GM35	27.60	35.38	25.83	3.27	0.93	6.99	(35.4)[7]	$SiC_{3.00}N_{1.88}O_{0.21}H_{0.94}Cl_{0.20}$	9.0
GM65	34.59	46.86	16.04	2.13	0.35	0.03	43.2	$SiC_{3.17}N_{0.93}O_{0.11}H_{0.28}Cl_{0.00}$	8.6
HN3$_a$	31.30	52.52	13.01	2.42	0.18	0.57	48.6	$SiC_{3.92}N_{0.83}O_{0.14}H_{0.16}Cl_{0.01}$	6.1
DiPhen	26.24	57.87	14.32	0.90	0.22	0.45	56.5	$SiC_{5.16}N_{1.09}O_{0.06}H_{0.23}Cl_{0.01}$	18.2
HN1$_a$	24.77	56.50	14.80	2.14	0.24	1.55	57.1	$SiC_{5.33}N_{1.20}O_{0.15}H_{0.27}Cl_{0.05}$	7.9
PSEDA-1[2] [44]	62.03	25.85	9.72	1.72	0.68	-	6.0	$SiC_{0.97}N_{0.31}O_{0.05}H_{0.30}$	6.5
PSEDA-2[3] [45]	73.83	13.12	6.50	4.16	2.39	-	-	$SiC_{0.42}N_{0.18}O_{0.10}H_{0.90}$	1.8
Dahn-1[4,5] [37]	33.2	50.5	15.4	-	0.90	-	46.5	$SiC_{3.56}N_{0.93}H_{0.75}$	-
Dahn-2[4,6] [37]	20.5	70.4	8.1	-	0.98	-	67.4	$SiC_{8.02}N_{0.79}H_{1.33}$	-
Dahn-3[4,6] [37]	28.4	58.4	12.2	-	0.96	-	54.5	$SiC_{4.08}N_{0.86}H_{0.94}$	-
Dahn-4[4,6] [37]	12.5	82.2	4.3	-	0.97	-	80.3	$SiC_{15.34}N_{0.69}H_{2.15}$	-

[1] Chlorine and hydrogen have not been determined for HTT1800 pyrolyzed at 1100 °C.

[2] Pyrolyzed at 1000 °C. The chlorine content was not given in literature.

[3] Sample PSEDA-1 with additional heat treatment under ar-atmosphere at 1000 °C for 1 h.

[4] Pyrolyzed at 1000 °C with $5\,^{\circ}C\cdot\mathrm{min}^{-1}$. No oxygen or chlorine content are given in literature.

[5] Derived from a single source precursor.

[6] Derived from blends from single source precursor and pitch.

[7] Amount of free carbon can only be approximated. A calculation according to Formula 3.3 is not possible. An explanation is given in the text.

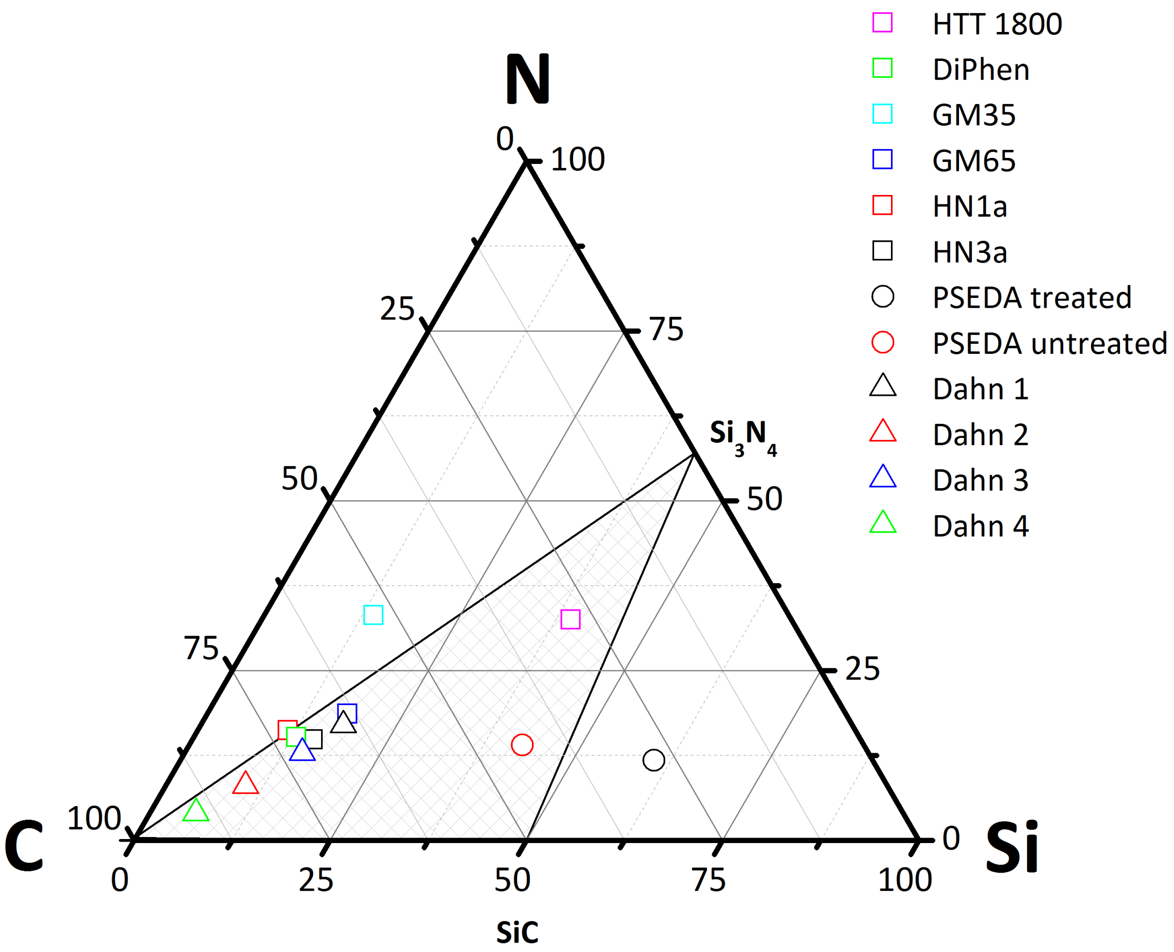

Figure 4.1: Composition diagram of SiCN ceramics listed in Table 4.1.1. Whereas the amount of carbon and nitrogen were directly taken from its measured values the amount of silicon was reduced by its portion formally bonded to oxygen. The graph additionally contains SiCN samples of Dahn et al. [37] Su et al. [44] and Feng [45].

silicon rich region of the composition diagram. The reasons of these exceptions have already been discussed before.

4.1.2 X-ray Diffraction

The X-ray diffraction pattern in Figure 4.2 reveal the amorphous nature of all investigated ceramics. No sharp reflexes are visible. It is known from literature that the onset temperature of crystallization depends on the precursor but it usually occurs at temperatures above 1300 °C. E.g. the first formation of crystalline α-Si_3N_4 for PHMS (copolymer of methyl- and dimethylsilazane units in the ratio 2:1) derived SiCN was found by TEM measurements at 1350 °C, whereas PVS (polyvinylsilazane) derived SiCN is completely amorphous at this tem-

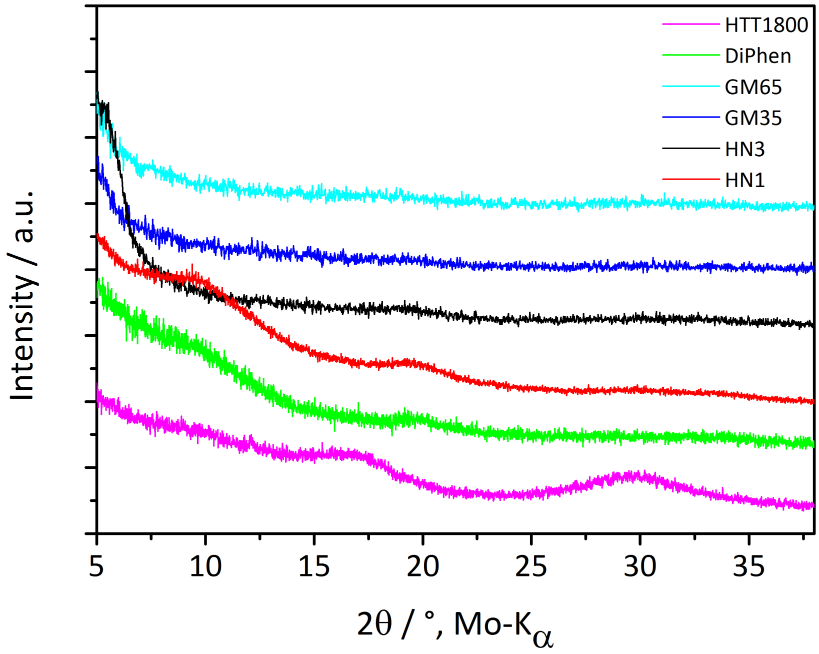

Figure 4.2: X-ray diffraction pattern of SiCN derived from HTT1800, HN1$_a$, HN3$_a$, GM35, GM65 and DiPhen pyrolyzed at 1100 °C.

perature and no crystallization occurs until temperatures as high as 1500 °C are reached.[89]

4.1.3 Raman Spectroscopy

The Raman spectra of the investigated samples along with the position and names of typical bands arising from carbon are shown in Figure 4.3. The origin of these bands are shortly summarized as follows:

A prominent band located at around 1575 cm^{-1} is attributed to the E_{2g}-mode, i.e. the stretching mode of the sp^2 C-C bonds, and is named the G-band.[90] The so called D-band is positioned at around 1355 cm^{-1} and arises from the breathing mode of sp^2 sixfold rings of carbon, also called A_{1g} mode.[90] This mode is inactive for perfect, infinite graphite crystals and only appears in the presence of disorder. The D-band can exhibit a shoulder at 1188 cm^{-1} which is attributed to mixed sp^2-sp^3 bands or C-C and C=C stretching vibration modes of a polyene-like structure (see [91] and references therein). This band is usually referred to as D4-band (sometimes also named I-band). A further band, the D3-band, is located between the D- and G-band of the spectra at around 1500 cm^{-1} and arises from amorphous carbon (see [92] and references therein). This vibration mode leads to a strong overlapping of the D- and G-band. The D2-band located at about 1620 cm^{-1} is usually visible as a shoulder at the right side of the G-band and originates from a graphitic lattice mode of graphene layers at the surface of a graphitic crystal (see [92] and references therein).

All spectra in Figure 4.3 clearly show the D- and G-band originating from the disordered free carbon phase of the ceramics. The maximum intensity of the disorder induced D-band is slightly higher than that of the G-band. The two bands are strongly overlapping indicating the presence of the D3-band and a shoulder at the left side of the D-band implies the existence of the D4-band. The D2-band is not visible in the detected spectra. Besides the already discussed modes between approximately 1000 cm^{-1} and 1700 cm^{-1} the spectra of the ceramics also show signals in the range of 2000 cm^{-1} up to 3500 cm^{-1}. These signals are overtones of the above described bands and are listed in Table 4.1.3. The 2*D4-, 2*D1- and G+D-band can be distinguished in Figure 4.3 but are very broad and hence overlapping strongly. The 2*D2-band is not visible which is in accordance with the absence of the D2-band.

A curve fitting as described in details in Chapter 3.3.4 allowed for the calculation of the lateral size of the carbon domains L_a by Equation 3.5. The applied fitting procedure of Janakiraman et al. [80] does not consider the 2D-band, being in perfect agreement with the measurements shown in Figure 4.3. The results of the curve fitting are summarized in

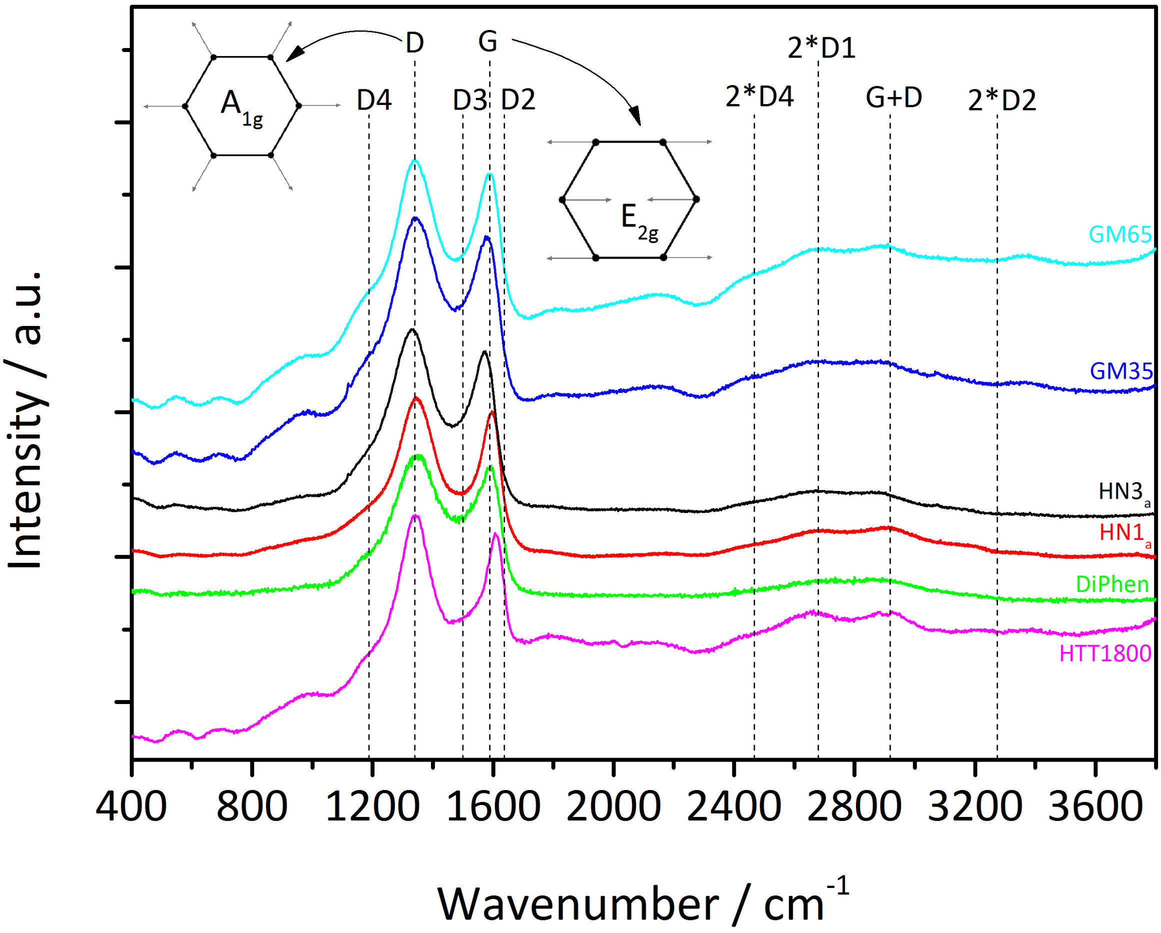

Figure 4.3: Raman spectra of HN1_a, HN3_a, GM35, GM65, DiPhen and HTT1800 pyrolyzed at 1100 °C. Additionally the carbon motions of the G-mode (E_{2g}) and D-mode (A_{1g}) are displayed.[81] The Spectra were recorded at 514.5 nm.

Table 4.2: Positions, names, references and origin of Raman bands of higher order between 2000 cm^{-1} and 3500 cm^{-1}.

Raman shift [cm^{-1}]	Name	Origin	Reference
2450	2*D4	first overtone of a Raman inactive graphitic lattice vibration mode at 1220 cm^{-1}	[93, 94]
2720	2*D1	first overtone of D1	[95]
2950	G+D	combination of D and G modes	[94, 95]
3240	2*D2	first overtone of D2	[94]

Table 4.3: Ratio of I(D)/I(G) and lateral size of the free carbon nano domains calculated according to Equation 3.5.

Precursor	I(D)/I(G)	L_a [nm]
$HN1_a$	1.05	1.4
$HN3_a$	1.15	1.4
GM35	1.47	1.6
GM65	1.72	1.8
DiPhen	1.52	1.7
HTT1800	1.57	1.7

Table 4.3. L_a was found to range from 1.4 nm for $HN1_a$ and $HN3_a$ to 1.8 nm for GM65. The condition of $L_a < 2$ nm [82] is therefore fulfilled and justifies the use of Equation 3.5.

All spectra are showing the typical features of a free carbon phase. Due to the high intensity of the D-band and the strong overlap of the signals of first and higher order it can be concluded that this phase is highly disordered. This qualitative results are in agreement with both, the absence of graphite reflections in the X-ray diffraction pattern and the calculation of the free carbon phase from elemental analysis. The lateral size of the carbon-nanodomains below 2 nm underlines the nano-structured character of the free carbon phase.

4.1.4 Galvanostatic Cycling with Potential Limitation

The discussion of the GCPL results includes various considerations on the storing sites for lithium ions in polymer-derived SiCN. Moreover, the influence of the nitrogen to oxygen ratio as well as the different microstructures of polysilazane and polysilylcarbodiimide derived ceramics on the electrochemical performance is addressed. As discussed in Chapter 2.4, Ahn et al. argue that only small capacities can be expected for nitrogen to oxygen ratios higher than 1, as the mixed bond network looses its ability to store lithium ions.[48] In addition, the phase separation within polysilylcarbodiimide derived SiCN leads to the formation of inactive $Si_3N_4$and SiC, i.e. no mixed bond amorphous network possibly allowing for lithium storage is present in this samples.

Figure 4.4 shows the delithiation capacities of the different ceramic materials cycled at rates from $C/20_C$ till $C/1_C$. Additionally, the corresponding current for each cycle and the theoretical capacity of graphite are displayed. In the following, first the carbon-rich ceramics are addressed in detail before discussing the carbon-poor sample derived from HTT1800. All carbon-rich ceramics exhibit delithiation capacities above 372 mAh·g^{-1} for rates of C/20$_C$ and C/10$_C$. The highest first cycle delithiation capacity is achieved for sample GM65 with 725 mAh·g^{-1}, the lowest first cycle delithiation capacity is measured for DiPhen with 463 mAh·g^{-1}. The samples GM65 and HN1$_a$ show a slight fading of capacity with ongoing cycling whereas the measured capacities for HN3$_a$, GM35 and DiPhen imply a stable cycling behavior. However, the initial first cycle delithiation capacities are not recovered for HN3$_a$ and GM35 during the last (134th) cycle. DiPhen is taking a special position among the samples as its delithiation capacity increases during cycling from 463 mAh·g^{-1} to 500 mAh·g^{-1}. Moreover, the loading of the electrode prepared from DiPhen is about three times higher than that of the other carbon-rich materials. Only little amounts of most materials were available, so electrode printing was performed by hand. DiPhen, in contrary, was available in larger amounts, so that a doctor blade was used for printing. The mass of active loading per square centimeter for all samples is given in Table 4.4. It is likely that the high loading of DiPhen leads to a reduced capacity in comparison to the other carbon-rich samples.[96]

All samples show a drop of the capacity when the current was increased. Nevertheless, some samples exhibit capacities still above the theoretical capacity of graphite at C/2$_C$ or C/1$_C$. Especially the ceramic derived from HN3$_a$ shows outstanding delithiation capacities of about 430 mAh·g^{-1} even at a cycling rate of C/1$_C$.

Even at a slow cycling rate of C/20 the electrode made from the ceramic derived from HTT1800 is almost inactive for lithium storage as the discharge capacity is limited to 23 mAh·g^{-1}. This is in accordance with the results published by Graczyk-Zajac et al. on HTT1800 [39] as well as Kolb et al. on VL20 [38] (VL20 being an antecessor of HTT1800). It is likely that most of the capacity originates from the conducting additive used for electrode preparation. It was shown that typical delithiation capacities of carbon black are in the order of 180 mAh·g^{-1} to 190 mAh·g^{-1}.[97, 98] Further discussion will therefore focus on the carbon-rich ceramics as HTT1800 is excluded as potential candidate for anodes.

The lithiation-delithiation curves corresponding to the measurements presented in Figure 4.4 are shown in Figure 4.5. For all materials the lithiation starts approximately at a potential below 1 V. However, the shape of the lithiation curve differs for HN3$_a$, GM65 and DiPhen from the samples derived from HN1$_a$ and GM35. Whereas the lithiation curve of the first

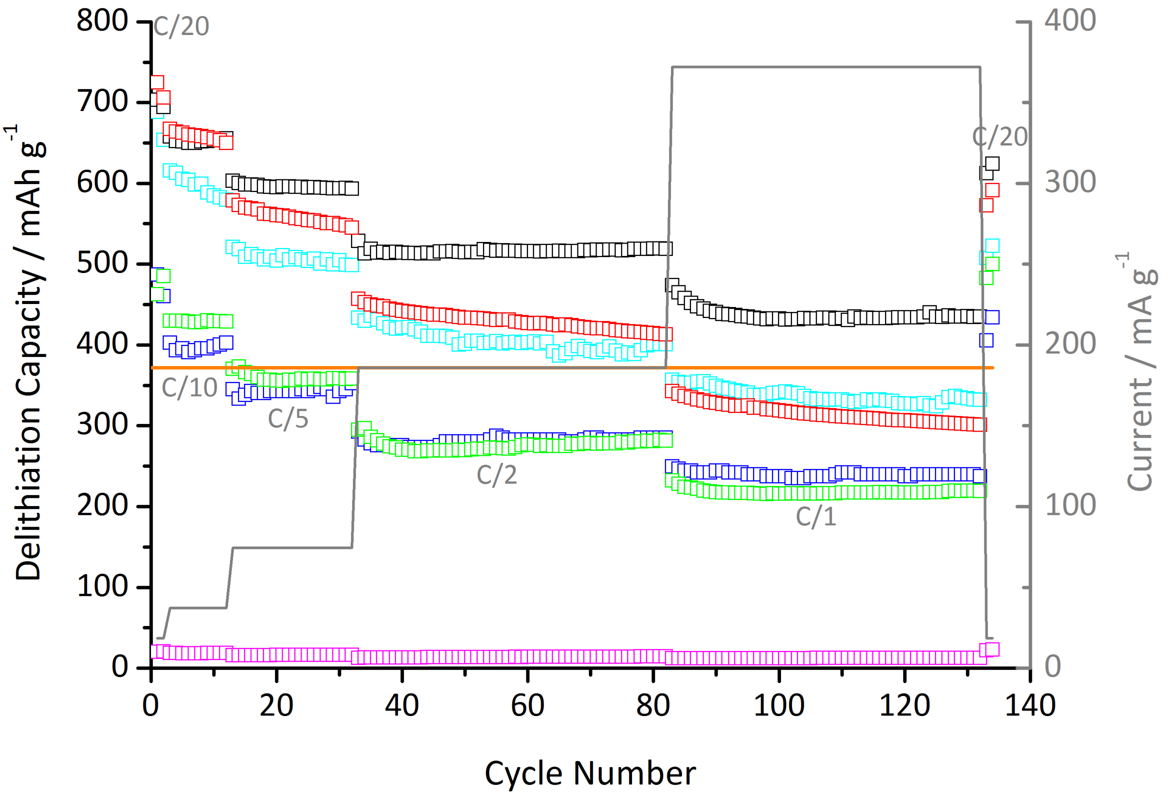

Figure 4.4: Delithiation capacities of □-HTT1800, □-HN1$_a$, □-HN3$_a$, □-GM35, □-GM65 and □-DiPhen. Additionally the applied current normalized to the active mass is displayed (—). The continuous straight line (—) is representing the theoretical capacity of graphite.

Table 4.4: Active mass, 1st cycle lithiation capacity, delithiation capacity and coulombic efficiency of the GCPL measurements displayed in Figure 4.4. Additionally the relative amount of capacity recovered below 1.5 V, taken from the lithiation-delithiation curves in Figure 4.5 for the 1st and 134th (last) cycle and the active mass of the electrodes are given.

Sample	Active mass [mg·cm^{-2}]	C$_{lith,1^{st}\ cycle}$ [mAh·g^{-1}]	C$_{delith,1^{st}\ cycle}$ [mAh·g^{-1}]	ζ [%]	1st cycle C$_{lith}$ < 1.5 V [%]	134th cycle C$_{lith}$ < 1.5 V [%]	ζ’ [%]
HTT1800	2.68	54	20	38	96	70	115
GM35	1.08	930	487	52	61	47	89
GM65	1.35	1212	725	60	88	75	82
HN1$_a$	0.88	1187	688	58	83	68	76
HN3$_a$	1.08	1078	703	65	91	83	89
DiPhen	3.04	748	463	62	94	88	108

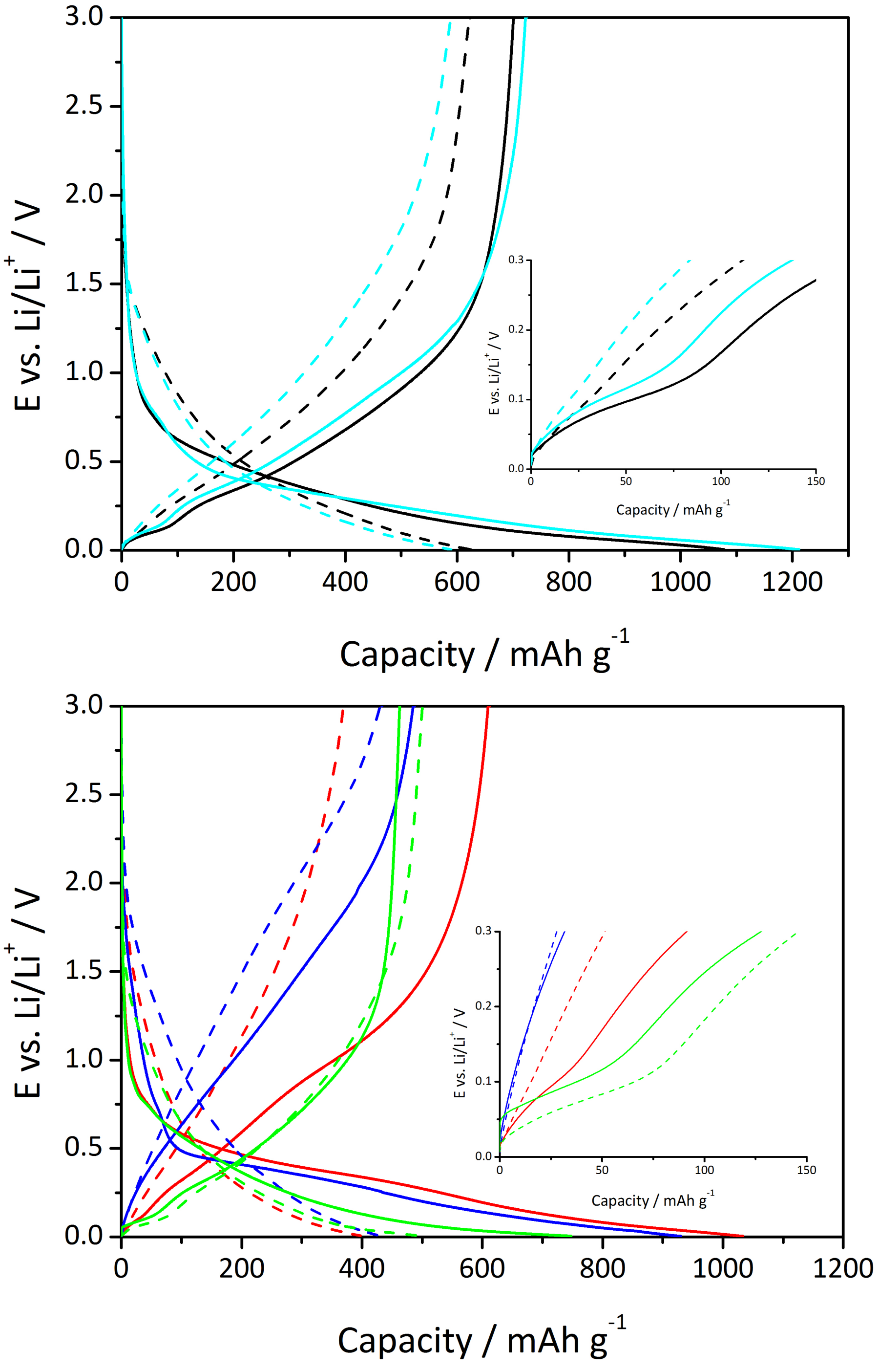

Figure 4.5: Top: 1^{st} cycle (continuous lines) and 134^{th} cycle (dashed lines) lithiation and delithiation curves of the polysilazane derived ceramics HN3$_a$ (–) and GM65 (–). **Bottom:** Lithiation and delithiation curves of the polysilylcarbodiimide derived ceramics HN1$_a$ (–), GM35 (–) and DiPhen (–).

three samples follows an exponential decay, the ceramics derived from $HN1_a$ and GM35 show a quasi plateau at about 0.5 V. This quasi plateau is only visible during the first cycle and does not appear with ongoing cycling.

The same samples differ also in the amount of capacity recovered during delithiation. For the samples derived from $HN3_a$, GM65 and DiPhen the capacity recovered below 1.5 V accounts for 88 % to 94 %. In contrast, for $HN1_a$ and GM35 this values is reduced to 83 % and 61 %, respectively. With ongoing cycling the delithiation potential for all samples is shifted to higher values resulting in a smaller portion of capacity recovered below 1.5 V. The exact values are given in Table 4.4.

The first delithiation curves registered for all samples, except of GM35, show a quasi plateau below 0.15 V as shown by the enlarged areas in Figure 4.5. This feature has also been described by Fukui et al. for anodes made from SiOC [50] and Single Particle Measurements on SiOC [99]. This low voltage plateau has been, in analogy to hard carbons, attributed to the presence of micropores. Disordered carbons are divided into two classes, the so called soft carbons and hard carbons, which can be distinguished by their ability to graphitize during a heat treatment. Soft carbons graphitize in a temperature range of 1500 °C to 3000 °C. Since the carbon layers in hard carbons are immobilized by cross-linking no graphitization occurs even at temperatures as high as 3000 °C.[100] For hard carbons it was proposed that lithium is adsorbed on the surfaces of pores which are formed by graphene sheets.[101, 102] This lithium storage mechanism also contributes to the high lithium storage capacity of hard carbons in comparison to graphite. Whereas the existence of pores has been proven with the help of small-angle X-ray scattering (SAXS) experiments, no pores have been detected for soft carbons [101], which is interesting insofar that the free carbon phase in polymer-derived ceramics consists of soft carbon.[32, 103] This will be also shown later in Chapter 4.3.3 when the influence of different pyrolysis temperatures is discussed. Despite the questionable categorization of the free carbon phase by Fukui et al., their SAXS measurements on SiOC showed the presence of a closed porosity of about 1 nm in diameter.[50] It is therefore concluded that the low voltage plateaus during delithiation for the SiCN ceramics investigated within this thesis also arise from micropores.

Figure 4.5 shows that the contribution of micropores to the overall discharge capacity vanished during ongoing cycling and that no plateau appears in the last (134^{th}) cycle anymore. This finding is again in agreement with the measurements performed on SiOC which also exhibit decrease in micropore activity during cycling.[50] Even though Figure 4.4 implied a stable cycling behavior for some of the measured samples, the vanishing of micropores and the shift to higher delithiation potentials reveal aging processes during cycling.

Table 4.4 also includes the first cycle lithiation capacities, the coulombic efficiencies and the cycling stability ζ', which is defined in Formula 4.1. The disadvantage of low coulombic efficiencies in comparison with other anode materials has already been mentioned in Chapter 2.4. The coulombic efficiencies for the carbon-rich ceramics range from 52 % for GM35 up to 65 % for $HN3_a$.

$$\zeta' = \frac{Cap_{delithiation}^{134^{th}\,cycle}}{Cap_{delithiation}^{1^{st}\,cycle}} \cdot 100\,\% \tag{4.1}$$

One reason for irreversible losses during the first cycle is the formation of a SEI at the anode but this does by far not account for it. In fact, the SEI formation is hardly visible in the lithiation-delithiation curves in Figure 4.5. There have been various studies on SiOC materials focusing on the high irreversible losses during the first cycle. Especially the role of oxygen was under investigation. Wilson et al. [52] and Xing et al. [53] reported that the irreversible capacity increases with the oxygen content. Materials close to a composition of silica were not taken into account as they reveal almost no activity. Liu et al. [49] found $SiOC_3$ and parts of the SiO_4 tetrahedra to be responsible for the irreversible losses. Ab initio calculations on the lithium insertion in SiOC showed that strong and irreversible bonding of lithium ions in the proximity of oxygen is likely to appear, supporting the experimental findings.[104] For the carbon-rich SiCN ceramics shown here the oxygen can clearly play only a minor role in the irreversible bonding of lithium ions. It was shown in Chapter 4.1.1 that the oxygen content after pyrolysis only amounts to 0.73 wt% to 3.27 wt%. Moreover, the phase separation, and therefore the absence of a mixed bond network, in polysilylcarbodiimide derived SiCN should suppress lithium insertion into the glass phase.

Based on the delithiation capacities in Figure 4.4 it is concluded that polymer-derived SiCN ceramics are suitable materials for applications as anodes in lithium ion batteries if they exhibit a certain amount of free carbon. The results are in contradiction to the hypothesis of Ahn. et al. [48] that a nitrogen to oxygen ratio smaller than one is necessary for SiCNO ceramics to achieve capacities exceeding the lithium storage ability of graphite. Their model is directly linked to the suggested storing mechanism of lithium in polymer-derived SiOC ceramics located in the nanodomain region (elemental compositions close to the tie-line between SiC-C in the Si-C-O phase diagram).[105] Accordingly, the majority of lithium is stored in the mixed bond tetrahedra (namely $SiOC_3$, SiO_2C_2 and SiO_3C) and the free carbon phase is contributing to the overall capacity only to an extend of graphite. Ahn et al. claim that by replacing oxygen with nitrogen, the mixed bond tetrahedra become unable to store lithium.[48] This is explained by the higher electronegativity of oxygen in comparison to nitrogen and therefore the differences in the covalency of the bonds. The sample derived from HTT1800 perfectly matches into the theory, whereas the samples with high carbon contents do not follow the proposed behavior. It should be noted that the samples analyzed by Ahn et al. contain only up to 26 wt% of free carbon.

4.2 Chemical Modification of HTT1800 with Divinylbenzene

The electrochemical measurements in Chapter 4.1.4 on electrodes prepared from HTT1800 derived SiCN showed that this material is inactive for lithium storage which was associated with the low free carbon content. In contrary, SiCN with a high free carbon content showed excellent performance. Yet, the synthesis of the carbon-rich SiCN precursor is time-consuming and its reproducibility is challenging. Commercial HTT1800 allows for a comparatively easy modification with divinylbenzene (DVB) to increase and control the carbon content of the ceramic and at the same time keeping a single source route. A short characterization of the modified precursor HTT1800 and the final ceramics as well as their electrochemical behavior will be presented in the following chapter. Both, the modification and the characterization have also been performed on the polysiloxane PolyR.[84]

4.2.1 Fourier Transform Infrared Spectroscopy

The FTIR spectra of HTT1800, HD1, HD2 and HD3 are presented in Figure 4.6. The spectra were normalized with respect to the band arising from Si-CH_3 at $1260\,\mathrm{cm}^{-1}$, assuming this group to be inactive during the modification procedure (also compare possible cross linking reaction of polysilazanes in Chapter 2.3). The Si-H-band at $2120\,\mathrm{cm}^{-1}$ is the basis for the monitoring of the hydrosilylation reaction. The enlargement of this band shows indeed a decrease in the intensity with increasing DVB content. However, the band does not disappear at stoichiometric and over-stoichiometric DVB content as expected for a complete consumption of Si-H groups and the influence of the increase in DVB content from HD1 to HD3 on the intensity is rather small. The incomplete reaction of the vinyl and Si-H groups could be due to steric hindering effects.

Comparable studies on PolyR showed a complete consumption of Si-H groups. PolyR exhibits much less Si-H groups in comparison to HTT1800, so that no steric hindering occurs.

4.2.2 Elemental Analysis

The results of the elemental analysis of HD1, HD2 and HD3 are summarized in Table 4.5. For better comparability, the results of SiCN derived from pure HTT1800 discussed in Chapter 4.1.1 are given, too.

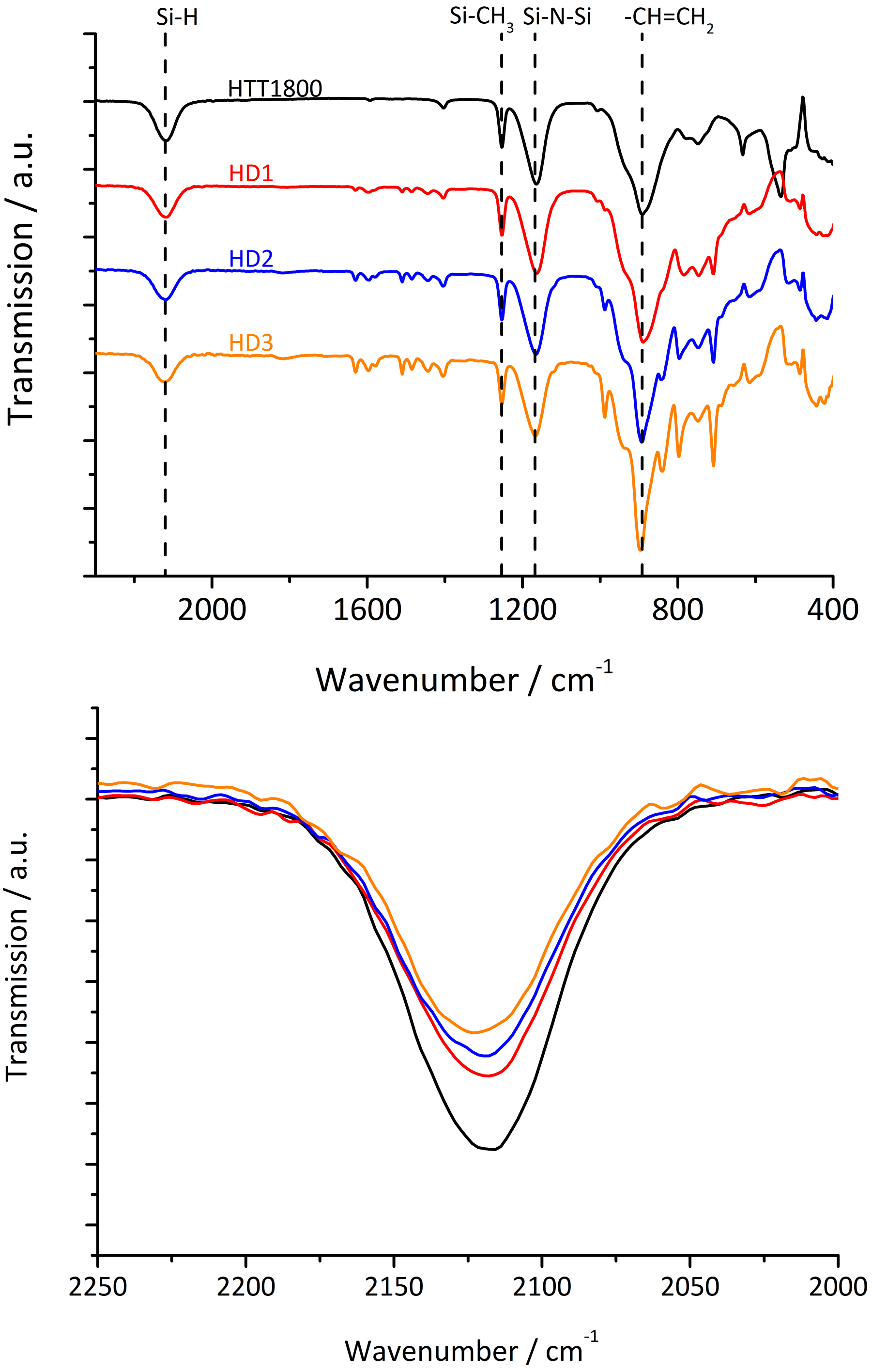

Figure 4.6: Top: FTIR spectra of HTT1800 and HTT1800 modified with DVB normalized to the intensity of the Si-CH$_3$ bands. **Bottom:** Enlarged FTIR spectra of the Si-H band.

Table 4.5: Results of elemental analysis for SiCN derived from HTT1800 and HTT1800 after modification with DVB at different ratios.

Precursor	Si [wt.%]	C [wt.%]	N [wt.%]	O [wt.%]	Free C [wt.%]	Sumformula
HTT1800	58.40	17.39	23.48	0.73	7.5	$SiC_{0.70}N_{0.81}O_{0.02}$
HD1	48.7	32.0	17.9	1.4	23.0	$SiC_{1.54}N_{0.74}O_{0.05}$
HD2	41.7	39.6	17.5	1.2	33.3	$SiC_{2.22}N_{0.84}O_{0.05}$
HD3	32.0	55.2	11.0	1.8	49.6	$SiC_{4.03}N_{0.69}O_{0.10}$

The results in Table 4.5 show a strong increase in the overall carbon content of the ceramics as well as the free carbon content with increasing DVB content. The free carbon content of pyrolyzed samples in dependence of the DVB to polymer ratio is given in Figure 4.7. No saturation in the carbon content took place, even when using over-stoichioemtric amounts of DVB. This is in contrast to the experiments done on PolyR, which shows a saturation in the free carbon content.[84]

4.2.3 Galvanostatic Cycling with Potential Limitation

The lithiation and delithiation capacities of the samples HTT1800, HD1, HD2 and HD3 are given in Figure 4.8. The variation in capacities among one particular charging/discharging rate were caused by a fluctuation of temperature during the measurement. The capacities increase with an increasing amount of free carbon. The capacities of HD1 derived ceramic are only slightly higher in comparison to HTT1800. The first cycle delithiation capacity increased from 20 $mAh \cdot g^{-1}$ to 69 $mAh \cdot g^{-1}$. The samples HD2 and HD3 show a much higher first cycle delithiation capacity, namely 278 $mAh \cdot g^{-1}$ and 347 $mAh \cdot g^{-1}$, respectively. HD3 is similar to $HN3_a$ with respect to the elemental composition, but cannot compete in performance. Even the already low 1^{st} cycle coulombic efficiency of $HN3_a$ is further reduced by another 5 %.

Figure 4.9 is showing the 1^{st} cycle delithiation capacity in dependence on the free carbon content for all ceramics presented in Chapter 4.1 and 4.2. An additional line is added to the graph showing the theoretical capacity value for a complete intercalation of graphite. The samples derived from HTT1800 and HD1 with a free carbon content below 25 wt% show capacities close to the theoretical line, whereas the samples with a free carbon content above

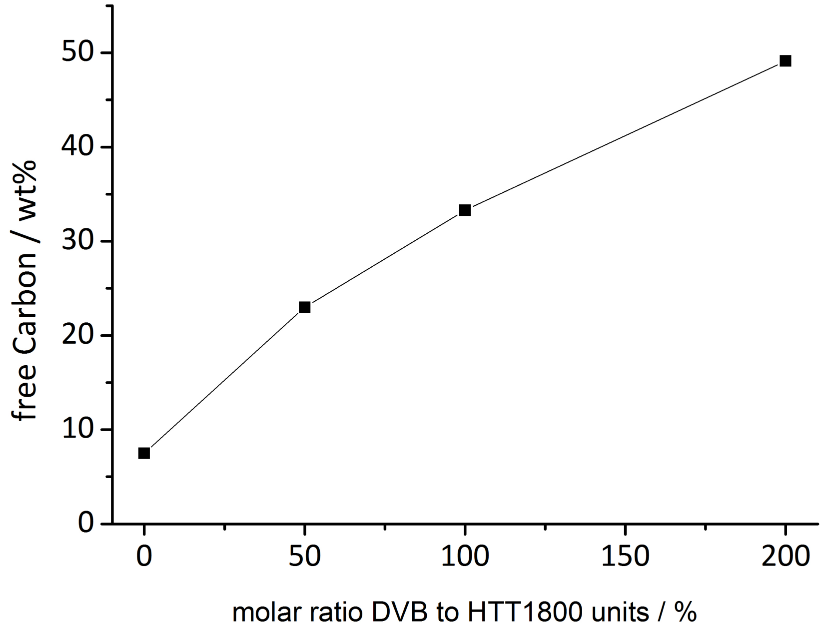

Figure 4.7: Free carbon content as function of the DVB to polymer ratio after pyrolysis at 1100 °C.

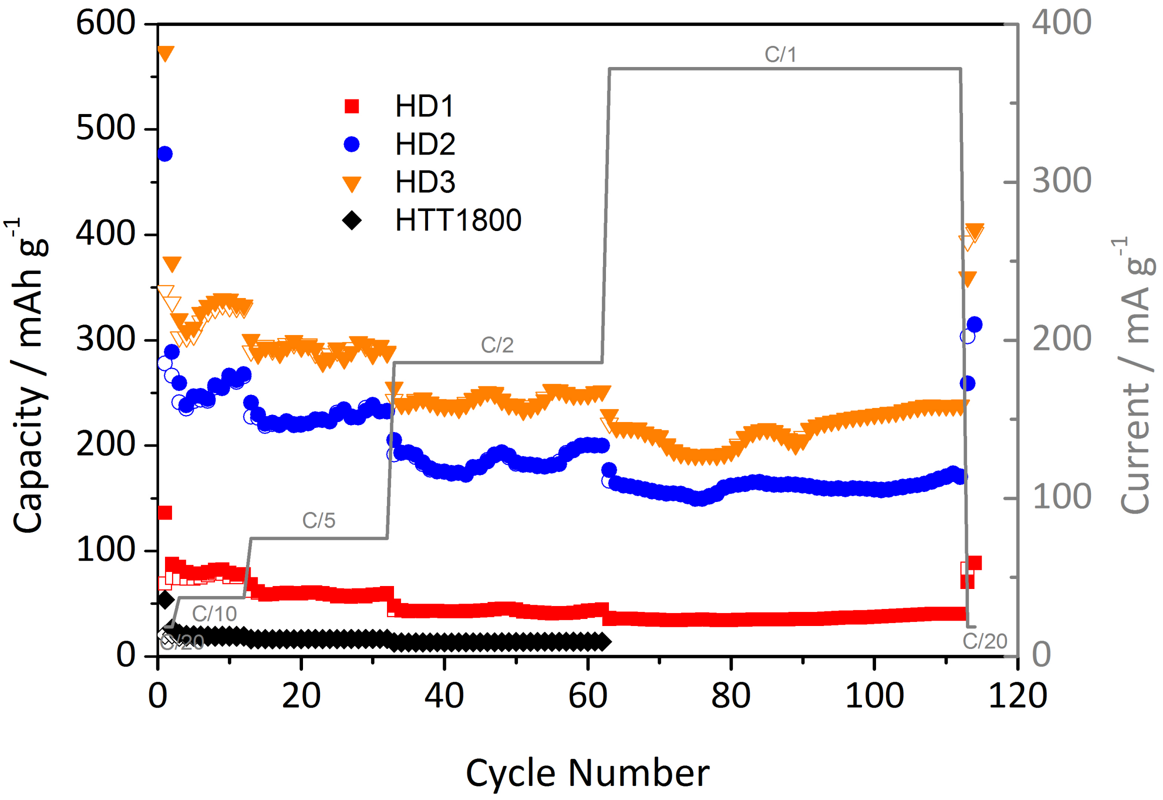

Figure 4.8: Lithiation and delithiation capacities of HTT1800, HD1, HD2 and HD3 at cycling rates between C/20 and C/1. The scattering of the capacity values can be attributed to temperature changes during the measurement.

30 wt% exhibit significantly higher capacities. The inability of SiCN anodes with a low free carbon content to sufficiently store lithium ions is also seen in the sample "'PDC1"' prepared by Ahn et al. [48]. This sample exhibits a free carbon content of 6.1 wt% and shows a 1^{st} cycle delithiation capacity of 38 mAh·g^{-1}. Within this context the research of Su et al. [44] and Feng [40] on PSEDA derived ceramics already discussed in Chapter 2.4 should be included, too. The PSEDA derived ceramic without further heat treatment exhibited a free carbon content of 6.0 wt% and the heat treated sample did not contain any free carbon phase according to the results of the elemental analysis. With respect to the statement above, no noteworthy reversible capacity would be expected from these samples, however, 1^{st} cycle delithiation capacities of roughly 456 mAh·g^{-1} and 550 mAh·g^{-1} were reported. However, a lack in clarity with respect to the free carbon content, specially on the heat treated sample, hinders the location of these samples within the composition diagram shown in Figure 4.9. As stated before, the elemental composition of the heat treated sample implies the absence of a free carbon phase. Anyhow, TEM pictures are presented showing graphitized carbon and solid state ^{13}C NMR spectra with strong signal at about 135 ppm arising from sp^2 hybridized carbons of a free carbon phase [89] are given. Moreover, the sample exhibits a high amount of oxygen with respect to the nitrogen content so that it is questionable if this material is not already behaving like a SiOC ceramic. This is of importance as reports on polymer-derived SiOC anode materials containing a low free carbon content showed high initial lithiation and delithiation capacities. SiOC derived of a blend of polyhydridomethylsiloxan with cyclic 1,3,5,7-tetramethyl-1,3,5,7 tetravinyl cyclotetrasiloxane contains 8 wt% of free carbon after pyrolysis at 1000 °C.[106] This ceramic showed a reversible 1^{st} cycle capacity of 493 mAh·g^{-1} but a strong fading with ongoing cycling.

Xing et al. [53] also suggested a carbon content of 30 at% for enhanced electrochemical performance of SiOC based anodes, supporting the idea of a threshold value. However, the value of the free carbon content of their samples should be located at only 10 wt% and therefore much below the values for SiCN.

There is obviously a strong discrepancy in the electrochemical behavior between SiOC and SiCN at low carbon contents, which should be looked at in more detail. Pradeep et al. [106] recently found a linear dependence of the 1^{st} cycle lithiation capacity with an increasing amount of the glassy $SiC_xO_{2(x-1)}$ phase ($0 \leq x \leq 1$). According to the linear behavior the highest 1^{st} cycle lithiation capacity is reached for 100 % of the mixed bond glass phase, i.e. no free carbon phase is present in the sample. The linear extrapolation of the lithiation capacity

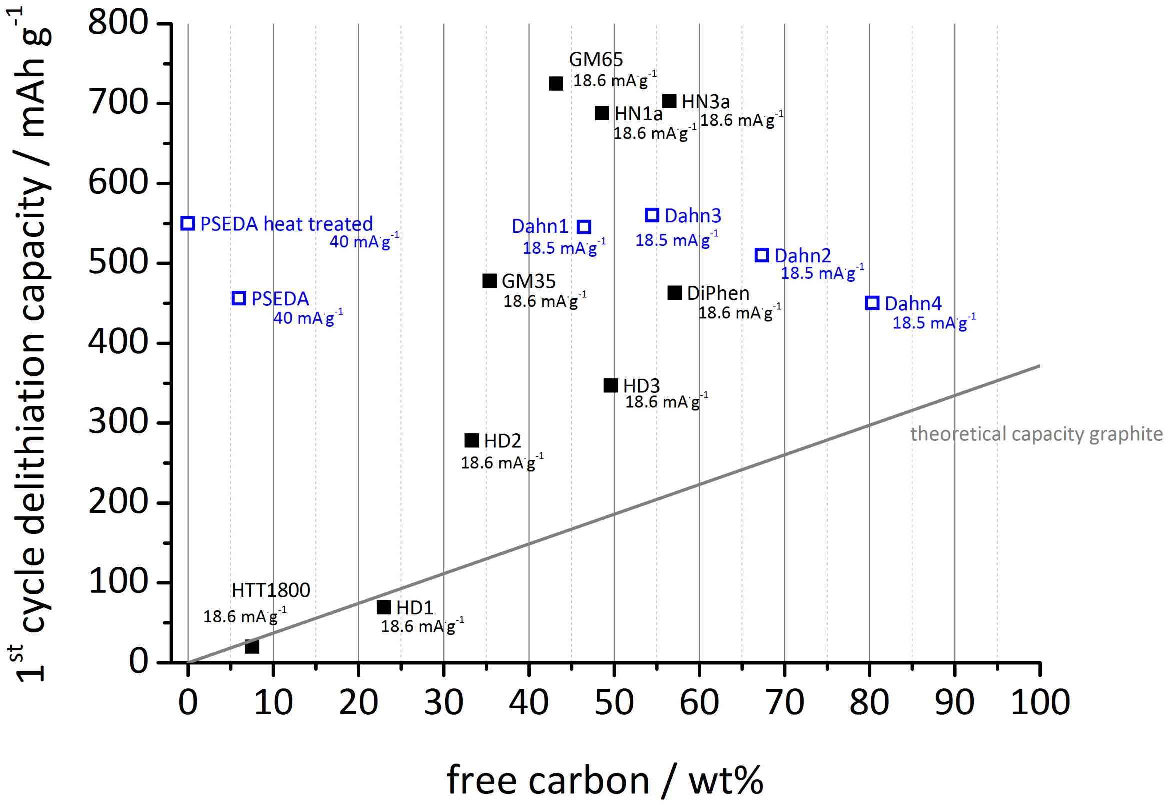

Figure 4.9: First cycle delithiation capacity of all investigated samples from Chapter 4.1 and 4.2 in dependence of their free carbon content. Literature values of Su et al. [44], Feng [40] and Dahn et al. [37] are included. The free carbon content of heat treated PSEDA was set to 0 %. For GM35 a free carbon content was assumed to 35.4 %. For a better comparison of the capacities the delithiation current for the literature data is given.

for this composition can be estimated to 1300 mAh·g^{-1}. However, it was found that at this boundary condition (no free carbon phase) SiOC shows no lithiation activity. According to the model of Pradeep et al. the lowest 1st cycle lithiation capacity of 350 mAh·g^{-1} is found for a material consisting only of the free carbon phase. This capacity value is almsost in accordance with the theoretical capacity of graphite. Moreover, a direct correlation of the irreversible capacity with increasing $SiC_xO_{2(x-1)}$ was found. The higher its portion of the ceramic, the higher the irreversible capacity would be. This findings are in good agreement with the models obtained from density functional theory (DFT) calculations of Kroll [104]. Whereas lithium (-ion) insertion into pure $SiC_xO_{2(x-1)}$ is unfavorable, the existence of a free carbon phase facilitates the insertion of lithium ions as it provides unfilled electronic states in the band gap of SiOC. In this case the interaction of lithium ions with oxygen exceeds the promotion energy for the electron and irreversible lithiation takes place. Due to the absence (little amount) of oxygen in the investigated SiCN this material shows almost no lithiation capacity if the free carbon amount is small and hence no irreversible bonding of lithium to oxygen takes place. However, at higher carbon contents SiCN exhibits excellent electrochemical properties. One could assume from the finding that i) the free carbon phase reversibly stores large amounts of lithium and is the major (only) storing site in SiCN and that ii) SiCN derived from polysilazanes should show small irreversible losses due to the absence (small amounts) of oxygen in the mixed bond network and iii) SiCN derived from polysilylcarboddimide should also show high coulombic efficiencies due to the absence of oxygen and the absence of a mixed bond network in general. The questions of storing sites in carbon-rich SiCN will be discussed in more detail in Chapter 4.3 giving experimental evidences. The above mentioned assumption of low irreversible losses in SiCN is clearly wrong as the results of GCPL measurements on different SiCN precursor have already shown. The question of the reason for low coulombic efficencies stays unsolved so far, as the formation of bonding between lithium and oxygen can be excluded as a major impact factor. In addition the absence of the mixed bond amorphous network in polysilycarbodiimide derived SiCN shows no benefits in terms of coulombic efficiencies in comparison to anode materials made from SiCN derived from polysilazanes. The investigated samples show even less irreversible losses in average for GM65 and $HN3_a$ (ζ=60 % and 65 %) in comparison to GM35, $HN1_a$ and DiPhen (ζ=52 %, 58 % and 62 %).

4.3 Poly(phenylvinylsilazane) and Poly(phenylvinylsilylcarbodiimide) Derived SiCN

The promising electrochemical properties of the SiCN ceramics derived from $HN1_a$ and $HN3_a$ are motivating further studies on this material class to address open questions like the dependence of this materials on the pyrolysis temperature, the storing sites of lithium cations and their dynamics. The following chapters will deal with these open questions. The materials pyrolyzed at different temperatures were characterized according to the known procedures from section 4.1. Additionally, selected samples were investigated with single particle microelectrode measurements and ^{29}Si, ^{13}C and ^{7}Li solid-state NMR studies. To process a sufficient amount of material for the additional investigation on SiCN derived from $HN1_a$ and $HN3_a$ and its composites with nano-silicon (see Chapter 4.4) a new batch of the polymers had to be synthesized; $HN1_b$ and $HN3_b$. In the following the ceramic samples will be named by the initial precursor and its pyrolysis temperature, e.g. the ceramic obtained from a pyrolysis of the precursor $HN1_b$ pyrolyzed at 1000 °C will be named "HN1-1000".

4.3.1 Elemental Analysis

The results of elemental analysis are summarized in Table 4.6 and visualized in Figure 4.10. The samples HN1-900 and HN1-1300 contain an excess of nitrogen. In comparison with the SiCN ceramic derived from GM35 which was discussed in section 4.1.1 the excess of nitrogen is much less pronounced. However, this leads, like for GM35, to a shift into the 3-field region of carbon, nitrogen and Si_3N_4, as can be seen in the ternary composition diagram in Figure 4.10.

The ceramics derived from $HN1_b$ and $HN3_b$ show a pronounced increase in the carbon content and free carbon content with increasing pyrolysis temperature. The amount of oxygen decreases with increasing temperature from 800 °C to 1100 °C. An exception of this tendency is seen when increasing the pyrolysis temperature from 800 °C to 900 °C for the $HN1_b$ based samples. Yet, the change of 0.11 wt% is within the measurement error and does not disprove the general trend of a decreasing oxygen content if the pyrolysis temperature is raised.

A further increase of pyrolysis temperature to 1300 °C leads to a significant increase in the oxygen content. This could be related to the use of the Al_2O_3-furnace instead of a Schlenk tube, which is necessary to achieve temperatures higher than 1100 °C. The origin of the chlorine in both samples has already been discussed in Chapter 4.1.1.

Table 4.6: Elemental composition of poly(phenylvinylsilazane) and poly(phenylvinylsilylcarbodiimide) derived SiCN ceramics pyrolyzed at different temperatures.

	$T_{pyrolysis}$ [°C]	Si [wt.%]	C [wt.%]	N [wt.%]	O [wt.%]	H [wt.%]	Cl [wt.%]	Free C [wt.%]	Sumformula	Ratio N/O
$HN1_b$	800	30.19	48.06	18.99	1.72	1.00	0.04	(48.1)	$SiC_{3.72}N_{1.26}O_{0.10}H_{0.92}$	12.6
	900	28.14	51.27	18.02	1.83	0.63	0.11	(51.3)	$SiC_{4.26}N_{1.28}O_{0.11}H_{0.62}$	11.2
	1000	28.10	53.31	16.55	1.60	0.41	0.03	52.6	$SiC_{4.44}N_{1.18}O_{0.10}H_{0.41}$	11.8
	1100	28.72	54.94	14.73	0.96	0.60	0.05	52.7	$SiC_{4.47}N_{1.03}O_{0.06}H_{0.58}$	17.5
	1300	24.81	55.97	15.04	3.79	0.27	0.12	(56.0)	$SiC_{5.27}N_{1.22}O_{0.27}H_{0.20}$	4.5
$HN3_b$	800	36.07	45.39	11.95	2.48	1.02	3.09	40.1	$SiC_{2.94}N_{0.66}O_{0.12}H_{0.79}Cl_{0.07}$	5.5
	900	35.71	46.72	12.00	1.94	0.56	3.07	41.2	$SiC_{3.06}N_{0.67}O_{0.10}H_{0.44}Cl_{0.07}$	7.1
	1000	34.06	48.85	12.21	1.36	0.11	3.41	44.0	$SiC_{3.35}N_{0.72}O_{0.07}H_{0.09}Cl_{0.08}$	10.3
	1100	34.41	47.71	13.28	0.87	0.27	3.46	43.3	$SiC_{3.24}N_{0.77}O_{0.04}H_{0.22}Cl_{0.01}$	17.4
	1300	32.06	50.68	12.70	1.24	0.29	3.03	47.0	$SiC_{3.70}N_{0.79}O_{0.07}H_{0.25}Cl_{0.07}$	11.7
PSEDA[1]	600	67.44	18.68	5.83	3.92	4.13	-	-	$SiC_{0.65}N_{0.17}O_{0.10}H_{1.70}$	1.7
	800	70.34	16.32	7.08	3.75	2.51	-	-	$SiC_{0.54}N_{0.20}O_{0.09}H_{0.99}$	2.2
	1000	62.03	25.85	9.72	1.72	0.68	-	6.0	$SiC_{0.97}N_{0.31}O_{0.05}H_{0.30}$	6.5
	1300	58.81	25.70	13.54	1.79	0.16	-	9.7	$SiC_{1.02}N_{0.46}O_{0.05}H_{0.08}$	8.6
	1400	61.83	23.73	12.64	1.64	0.16	-	5.8	$SiC_{0.90}N_{0.41}O_{0.05}H_{0.07}$	8.8
	1500	68.19	25.25	4.24	2.10	0.22	-	-	$SiC_{0.87}N_{0.12}O_{0.05}H_{0.09}$	2.3

[1] Taken from Reference [44]. The chlorine content has not been given.

From the composition diagram the samples of both precursors are located close to each other and close to the tie-line of C-Si_3N_4. In contrast, the samples investigated by Su et al. [44] differ strongly in composition and are located around the tie-line of SiC and Si_3N_4.

All the measurements presented in table 4.6 have been performed under inert gas atmosphere. For low pyrolysis temperatures however, the elemental composition changes when exposed to ambient atmosphere. For HN3-800 the oxygen content increases to 11.8 wt% and the amount of nitrogen decreases to 7.4 wt% when stored in air for 24 h. For higher pyrolysis temperatures the ceramic stays almost unaffected by the exposure to air within this time scale. The reactivity on air is of importance during the electrode preparation. The slurry preparation, as well as its printing on copper foil and the first drying step at 40 °C were all performed at ambient atmosphere.

Although the same experimental procedure was applied for the synthesis of the second batch, the elemental composition of $HN1_b$ and $HN3_b$ prolyzed at 1100 °C differ significantly from the composition of $HN1_a$ and $HN3_a$ pyrolyzed at 1100 °C. The free carbon content is for both samples reduced by about 5 wt%. In return the silicon content rose by about 3-4 wt%. It was possible to further reduce the oxygen content from more than 2 wt% to below 1 wt%. For $HN1_b$ it was also possible to completely prevent a chlorine contamination. In contrary, the amount of chlorine for $HN3_b$ increased strongly.

4.3.2 X-ray Diffraction

The X-ray diffraction pattern of the ceramics pyrolyzed at different temperatures are shown in Figure 4.11. In addition to the pyrolysis temperatures of up to 1300 °C the X-ray diffraction pattern of $HN1_b$ and $HN3_b$ pyrolyzed at 1700 °C are shown in Figure 4.12. All samples up to 1300 °C are X-ray amorphous and do not exhibit sharp reflexes. However, the diffraction pattern show broad signals at around 20° and around 32°. These features are typical for disordered soft carbons and arise from (002) planes of graphite-like nano-crystallites and the convolutions of (10) hk two-dimensional line and the broad and week (004)-reflection, respectively.[107]

These broad signals did not occur for HN3-1000 which implies the absence of a free carbon phase within this particular sample. However, the results from elemental analysis and the calculation of the amount of free carbon in section 4.3.1 are clearly in contradiction with this results. Furthermore, the Raman spectroscopy measurements in the following chapter show

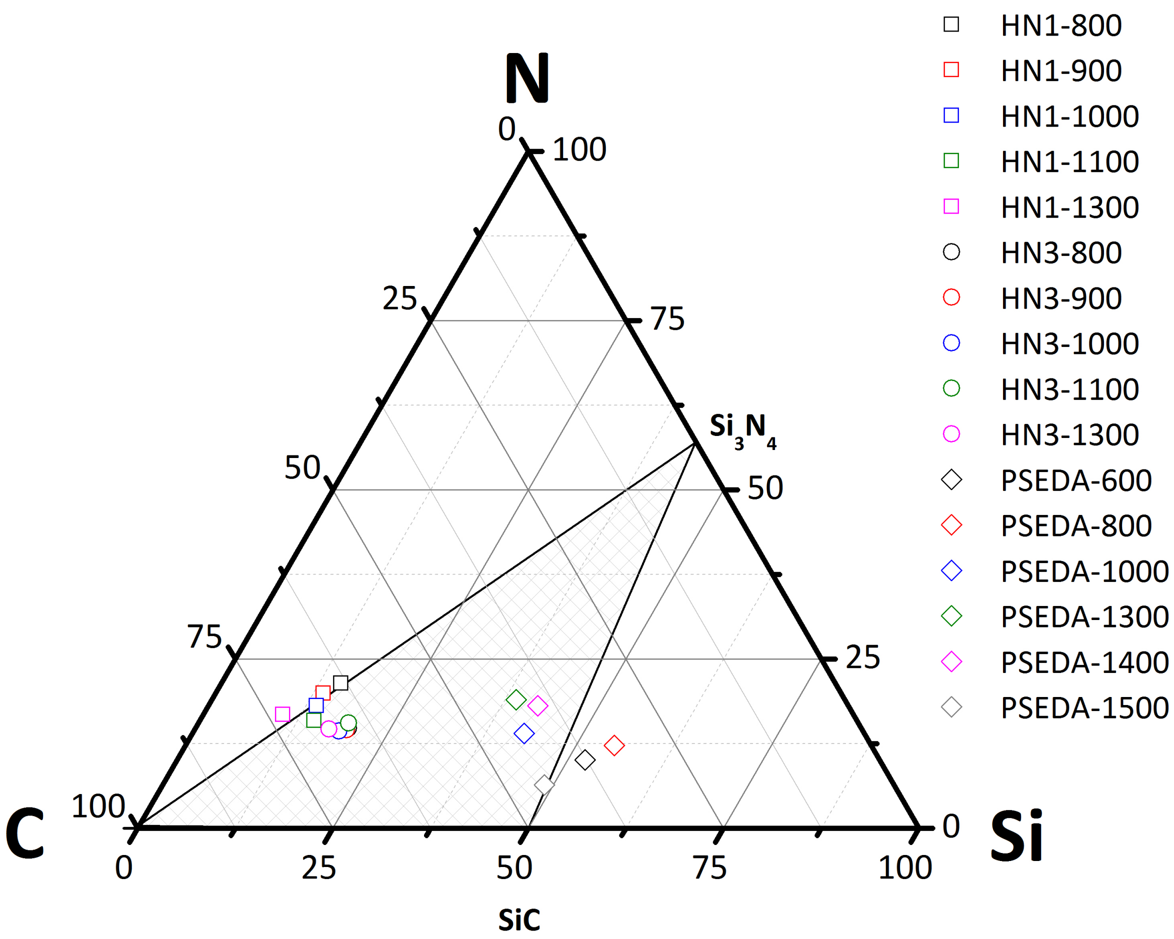

Figure 4.10: Composition diagram of SiCN ceramics listed in Table 4.6. For a comparison additional SiCN ceramics derived from PSEDA at different temperatures investigated by Su et al. [44] were included. Whereas the amount of carbon and nitrogen were directly taken from its measured values the amount of silicon was reduced by its portion formally bonded to oxygen.

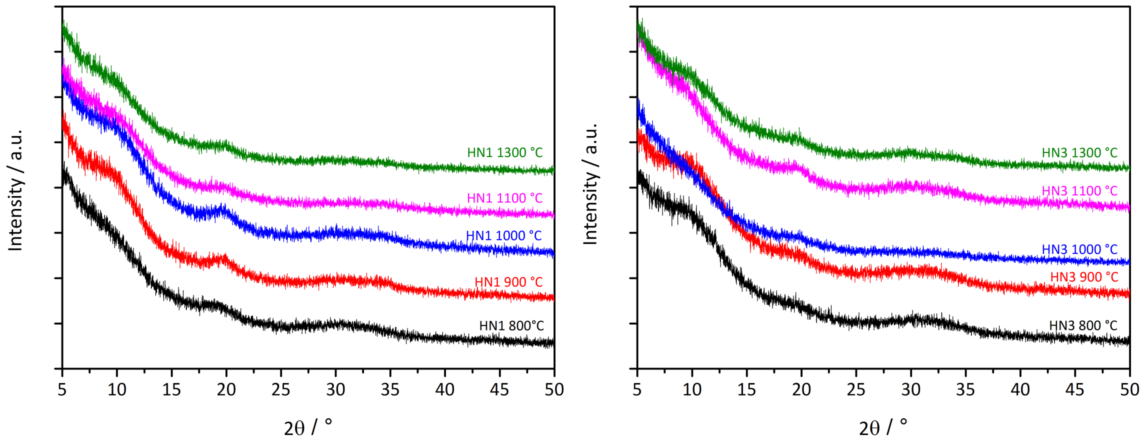

Figure 4.11: X-ray diffraction pattern of SiCN ceramics derived from HN1$_b$ (left) and HN3$_b$ (right).

the characteristic features of a free carbon phase. The reason for the absence of the broad bands stays unclear.

The samples pyrolyzed at 1700 °C exhibit sharp reflexes which arise from crystalline α- and β-SiC. No crystalline Si_3N_4 or carbon is visible in the X-ray diffraction pattern. The crystallization onset at temperatures above 1300 °C is therefore in agreement with the experiments of Bill et al. [89] on SiCN derived from PHMS and PVS. However, in contrary to HN1$_b$ and HN3$_b$ crystalline α-Si_3N_4 was found. The obtained results for HN1$_b$ are in perfect agreement with investigation done on poly(phenylvinylsilylcarbodiimide) by Mera et al. [32]. They observed an onset temperature of the crystallization for this particular material at around 1400 °C. For a pyrolysis temperature of 2000 °C the X-ray diffraction pattern additionally exhibited a signal arising from graphite. The absence of crystalline Si_3N_4 can be explained by the large amount of carbon in the ceramics derived from HN1$_b$ and HN3$_b$, which hinders the crystallization of amorphous Si_3N_4.[30]

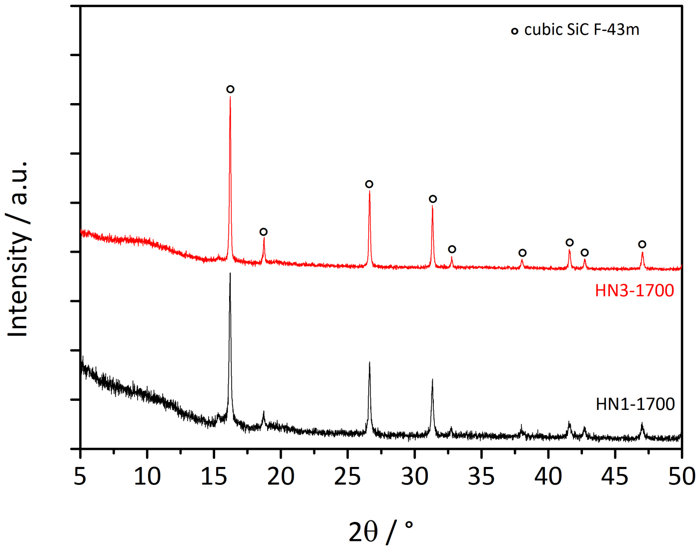

Figure 4.12: X-ray diffraction pattern of SiCN ceramics derived from HN1_b and HN3_b pyrolyzed at 1700 °C.

4.3.3 Raman Spectroscopy

The typical features of the Raman spectra of carbon-rich polymer-derived ceramics and its origins have already been discussed in Chapter 4.1.3. Each vibration mode was linked to an exact wave number. However, in reality this approach presents certain deficiencies. E.g. the position of the G-band changes for non-ideal graphitic materials.[81, 108]. The changes in the carbon spectra can be predicted by the so called three-stage model proposed by Ferrari et al..[81] Within *stage one* only sp^2 carbons exist and a shift to higher wavenumbers is observed when going from graphite to nanocrystalline graphite (nc-graphite). At the same time the D-band appears in the spectrum. The excitation wavelength of the laser does not influence the band position within stage one. *Stage two* refers to the effects on the spectra during the transition of nc-graphite to amorphous carbon (a-C). The amorphous carbon is characterized by mainly sp^2 distorted sixfold rings or rings of other order and up to 20 % sp^3 carbons. Several effects on the Raman spectra are visible within stage two as the disorder increases: The G-band is shifted to lower wavenumbers, the FWHM of the G-band is diminished and the I(D)/I(G) is becoming smaller. *Stage three* is characterized by an increase of sp^3 carbons from 20 % up to 85 % and a transformation of the ring-structure to a chain structure and a transition from a-C to tetrahedral amorphous carbon (ta-C). The band positions are shifted to smaller wavenumbers and I(D)/I(G) is becoming very small or even 0. The excitation wavelength in stage two and stage three has a major impact on the position of the G-band.

Figure 4.13 shows the spectra of HN1$_b$ and HN3$_b$ pyrolyzed at temperatures of 800 °C, 900 °C, 1000 °C, 1100 °C and 1300 °C. In addition the position of the typical bands for disordered carbon is given according to the literature values. All spectra show the characteristic features of the free carbon phase, i.e. strong D- and G-bands which are overlapping, implying the existence of the D3-band. The D4-band is also well visible. The D2-band at 1620 cm^{-1} is not visible. The overtones between 2000 cm^{-1} and 3500 cm^{-1} are visible, however, they are very broad. On first sight no differences in the spectra are visible throughout the investigated temperature range, e.g. the D4-band is visible for all recorded spectra, the maximum intensity for the D-band is above the intensity for the G-band and no sharpening of the signals over the overtones is visible.

For an exact determination of the band positions, their FWHM and their intensity, curve fitting has been done as described in subsection 3.3.4. The fitting procedure does not consider

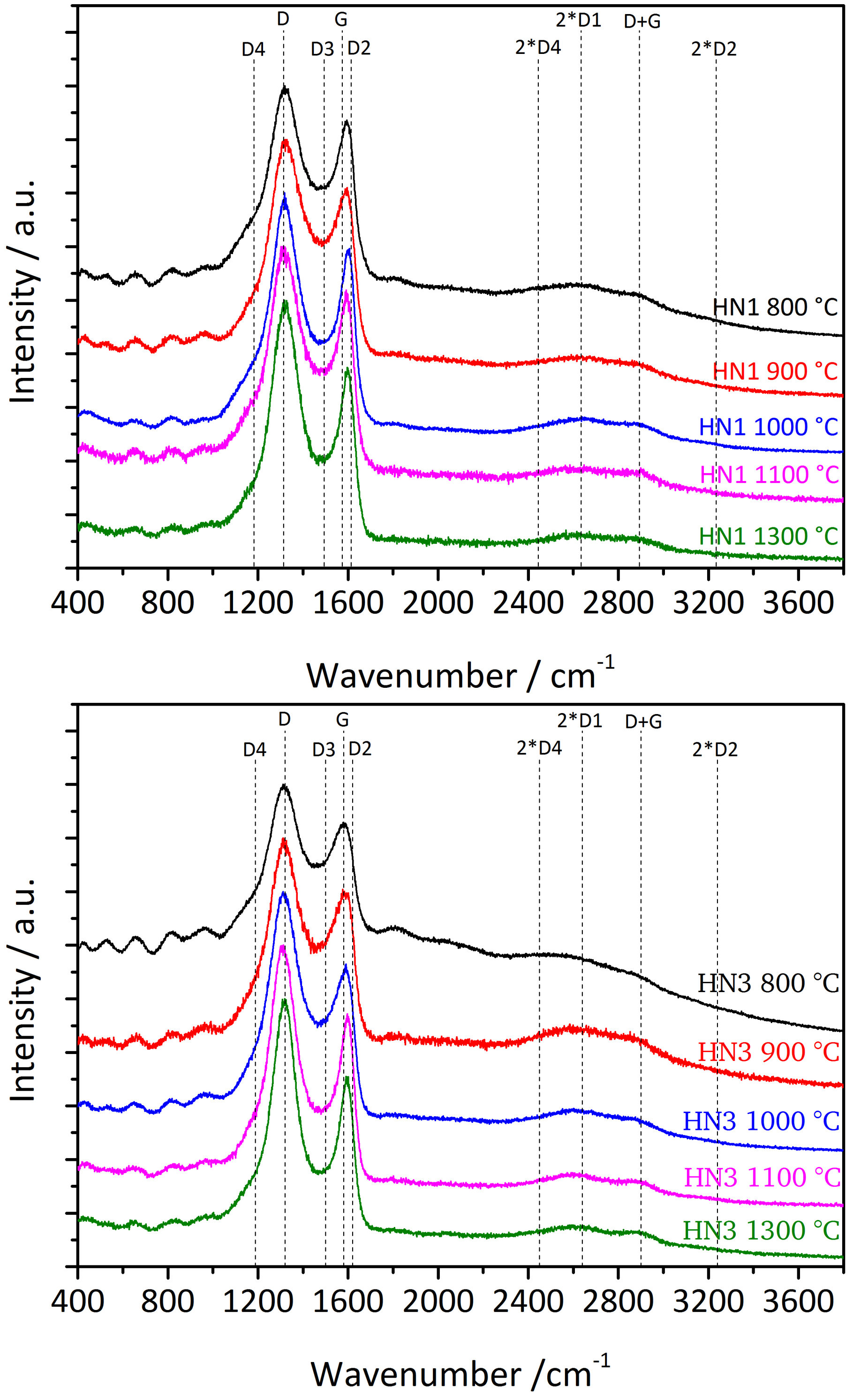

Figure 4.13: Raman spectra of SiCN ceramics derived from $HN1_b$ (top) and $HN3_b$ (bottom) pyrolyzed at temperatures between 800 °C and 1300 °C.

the presence of a D2-band which is in agreement to its absence in the spectra shown here. Figure 4.14 shows the evolution of the D-band position, G-band position, the FWHM of the D-band, the FWHM of the G-band and the intensity ratio I(D)/I(G) for $HN1_b$ and $HN3_b$ pyrolyzed at temperatures between 800 °C and 1300 °C. As discussed for the three-stage model above, the determination of these values allows to withdraw some conclusions on the ordering of the free carbon phase of the ceramic. With increasing order the position of the D- and G- band is shifted to higher wavenumbers. At the same time the decrease in disorder leads to a decrease in the FWHM of both bands and I(D)/I(G).[81] In addition the bands arising from vibrations of higher order are also getting more distinct with increasing order in the free carbon phase.

The ceramics derived from $HN1_b$ show practically no shift of the D- and G-band towards higher wavenumbers over the whole temperature range. The FWHM decreases at the same time by 19 cm^{-1} for the D-band and 7 cm^{-1} for the G-band, respectively. The I(D) to I(G) ratio increases slightly from 1.5 to 1.7. The changes for the band position and the FWHM for the ceramics derived from $HN3_b$ show slightly higher changes in shift and FWHM. The D-band is shifted by 4 cm^{-1} and the G-band is shifted by 16 cm^{-1}. The FWHM decreases by 49 cm^{-1} and 19 cm^{-1}, respectively. On the contrary the I(D) to I(G) ratio decreases from 1.8 to 1.7. Within the measured temperature range the most significant changes were seen between pyrolysis temperatures of 800 °C and 900 °C for $HN3_b$ derived samples and between 1100 °C and 1300 °C for $HN1_b$ derived samples.

Especially the small changes in FWHM and the little changes in the I(D) to I(G) ratio are in strong contrast to the findings of Janakiraman et al. [80] on dense polysilazane-derived SiCN, fabricated by a casting technique. Janakiraman et al. measured a decrease of the FWHM of the D-band of approximately 150 cm^{-1} and 90 cm^{-1} for the G-band, respectively, in a temperature range of 900 °C to 1300 °C. The I(D) to I(G) strongly increased from 1.6 to 2.8. In parallel both band positions shifted by approximately 10 cm^{-1} to higher wave numbers. Both studies have been performed with the same excitation wavelength of 632.8 nm, so that the differences can not be explained by the influence of the excitation wavelength. However, the systems obviously differ strongly from each other. E.g. no D- and G-band was visible in the Raman spectra of Reference [80] for a pyrolysis temperature of 800 °C due to high background signals arising from the photo luminescence. Moreover the elemental composition with respect to the amount of carbon and the pyrolysis procedure differ strongly.

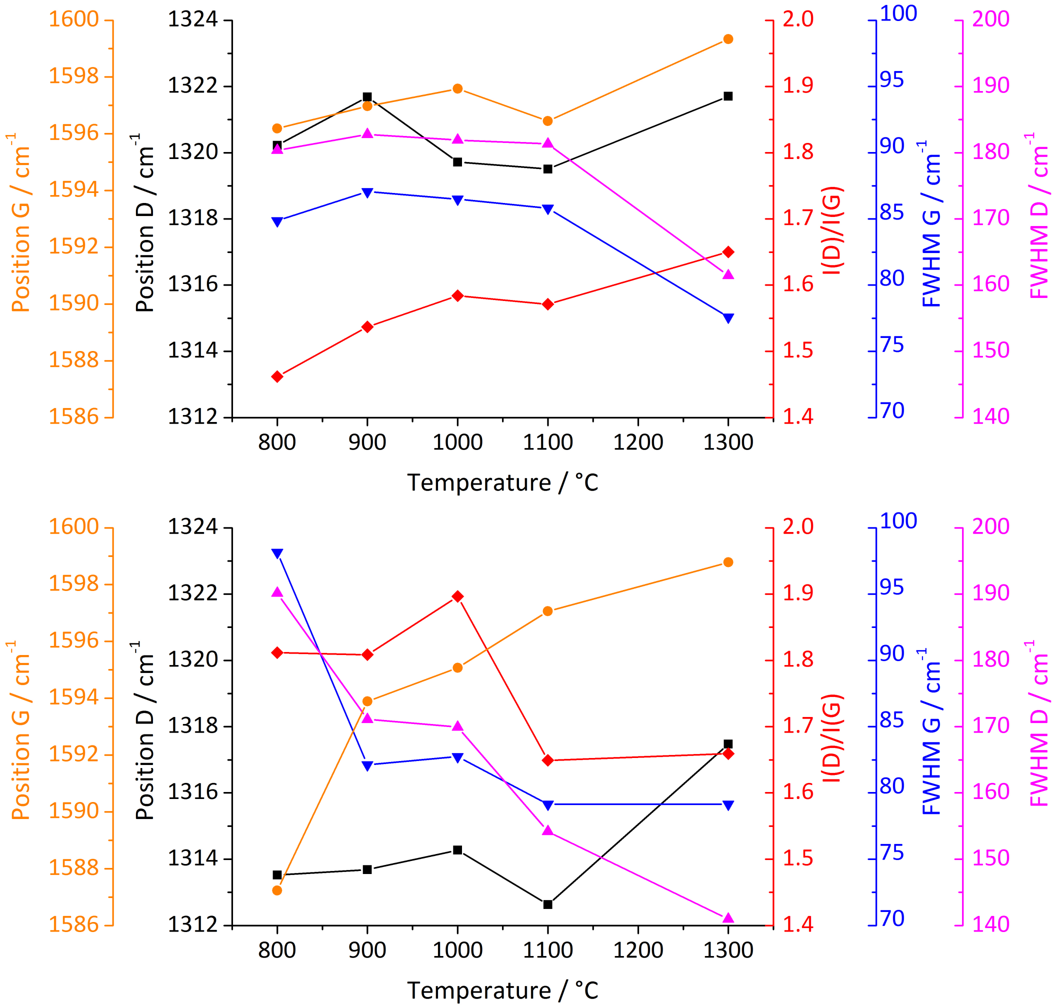

Figure 4.14: Top: Evolution of the D- and G-band position, the FWHM of the D- and G-band and the intensity ratio I(D)/I(G) with increasing pyrolysis temperature of HN1$_b$. **Bottom:** Evolution of the D- and G-band position, the FWHM of the D- and G-band and the intensity ratio I(D)/I(G) with increasing pyrolysis temperature of HN3$_b$.

Concluding, the changes in free carbon phase within the investigated temperature range are smaller than expected. Especially the little changes in the I(D) to I(G) ratio is supporting this finding. However, the decrease of the FWHM in both systems proves the increasing order of the free carbon phase at higher pyrolysis temperatures.

The Raman spectra of $HN1_a$ and $HN3_b$ ceramics after an additional heat treatment at 1700 °C are given in Figure 4.15. Two spectra for each material are presented (red and black curve) to show the significant inhomogeneities within the samples. The intensity ratios of D to G differ strongly among each material. For the sample derived from $HN1_b$ the intensity ratio even inverts, i.e. the maximum intensity of the G-band is higher than that of the D-band. For one spectra of each material an additional signals arises at $796\,cm^{-1}$. This band can be attributed to the transverse optic mode (TO) of silicon carbide SiC.[109] This particular spectra also shows a pronounced 2*D1-band in comparison to the samples which do not exhibit SiC signals. The presence of SiC is in agreement with the X-ray diffraction pattern discussed in Chapter 4.3.2. During the measurements it was observed that the differences in the Raman spectra can be correlated to the particle size. Whereas big particles in the range of several micrometers did not show Raman activity of SiC, areas of smaller particles well below $1\,\mu$m did. The heat treatment was done on already milled ceramics. Therefore the particle size obviously strongly influences the microstructure evolution of SiCN during the pyrolysis.

Due to the huge differences in the maximum intensities no I(D) to I(G) ratio is given for the samples pyrolyzed at 1700 °C. The change in D- and G-band position for both samples is negligible changing to $1323\,cm^{-1}$ and $1605\,cm^{-1}$ for $HN1_b$ and to $1322\,cm^{-1}$ and $1596\,cm^{-1}$ for $HN3_b$, respectively. The FWHM of the D- and G-band decreased strongly to $63\,cm^{-1}$ and $48\,cm^{-1}$ for $HN1_b$ and $58\,cm^{-1}$ and $65\,cm^{-1}$ for $HN3_b$, respectively (values from curve fitting were averaged over three measurements taken at particles of different sizes). This strong decrease in FWHM and the distinct bands arising from vibration modes of higher order show the increase of order in the free carbon phase and supports its classification as soft carbon.

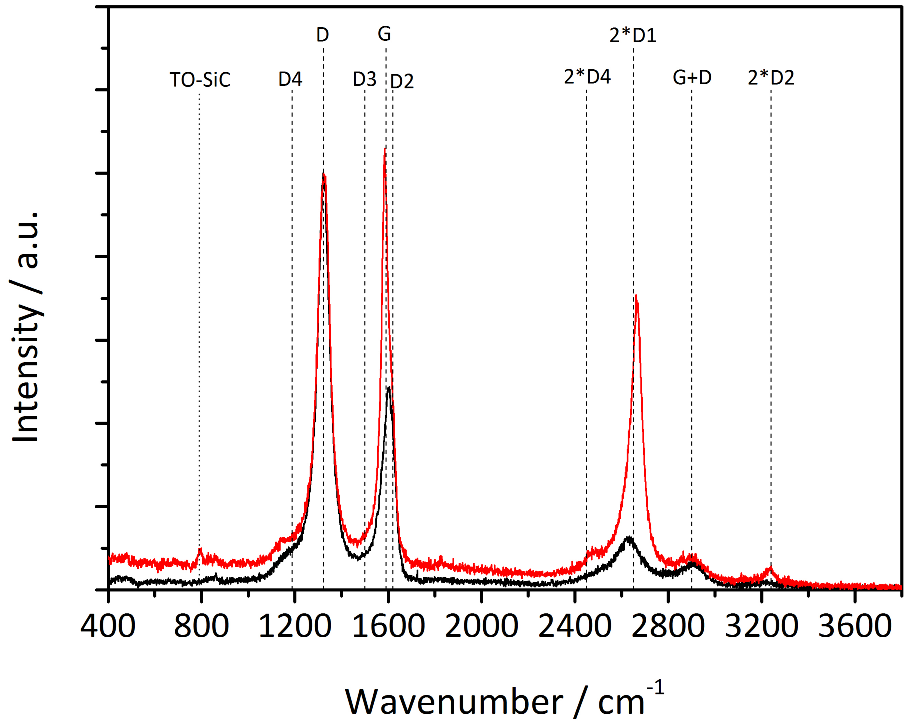

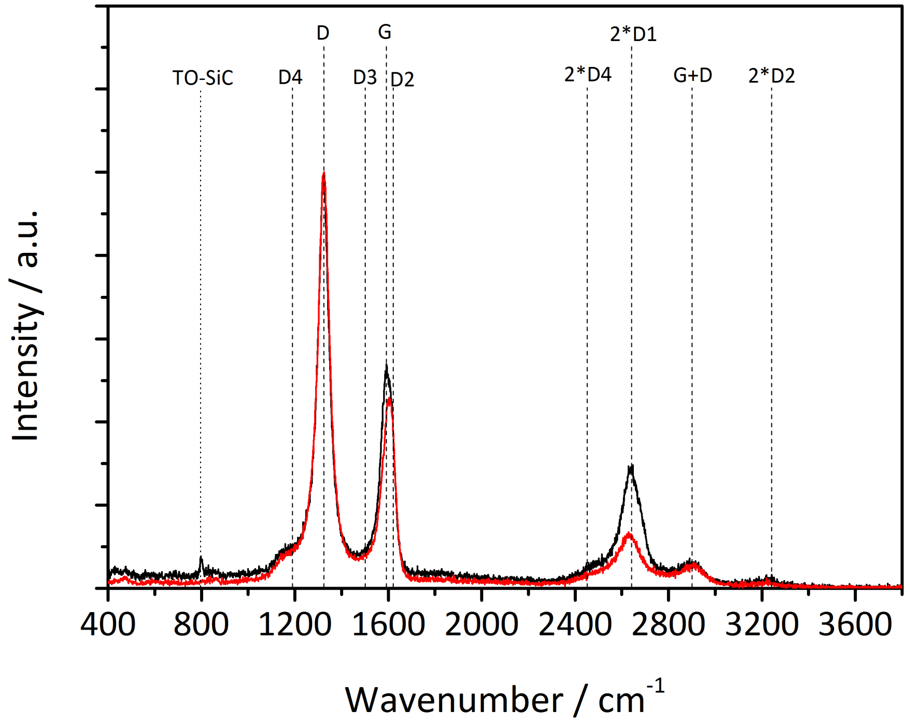

Figure 4.15: Top: Raman spectra of HN1_b pyrolyzed at 1700 °C. **Bottom:** HN3_b pyrolyzed at 1700 °C. The inhomogeneities of the samples after pyrolysis are seen by the TO mode of SiC, which only appears for measurements on small particles.

Table 4.7: D_{50} values and SSA of $HN1_b$ and $HN3_b$ pyrolyzed at different temperatures after grinding and sieving.

Sample	D_{50} [μm]	SSA [$m^2 \cdot g^{-1}$]	Sample	D_{50} [μm]	SSA [$m^2 \cdot g^{-1}$]
HN1-800	5.7	16.49	HN3-800	12.4	18.03
HN1-900	8.2	18.42	HN3-900	14.9	11.54
HN1-1000	7.6	10.38	HN3-1000	6.8	19.77
HN1-1100	11.6	9.87	HN3-1100	10.5	14.59
HN1-1300	8.9	-	HN3-1300	13.5	-

4.3.4 Particle Size Distribution and Specific Surface Area

The D_{50} values for all ceramic powders after grinding and sieving along with the specific surface areas (SSA) are given in Table 4.7. All ceramics exhibited a non-porous behavior. The SSA was found to be in the range of $10\,m^2 \cdot g^{-1}$ to $20\,m^2 \cdot g^{-1}$.

4.3.5 Galvanostatic Cycling with Potential Limitation

Figure 4.16 is showing the discharge capacities of $HN1_b$ and $HN3_b$ pyrolyzed at temperatures between 800 °C and 1300 °C. The materials derived from both precursors show the highest first cycle delithiation capacity when pyrolyzed at 800 °C. With increasing pyrolysis temperature the first cycle delithiation capacity continuously decreases from $674\,mAh \cdot g^{-1}$ at 800 °C to $282\,mAh \cdot g^{-1}$ at 1300 °C for $HN1_b$ derived ceramics and from $587\,mAh \cdot g^{-1}$ at 800 °C to $321\,mAh \cdot g^{-1}$ at 1300 °C for the samples derived from $HN3_b$, respectively. This tendency is visualized in Figure 4.17 along with the first cycle coulombic efficiency which reaches a maximum at 62 % for $HN1_b$ and 64 % for $HN3_b$ at 1100 °C. The trend of decreasing capacities with increasing pyrolysis temperature is not matching the results of Su et al. [44]. They observed only small first cycle capacities for their samples pyrolyzed at 600 °C and 800 °C while the sample pyrolyzed at 1000 °C shows a maximum in capacity which decreases again with rising pyrolysis temperatures. Even though the results are in contrast to the work of Su et al. they match the Raman measurements and the elemental analysis presented in Chapter 4.3.3 and Chapter 4.3.1, respectively. The number of lithium ions per carbon atom which can be stored in the free carbon phase decreases with higher pyrolysis temperatures due to the increased order. This effect can not be counter balanced by the rise in the free carbon amount. The trend of decreasing first cycle capacities with increasing pyrolysis temperatures were also obtained by Kaspar et al. [103] and Fukui et al. [110] for SiOC.

It is also likely that the higher oxygen amount at lower pyrolysis temperatures attributes to a certain extend to the higher 1^{st} cycle delithiation capacities.

The samples pyrolyzed at lower temperatures of 800 °C, 900 °C and 1000 °C show a decreased delithiation capacity during the second cycle. For pyrolysis temperatures of 1100 °C and 1300 °C the materials show stable cycling behavior from the beginning. Some samples demonstrate increasing delithiation capacities. This trend is also reflected in the cycling stability ζ' after 134 cycles. The percentage of capacity recovered after 134 cycles increases with an increase in pyrolysis temperature. The delithiation capacity for samples pyrolyzed at temperatures higher than 1000 °C even exceed the capacities recovered during the first cycle. Only HN3-1000 is clearly showing a different behavior. It is having much higher capacities and shows "noice" during cycling. The high delithiation capacities of HN3-1000 might arise from the low loading of the electrodes. Moreover, the particle size of this sample is significantly smaller than for the powders derived from $HN3_b$ as has been shown in Chapter 4.3.4. The mass of active loading is given in Table 4.8.

Especially the electrochemical performance of HN3-1300 attracts attention in terms of its rate capability and cycling stability. The drop in capacity when increasing the C-rate is significantly lower than for all the other samples, resulting in the highest delithiation capacities at current rates of $C/1_C$.

Figure 4.18 displays the voltage vs. capacity curves of the 1^{st} and 134^{th} cycle corresponding to the lithiation and delithiation data presented in Figure 4.16. The curves have been normalized to 100 % of the capacity. For all samples the onset of lithiation is at approximately 1 V. The shape of the delithiation curves of HN3-1000 to HN3-1300 follows the behavior reported for $HN3_a$, GM65 and DiPhen derived ceramics discussed in Chapter 4.1.4; i.e. they exhibit micropore activity during delithiation at potentials of 0.15 V and an almost linear slope up to about 1.3 V. At potentials above 1.3 V almost no capacity retention is observed. The curves for HN3-800 and HN-900 differ significantly in their shape compared to the samples pyrolyzed at higher temperatures. They do not exhibit any micropore activity and the shape of the curves is similar to the delithiation curves obtained for hydrogen containing soft carbons presented e.g. by Zheng et al. [111, 112], i.e. a plateau at about

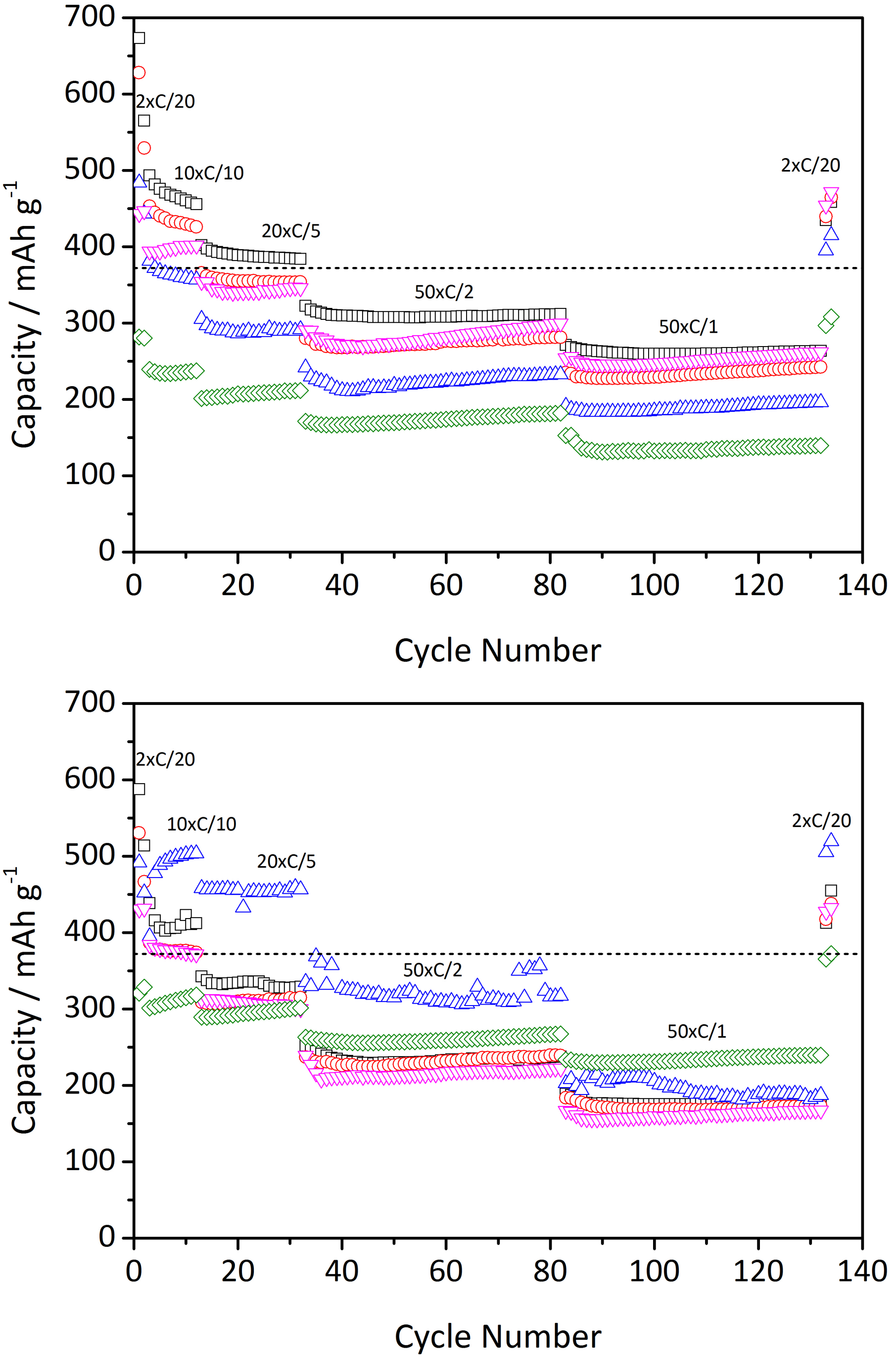

Figure 4.16: Delithiation capacities at different cycling rate for SiCN derived from $HN1_b$ (top) and $HN3_b$ (bottom) pyrolyzed at temperatures between 800 °C and 1300 °C. □: 800 °C; ○: 900 °C; △: 1000 °C; ▽: 1100 °C and ◇: 1300 °C. The dotted line (- - -) is showing the theoretical capacity of graphite.

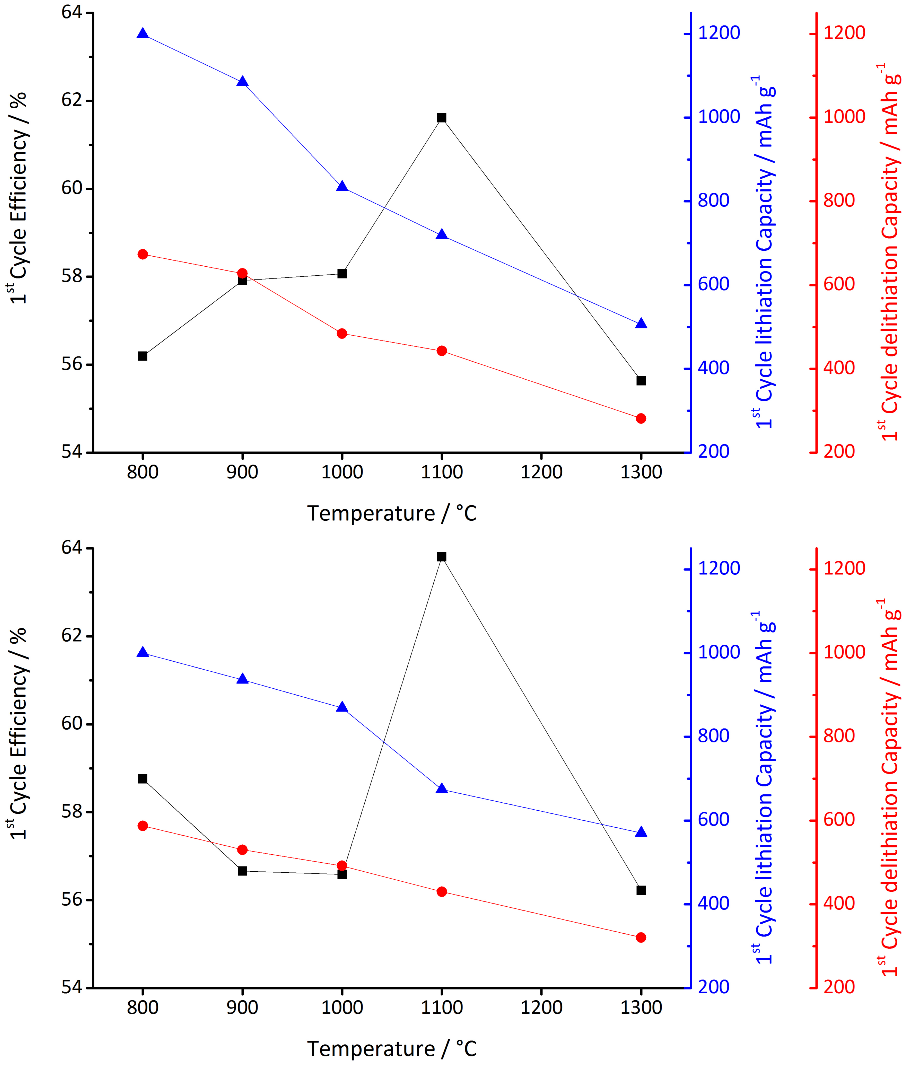

Figure 4.17: Coulombic efficiency, 1st cycle lithiation capacity and 1st cycle delithiation capacity of HN1$_b$ (top) and HN3$_b$ (bottom) derived ceramics in dependence of the pyrolysis temperature.

Table 4.8: Loading of active mass, 1st cycle lithiation and delithiation capacity, coulombic efficiency and cycling stability of the GCPL measurements displayed in Figure 4.16.

Sample	Active mass [mg·cm^{-2}]	C$_{lith,1^{st}\ cycle}$ [mAh·g^{-1}]	C$_{delith,1^{st}\ cycle}$ [mAh·g^{-1}]	ζ [%]	ζ' [%]
HN1-800	0.93	1199	674	56	68
HN1-900	1.35	1084	628	58	74
HN1-1000	3.80	834	484	58	86
HN1-1100	2.59	719	443	62	107
HN1-1300	2.47	506	282	56	109
HN3-800	2.86	1000	587	59	77
HN3-900	2.81	936	530	57	82
HN3-1000	1.27	869	492	57	106
HN3-1100	2.62	674	430	64	100
HN3-1300	2.35	571	321	56	116

1 V is visible during delithiation. This implies that the hydrogen detected with elemental analysis is partly located in the free carbon phase for HN3-800 and HN3-900. The results from elemental analysis (compare Table 4.6) have shown that the hydrogen content at these pyrolysis temperatures is significantly higher than for the samples HN3-1000 to HN3-1300. At higher pyrolysis temperatures the hydrogen is obviously removed or at least reduced from the free carbon phase. As consequence of the higher hydrogen content the hysteresis for these samples is significantly increased.

The lithiation and delithiation curves of HN1$_b$ also show a contribution of micropores to the capacity at a pyrolysis temperature of 1000 °C and above. However, the shape of the delithiation curve is exhibiting the plateau at about 1 V being characteristic for lower pyrolysis temperatures. A comparison between the hydrogen amounts of HN1-900 and HN1-1000 shows that the decrease is not as strong as for HN3-900 and HN3-1000.

For a more quantitative description of the hysteresis the average lithiation and delithiation potentials for the 1st and 134th cycle have been calculated. The average potentials were calculated by integrating the voltage-capacity curve and dividing the obtained value by the measured capacity. The difference of the delithiation potential and the lithiation potential

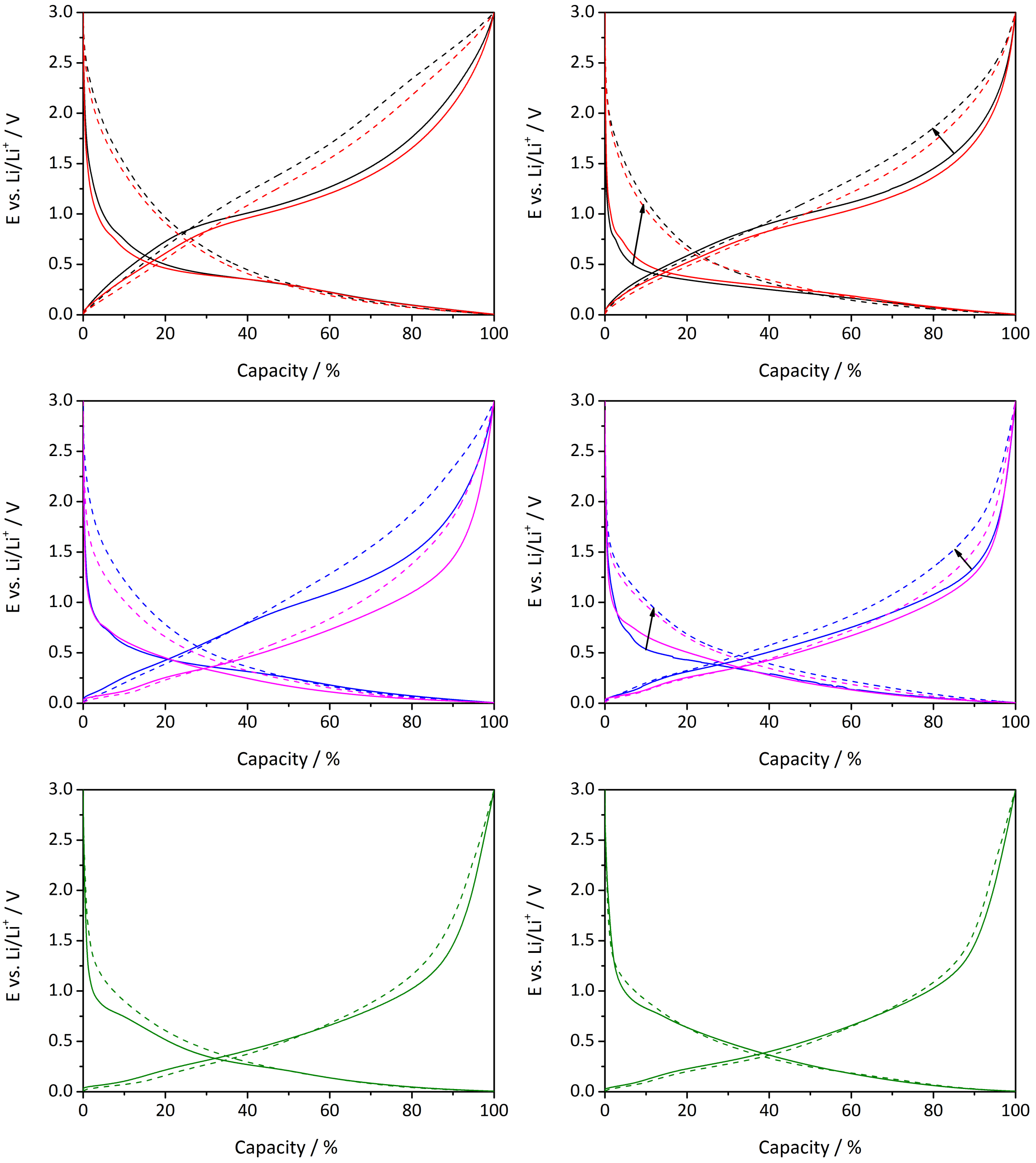

Figure 4.18: 1st (continuous lines) and 134th (dashed lines) lithiation and delithiation curves of the polysilylcarbodiimide derived ceramics HN1$_b$ (left) and polysilazane derived ceramics HN3$_b$ (right). 800 °C: —; 900 °C: —; 1000 °C: —; 1100 °C: —; 1300 °C: —. The arrows are indicating the shift to higher lithiation and delithiation potentials with ongoing cycling.

gives rise to the hysteresis. The evolution of the average lithiation and delithiation potential for the first and 134^{th} cycle and the hysteresis in dependence of the pyrolysis temperature is shown in Figure 4.19. The average lithiation potential for the 1^{st} cycle for $HN1_b$ derived ceramics is almost unaffected by the pyrolysis temperature. For $HN3_b$ derived ceramics it increases slightly from 240 mV to 370 mV. The 134^{th} cycle shows a continuous decrease in the average lithiation potential by 200 mV for $HN1_b$ derived ceramics between 800 °C and 1300 °C and almost no changes for $HN3_b$ derived ceramics, respectively. Both materials show a clear tendency for the average delithiation potential to decrease with increasing pyrolysis temperature. For $HN1_b$ derived ceramics the potential decreases overall by 550 mV and 370 mV for $HN3_b$, respectively. The decrease in delithiation potential with higher pyrolysis temperatures is even more pronounced for the 134^{th} cycle. Due to the strong decrease in delithiation potential with increasing temperature the hysteresis decreases significantly for increasing pyrolysis temperatures. For a pyrolysis temperature of 1300 °C a hysteresis of only 370 mV for $HN1_b$ and 330 mV for $HN3_b$ is achieved. These values are in the same order as values found for polysiloxane derived ceramics located at the C-SiC line of a ternary SiOC composition diagram [53], i.e. for compositions with only a small amount of oxygen. It was found in the same study that an increase in the oxygen content shifted the average delithiation potential to higher potentials.

A significant decrease in the hysteresis with increasing pyrolysis temperatures was also found for anodes made from SiOC [110] and for pure disordered carbons. The high hysteresis at low pyrolysis temperatures was explained by a kinetic hindrance of diffusion due to an transformation of sp^2 hybridized, hydrogen terminated edge carbons into sp^3 hybridized carbons and vice versa during lithiation and delithiation.[112, 113] Ahn et al. [114] studied the reasons for a high hysteresis of SiOC pyrolyzed at 1000 °C and attributed it partly to kinetic effects and partly to a thermodynamic limitation of lithium insertion in the SiOC network.

The presented voltage vs. capacity in Figure 4.18 curves also exhibit aging of the samples. The lithiation and delithiation potentials in the 134^{th} cycle are shifted to higher potentials in comparison with the potentials obtained in the 1^{st} cycle. This effect is decreasing with higher pyrolysis temperatures. The calculation of the precise potentials given in Figure 4.19 also allows for a quantitative description of the aging. The shift to higher delithiation potentials with ongoing cycling is reflected by the difference in the average potential during the 134^{th} cycle and 1^{st} cycle. At a pyrolysis temperature of 800 °C the average potentials are shifted

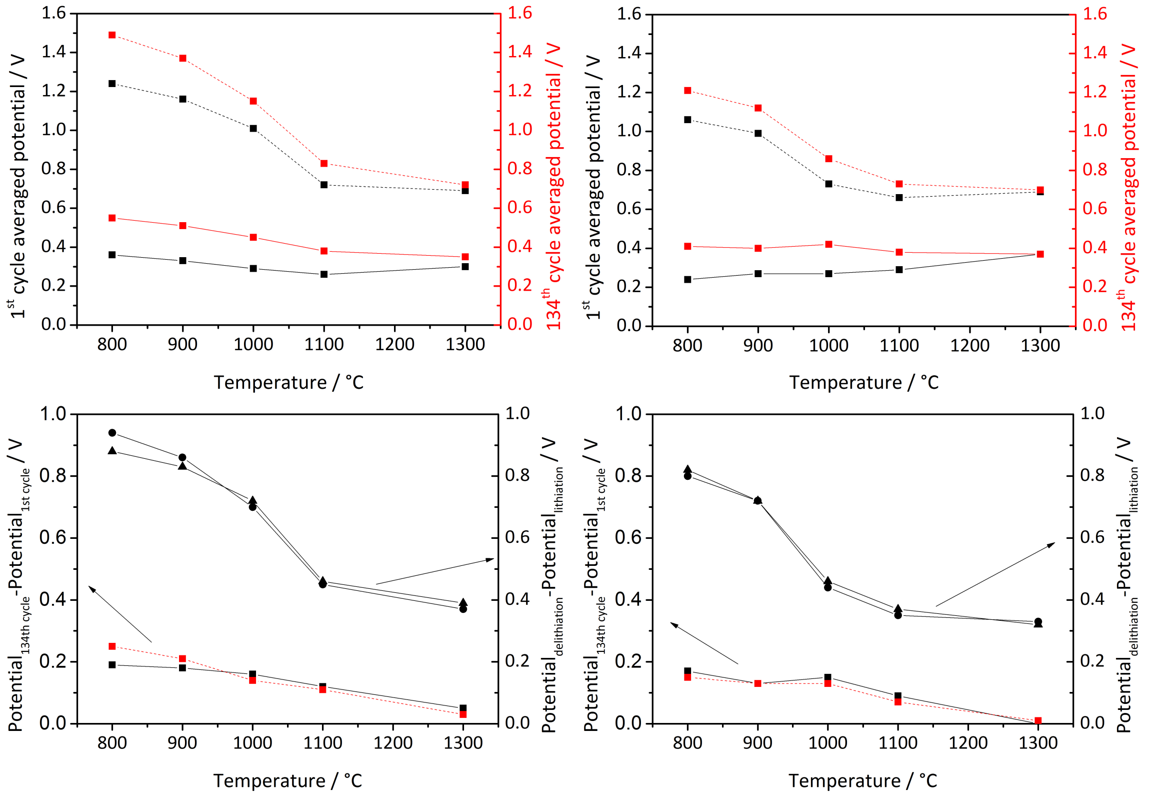

Figure 4.19: The upper graphs show the average lithiation potential during the 1^{st} cycle (■ connected by solid black line) and 134^{th} cycle (■ connected by solid red line) and the average delithiation potential during the 1^{st} cycle (□ connected by dashed black line) and 134^{th} cycle (■ connected by dashed red line) of HN1_b (left) and HN3_b (right) pyrolyzed at different temperatures, respectively. The lower graphs are showing the shift of the lithiation potential (■ connected by solid line) and the shift of the delithiation potential (■ connected by dashed line) which occurs during cycling on the left y-axis. The evolution of the hysteresis with pyrolysis temperature in the 1^{st} cycle (△ connected by solid black line) and 134^{th} cycle (○ connected by solid black line) are given on the right y-axis.

by about 200 mV. This shift is getting smaller with increasing pyrolysis temperature and eventually becomes zero for a pyrolysis temperature of 1300 °C. The size of the hysteresis stays almost unaffected during cycling as the shift of the average potential is the same for lithiation and delithiation.

To get a better impression about the stability of the SiCN materials a long term measurement was performed on HN1-1100. To decrease the overall measurement time the sample was cycled at a rate of $C/1_C$ for 200 cycles followed by one cycle at a rate of $C/20_C$. This procedure was repeated 12 times, so that all together 2412 cycles were performed. The measured delithitaion capacities are given in Figure 4.20. The electrochemical performance (in the beginning) of the electrode is similar to the electrode performance of HN1-1100 presented before in Figure 4.16. The 1^{st} cycle delithiation capacity at $C/1_C$ is 222 mAh·g^{-1} (average delithiation capacity at $C/1_C$ in Figure 4.16 is 252 mAh·g^{-1}) and at the delithiation capacity in the 201^{st} cycle measured at a rate of $C/20_C$ amounts 450 mAh·g^{-1} (463 mAh·g^{-1} for the sample in Figure 4.16 averaged over all four cycles recorded at $C/20_C$). The active loading is also similar with 2.86 mg·cm^{-2} (compared to 2.59 mg·cm^{-2} for the sample presented in Figure 4.16). Also the stability is the same if only the first 134 cycles are taken into consideration (108 % to 107 %). The sample reaches a maximum in capacity after 62 cycles and starts to fade with continued cycling. After intermediate cycling at $C/20_C$ the delithiation capacity recovers to a certain extend. Still, the cell reaches its end of life (capacity drops below 80 %) after 363 cycles. This is, however, only true for the delithiation capacities of the comparable fast cycling rate of $C/1_C$. If the "80 % criteria" is applied on the delithiation capacities obtained at slow cycling rates, the cell is still intact, even after more than 2400 cycles (ζ'=88 % in the 2412^{th} cycle with respect to the capacity obtained in the 201^{st} cycle). It can therefore be concluded that the ceramic itself is still intact for lithium storage. The reason for the fading at fast cycling rates is probably the increase of the charge transfer resistance R_{ct} with prolonged cycling which limits the charge rate exchange at high cycling rates. It has been already seen in Figure 4.18 that electrodes alter during cycling affecting the lithiation and delithiation potential. For slow rates the influence on the charge rate exchange seems to be of minor importance.

To sum up the results of the GCPL measurements, higher pyrolysis temperatures present some benefits to the electrochemical performance of polymer-derived SiCN. The cycling stability of the ceramics increases in terms of capacity and average potential, the rate capability increases and the hysteresis decreases. In contrary the capacity, especially at slow cycling rates, is diminished.

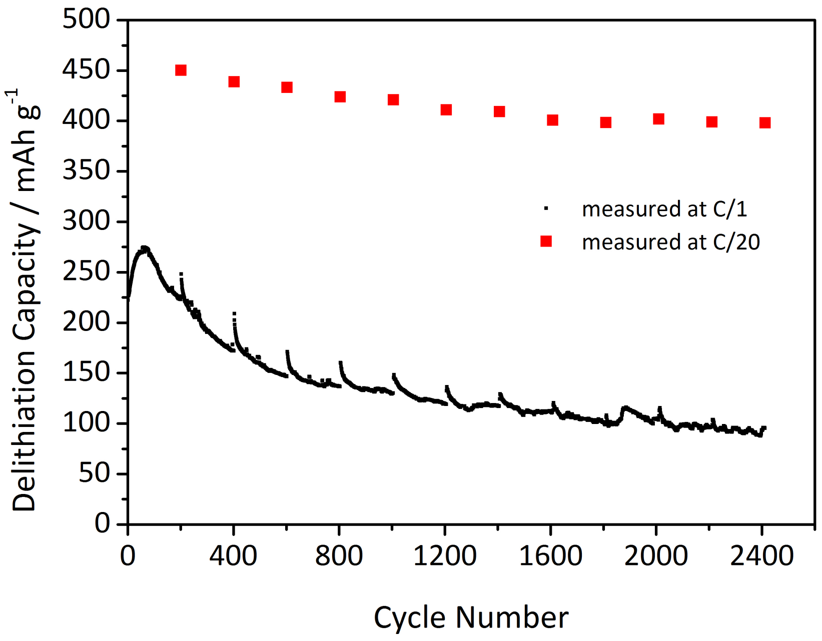

Figure 4.20: Long term GCPL measurement of HN1-1100. The delithiation capacities recorded at C/1_C are marked with small black squares ■, the intermediate slow cycling at C/20_C are highlighted by the red squares 🟥.

4.3.6 Scanning Electron Microscopy

Figure 4.21 and Figure 4.22 show the SEM pictures of pristine (uncycled) and cycled electrodes of HN1_b and HN3_b pyrolyzed at 800 °C and 1300 °C at magnification of x2500. The pristine electrodes show the ceramic particles embedded into a well distributed, porous matrix of conducting additive and binder. The pictures confirm the results of the particle size measurements. The fibers on the cycled electrodes are due to the glass fiber separator used. The cycled electrodes of the samples pyrolyzed at 1300 °C show only little changes in comparison to the pristine electrodes. The ceramic particles as well as the additives are still visible. A closer look however reveals that film formation has occurred on the additives. The porosity is reduced and it seems like the carbon particles are grown together. The impact of cycling the electrodes with the active material pyrolyzed at 800 °C is seen very clearly. The morphology of the electrodes has changed completely. A strong film formation has occurred. It is not possible to distinguish among single ceramic particles or active material and additives. The film formation is even so pronounced that some glass fibers of the separator have been encapsulated completely. The strong film formation on the electrodes may explain the shift in the lithiation and delithiation potential and the fading of the capacity presented in Chapter 4.3.5 which was related to an increase in R_{ct} .

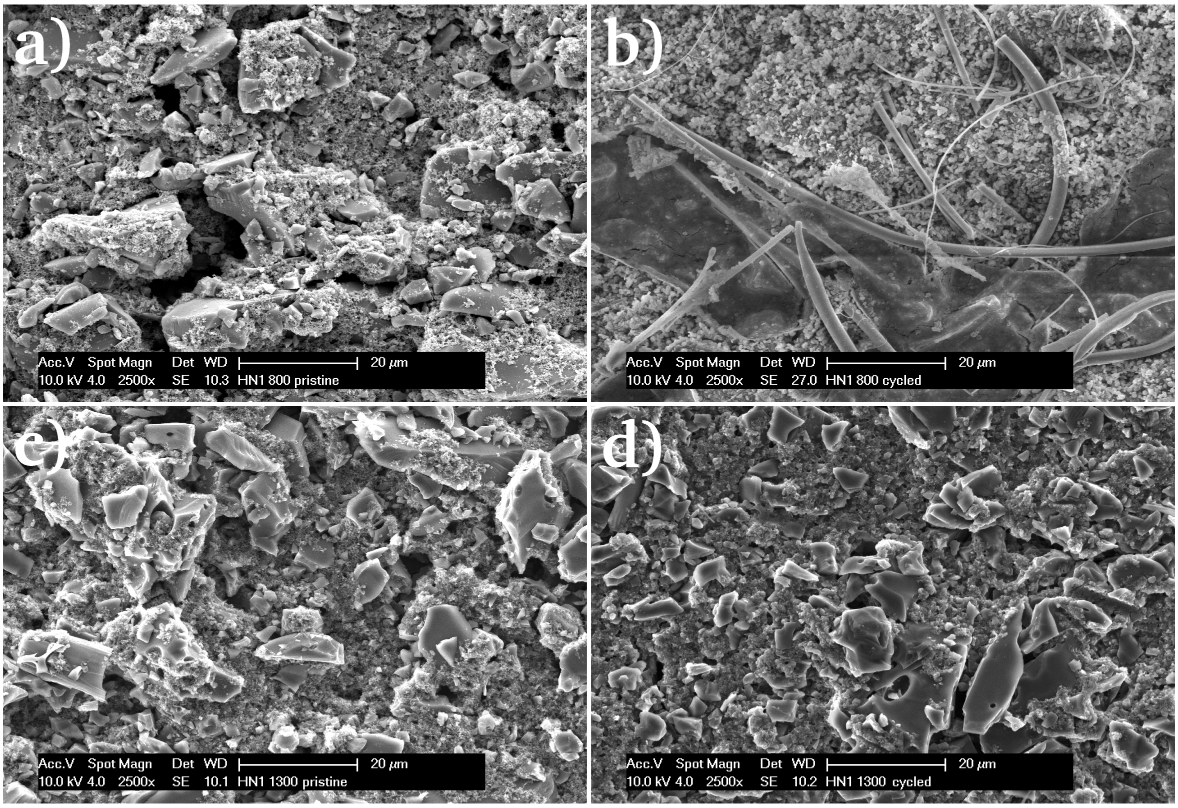

Figure 4.21: SEM pictures at a magnification of 2500x of HN1-800 pristine (a) and cycled (b) and HN1-1300 pristine (c) and cycled (d).

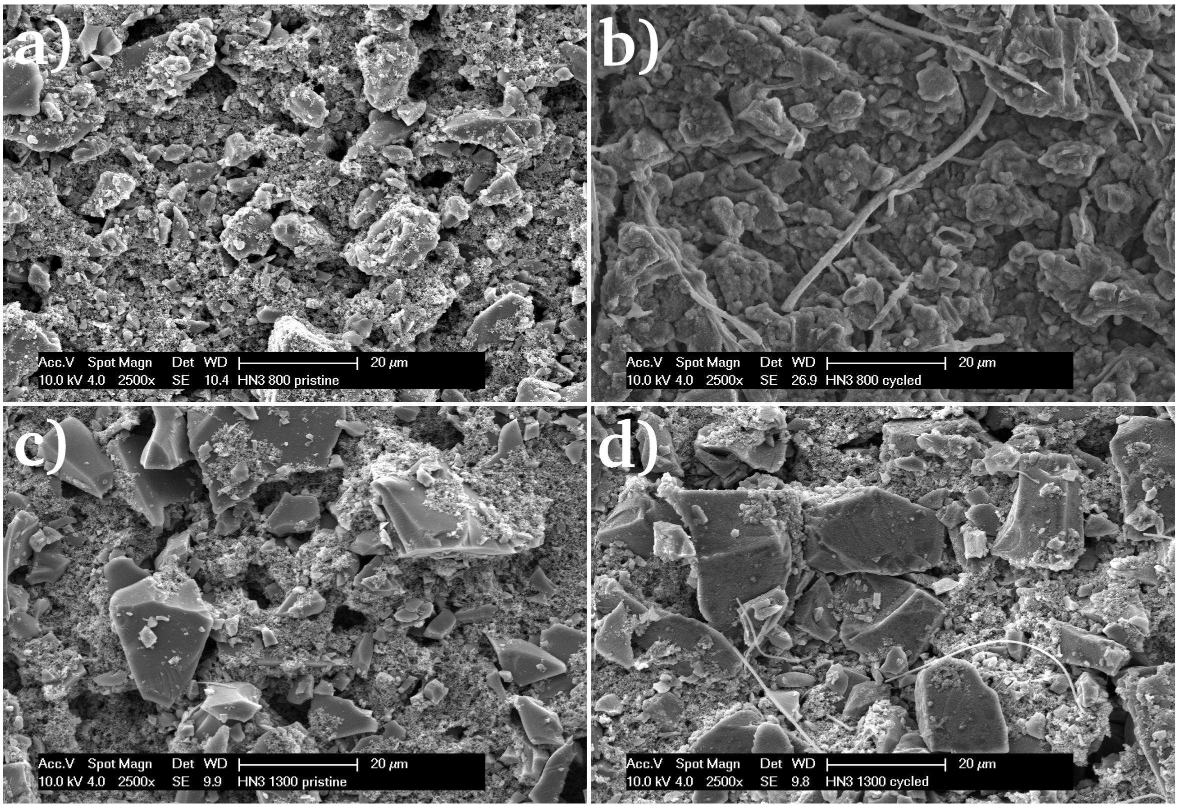

Figure 4.22: SEM pictures at a magnification of 2500x of HN3-800 pristine (a) and cycled (b) and HN3-1300 pristine (c) and cycled (d).

4.3.7 Single Particle Measurements

So far, only electrochemical measurements of the active materials as "powder electrodes" have been presented. However, these electrodes posses a high fraction of additives, namely Carbon Black Super P® and PVDF, influencing the performance of the electrodes. Moreover, the composition, the porosity and the thickness of the electrodes can have a significant impact on the obtained results. Yet, it is of great interest to gain insight into the intrinsic properties of the active material. For this reason Single Particle Measurements on $HN1_b$ and $HN3_b$ pyrolyzed at 800 °C and 1300 °C were performed at electrolyte temperatures of 25 °C (room temperature RT) and at 60 °C. A detailed description of the experimental setup and evaluation of the data was already given in subsection 3.4.4.

In the following the evaluation and discussion of the measurement of HN3-1300 at an electrolyte temperature of 60 °C is shown as an example. The obtained data from the rate tests for all performed measurements, including the Tafel plots for DODs between 10 % and 50 %, the initial cycling and the stability check are given in the Appendix A.

A picture of the measured particle recorded with the microscope at a magnification of 300x is shown at the right side of Figure 4.23. The size given in the picture is only a rough value used for a first estimation of the particle size directly at the measurement set up. Moreover, it allows for marking the measured particle. A more precise determination of the measured particle size was performed after the measurement. From Figure 4.23 the diameter of the particle was measured to 18.6 μm. The left hand side of Figure 4.23 is showing the initial three lithiation and delithiation cycles of HN3-1300 measured at 1 nA and 60 °C. The first cycle lithiation curve differs strongly from the second and third cycle lithiation curve which can be partly explained by the formation of an SEI visible in the shoulder of the 1^{st} cycle lithiation curve between approximately 0.75 V and 0.5 V and other possible irreversible reactions taking place. The first cycle lithiation capacity amounts to 1.07 nAh and the first cycle delithiation capacity amounts to 0.35 nAh. The coulombic efficiency ζ for the first cycle was calculated to 33.4 %. Assuming a density of the material[1] of about 2.0 $g \cdot cm^{-3}$ and a spherical shape of the particle the specific capacity accounts 53 $mAh \cdot g^{-1}$. Both, coulombic efficiency and capacity are much lower than measured for composite electrodes of HN3-

---

[1] Literature values for bulk samples of polymer derived SiCN vary from 1.85 $g \cdot cm^{-3}$ to 2.3 $g \cdot cm^{-3}$ depending on the precursor, the processing route and the pyrolysis temperature.[80, 115, 116]

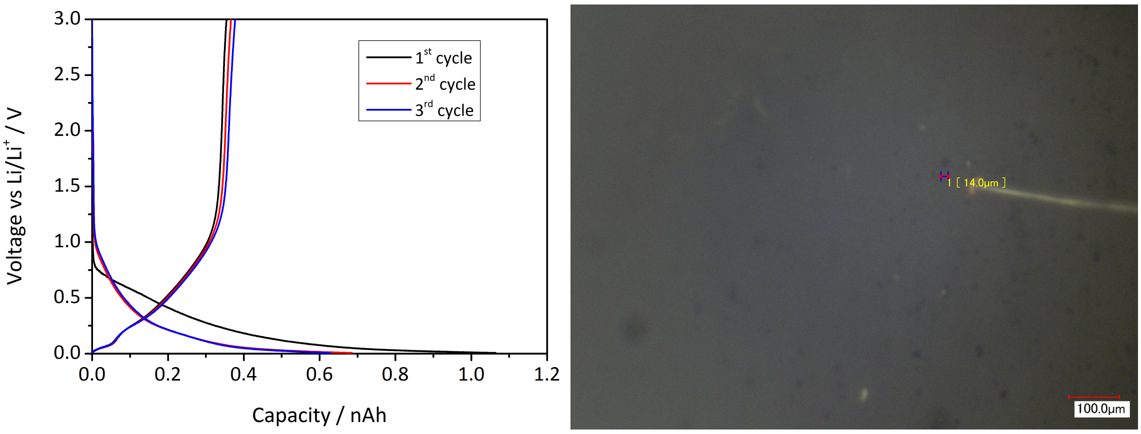

Figure 4.23: Left: Three initial cycles of HN3-1300 at 1 nA and an electrolyte temperature of 60 °C. **Right:** Microscope picture of the measured particle.

1300 with 7.5 wt% of Carbon Black and 7.5 wt% of PVDF (ζ=56 %, capacity=571 mAh·g^{-1} at 18.6 mA·g^{-1}) in 1 M LiPF$_6$ in EC:DMC 1:1 wt%. The delithiation capacity shows no fading during the first three cycles and even increases slightly. However, the coulombic efficiency is still far away from 100 % ($\zeta_{2^{nd}cycle}$=53 %, $\zeta_{3^{rd}cycle}$=60 %), meaning that strong irreversible reactions are still taking place. This is in contrast to the measurements done on the powder electrodes, which exhibited a coulombic efficiency in the second cycle of 93 % for HN3-1300.

At low potentials a quasi-plateau is visible during discharge which is attributed to micropore activity in the materials. The stable cycling behavior and the contribution of micropores to the capacity are in accordance with the measurements performed on composite electrodes.

The delithiation curves of the rate test are shown in Figure 4.24. The recovered capacity remains stable (or even increases) up to 5 nA. At a delithiation current of 100 nA the capacity amounts 49 % of the capacity recovered at 1 nA. With increasing current the delithiation potential is shifted to higher values. At 100 nA the delithiation starts at potentials as high as 1 V.

After the rate test a complete lithiation and delithiation at 1 nA was performed and compared to the first cycle of the rate test to control the stability of the electrochemical response after prolonged cycling at high rates. The lithiation and delithiation curves for HN3-1300 before and after the rate test are given in Figure 4.25. The delithiation potential is slightly shifted to higher potentials which is not matching the results of the GCPL measurements performed on the powder electrodes. The increase has only been observed for ceramics pyrolyzed at temperatures up to 1000 °C, whereas the ceramics obtained at a pyrolysis temperature

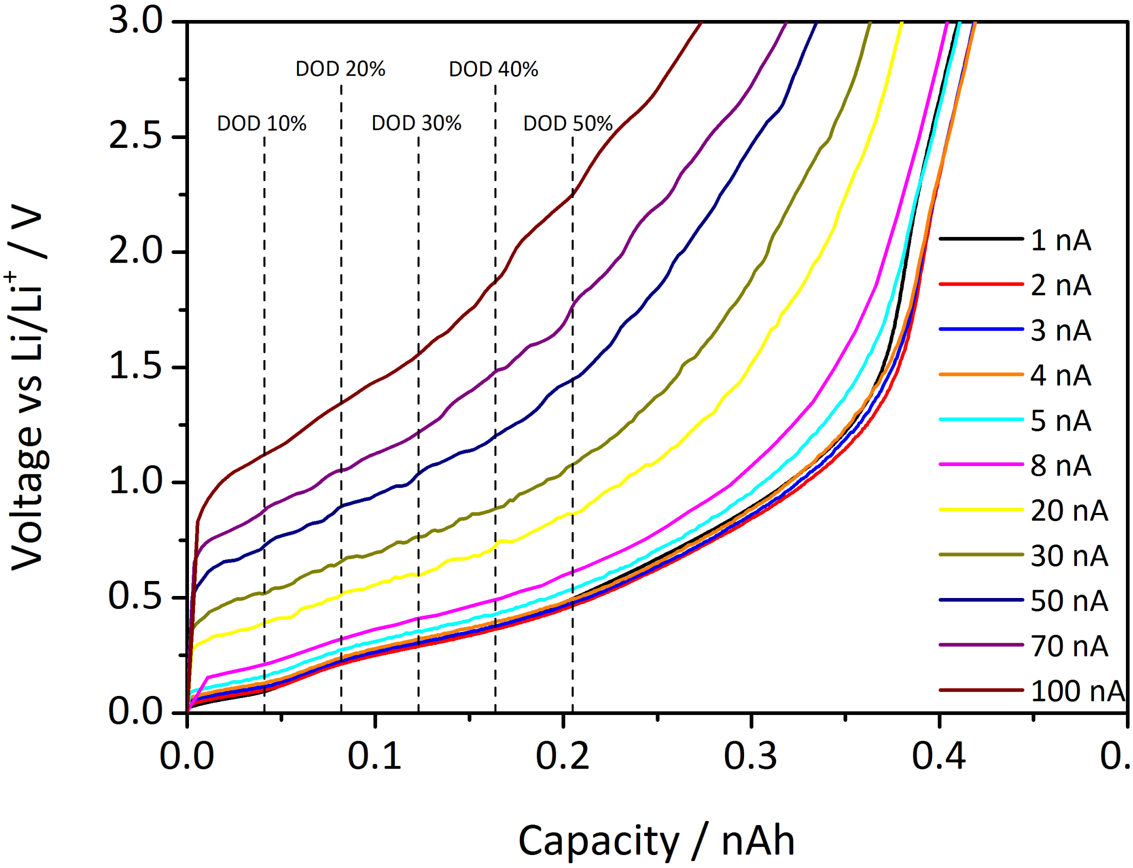

Figure 4.24: Rate capability for HN3-1300 at an electrolyte temperature of 60 °C. The lithiation current was constant for all cycles at 1 nA. The delithiation currents are given in the legend. Additional the DODs used for the evaluation of D$_{min}$ and R$_{ct}$ are marked.

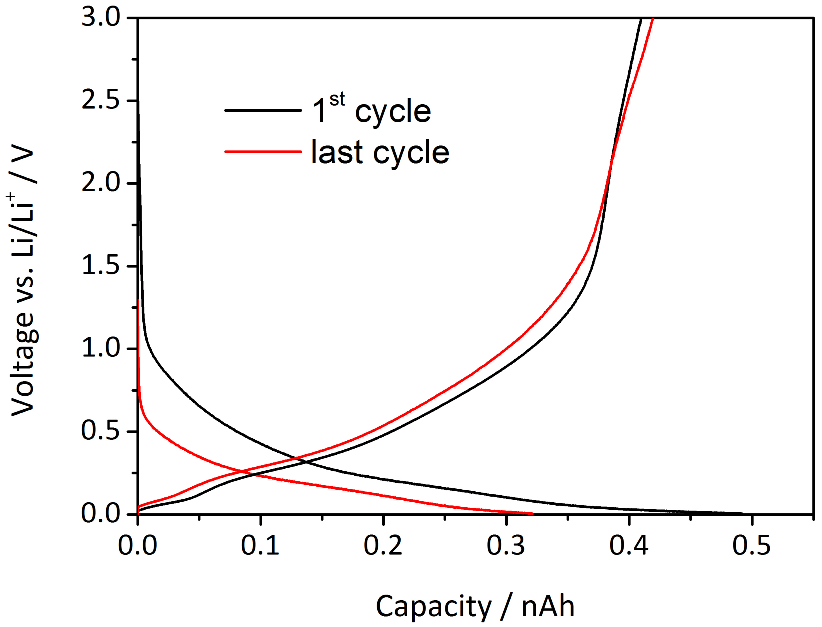

Figure 4.25: First lithiation-delithiation cycle of rate test at 1 nA and lithiation-delithiation cycle at 1 nA after the rate test.

of 1100 °C and 1300 °C showed stable lithiation and delithiation potentials with prolonged cycling. The huge differences in the lithiation capacity of Figure 4.25 are due to the rate test before the last cycle. Due to the high delithiation current of 100 nA the particle remains partially lithiated after lithium extraction. For low currents of 1 nA till 5 nA the particle was in a completely delithiated state.

Figure 4.26 presents the Tafel plot for the sample HN3-1300 at at DOD of 10 % and an electrolyte temperature of 60°. The linear region of the Tafel plot starts at a current of 2 nA. The last data point on the linear segment was recorded at 5 nA.

The charge transfer resistance R_{ct} and the minimum diffusion coefficient D_{min} obtained from the Tafel plots for all investigated samples at a DOD of 10 %, 20 %, 30 %, 40 % and 50 % are summarized in Table 4.9. A visualization of Table 4.9 is given in Figure 4.28. Table 4.9 also contains the specific capacity values of the measured particles based on the first cycle of the rate test, the particle radius taken from the microscope pictures and an assumed density of 2 $g{\cdot}cm^{-3}$. As the specific capacity depends on the particle radius by the power of three and the exact density of the particle is unknown, large errors can be assumed which make a comparison to the data obtained from the powder electrodes invalid. Never the less, a clear trend is visible among the samples pyrolyzed at different temperatures. In

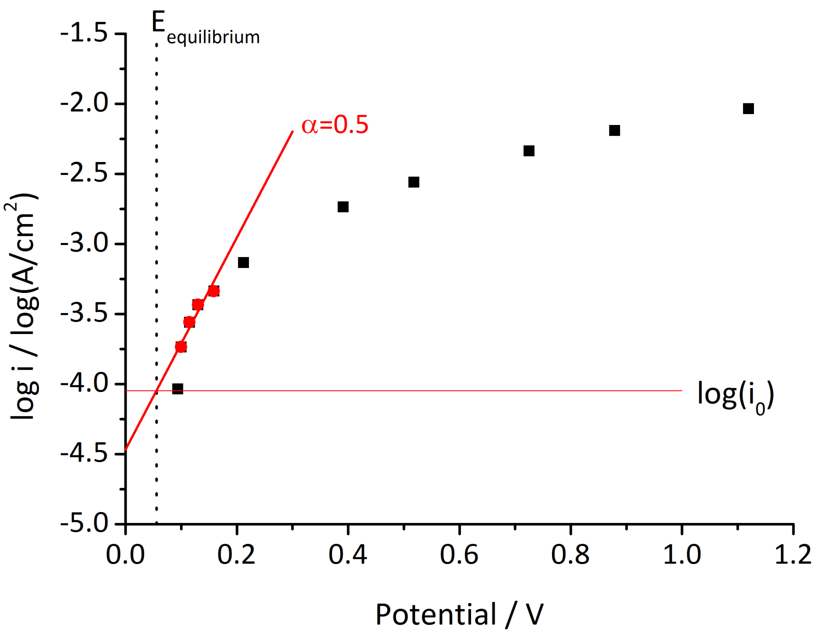

Figure 4.26: Tafel plot of HN3-1300 at an electrolyte temperature of 60 °C and a DOD of 10 %.

analogy to the powder electrodes and regardless of the electrolyte temperature, the particles pyrolyzed at 1300 °C exhibit lower capacities than the particles pyrolyzed at 800 °C. This effect would probably be even stronger if the increase of density of SiCN with increasing pyrolysis temperature is taken into consideration.[80]

The lowest R_{ct} at a DOD of 10 % of all samples was measured at an electrolyte temperature of 60 °C for HN1-1300 amounting 41 Ohm·cm^2, the highest value with 1904 Ohm·cm^2 was obtained for HN3-1300 at RT. The Single Particle Measurements of HN1$_b$ at an electrolyte temperature of 25 °C and HN1$_b$ and HN3$_b$ at an electrolyte temperature of 60 °C show that R_{ct} is strongly reduced by increasing the pyrolysis temperature from 800 °C to 1300 °C. Only the values obtained for HN3$_b$ measured at an electrolyte temperature of 25 °C deviate from this trend. However, the measurement of HN3-1300 should be repeated, as the date points recorded are not likely to include the whole linear region of the Tafel plot. In general, the values for R_{ct} at a DOD of 10 % are one to two magnitudes higher than measured for a single particle of SiOC by Fukui et al. [99] with 46 Ohm·cm^2 at 10 % DOD. Exclusively sample HN1-1300 measured at an electrolyte temperature of 60 °C is giving the same R_{ct}. Yet, the value of R_{ct} for SiOC was obtained at room temperature.

The minimum diffusion coefficient for all SiCN samples was measured in the range of $3.2 \cdot 10^{-9}$ cm^2·s^{-1} to $6.4 \cdot 10^{-11}$ cm^2·s^{-1}. The minimum diffusion coefficient for SiOC determined from single particle measurements was not given by Fukui et al.[99], but the evaluation of their published data allowed to estimate it to be about $5.6 \cdot 10^{-10}$ $cm^2 \cdot s^{-1}$ and therefore at about the same order of magnitude. The results of D_{min} are also in good agreement with literature date obtained from measurements performed on SiOC based powder electrodes using various techniques like potentiostatic intermittent titration technique (PITT), galvanostatic intermittent titration technique (GITT) and electrochemical impedance spectroscopy (EIS), ranging, depending on the applied method, from 10^{-11} $cm^2 \cdot s^{-1}$ to 10^{-10} $cm^2 \cdot s^{-1}$.[117]

Compared to other electrode materials, the values of the D_{min} for polymer-derived ceramics from Single Particle Measurements are two orders of magnitude smaller than estimated for a graphite single particle with $8.3 \cdot 10^{-8}$ $cm^2 \cdot s^{-1}$ [118] but in the same order of $LiCoO_2$ with $>10^{-10}$ $cm^2 \cdot s^{-1}$ [119]. The minimum diffusion coefficient of $LiFePO_4$ is one magnitude of order higher than for polymer-derived ceramics amounting to about $2.7 \cdot 10^{-9}$ $cm^2 \cdot s^{-1}$.[120]

With respect to R_{ct} also the SEI formation and the electrical conductivity have to be considered. From the performed measurements it is not possible to determine its influence. It is questionable if it can be neglected because of the strong film formation which occurred on the electrodes made of SiCN pyrolyzed at 800 °C with prolonged cycling (compare SEM pictures in Chapter 4.3.6. Please note that for Single Particle Measurements an electrolyte different from the standard one was used, possibly effecting the formation and composition of the SEI). Additionally, a low electrical conductivity of the ceramics would contribute to the measured overpotentials. Fukui et al. determined the electrical conductivity for their specific SiOC ceramic powder in the order of 10^{-1} $S \cdot cm^{-1}$ [99]. Therefore it was not considered to affect the measured R_{ct}. No measurements on the electrical conductivity of HN1-800, HN3-800, HN1-1300 and HN1-1300 have been performed so far. Gao et al. [121] conducted impedance measurements on a SiCN ceramic derived from polymethylvinylsilazane, showing a tremendous increase in conductivity with increasing pyrolysis temperature. The specific conductivity for this sample ranged from the order of 10^{-7} $S \cdot cm^{-1}$ at 1100 °C to 10^{-4} $S \cdot cm^{-1}$ at 1300 °C.[2] The specific conductivity of SiCN derived from the same precursor was also determined by Trassl et al. [122]. They also found an increase in conductivity with increasing pyrolysis temperature but the conductivity values were higher, being in the order of 10^{-5} $S \cdot cm^{-1}$ at 1000 °C and 10^{-3} $S \cdot cm^{-1}$ at 1200 °C. However, the free carbon content of these samples was much lower than that of the samples investigated by Single Particle Mea-

---

[2] The specific conductivity of the samples was estimated from the Nyquist plots and sample dimensions given within the thesis.

Table 4.9: Charge transfer resistance, minimum Diffusion coefficient and specific capacity of HN1$_b$ and HN3$_b$ pyrolyzed at 800 °C and 1300 °C for a DOD of 10 % till 50 %. The measurements were performed at electrolyte temperatures of 25 °C and 60 °C.

Sample	Temp	DOD 10 %		DOD 20 %		DOD 30 %		DOD 40 %		DOD 50 %		
		R_{ct} [$\Omega\cdot cm^2$]	D_{min} [$cm^2\cdot s^{-1}$]	R_{ct} [$\Omega\cdot cm^2$]	D_{min} [$cm^2\cdot s^{-1}$]	R_{ct} [$\Omega\cdot cm^2$]	D_{min} [$cm^2\cdot s^{-1}$]	R_{ct} [$\Omega\cdot cm^2$]	D_{min} [$cm^2\cdot s^{-1}$]	R_{ct} [$\Omega\cdot cm^2$]	D_{min} [$cm^2\cdot s^{-1}$]	Capacity[2] [$mAh\cdot g^{-1}$]
HN1-800	RT	799	$2.0\cdot10^{-10}$	$2.2\cdot10^{3}$	$1.4\cdot10^{-10}$	$9.6\cdot10^{3}$	$1.4\cdot10^{-10}$	$31.6\cdot10^{3}$	$8.9\cdot10^{-11}$	[1]	[1]	209
HN1-1300		223	$2.7\cdot10^{-10}$	288	$2.7\cdot10^{-10}$	566	$1.9\cdot10^{-10}$	$1.0\cdot10^{3}$	$1.9\cdot10^{-10}$	$5.3\cdot10^{3}$	$1.9\cdot10^{-10}$	110
HN3-800		$1.1\cdot10^{3}$	$2.1\cdot10^{-10}$	$3.2\cdot10^{3}$	$2.1\cdot10^{-10}$	$7.2\cdot10^{3}$	$2.1\cdot10^{-10}$	$14.1\cdot10^{3}$	$2.1\cdot10^{-10}$	$154.0\cdot10^{3}$	$1.7\cdot10^{-10}$	207
HN3-1300		$1.9\cdot10^{3}$	$1.4\cdot10^{-10}$	[1]	[1]	[1]	[1]	[1]	[1]	[1]	[1]	148
HN1-800	60°C	$1.4\cdot10^{3}$	$3.0\cdot10^{-10}$	$8.6\cdot10^{3}$	$1.7\cdot10^{-10}$	$41.5\cdot10^{3}$	$1.4\cdot10^{-10}$	$175.5\cdot10^{3}$	$1.0\cdot10^{-10}$	[1]	[1]	186
HN1-1300		41	$3.2\cdot10^{-9}$	53	$1.8\cdot10^{-9}$	116	$1.8\cdot10^{-9}$	337	$1.8\cdot10^{-9}$	$2.6\cdot10^{3}$	$1.1\cdot10^{-9}$	165
HN3-800		$1.1\cdot10^{3}$	$1.1\cdot10^{-10}$	$3.4\cdot10^{3}$	$1.1\cdot10^{-10}$	$10.1\cdot10^{3}$	$1.1\cdot10^{-10}$	$22.3\cdot10^{3}$	$9.1\cdot10^{-11}$	$45.9\cdot10^{3}$	$6.7\cdot10^{-11}$	310
HN3-1300		320	$4.9\cdot10^{-10}$	681	$4.9\cdot10^{-10}$	$1.0\cdot10^{3}$	$4.9\cdot10^{-10}$	$1.1\cdot10^{3}$	$3.8\cdot10^{-10}$	$1.4\cdot10^{3}$	$3.8\cdot10^{-10}$	61

[1] Determination of the linear part of the Tafel plot and therefore calculation of D_{min} and R_{ct} not possibly from measurement because of high polarization.

[2] The specific capacity was determined from the 1st delithiation cycle of the rate test (1 nA) assuming a density of the particles of 2 g·cm^{-3}.

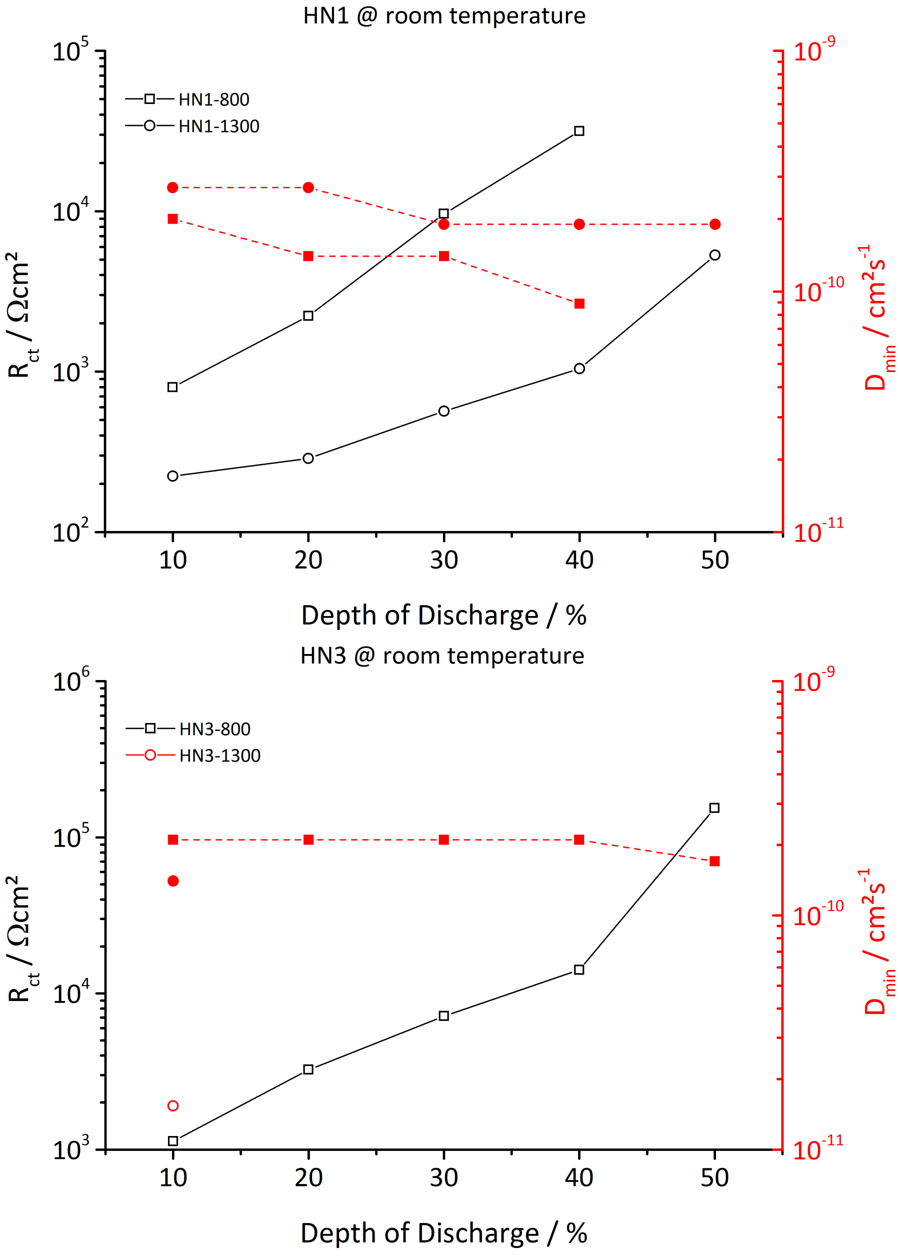

Figure 4.27: D_{min} and R_{ct} obtained from the Single Particle Measurements. Values are given in dependence of the Depth of Discharge for $HN1_b$ and $HN3_b$ pyrolyzed at 800 °C and 1300 °C at an electrolyte temperature of 25 °C.

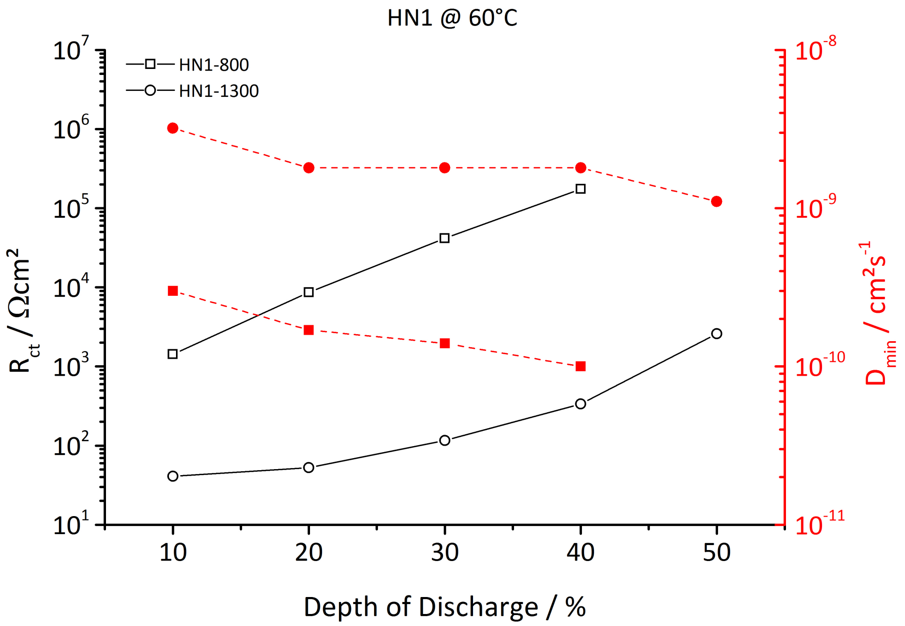

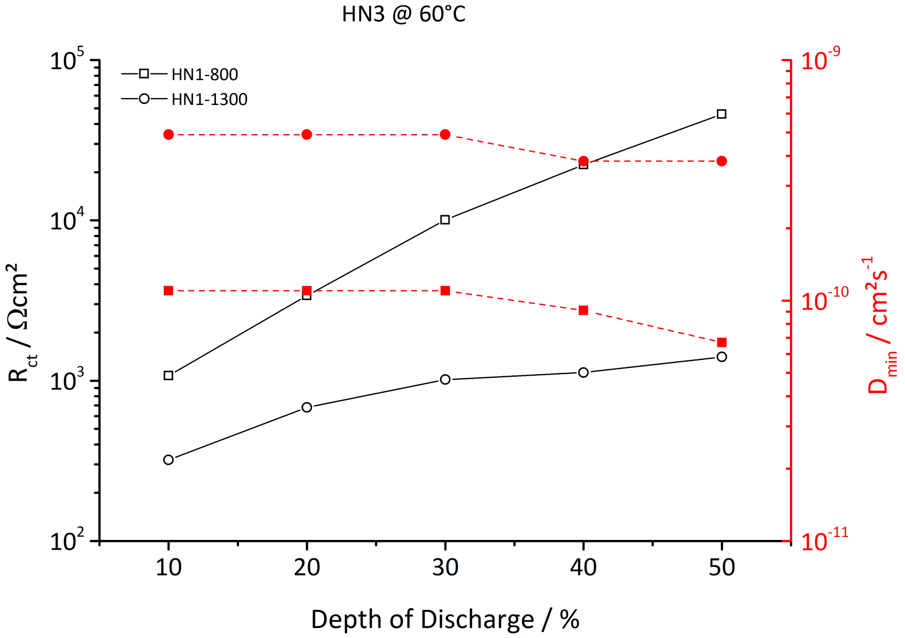

Figure 4.28: D$_{min}$ and R$_{ct}$ obtained from the Single Particle Measurements. Values are given in dependence of the Depth of Discharge for HN1$_b$ and HN3$_b$ pyrolyzed at 800 °C and 1300 °C at an electrolyte temperature of 60 °C.

surements shown above, amounting only 18.5 wt%[3] and 21.4 wt%[4], respectively. Haluschka et al. also found a dependence of the conductivity of polymer derived silicon carbonitrides from the pyrolysis temperature.[123] Within their work SiCN samples with a free carbon content of about 6 wt% were found to show specific conductivities in the order of 10^{-8} S·cm^{-1} at 1100 °C to 10^{-7} S·cm^{-1} at 1300 °C. Haluschka et al. assigned the beneficial influence of higher pyrolysis temperatures on the conductivity to an increase in the ratio of carbon atoms with a sp^2 hybridization to carbon atoms with a sp^3 hybridization.[123] Gao additionally accounted an increased order in the SiC phase for the higher conductivity.[121] The reported literature values show a tendency of improved conductivity with increasing free carbon content which is also in agreement with Reference [124].

The increase in conductivity with temperature could be an explanation for the lower R_{ct} for the materials pyrolyzed at 1300 °C in comparison to the materials pyrolyzed at 800 °C. The high carbon content of HN1$_b$ and HN3$_b$ derived ceramics could lead to the formation of a percolation network, and therefore an abrupt increase in the specific conductivity of several orders of magnitude. Studies on composite materials prepared of low-carbon SiCN and carbon nanotubes CNTs showed an increase in conductivity from 10^{-9} S·cm^{-1} to 10^{-2} S·cm^{-1} as 2 vol% of CNTs were added.[125] However, it is difficult to judge the influence of the conductivity on R_{ct} for the materials investigated without reliable values of specific conductivity measurements.

The determination of the particle size used for the calculation of D_{min} and R_{ct} in Table 4.9 can be considered as the major source for errors. It was possible to recover a particle and transfer it to a SEM (micro-electrode was replaced by tweezers actuated by the micromanipulator) to get an impression about the deviation of the assumed particle shape and size to the real shape and size. A comparison of the microscope picture with the picture recorded at the SEM is shown in Figure 4.29. Whereas the two dimensional picture of the microscope shows a round particle the SEM picture reveals a rather egg-shaped geometry of the particle. In consequence the determined diameter of the particle strongly depends on the perspective. An electrochemical impedance study on the single particles would allow for the evaluation of the precision of the obtained values from single particle measurements. However, the attempts to measure the impedance of the single particles after the rate test were futile.

---

[3] Based on the elemental composition after a pyrolysis at 1100 °C

[4] Calculated from the elemental composition measured after a pyrolysis at 1000 °C

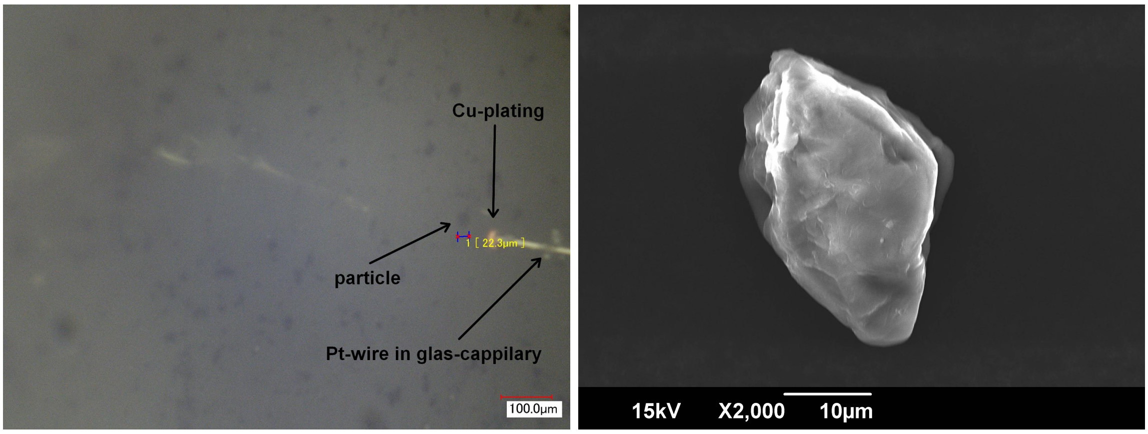

Figure 4.29: Left: Picture of particle taken with the microscope at a magnification of x300. **Right:** Picture of the same particle taken at a SEM at a magnification of x2000.

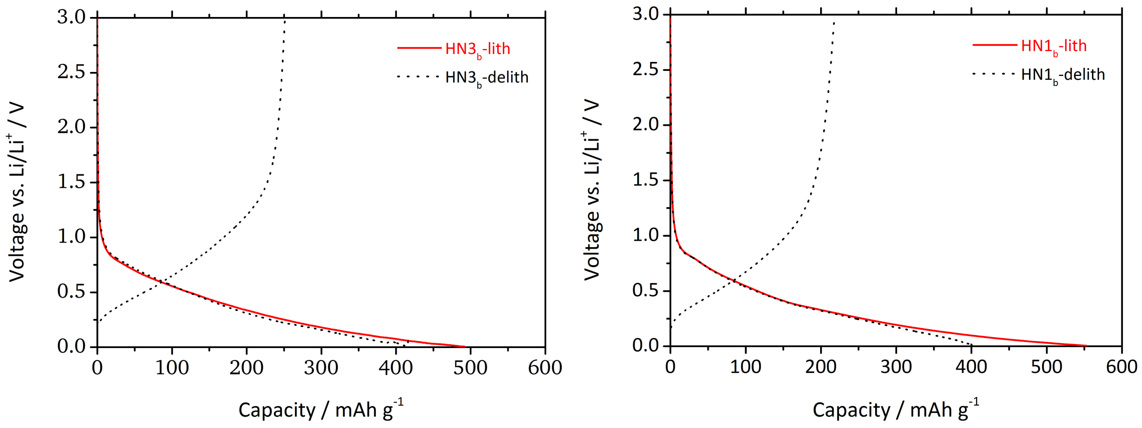

Figure 4.30: Lithiation curves of HN1$_b$-lith and HN3$_b$-lith and lithiation-delithiation curves of HN1$_b$-delith and HN3$_b$-delith.

4.3.8 Solid State ^{29}Si, ^{13}C and ^{7}Li NMR Measurements

Solid State ^{29}Si, ^{13}C and ^{7}Li NMR measurements were conducted to gain insight into the storing sides and dynamics of lithium ions in polymer-derived ceramics. The samples were prepared as described in Chapter 3.4.5. The charge-discharge curves of HN3$_b$-lith, HN3$_b$-delith, HN1$_b$-lith and HN1$_b$-delith are shown in Figure 4.30. The cycling behavior of the pellets differs significantly from the cycling behavior of the powder electrodes discussed in Chapter 4.3.5. Both samples do not exhibit a quasi plateau during delithiation at a potential of 0.15 V suggesting the absence of micropore activity. A comparison of the lithiation and delithiation capacities in Table 4.10 also shows that capacities of the pellets are well below the capacities achieved for the powder electrodes and the average lithiation and delithiation potentials are shifted to higher voltages. The reason for the differences in electrochemical behavior can be explained by the differences in electrode thickness. The low cycling rate of C/100$_C$ used for electrochemical experiments was insufficient to counter the influence of the electrode preparation. The comparison between the electrochemical measurements on the pellets and the powder electrodes also shows that the already small 1st cycle coloumbic efficiency is further reduced.

4.3.8.1 Room Temperature ^{29}Si, ^{13}C and ^{7}Li NMR Measurements

Figure 4.31 shows the ^{7}Li, ^{29}Si and ^{13}C NMR spectra recorded at 300 K and 116.64 MHz. The ^{7}Li NMR spectra are practically the same for the HN1$_b$ and HN3$_b$ derived ceramics. The

Table 4.10: Comparison of the 1^{st} cycle electrochemical parameters between the pellets $HN1_b$ and $HN3_b$ and the corresponding powder electrodes made of $HN1_b$ and $HN3_b$ pyrolyzed at 1100 °C.

Sample	C_{lith} $[mAh \cdot g^{-1}]$	C_{delith} $[mAh \cdot g^{-1}]$	Coulombic efficiency ζ [%]	average lithiation potential [V]	average delithiation potential [V]
$HN1_b$ delithiated	404	218	54	0.38	0.87
$HN1_b$ powder 1^{st} cycle	719	443	62	0.26	0.72
$HN3_b$ delithiated	416	251	60	0.36	0.87
$HN3_b$ powder 1^{st} cycle	674	430	64	0.29	0.66

spectra of the delithiated samples show a smaller shift in comparison to the lithiated samples. This finding suggest that the irreversible losses during the first cycle are attributed to sites with a more isotropic surrounding. The similarity in the ^{7}Li NMR spectra furthermore suggest that the differences in the starting precursor are not influencing the lithium dynamics and imply equal storing sites in both materials. All ^{7}Li NMR signals show a symmetric shape of the signals. ^{7}Li NMR Studies of Fukui et al. [50] on two different fully lithiated SiOC ceramics showed a asymmetrical signal for ceramics exhibiting a high contribution of micropore activity to the overall capacity whereas the sample revealing almost no micropore activity show a symmetrical shape of the signal. The absence of micropore activity in the electrochemical charge-discharge curves presented in Figure 4.30 are therefore in accordance with the measured ^{7}Li NMR spectra. It is likely that the use of printed powder electrodes for the NMR measurements would show the reported unsymmetrical shape of the ^{7}Li NMR spectra.

The effect of lithiation on the solid state ^{29}Si spectra differs for $HN1_b$ and $HN3_b$ derived ceramics. Both spectra in the pristine state are the same, yielding a symmetric shape of the signal. The lithiation of $HN1_b$ derived SiCN does not have an effect on this signal. However, for the sample derived from $HN3_b$ a slight broadening of the signal is visible in the lithiated state. This broadening is completely reversible during discharge. This finding suggests that the mixed bond amorphous network in the polysilazane derived ceramic contributes to the reversible storage of lithium ions, whereas the phase separation in polysilylcarbodiimide derived ceramics leads to electrochemically inactive regions of SiC and Si_3N_4. It should be mentioned that many other papers regarding ^{29}Si NMR measurements on SiCN ceramics

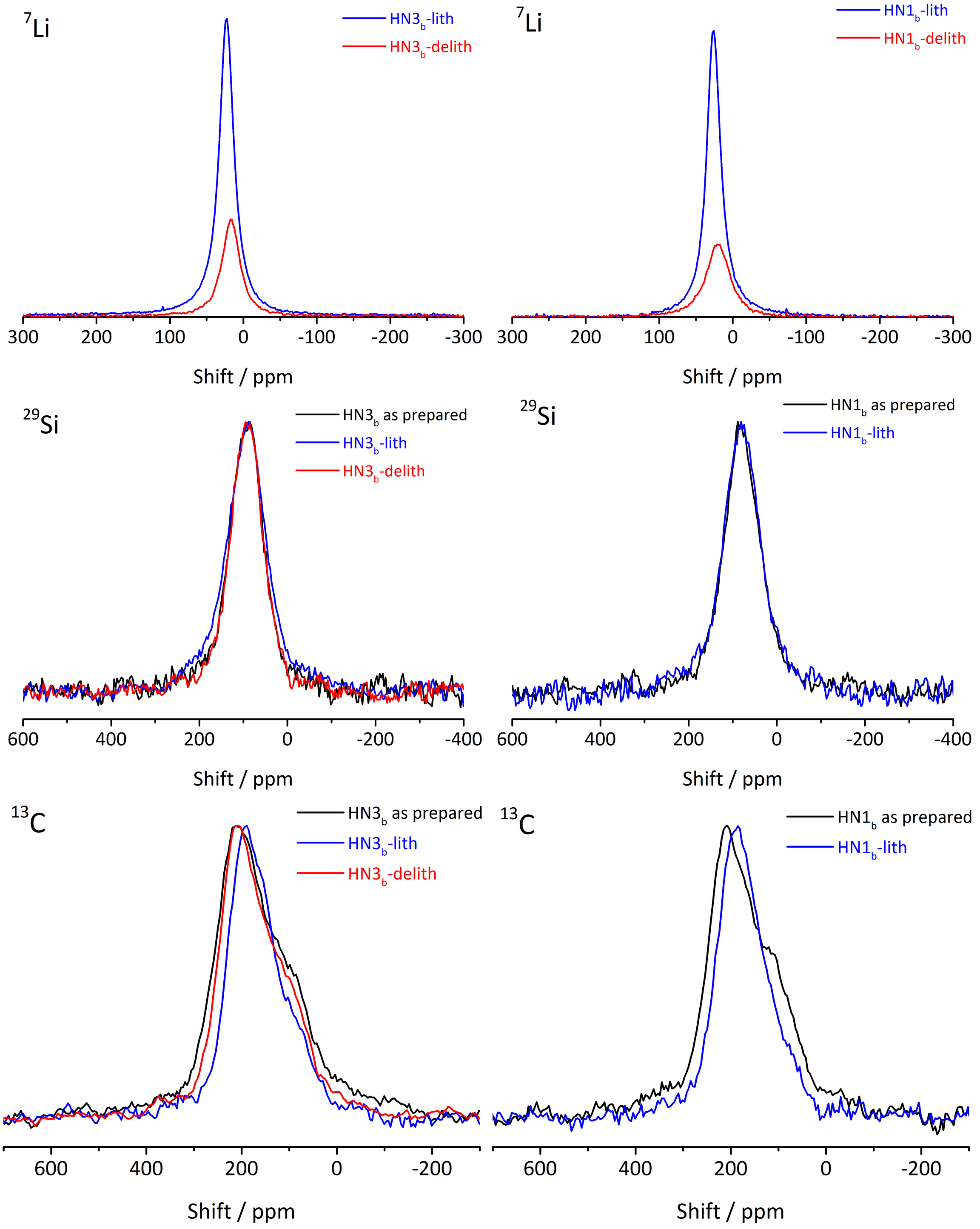

Figure 4.31: Solid State ^{29}Si, ^{13}C and ^{7}Li NMR spectra recorded at 300 K and 116.64 MHz.

distinguish between different Si surroundings. This is, however, not possible for the spectra presented in Figure 4.31 because of the performed wide-line investigation.

The ^{13}C NMR spectra for the as-prepared samples can clearly be resolved into two major carbon environments. The main peak is located at approximately 200 ppm and the shoulder is located at 90 ppm. The difference of 110 ppm in the two signals suggests to assign the main peak to sp^2 carbons of the free carbon phase and the shoulder to sp^3 carbons of the free carbon phase. It has been shown by Bill et al. [89] that polymer-derived ceramics exhibit sp^3 carbons after pyrolysis. Usually the amount of sp^2 increases with increasing pyrolysis temperature. Parts of the sp^3 carbon sites could also originate from the additives PVDF and Carbon Black Super P® used for the electrode preparation.

Lithiation of the samples influences the obtained ^{13}C NMR spectra by reducing their anisotropy. This change is mostly reversible by a delithiation of the stored lithium. The significant influence of lithium insertion into the ceramics on the ^{13}C NMR spectra suggests that the free carbon phase is the main storing site for lithium ions regardless of the starting precursor. The finding that the ceramic matrix is not (hardly) contributing to the high capacities of carbon-rich polymer-derived SiCN is unfounded as it has been shown that disordered carbons can exhibit capacities up to 2000 mAh·g^{-1}. [126]

4.3.8.2 Lithium Dynamics in SiCN

Figure 4.32 is showing the FWHM at 116.64 MHz and 31.1 MHz and the spin-spin relaxation rate (T_2^{-1}) at 116.64 MHz of the ^{7}Li NMR spectra in dependence of the temperature for the fully lithitated sample derived from HN3$_b$. At both frequencies the FWHM increases strongly with decreasing temperature up to a temperature of 190 K. Below 190 K a linear dependence of the FWHM occurs. T_2^{-1} is showing the same temperature dependence below 190 K which is typical for the slow motion regime where T_2^{-1} is proportional to the FWHM. The FWHM above 190 K is independent of the frequency applied, whereas the FWHM below 190 K is strongly reduced for lower frequencies. The onset temperature T_{onset} of the rigid lattice regime (RL regime) can therefore be determined as 190 K. Above the onset of the RL regime hopping diffusion takes place, leading to motional narrowing of the FWHM.

Usually the activation energy E_A of lithium motion can be determined from the motional narrowing limit where T_2^{-1} is not longer proportional to the FWHM but to the correlation time τ_c. However, the motional narrowing limit was not reached at the highest accessible

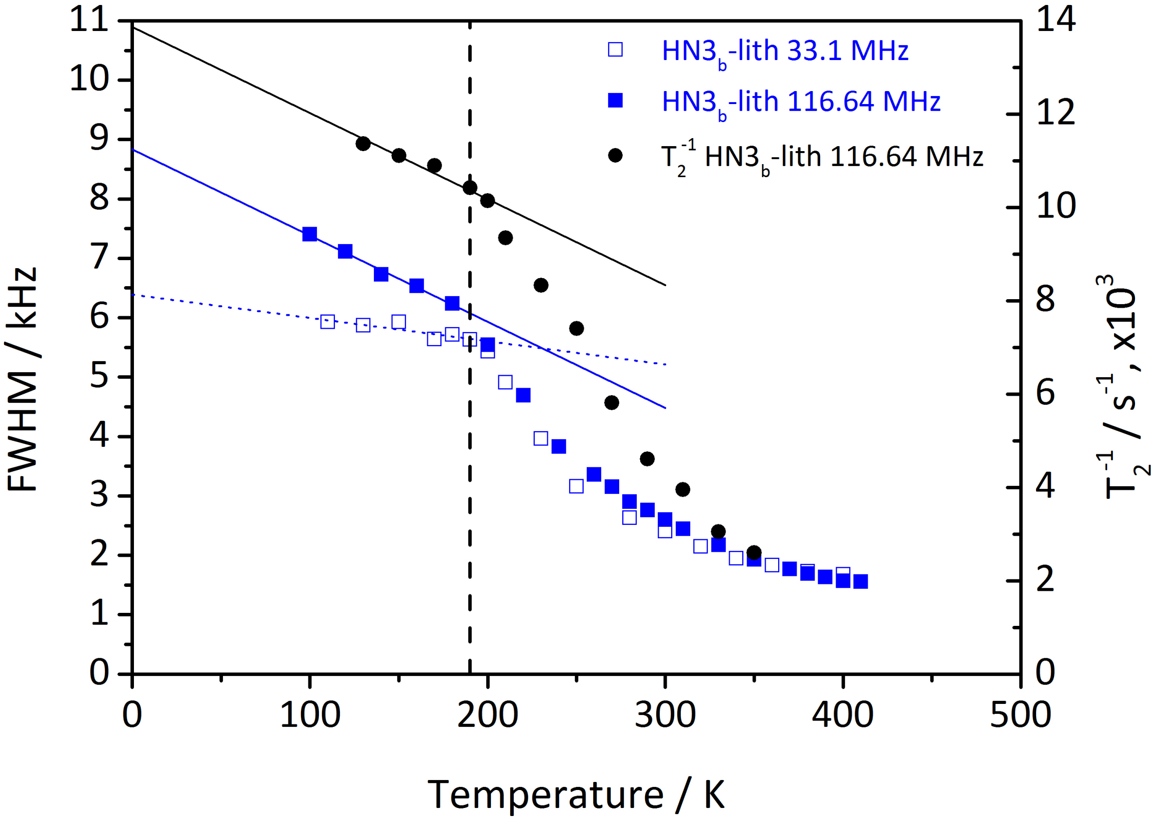

Figure 4.32: FWHM at 116.64 MHz and 31.1 MHz and the spin-spin relaxation rate T_2^{-1} at 116.64 MHz of the ^{7}Li spectra in dependence of the temperature for the fully lithiated sample derived from HN3$_b$.

temperature for the measurement setup, namely 420 K. Therefore E_A was estimated by an empirical formula (Formula 4.2 taken from the literature [127]).

$$E_A \approx 1.617 \cdot 10^{-3} \cdot T_{onset} \tag{4.2}$$

With respect to T_{onset}=190 K, E_A can be calculated to 0.31 eV. This values is comparable to E_A observed in the lithium silicon alloy $Li_{12}Si_7$ amounting 0.32 eV [128] but higher than the E_A obtained for the fullerene based compound Li_4C_{60} which was determined to 0.19 eV.[129] A study on the lithium motion in the stage-1 graphite intercalation compound LiC_6 by Langer et al. showed an onset of the rigid-lattice regime at 285 K and an activation energy of 0.53 eV.[130] The small activation energy of lithium motion in carbon-rich SiCN in comparison to graphite might be of advantage for low temperature applications.

The temperature dependence of the spin-lattice relaxation rate T_1^{-1} is displayed in Figure 4.33. In contrast to the prediction of the Bloembergen, Purcell and Pound model (BPP model) [131] no maximum in the temperature behavior of T_1^{-1} is reached. From this finding it can be concluded that the system is in the low temperature limit over the whole investigated temperature range. Another deviation of the BPP model is seen in the dependence of the Larmor frequency (ω_L) from T_1^{-1} which is $T_1^{-1} \propto {\omega_L}^{-3/2}$.[5] This dependency is a typical behavior for structural disorder and Coulomb interaction [132], being in accordance with the X-ray diffraction and Raman measurements presented in Chapter 4.3.2 and 4.3.3 revealing the amorphous and disordered structure of the ceramics and the free carbon phase, respectively. The dependency of T_1^{-1} on ${\omega_L}^{-3/2}$ suggests a continuum diffusion of the lithium ions rather than a jump diffusion which can be explained by the varying distances of the atoms in disordered materials.[127, 133] As a consequence of continuum diffusion it can be supposed that T_1^{-1} is also proportional to $\tau_c^{-1/2}$, with τ_c given in Formula 4.3 and k_b being the Boltzmann constant.

$$\tau_c = \tau_0 \cdot exp\left(\frac{E_A}{k_B T}\right) \tag{4.3}$$

Figure 4.34 is showing the Arrhenius plot of T_1^{-1} and T_2^{-1} at 116.64 MHz and $T_{1\rho}^{-1}$ at 50 kHz. The Arrhenius plot shows a background contribution to T_1^{-1} visible at low temperatures arising from a non-diffusion influence on the spin-lattice relaxation. Supposing a linear depen-

---

[5] according to the BPP model T_1^{-1} is proportional to ${\omega_L}^2$.

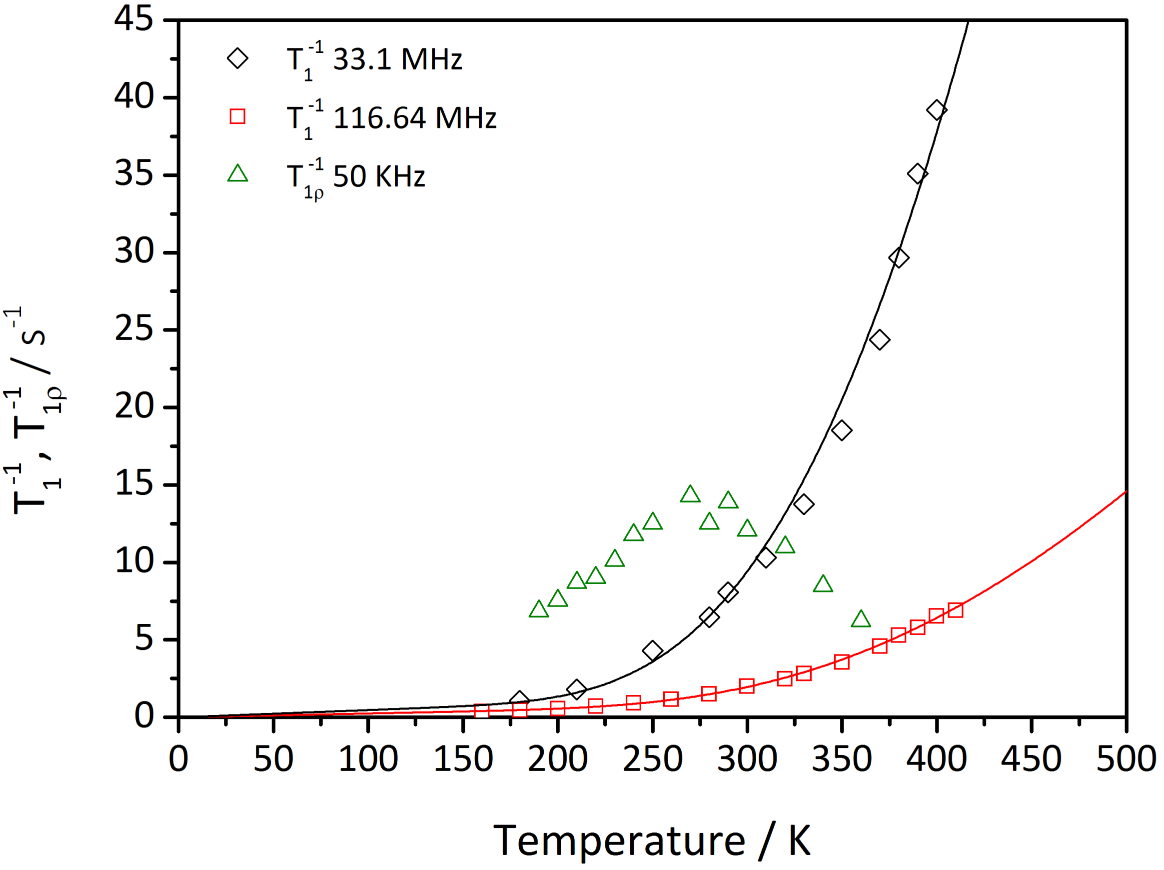

Figure 4.33: Spin-lattice relaxation rate of the ^{7}Li spectra in dependence of the temperature in the laboratory frame T_1^{-1} at 116.64 MHz and 33.1 MHz and in the rotating frame $T_{1\rho,l}^{-1}$ at 50 kHz measured for HN3$_b$-lith.

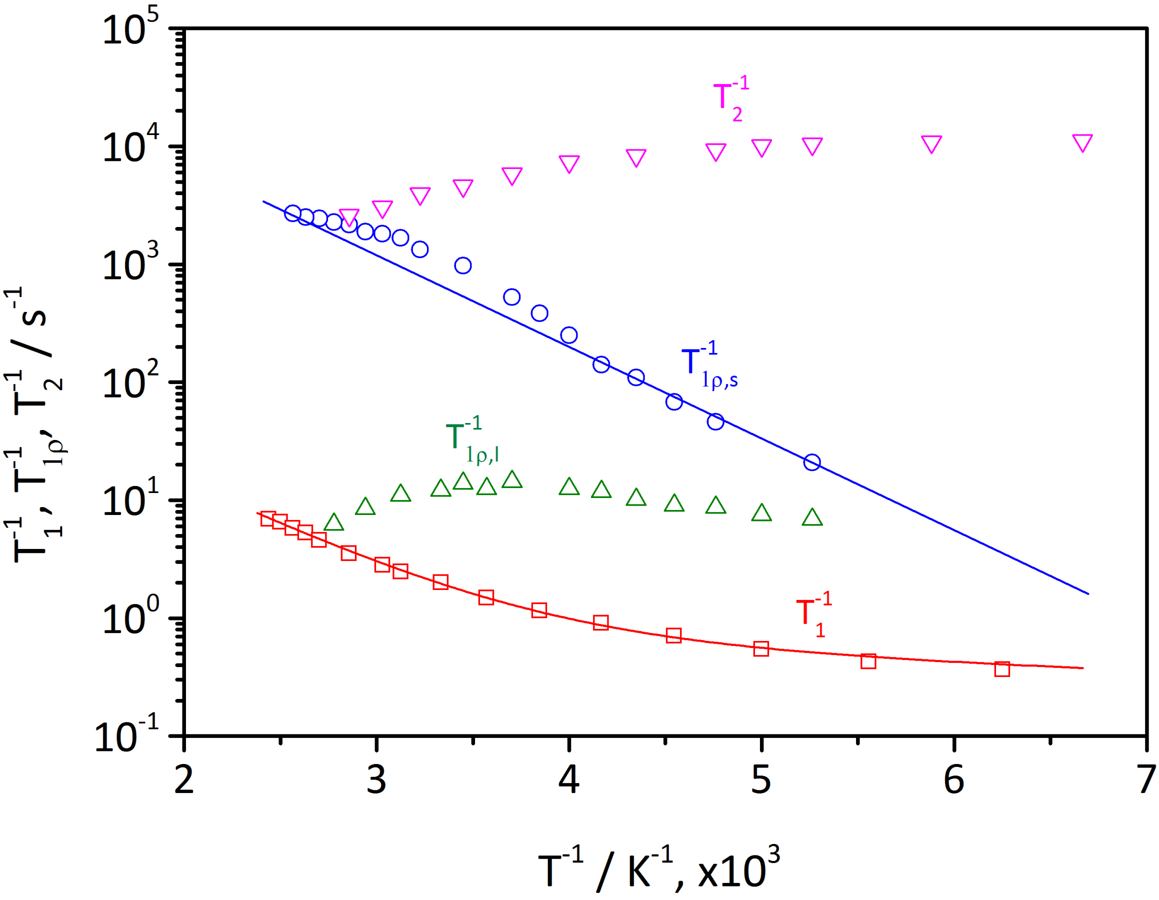

Figure 4.34: Arrhenius plot of ^{7}Li NMR investigation on HN3$_b$-lith of T_1^{-1} and T_2^{-1} at 166.64 MHz and $T_{1\rho,s}^{-1}$ and $T^{-1}{}_{1\rho,l}$ at 50 kHz.

dence of the background contribution, the temperature dependence of T_1^{-1} can be described by Equation 4.4 with a_0 and c_0 being constants.

$$T_1^{-1} = a_0 \frac{1}{\sqrt{\tau_C}} \omega_L^{-\frac{3}{2}} + c_0 \omega^{-\frac{1}{2}} T \tag{4.4}$$

It can be seen from the fittings in Figure 4.34 and 4.33 that Equation 4.4 describes the temperature dependence of on T_1^{-1} using the determined value of E_A of 0.31 eV and assuming τ_0 to be 1.3 ps.

HN1$_b$-lith was investigated at 116.64 MHz in analogy to HN3$_b$-lith. The onset of the RL-regime was also found at 190 K and a fitting of the results according to Formula 4.4 was successful using the parameters determined for HN3$_b$-lith. From this finding it can be concluded that the local diffusion processes are independent of the initial precursor used, i.e. the different microstructures of the ceramics.

For the HN3$_b$ based material also the rotating frame relaxation rate $T_{1\rho}^{-1}$ has been measured. As mentioned in Chapter 3.4.5 the determination of $T_{1\rho}^{-1}$ gives insights into the slow motions of the lithium ions. $T_{1\rho}^{-1}$ was determined in two different ways, namely at short times ($T_{1\rho,s}^{-1}$) when the $M_\rho(t)=M_\rho(0)/e$ and from the fit of the decay after long times ($T_{1\rho,l}^{-1}$), respectively. As shown in Figure 4.33 $T_{1\rho,l}^{-1}$ reveals a maximum close to a temperature of 260 K. At this temperature $2\omega_1\tau_c=1$ is fulfilled (ω_1 being the Larmor frequency in the RL regime) using E_A and τ_0 determined above. This supports the rightness of this characteristic values and supports the assumption of an activation law for lithium ion motion, once again.

In contrary, no maximum was found for $T_{1\rho,s}^{-1}$ as shown in Figure 4.34. At low temperatures the data points can be fitted with Formula 4.4 and an E_A of 0.31 eV but the fit does not match the data points measured at higher temperatures. Moreover, the obtained values $T_{1\rho,l}^{-1}$ are too small in comparison with the data of T_1^{-1}. These discrepancies suggest that the slow motion of the lithium ions is rather complex in comparison with the fast motion which is defined by an activation law.

4.4 Composites

Within this chapter the influence of a polymer-derived SiCN matrix on the cycling behavior of elemental silicon will be discussed. First, the effect of different precursors and compositions is addressed. Furthermore, the effect of carbon coating on the silicon particles embedded in the matrix will be presented. Finally, the effect of hollow spaces around the embedded silicon is shown.

4.4.1 Silicon Embedded into Carbon-Poor and Carbon-Rich SiCN Matrices

Figure 4.35 is showing X-ray diffraction pattern of the nano silicon powder as-received and the silicon-SiCN composites. All composites are showing reflexes arising from the crystalline silicon embedded in the ceramic. HTT:Si-1:1 and HTT:Si-4:1 are showing an additional broad reflex at approximately 16° which is absent for the carbon-rich composites. This signal can be assigned to a silicon carbide phase formed during the pyrolysis, which exhibits its reflex with the highest intensity at this angle[6]. A Rietveld refinement has been conducted on the diffraction pattern of the as-received silicon powder and the composite HTT:Si-1:1 to check if the crystallite size of the silicon powder was affected by the pyrolysis. For the pure powder the crystallite size was calculated to 52 nm and for the composite a crystallite size of 44 nm was determined (the figures of the Rietveld refinement are given in the Appendix B). The determined value for the silicon nano powder is therefore larger than the values provided by the supplier (30-50 nm). Based on the Rietveld refinement no crystal growth can be detected due the heat treatment, but a decrease in crystallite size occurs.

The Raman measurements of the nano silicon powder and HTT:Si-1:1 are shown in Figure 4.36. Both spectra are showing the typical bands of crystalline silicon at about 520 cm^{-1} arising from the optical first-order phonons (LTO) and between 900 cm^{-1} and 1100 cm^{-1} originating from the second-order transversal optical phonons.[134, 135] For HTT:Si-1:1 additionally the Raman bands of the free carbon phase are visible, which have been described in detail in Chapter 4.1.3. The transverse optic mode of silicon carbide at 796 cm^{-1} [109] is not seen in the spectra.

It can be concluded from the the broad signal at 16° in the X-ray diffraction spectra that a reaction between the free carbon phase and the silicon powder took place, resulting in

---

[6] e.g. powder diffraction files [29-1129], [65-360], [72-18], [73-1665] and [74-2307].

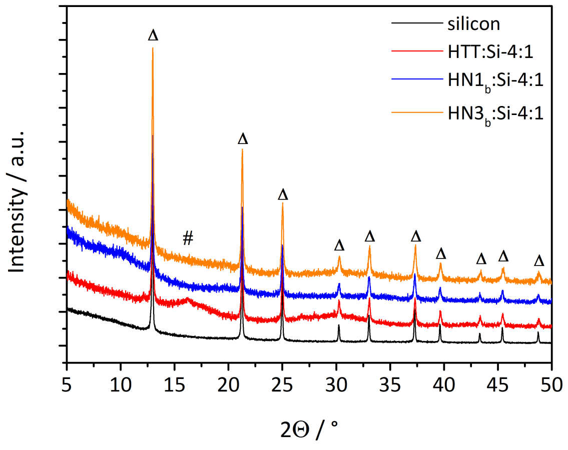

Figure 4.35: X-ray diffraction pattern of SiCN-Silicon composites and nano silicon powder in a 2Θ range of 5° to 50° measured with molybdenum K_α radiation. The silicon reflexes according to the powder diffraction files [27-1402] are marked with Δ and the (111)-reflex of SiC according to the powder diffraction file [29-1129] is marked by **#**. **Left:** Composition with 20 wt% silicon. **Right:** Compositions with 50 wt% silicon.

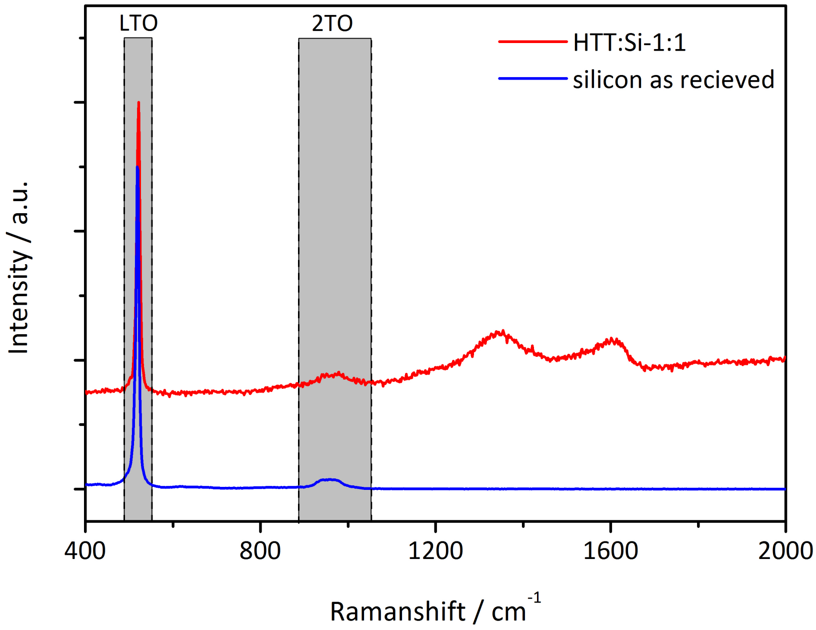

Figure 4.36: Raman spectra of nano silicon powder as-received and HTT:Si-1:1.

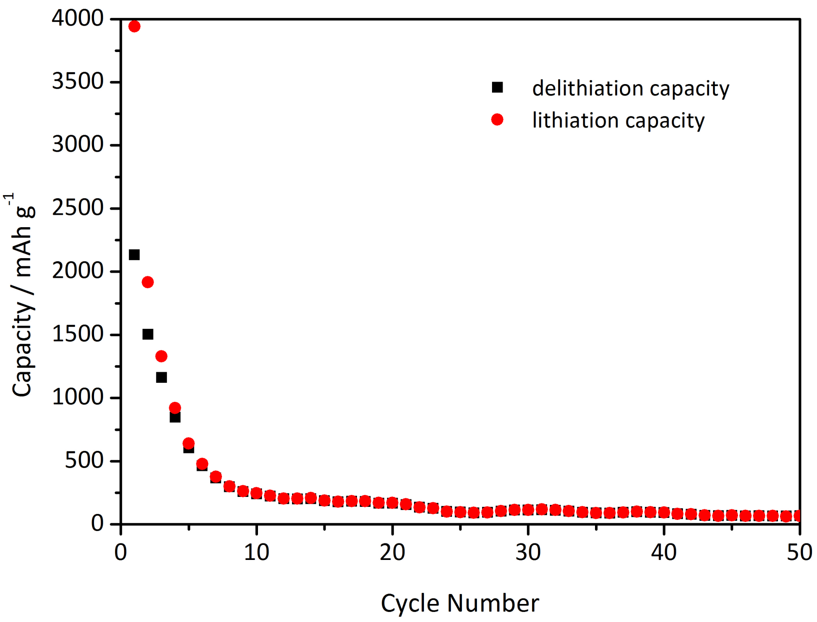

Figure 4.37: Alloying and dealloying capacities of a silicon reference electrode cycled at C/50_{Si}.

the formation of SiC. The decrease in silicon crystallite size calculated from the Rietveld refinement indicates that SiC is formed at the surface of silicon. However, this reaction is by far not strong enough to consume the majority of the electrochemically active species. Indeed, from the presented Raman spectra only the presence of the elements and no SiC is visible. For the composites based on carbon-rich precursor no SiC reflexes are visible at all.

Figure 4.37 is showing the alloying and dealloying capacities of an electrode prepared from the nano silicon powder. The cell already reaches its end of life during the second cycle if 80 % of the initial capacity is taken as a basis.

Figure 4.38 is showing the charge and discharge capacities for 100 cycles of the composite materials HTT:Si-4:1, HN1_b:Si-4:1 and HN3_b:Si 4:1 at a C-rate of C/50_{Si}. The addition of 20 wt% of the nano silicon powder to the ceramic derived from HTT1800 did not show an effect on the capacity in comparison to the pure ceramic (compare Chapter 4.1.4), the material can still be considered to be almost inactive for lithium storage. A first cycle lithiation capacity of about 700 mAh·g^{-1} would be reached if the full theoretical capacity of silicon (3579 mAh·g^{-1} for $Li_{15}Si_4$) in the matrix would be active. The silicon which has been shown to be present in the composite material by X-ray diffraction and Raman measurements is obviously electrochemically inactive due to ceramic matrix. The alloying is likely to be suppressed by the small electrical conductivity of the ceramic matrix. The electrical conductivity of HTT1800 pyrolyzed at 1100 °C was determined to amount to 10^{-9} S·cm^{-1}.[125] Even though the formation of SiC [123] and the presence of silicon (conductivity about 10^{-4} S·cm^{-1} [136]) can enhance the electrical conductivity, the influence is obviously too small to allow for a fast transport of the electrons or no pathway for electron transport exists.

The 1st cycle lithiation capacities of HN1$_b$:Si-4:1 is 596 mAh·g^{-1} and the 1st cycle lithiation capacity of HN3$_b$:Si-4:1 amounts to 674 mAh·g^{-1}. The 1st cycle delithiation capacities of HN1$_b$:Si-4:1 is 303 mAh·g^{-1} and the 1st cycle delithiation capacity of HN3$_b$:Si-4:1 amounts 277 mAh·g^{-1}. These values are lower than for pure HN1$_b$ and pure HN3$_b$ pyrolyzed at 1100 °C which were 719 mAh·g^{-1} and 354 mAh·g^{-1} for HN1-1100 and 674 mAh·g^{-1} and 312 mAh·g^{-1} for HN3-1100 at a C-rate of C/5$_C$ (please note that the currents of C/50$_{Si}$ and C/5$_C$ are of comparable magnitude, namely 71.6 mA·g^{-1} and 74.4 mA·g^{-1}, respectively). Several reasons could explain the decreased capacities: i) the stiff ceramic matrix does not allow for a high lithium uptake in the silicon particles due to a strong suppression of the volume increase related to the alloying process or ii) the formation of SiC, being inactive for lithium storage [137], reduces the first cycle delithiation capacity.

The cycling stability is improved for the composites in comparison to the pure silicon electrode. However, a continuous fading in capacity is observed with ongoing cycling. For HN1$_b$:Si-4:1 the end of life is reached after eleven cycles and HN3$_b$:Si-4:1 can be cycled 18 times before the delithiation capacity falls below 80 % of the 1st cycle delithiation capacity.

The 1st cycle and 2nd cycle lithiation and delithiation curves corresponding to Figure 4.38 are shown in Figure 4.39. No graph for HTT:Si-4:1 is given due to its electrochemical inactivity. The average lithiation potential are slightly shifted to lower potentials of 155 mV and 224 mV in comparison to the pure ceramics which exhibited average 1st cycle lithiation potentials of 260 mV and 290 mV, respectively. Whereas the pure materials exhibited a continuous decrease in potential with lithiation the composite materials exhibit an almost flat plateau close to zero volt at a DOC of about 80 %. The rise in the average lithiation potentials to 290 mV and 299 mV in the 2nd cycle can be assigned to the transformation of crystalline silicon to amorphous silicon [56, 57], though the pure ceramics also showed a rise in lithiation potential at a pyrolysis temperature of 1100 °C.

The lithiation and delithiation capacities for 50 cycles of the composite material with 50 wt% of silicon after pyrolysis are plotted in Figure 4.40. The lithiation and delithiation capacities

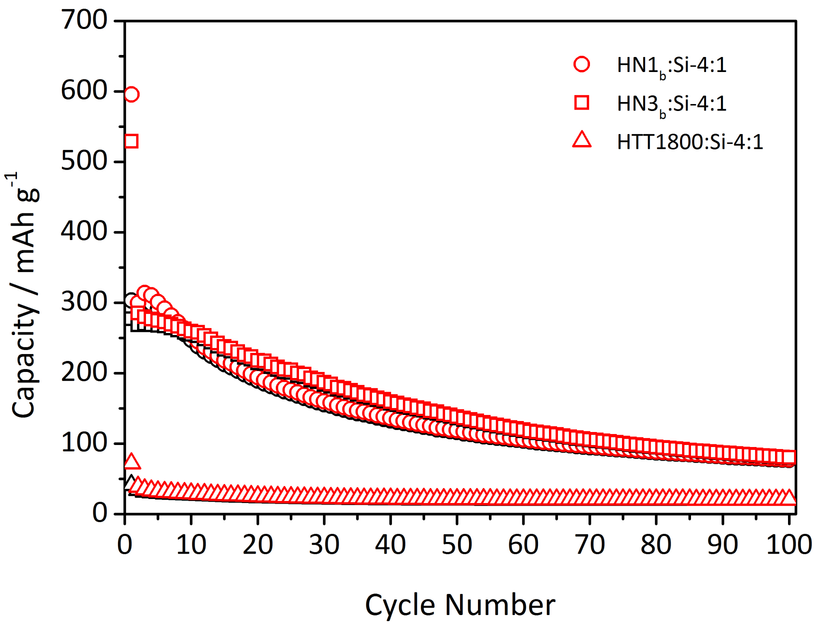

Figure 4.38: Lithiation (black) and delithiation (red) capacities of HTT:Si-4:1, HN1$_b$:Si-4:1 and HN3$_b$:Si 4:1 at C/50$_{Si}$

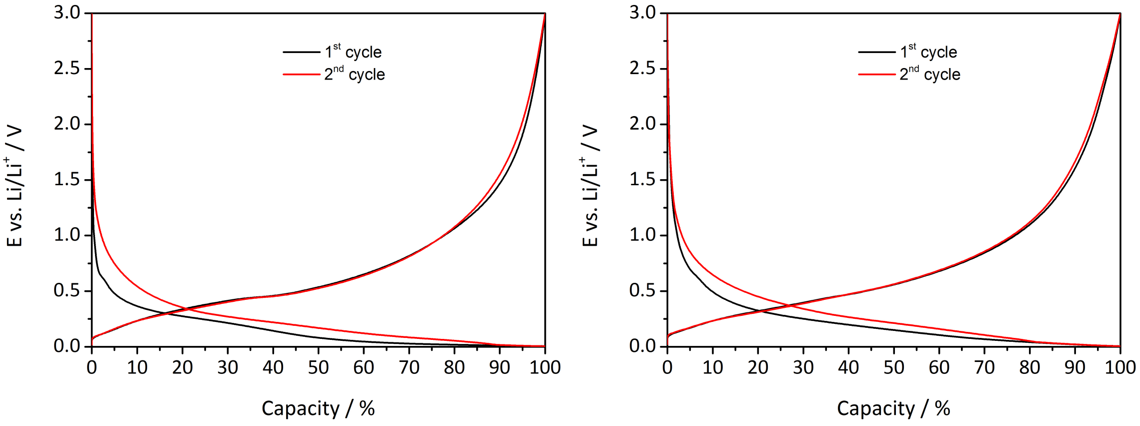

Figure 4.39: **Left:** 1st cycle and 2nd cycle lithiation and delithiation curves of HN1$_b$:Si-4:1 normalized to 100 %. **Right:** 1st cycle and 2nd cycle lithiation and delithiation curves of HN3$_b$:Si-4:1 normalized to 100 %

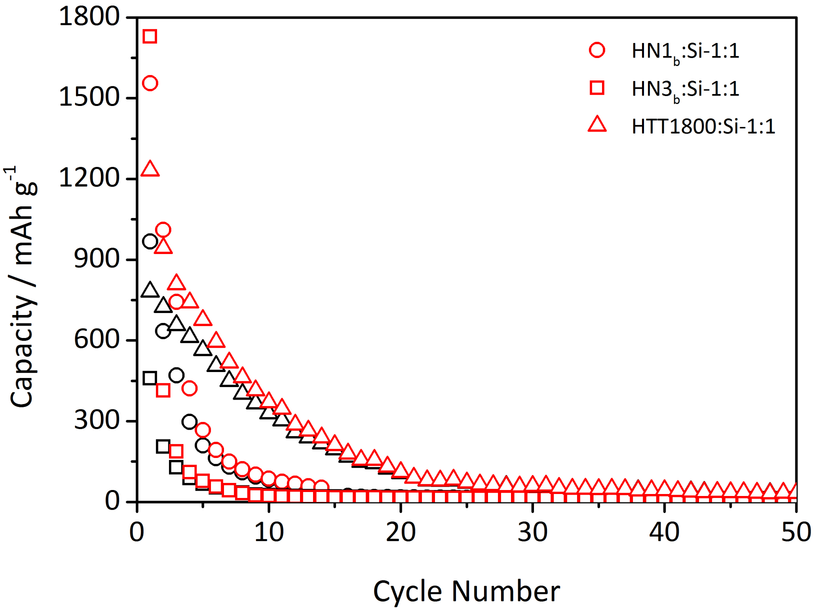

Figure 4.40: Lithiation (black) and delithiation (red) capacities of HTT:Si-1:1, HN1:Si-1:1 and HN3:Si 1:1 at C/50$_{Si}$

for all three composites exceed the capacities of the composites with a weight ratio of 4:1 as well as of the pure ceramics. This is however, on the cost of cycling stability. The end of cycle life for the carbon-rich composites is already reached in the 2nd cycle, for HTT:Si-1:1 the capacity fell below the limit within the 4th cycle.

The according 1st cycle and 2nd cycle lithiation and delithiation curves of Figure 4.40 are shown in Figure 4.41. The electrochemical activity of silicon for the composites with 50 wt% can be clearly seen in the electrochemical data obtained from the GCPL measurements, namely a shift to higher alloying potentials due to the amorphitization of the silicon nano particles.

4.4.2 Silicon Covered with Carbon and Embedded into SiCN Derived from HTT1800

To activate the alloying of silicon in HTT:Si-4:1 the conductivity of the composite was enhanced by a carbon coating of the silicon powder as described in Chapter 3.2. The alloying reaction of lithium and silicon was not achieved by coating the powder after pyrolysis. Only the capacity was slightly increased from 22 mAh·g^{-1} to about 73 mAh·g^{-1} as shown in Figure 4.42. The increase can be attributed to the lithium storage sites in the carbon coating

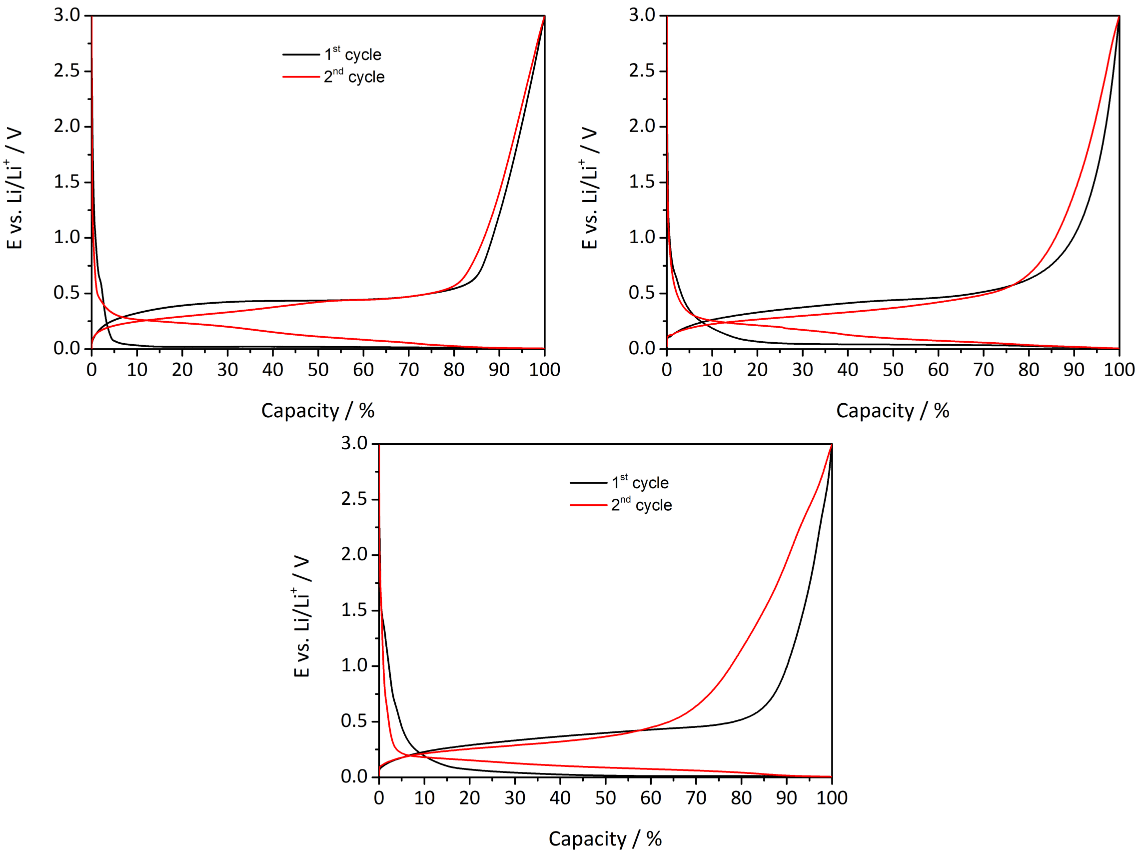

Figure 4.41: Top left: 1^{st} cycle and 2^{nd} cycle lithiation and delithiation curves of HTT:Si-1:1 normalized to 100 %.**Top right:**. 1^{st} cycle and 2^{nd} cycle lithiation and delithiation curves of HN1_b:Si-1:1 normalized to 100 %. **Bottom:** 1^{st} cycle and 2^{nd} cycle lithiation and delithiation curves of HN3_b:Si-1:1 normalized to 100 %.

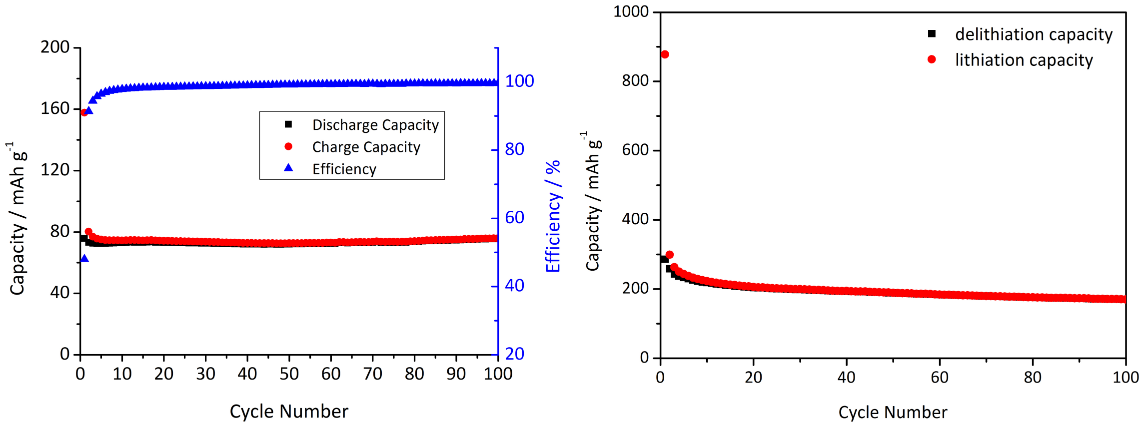

Figure 4.42: Left: Lithiation and delithiation capacities of HTT:Si-4:1 covered with an additional layer of carbon. **Right:** Lithiation and delithiation capacities of fructose carbonized at 600 °C.

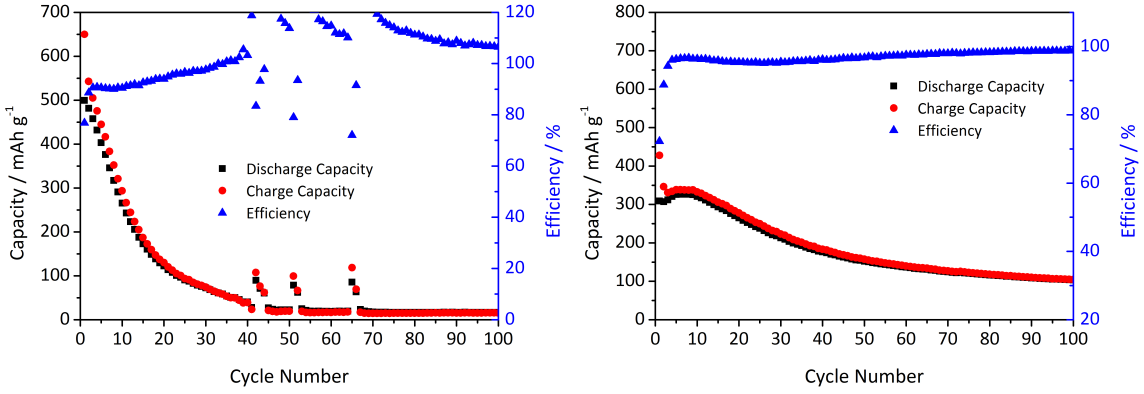

Figure 4.43: Left: Lithiation and delithiation capacities of Si:30F:SiCN. **Right:** Lithiation and delithiation capacities of Si:60F:SiCN.

itself. E.g. GCPL measurements on pure carbons derived from fructose at a carbonization temperature of 600 °C exhibited a 1^{st} delithiation capacity of 286 $\mathrm{mAh{\cdot}g^{-1}}$ (see Figure 4.42).

The lithiation and delithiation capacities of Si:30F:SiCN and Si:60F:SiCN are given in Figure 4.43. Both materials show a strong increase in the lithiation and delithiation capacity in comparison to HTT:Si-4:1. In return, the accessibility of silicon leads to a fading of the capacities. The fading is pronounced for Si:30F:SiCN reaching its end of life after 6 cycles. The high amount of carbon in Si:60F:SiCN has a beneficial effect on the cycling stability of the composite, reaching the end of life after 24 cycles.

4.4.3 Silicon-SiCN Composites with Cavities around the Silicon Particles

During the additional heat treatment of Si:30F:SiCN and Si:60F:SiCN on air carbon burning is expected. In particular the carbon coating on the silicon particles should react with the oxygen of the air forming gaseous carbon dioxide and carbon monoxide, leaving behind cavities around the silicon particles. It was shown in several publications that the creation of free space for the volume expansion of silicon during alloying leads to significant improvements in the cycling stability of silicon.[69, 70, 71, 72]. To monitor the reaction of the free carbon phase with the oxygen and therefore the outgasing and mass loss, a TGA in combination with FTIR spectroscopy was performed on Si:30F:SiCN. The recorded data are shown in the upper part of Figure 4.44. Besides the mass loss of the sample, the temperature program and the integrated FTIR-signals for carbon monoxide and carbon dioxide are displayed in dependence of the measurement time.

At low temperatures up to 210 °C the mass of Si:30F:SiCN decreases slightly, probably due to the desorption of CO_2 and water. The mass gain between 210 °C (110 min) and 430 °C (240 min) might arise from an oxidation of the silicon. The measurement revealed the onset of the highest mass loss at approximately 450 °C (250 min). The mass loss is accompanied by an increase in the intensity of FTIR signals arising from carbon monoxide and carbon dioxide, clearly indicating that the carbon originating from the fructose precursor is reacting with the oxygen. In total a mass loss of about 5.5 wt% is achieved, but the annealing time of 5 h is not long enough to completely burn the carbon. The existence of residual carbon is of advantage as a complete oxidation would again cause problems with the electrical conductivity as observed for the samples HTT:Si-4:1 in Chapter 4.4.1. To validate that the SiCN ceramic, including the free carbon phase, is unaffected by the heat treatment an additional TGA on a reference material consisting of SiCN derived from HTT1800 and pyrolyzed at 1100 °C was done. The TGA curve of the reference sample presented at the bottom of Figure 4.44 shows a continous decrease in the mass up to about 350 °C which is accompanied by an increase in the integrated intensity of the CO_2-band between 2290 to 2276 cm^{-1} and is also assigned to CO_2-desorption. No mass loss occurs between 315 °C (175 min) and 440 °C (245 min). Afterward mass loss and integrated intensity of the CO_2-band start rising again. In total the mass of the reference decreases by 0.5 wt% which justifies the assumption that the ceramic stays unaffected by the heat treatment.

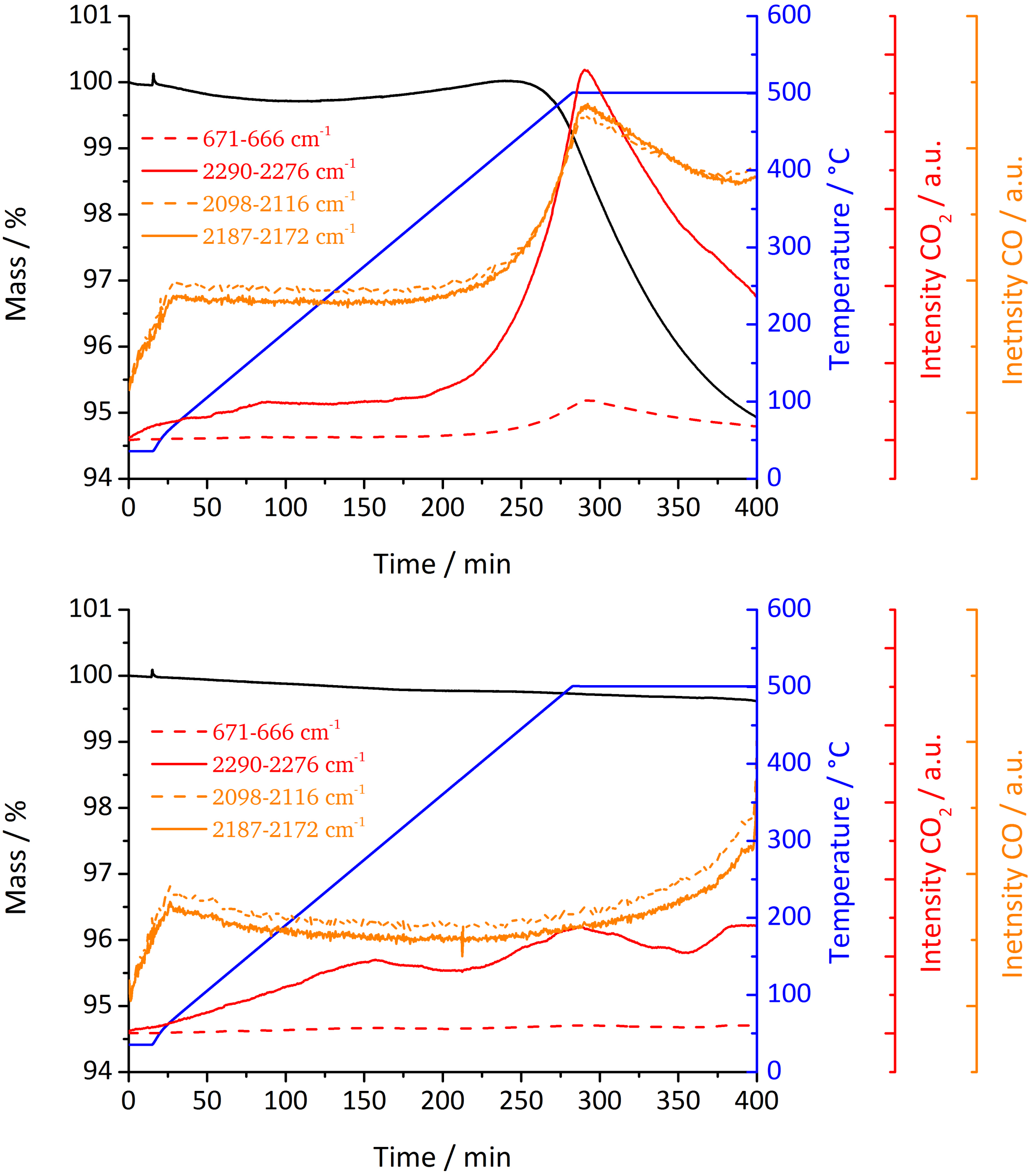

Figure 4.44: Top: TGA of Si:30F:SiCN. **Bottom:** TGA of pure SiCN derived from HTT1800 at a pyrolysis temperature of 1100 °C. The left y-axis displays the change in sample mass. The right hand y-axes show the temperature and the integrated intensity of the CO and CO_2 bands measured by FTIR spectroscopy.

Table 4.11: Conductivity obtained from 4-Point measurements of selected composite powders mixed with carbon black and PVDF and pressed to pellets.

Precursor	Conductivity [mS·cm^{-1}]
SiCN	50
Si-SiCN	44
Si-30F-SiCN	122
Si-60F-SiCN	250
Si-F-SiCN-(30)	98
Si-F-SiCN-(60)	159

The conductivity of the pellets prepared from Si:F:SiCN(30) decreased due to the heat treatment as shown in Table 4.11 but is still higher than that of the material prepared without a carbon covering. Please note that the values for the conductivity are not absolute values of the composites due to the addition of Carbon Black Super P® and PVDF and can only be compared relatively among each other. As no TEM measurements were available and the resolution of the SEM was not sufficient to give a visual prove of the creation of cavities, BET measurements were performed. The non-treated Si:60F:SiCN exhibited an active surface area of 12.22 m^2·g^{-1}. This value is comparable to the SSA of HN1-1100 (9.87 m^2·g^{-1}) or HN3-1100 (14.59 m^2·g^{-1}) presented in Chapter 4.3.4. The BET active surface increased significantly due to the annealing on air to 166.5 m^2·g^{-1}. The effect of the heat treatment on air can also be seen in the porosity of the sample. The untreated sample Si:60F:SiCN showed, in analogy to the pure ceramics investigated in Chapter 4.3.4, no porosity. The BET isotherms of the heat treated sample Si:F:SiCN revealed a porosity of the sample, but it was not possible to determine its size.

The lithiation and delithiation capacities of Si:F:SiCN(30) and Si:F:SiCN(60) are given in Figure 4.45. The first cycle lithiation capacities are of a similar magnitude (565 mAh·g^{-1} for Si:F:SiCN(30) and 530 mAh·g^{-1} for Si:F:SiCN(60)) as both samples contain the same amount of silicon and ceramic, whereas the carbon coating was removed to a large extend. No improvement of the stability was achieved in comparison with the untreated composites.

It can be seen from Figure 4.46 that after an additional coating step the cycling stability of Si:F:SiCN(30) and Si:F:SiCN(60) was significantly enhanced. The end of life was reached

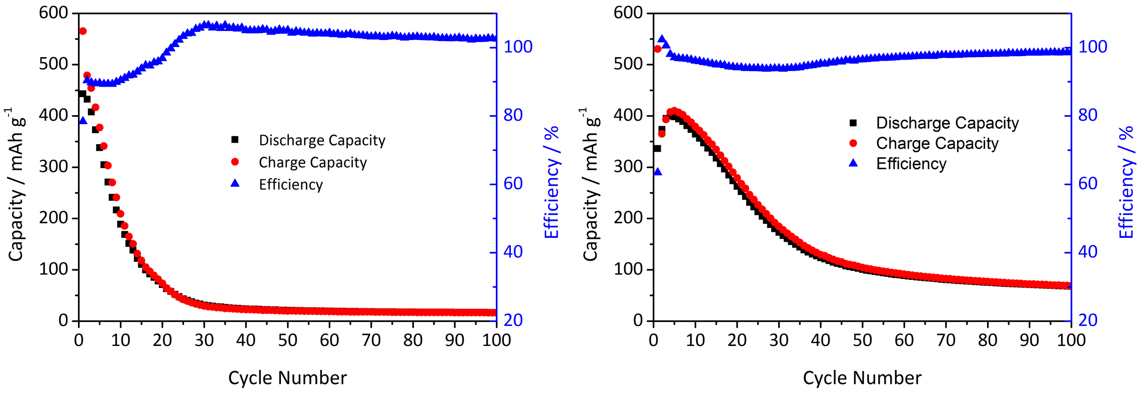

Figure 4.45: Left: Lithiation and delithiation capacities of Si:F:SiCN(30) at C/50$_{Si}$. **Right:** Lithiation and delithiation capacities of Si:F:SiCN(60) at C/50$_{Si}$.

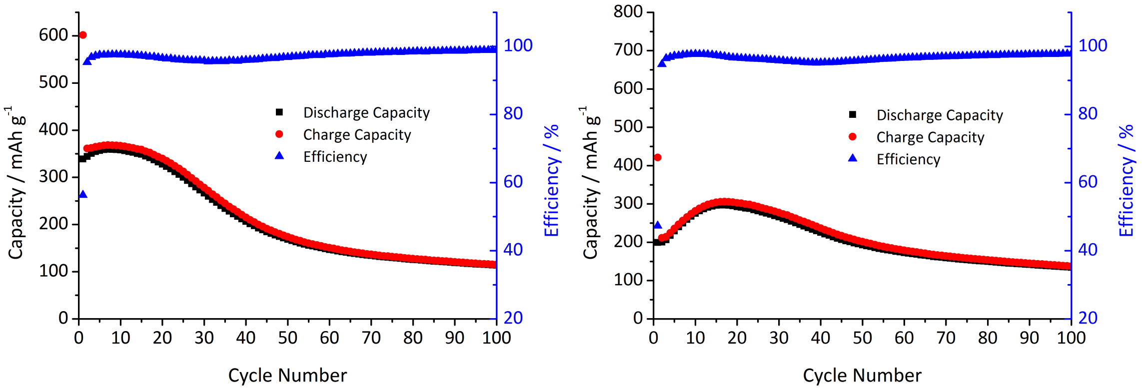

Figure 4.46: Left: Lithiation and delithiation capacities of Si:F:SiCN(30):30F at C/50$_{Si}$. **Right:** Lithiation and delithiation capacities of Si:F:SiCN(60):30F at C/50$_{Si}$.

after 30 cycles and 70 cycles, respectively. However, the consideration that 80 % of the initial delithiation capacity defines the end of cycle life may be misleading for Si:F:SiCN(60). The initial delithiation capacity is quite low, amounting only 199 mAh·g^{-1}, and increases continuously till the 17th cycle where it reaches a maximum with 297 mAh·g^{-1}.

In order to find out whether the heat treatment or the outer coating is responsible for the increased cycling stability, an additional GCPL measurement was performed on Si:30F:SiCN:30F, i.e. the carbon on the silicon particles was not removed. It can be seen from Figure 4.47 that the cycling stability is comparable to that composite material with a heat treatment on air. The end of life of Si:30F:SiCN:30F was reached after 29 cycles. The 1st cycle delithiation capacity is, however, 77 mAh·g^{-1} higher than for Si:F:SiCN(30):30F.

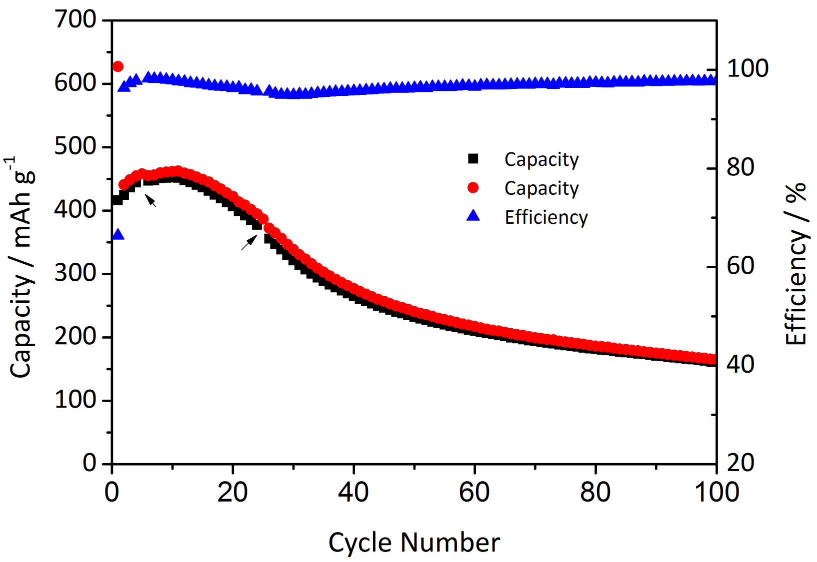

Figure 4.47: Lithiation and delithiation capacities of Si:30F:SiCN:30F at C/50$_{Si}$. The arrows are marking an interruption of the measurement due to a power black out.

In summary, several aspects for the application of composite materials of SiCN and a nano silicon powder have to be taken into consideration. First, the set up of the composite must allow for an alloying of the silicon particles. It was shown that this can be achieved by a coating of the silicon particles. The introduction of high porosity by burning the carbon coating on the silicon particles did not show a beneficial effect on the cycling stability and the so obtained composite materials suffered from low specific capacities. However, an additional outer coating with carbon enhanced the cycling stability up to 70 cycles.

5 Summary and Outlook

In the first part of the thesis several ceramics derived from polysilazanes and polysilylcarboddimides were studied with respect to their potential use as anode material in lithium-ion batteries. It was shown that 1^{st} cycle specific delithiation capacities as high as 725 mAh·g^{-1} were obtained for carbon-rich ceramics whereas samples containing low amounts of free carbon were (almost) inactive for lithium storage. Even after prolonged cycling, capacities of up to 624 mAh·g^{-1} were achieved from polysilazane HN3_a. Figure 5.1 presents the total battery capacity in dependence of the anode capacity already shown in Chapter 2.2.[14] In addition a data point at an anode capacity of 624 mAh·g^{-1} is added. The use of HN3_a derived SiCN would increase the total capacity of a cell by 3.7 mAh·g^{-1} or 6.5 % in comparison to the same cell working with a graphite anode. This value is already half of the desired improvement of 11.7 % reached by an anode with a specific capacity of 1200 mAh·g^{-1}. Moreover, the measurements showed that carbon-rich SiCN materials can exhibit good rate capabilities with 430 mAh·g^{-1} at a cycling rate of C/1_C, being important for practical applications. It is likely that the electrochemical performance, in particular the rate capability of the materials, can be further increased by an improved electrode engineering.

The ^{29}Si, ^{13}C and ^{7}Li solid-state NMR measurements revealed that lithium is stored in the free carbon phase. For polysilazane derived SiCN a minor fraction of lithium was also found in the mixed bond network. An attempt to visualize the findings of the solid-state NMR measurements is shown in Figure 5.2. However, the electrochemical measurements on the probed samples revealed a discrepancy between the printed powder electrodes and pressed pellets investigated by solid state NMR measurements, namely the absence of micropore activity, lower capacities and higher lithiation and delithiation potentials. Voltage vs. capacity curves of various printed powder ceramics showed that micropores are likely to contribute to the reversible storing of lithium, as it was found by Fukui et al. [50] for SiOC. The determination of the lithium dynamics showed that the continuum diffusion of lithium can be described by an activation law with E_A=0.31 eV regardless of the precursor used.

A detailed study on the influence of pyrolysis temperatures between 800 °C and 1300 °C on poly(phenylvinylsilylcarbodiimide) and poly(phenylvinylsilazane) was presented. The results of the investigation are summarized in the following:

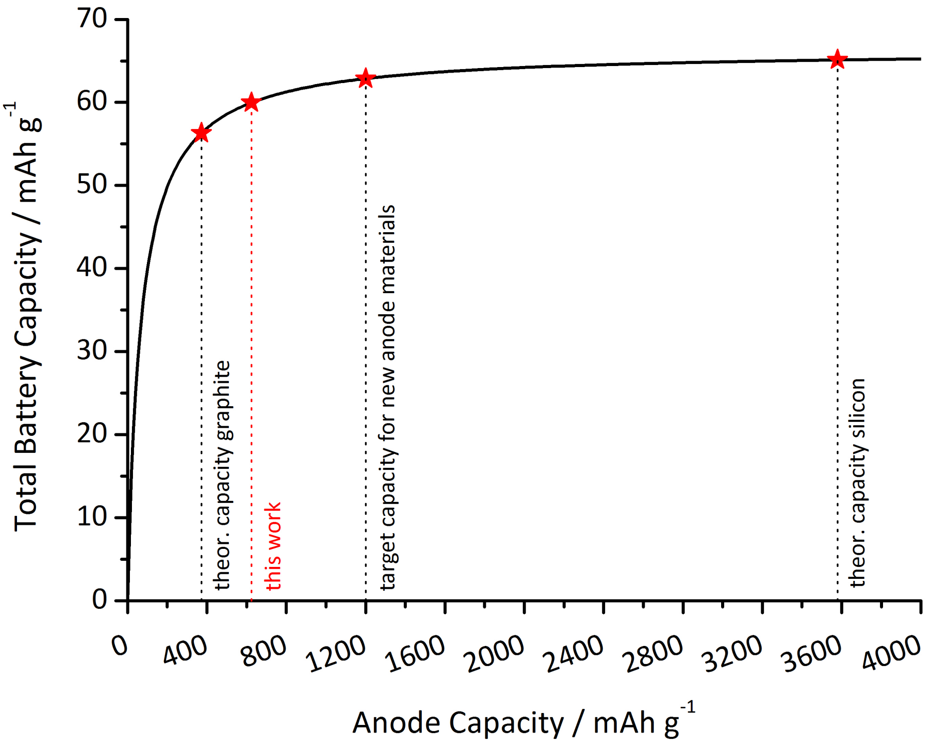

Figure 5.1: Total cell capacity in dependence of the specific anode capacity calculated according to Equation 2.18 assuming $C_{Cathode}$ to be 135 mAh·g^{-1} and Q_{others} to be 130.4 mAh·g^{-1}. The example is based on a Sony 18650G8 cell and is taken from Kasavajjula et al. [14]. The vertical lines correspond to the theoretical capacity of graphite, silicon (at room temperature) and 1200 mAh·g^{-1} representing a target capacity for new anode materials. Additionally the value of SiCN derived from HN3$_a$ at a rate of C/20$_C$ after 134 cycles was added to visualize the possible improvement in total cell capacity.

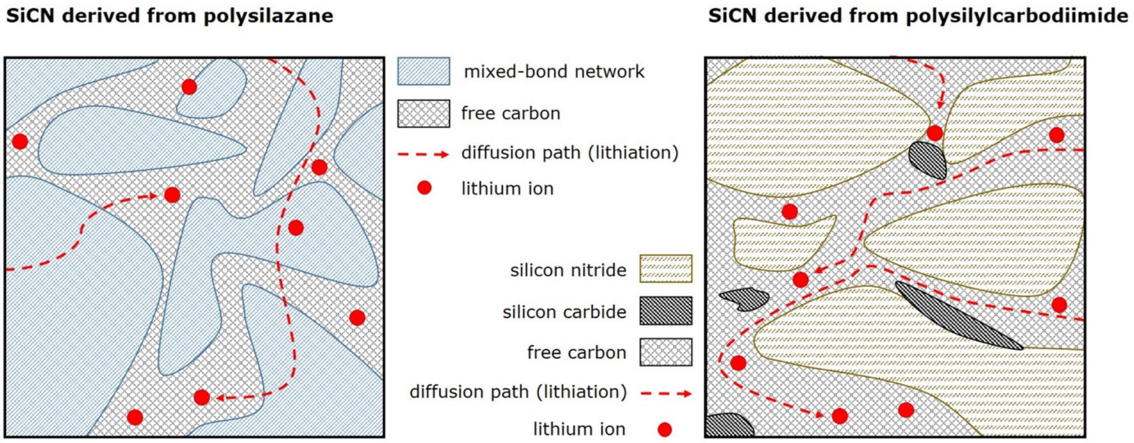

Figure 5.2: Schematic drawing of storing sites and diffusion paths in SiCN derived from polysilazane and polysilylcarbodiimide based on the findings of the solid state NMR measurements.

i) decrease of the hysteresis

The hysteresis decreased with an increase in pyrolysis temperature. This effect is, in analogy to pure disordered carbons, correlated to the hydrogen content in the ceramics and the associated change in carbon hybridization from sp^2 to sp^3.

ii) decrease in the specific capacity

The specific capacity of the ceramics decreased with increasing pyrolysis temperature due to the higher ordering of the free carbon phase hence a decreasing amount of possible storing sites for lithium ions. The finding of higher order with an increase of the pyrolysis temperature was confirmed by Raman spectroscopy measurements.

iii) improved stability

An increase of the pyrolysis temperature leads to an increased stability. This includes, inter alia, a stable elemental composition if the ceramics are exposed to air. The decrease in delithiation potential during the first few cycles for ceramics pyrolyzed at lower temperatures is correlated to the increase of oxygen during the exposure to air. The ongoing reactions could be prevented by a complete fabrication of the electrodes under inert gas atmosphere or by using a dry room environment to avoid the air moisture. Moreover, the strong film formation, probably due to electrolyte decomposition, seen on the electrode surfaces of SiCN pyrolyzed at 800 °C is suppressed at 1300 °C. The reason for the strong film formation at a lower pyrolysis temperature remained unclear. It is likely that the film formation also influences the lithiation and delithiation potentials which are shifted to higher potentials during ongoing cycling. However, it has been shown on different electrode materials that an appropriate choice of electrolyte or the addition of additives to the electrolyte can significantly enhance the performance of the SEI and prevent an ongoing decomposition of the electrolyte.

iv) improved rate capability

The rate capability of the ceramics increased with increasing pyrolysis temperature. Single Particle Measurements have shown that the minimum diffusion coefficient increased and the charge transfer resistance decreased after annealing of SiCN at a pyrolysis temperature of 1300 °C.

The choice of pyrolysis temperature is therefore always a tradeoff between its influence on the hysteresis, rate capability and stability on one hand and the specific capacity on the other hand. Starting from a pyrolysis temperature of 1000 °C the electrochemical behavior of the free carbon phase might be best described by mixed characteristics of soft carbons and hard carbons. The voltage vs. capacity curves show the micropore activity during the delithiation which is known from hard carbons. In contrary, the lithiation potential is high enough to reduce the risk of lithium plating.

The synthesis of stable composites of SiCN with nanosilicon showed no benefits in comparison to other approaches for the stabilization of silicon so far. A possible solution could be the in-situ formation of free silicon (shift into the ternary phase composition diagram in the field of silicon, silicon nitride and silicon carbide) during the ceramization process by the synthesis of an appropriate silicon-rich precursor. The in-situ formation of free silicon could lead to very small silicon clusters in the range of a few nanometers and would also ensure a homogeneous distribution. A possible drawback of this ceramic for its application in lithium-ion batteries could be its low conductivity. However, the commercialization of $LiFePO_4$ showed that there are solutions to use materials with a poor electronic conductivity. A possible solution for SiCN could be the incorporation of small amounts of CNTs into SiCN ceramics.[125] In order to gain exact information on the storing sites and dynamics of lithium in printed powder electrodes it is of great importance to improve the procedure of sample preparation. A possible solution would be the use of pouch cells for electrochemical testing. The utilization of pouch cells would provide a sufficient amount of material for the NMR investigation and the fabrication procedure of the electrodes would be equal to the procedure for the printed powder electrodes. The active material could be either scratched off the copper current collector after the electrochemical testing or be removed by dissolving the PVDF with NMP. Moreover, the use of pouch cells could allow for in-situ NMR measurements. In-situ NMR measurements would have the benefit to avoid influences of the material preparation, like washing the electrodes in DMC, prior to the NMR measurements. It would also allow to perform all measurements at the same sample, avoiding uncertainties due to possible differences among the investigated samples. It also facilitates the measurement of the lithium dynamics at different lithiation states, the reduction of the sample amount needed and a shorter preparation time.

The elimination of the high irreversible losses during the 1^{st} cycle is a major challenge for the commercialization of PDCs in lithium-ion batteries. The question of the 1^{st} cycle irreversible capacity and the resulting low coulombic efficiency remains unclear. The ^{29}Si and ^{13}C NMR spectra of the pristine material and the delithiated sample were the same, implying that the lithium is not irreversibly stored in their surrounding. The role of nitrogen was not investigated so far.

Bibliography

[1] *National Development Plan for Electric Mobility*, Federal Governemt of Germany, Federal Ministry for the Environment, Nature Conservation and Nuclear Safety, 2009

[2] *The European Strategic Energy Technolgy Plan - Towards a low-carbon future*, European Comission, 2007

[3] J. O. Besenhard and H. P. Fritz, *Cathodic reduction of graphite in organic solutions of alkali and* NR_4 *salts*, Journal of Electroanalytical Chemistry and Interfacial Electrochemistry, 53(1974), 329–333

[4] J. O. Besenhard, *The electrochemical preparation and properties of ionic alkali metal- and* NR_4*-graphite intercalation compounds in organic electrolytes*, Carbon, 14(1976), 111–115

[5] http://www.sony.net/SonyInfo/News/Press/200502/05 006E/, 15th of February 2005

[6] R. Donnerbauer, *Batterien sind zentrale Bausteine der Energiezukunft*, Ingenieur.de, 2012

[7] www.handelsblatt.com/unternehmen/industrie/steigende-nachfrage-tesla-faehrt-die-elektroauto-produktion hoch/8610346.html, 2013

[8] B. Scrosati and J. Garche, *Lithium batteries: Status, prospects and future*, Journal of Power Sources, 195(2010), 2419–2430

[9] C. H. Hamann, A. Hamnett and W. Vielstich, *Electrochemistry*, second edition, Wiley-VCH Verlag GmbH & Co. KGaA, 2007

[10] J.-K. Park, *Principles and Applications of Lithium Secondary Batteries*, first edition, Wiley-VCH Verlag GmbH & Co. KGaA, 2012

[11] P. G. Bruce (editor), *Solid State Electrochemistry*, Cambridge University Press, 1995

[12] M. N. Obrovac and L. J. Krause, *Reversible Cycling of Crystalline Silicon Powder*, Journal of the Electrochemical Society, 154(2007), A103–A108

[13] J. Wang and X. Sun, *Understanding and recent development of carbon coating on* $LiFePO_4$ *cathode materials for lithium-ion batteries*, Energy and Environmental Science, 5(2012), 5163–5185

[14] U. Kasavajjula, C. Wang and A. J. Appleby, *Nano- and bulk-silicon-based insertion anodes for lithium-ion secondary cells*, Journal of Power Sources, 163(2007), 1003–1039

[15] J. B. Goodenough and Y. Kim, *Challenges for Rechargeable Li Batteries*, Chemistry of Materials, 22(2010), 587–603

[16] P. Colombo, R. Riedel, G. D. Soraru and H.-J. Kleebe (editors), *Polymer Derived Ceramics: From Nano-Structure to Applications*, first edition, DEStech Publications, Inc, 2010

[17] R. Müller, VEB Silikonchemie, Patent DD-5448, 1942

[18] E. G. Rochow, General Electric, U.S. Patent Number 2380995, 1941

[19] R. D. Miller and J. Michl, *Polysilane high polymers*, Chemical Reviews, 89(1989), 1359–1410

[20] K. Shiina and M. Kumada, *Thermal Rearrangement of Hexamethyldisilane to Trimethyl (dimethylsilylmethyl)silane*, The Journal of Organic Chemistry, 23(1958), 139–139

[21] A. Greiner, *Keramiken aus Silylcarbodiimiden*, Ph.D. thesis, Technische Hochschule Darmstadt, 1997

[22] A. S. Gordetsov, V. P. Kozyukov, I. A. Vostokov, S. V. Sheludyakova, Y. I. Dergunov and V. F. Mironov, *Preparation and Properties of Carbodi-imides and Cyanamides Containing Silicon, Germanium, Tin, and Lead*, Russian Chemical Reviews, 51(1982), 485

[23] I. A. Vostokov, Y. I. Dergunov and A. S. Gordetsov, *Reactions of Si-organic, Ge-organic and Sn-organic Compounds With Dicyandiamide - New Method For Preparation of Organoelemental Carbodiamides*, Zhurnal Obshchei Khimii, 47(1977), 1769–1771

[24] A. Obermeyer, A. Kienzle, J. Weidlein, R. Riedel and A. Simon, *Die Kristall- und Molekulstrukturen von* (Me_2SiNCN)*, (1) und* $Me_3SiNCNSiMe_3$ *(2)*, Zeitschrift für anorganische und allgemeine Chemie, 620(1994), 1357–1363

[25] A. Kienzle, F. Aldinger, A. Obermeyer, A. Simon and R. Riedel, *Synthese und Struktur des ersten oligomeren cyclischen Dimethylsilyl-substituierten Carbodiimids*, Chemische Berichte, 126(1993), 2569–2571

[26] E. Kroke, Y.-L. Li, C. Konetschny, E. Lecomte, C. Fasel and R. Riedel, *Silazane derived ceramics and related materials*, Materials Science and Engineering: R: Reports, 26(2000), 97–199

[27] S. Yajima, Y. Hasegawa, J. Hayashi and M. Iimura, *Synthesis of continuous silicon carbide fibre with high tensile strength and high Young's modulus*, Journal of Materials Science, 13(1978), 2569–2576

[28] R. M. Laine and F. Babonneau, *Preceramic polymer routes to silicon carbide*, Chemistry of materials, 5(1993), 260–279

[29] G. D. Soraru, F. Babonneau and J. D. Mackenzie, *Structural concepts on new amorphous covalent solids*, Journal of Non-Crystalline Solids, 106(1988), 256–261

[30] Y. Iwamoto, W. Völger, E. Kroke and R. Riedel, *Crystallization Behavior of Amorphous Silicon Carbonitride Ceramics Derived from Organometallic Precursors,* Journal of the American Ceramic Society, 84(2001), 2170–78

[31] P. Colombo, G. Mera, R. Riedel and G. D. Soraru, *Polymer-Derived Ceramics: 40 Years of Research and Innovation in Advanced Ceramics*, Journal of the American Ceramic Society, 93(2010), 1805–1837

[32] G. Mera, R. Riedel, F. Poli and K. Müller, *Carbon-rich SiCN ceramics derived from phenyl-containing poly(silylcarbodiimides)*, Journal of the European Ceramic Society, 29(2009), 2873–2883

[33] R. Morcos, G. Mera, A. Navrotsky, T. Varga, R. Riedel, F. Poli and K. Müller, *Enthalpy of Formation of Carbon-Rich Polymer-Derived Amorphous SiCN Ceramics*, Journal of the American Ceramic Society, 91(2008), 3349–3354

[34] G. Mera, A. Tamayo, H. Nguyen, S. Sen and R. Riedel, *Nanodomain Structure of Carbon-Rich Silicon Carbonitride Polymer-Derived Ceramics*, Journal of the American Ceramic Society, 93(2010), 1169–1175

[35] Y. Gao, G. Mera, H. Nguyen, K. Morita, H.-J. Kleebe and R. Riedel, *Processing route dramatically influencing the nanostructure of carbon-rich SiCN and SiBCN polymer-derived ceramics. Part I: Low temperature thermal transformation*, Journal of the European Ceramic Society, 32(2012), 1857–1866

[36] G. Mera, A. Navrotsky, S. Sen, H.-J. Kleebe and R. Riedel, *Polymer-derived SiCN and SiOC ceramics - structure and energetics at the nanoscale*, Journal of Materials Chemistry A, 1(2013), 3826–3836

[37] J. R. Dahn, A. M. Wilson, W. Xing and G. A. Zank, *Electrodes for Lithium Ion Batteries using Polysilazanes Ceramic with Lithium*, Dow Corning Corporation, U.S. Patent Number 5631106, 1997

[38] R. Kolb, C. Fasel, V. Liebau-Kunzmann and R. Riedel, *SiCN/C-ceramic composite as anode material for lithium ion batteries*, Journal of the European Ceramic Society, 26(2006), 3903–3908

[39] M. Graczyk-Zajac, C. Fasel and R. Riedel, *Polymer-derived-SiCN ceramic/graphite composite as anode material with enhanced rate capability for lithium ion batteries*, Journal of Power Sources, 196(2011), 6412–6418

[40] Y. Feng, N.-N. Feng and G.-X. Du, *Preparation and Electrochemical Performance of Polymer-derived SiCN-graphite Composite as Anode Material for Lithium Ion Batteries*, International Journal of Electrochemical Science, 7(2012), 3135–3140

[41] Y. Feng, G.-X. Du, X.-J. Zhao and E.-C. Yang, *Preparation and electrochemical performance of SiCN-CNTs composite anode material for lithium ion batteries*, Journal of Applied Electrochemistry, 41(2011), 999–1002

[42] M. Wilamowska, M. Graczyk-Zajac and R. Riedel, *Composite materials based on polymer-derived SiCN ceramic and disordered hard carbons as anodes for lithium-ion batteries*, Journal of Power Sources, 244(2013), 80–86

[43] Y. Chen, C. Li, Y. Wang, Q. Zhang, C. Xu, B. Wei and L. An, *Self-assembled carbon-silicon carbonitride nanocomposites: high-performance anode materials for lithium-ion batteries*, Journal of Materials Chemistry, 21(2011), 18186–18190

[44] D. Su, Y.-L. Li, Y. Feng and J. Jin, *Electrochemical Properties of Polymer-Derived SiCN Materials as the Anode in Lithium Ion Batteries*, Journal of the American Ceramic Society, 92(2009), 2962–2968

[45] Y. Feng, *Electrochemical properties of heat-treated polymer-derived SiCN anode for lithium ion batteries*, Electrochimica Acta, 55(2010), 5860–5866

[46] J. Kaspar, G. Mera, A. P. Nowak, M. Graczyk-Zajac and R. Riedel, *Electrochemical study of lithium insertion into carbon-rich polymer-derived silicon carbonitride ceramics*, Electrochimica Acta, 56(2010), 174–182

[47] M. Graczyk-Zajac, G. Mera, J. Kaspar and R. Riedel, *Electrochemical studies of carbon-rich polymer-derived SiCN ceramics as anode materials for lithium-ion batteries*, Journal of the European Ceramic Society, 30(2010), 3235–3243

[48] D. Ahn and R. Raj, *Cyclic stability and C-rate performance of amorphous silicon and carbon based anodes for electrochemical storage of lithium*, Journal of Power Sources, 196(2011), 2179–2186

[49] X. Liu, M.-C. Zheng and K. Xie, *Mechanism of lithium storage in SiOC composite anodes*, Journal of Power Sources, 196(2011), 10667 – 10672

[50] H. Fukui, O. Hisashi, T. Hino and K. Kanamura, *A Si-O-C Composite Anode: High Capability and Proposed Mechanism of Lithium Storage Associated with Microstructural Characteristics*, ACS Applied Materials and Interfaces, 4(2010), 998–1008

[51] A. Wilson, J. Reimers, E. Fuller and J. Dahn, *Lithium insertion in pyrolyzed siloxane polymers*, Solid State Ionics, 74(1994), 249–254

[52] A. M. Wilson, W. Xing, G. Zank, B. Yates and J. R. Dahn, *Pyrolysed pitch-polysilane blends for use as anode materials in lithium ion batteries II: the effect of oxygen*, Solid State Ionics, 100(1997), 259–266

[53] W. Xing, A. M. Wilson, K. Eguchi, G. Zank and J. R. Dahn, *Pyrolyzed Polysiloxanes for Use as Anode Materials in Lithium-Ion Batteries*, Journal of The Electrochemical Society, 144(1997), 2410–2416

[54] H. Jung, M. Park, Y.-G. Yoon, G.-B. Kim and S.-K. Joo, *Amorphous silicon anode for lithium-ion rechargeable batteries*, Journal of Power Sources, 115(2003), 346–351

[55] C. J. Wen and R. A. Huggins, *Chemical Diffusion In Intermediate Phases In the Lithium-silicon System*, Journal of Solid State Chemistry, 37(1981), 271–278

[56] M. N. Obrovac and L. Christensen, *Structural Changes in Silicon Anodes during Lithium Insertion/Extraction*, Electrochemical and Solid-State Letters, 7(2004), A93–A96

[57] J. Li and J. R. Dahn, *An In Situ X-Ray Diffraction Study of the Reaction of Li with Crystalline Si*, Journal of The Electrochemical Society, 154(2007), A156–A161

[58] M. Wachtler, J. O. Besenhard and M. Winter, *Tin and tin-based intermetallics as new anode materials for lithium-ion cells*, Journal of Power Sources, 94(2001), 189–193

[59] X. H. Liu, L. Zhong, S. Huang, S. X. Mao, T. Zhu and J. Y. Huang, *Size-dependent fracture of silicon nanoparticles during lithiation*, ACS Nano, 6(2012), 1522–1531

[60] J. Saint, M. Morcrette, D. Larcher, L. Laffont, S. Beattie, J.-P. Pérès, D. Talaga, M. Couzi and J.-M. Tarascon, *Towards a Fundamental Understanding of the Improved Electrochemical Performance of Silicon Carbon Composites*, Advanced Functional Materials, 17(2007), 1765–1774

[61] X. Yang, Z. Wen, X. Zhu and S. Huang, *Preparation and electrochemical properties of silicon/carbon composite electrodes*, Elechtrochemical and Solid State Letters, 8(2005), A481–A483

[62] X. L. Yang, Z. Y. Wen, X. X. Xu, B. Lin and Z. X. Lin, *High-performance silicon/carbon/graphite composites as anode materials for lithium ion batteries*, Journal of the Electrochemical Society, 153(2006), A1341–A1344

[63] I.-S. Kim and P. N. Kumta, *High capacity Si/C nanocomposite anodes for Li-ion batteries*, Journal of Power Sources, 136(2004), 145–149

[64] I.-S. Kim, G. E. Blomgren and P. N. Kumta, *Si-SiC nanocomposite anodes synthesized using high-energy mechanical milling*, Journal of Power Sources, 130(2004), 275–280

[65] N. Dimov, S. Kugino and M. Yoshio, *Carbon-coated silicon as anode material for lithium ion batteries: advantages and limitations*, Electrochimica Acta, 48(2003), 1579–1587

[66] W. Liu, J. Wang, H. Wu, D. Shieh, M. Yang and N. Wu, *Electrochemical characterizations on Si and C-coated Si particle electrodes for lithium-ion batteries*, Journal of the Eletrochemical Society, 152(2005), A1719–A1725

[67] D. Mazouzi, B. Lestriez, L. Roue and D. Guyomard, *Silicon Composite Electrode with High Capacity and Long Cycle Life*, Electrochemical and Solid State Letters, 12(2009), A215–A218

[68] C. Martin, M. Alias, F. Christien, O. Crosnier, D. Belanger and T. Brousse, *Graphite-Grafted Silicon Nanocomposite as a Negative Electrode for Lithium-Ion Batteries*, Advanced Materials, 21(2009), 4735–4741

[69] H. Wu, G. Zheng, N. Liu, T. J. Carney, Y. Yang and Y. Cui, *Engineering Empty Space between Si Nanoparticles for Lithium-Ion Battery Anodes*, Nano Letters, 12(2012), 904–909

[70] L. Yue, W. Zhang, J. Yang and L. Zhang, *Designing Si/porous-C composite with buffering voids as high capacity anode for lithium-ion batteries*, Electrochimica Acta, 125(2014), 206–217

[71] X. yang Zhou, J. jing Tang, J. Yang, J. Xie and L. lu Ma, *Silicon@carbon hollow core-shell heterostructures novel anode materials for lithium ion batteries*, Electrochimica Acta, 87(2013), 663–668

[72] X. Li, P. Meduri, X. Chen, W. Qi, M. H. Engelhard, W. Xu, F. Ding, J. Xiao, W. Wang, C. Wang, J.-G. Zhang and J. Liu, *Hollow core–shell structured porous Si–C nanocomposites for Li-ion battery anodes*, Journal of Materials Chemistry, 22(2012), 11014–11017

[73] C. K. Chan, H. Peng, G. Liu, K. McIlwrath, X. F. Zhang, R. A. Huggins and Y. Cui, *High-performance lithium battery anodes using silicon nanowires*, Nature Nanotechnology, 3(2008), 31–35

[74] C. K. Chan, R. Ruffo, S. S. Hong, R. A. Huggins and Y. Cui, *Structural and electrochemical study of the reaction of lithium with silicon nanowires*, Journal of Power Sources, 189(2009), 34–39

[75] A. Vlad, A. L. M. Reddy, A. Ajayan, N. Singh, J.-F. Gohy, S. Melinte and P. M. Ajayan, *Roll up nanowire battery from silicon chips*, Proceedings of the National Academy of Sciences, 109(2012), 15168–15173

[76] X. Liu, K. Xie, J. Wang, C. Zheng and Y. Pan, *Si/Si-O-C composite anode materials exhibiting good C rate performances prepared by a sol-gel method*, Journal of Materials Chemistry, 22(2012), 19621–19624

[77] J. Kaspar, M. Graczyk-Zajac, S. Lauterbach, H.-J. Kleebe and R. Riedel, *Silicon oxycarbide/nano-silicon composite anodes for Li-ion batteries: Considerable influence of nano-crystalline vs. nano-amorphous silicon embedment on the electrochemical properties*, Journal of Power Sources, (2014), accepted manuscript

[78] J. R. Szczech and S. Jin, *Nanostructured silicon for high capacity lithium battery anodes*, Energy and Environmental Science, 4(2011), 56–72

[79] W.-J. Zhang, *A review of the electrochemical performance of alloy anodes for lithium-ion batteries*, Journal of Power Sources, 196(2011), 13–24

[80] N. Janakiraman and F. Aldinger, *Fabrication and characterization of fully dense Si-C-N ceramics from a poly(ureamethylvinyl)silazane precursor*, Journal of the European Ceramic Society, 29(2009), 163–173

[81] A. C. Ferrari and J. Robertson, *Interpretation of Raman spectra of disordered and amorphous carbon*, Physical Review B, 61(2000), 14095–14107

[82] N. Larouche and B. L. Stansfield, *Classifying nanostructured carbons using graphitic indices derived from Raman spectra*, Carbon, 48(2010), 620–629

[83] A. Bard and L. Faulkner, *Electrochemical Methods: Fundamentals and Applications*, Wiley-VCH Verlag GmbH & Co. KGaA, 1980

[84] G. Liu, J. Kaspar, L. M. Reinold, M. Graczyk-Zajac and R. Riedel, *Electrochemical performance of DVB-modified SiOC and SiCN polymer-derived negative electrodes for lithium-ion batteries*, Electrochimica Acta, 106(2013), 101–108

[85] L. M. Reinold, M. Graczyk-Zajac, Y. Gao, G. Mera and R. Riedel, *Carbon-rich SiCN ceramics as high capacity/high stability anode material for lithium-ion batteries*, Journal of Power Sources, 236(2013), 224–229

[86] S.-H. Baek, L. M. Reinold, M. Graczyk-Zajac, R. Riedel, F. Hammerath, B. Büchner and H.-J. Grafe, *Lithium dynamics in carbon-rich polymer-derived SiCN ceramics probed by nuclear magnetic resonance*, Journal of Power Sources, 253(2014), 342–348

[87] S. J. Widgeon, S. Sen, G. Mera, E. Ionescu, R. Riedel and A. Navrotsky, *^{29}Si and ^{13}C Solid-State NMR Spectroscopic Study of Nanometer-Scale Structure and Mass Fractal*

Characteristics of Amorphous Polymer Derived Silicon Oxycarbide Ceramics, Chemistry of Materials, 22(2010), 6221–6228

[88] I. M. Arafa and M. Al-Atrash, *Synthesis and Charaterization of Diaminecarbosilazane-containing Polymers*, Journal of Macromolecular Science, Part A, 39(2002), 1475–1486

[89] J. Bill, J. Seitz, G. Thurn, J. Durr, J. Canel, B. Z. Janos, A. Jalowiecki, D. Sauter, S. Schempp, H. P. Lamparter, J. Mayer and F. Aldinger, *Structure analysis and properties of Si-C-N ceramics derived from polysilazanes*, Physica Status Solidi A - Applied Research, 166(1998), 269–296

[90] F. Tuinstra and J. L. Koenig, *Raman Spectrum of Graphite*, The Journal of Chemical Physics, 53(1970), 1126–1130

[91] B. Dippel, H. Jander and J. Heintzenberg, *NIR FT Raman spectroscopic study of flame soot*, Physical Chemistry Chemical Physics, 1(1999), 4707–4712

[92] A. Sadezky, H. Muckenhuber, H. Grothe, R. Niessner and U. Pöschl, *Raman microspectroscopy of soot and related carbonaceous materials: Spectral analysis and structural information*, Carbon, 43(2005), 1731–1742

[93] R. Al-Jishi and G. Dresselhaus, *Lattice-dynamical model for graphite*, Physical Review B, 26(1982), 4514–4522

[94] Y. Wang, D. C. Alsmeyer and R. L. McCreery, *Raman spectroscopy of carbon materials: structural basis of observed spectra*, Chemistry of Materials, 2(1990), 557–563

[95] A. Cuesta, P. Dhamelincourt, J. Laureyns, A. Martinez-Alonso and J. Tascon, *Raman microprobe studies on carbon materials*, Carbon, 32(1994), 1523–1532

[96] H. Buqa, D. Goers, M. Holzapfel, M. Spahr and P. Novak, *High rate capability of graphite negative electrodes for lithium-ion batteries*, Journal of the Electrochemical Society, 152(2005), A474–A481

[97] L. Fransson, T. Eriksson, K. Edström, T. Gustafsson and J. O. Thomas, *Influence of carbon black and binder on Li-ion batteries*, Journal of Power Sources, 101(2001), 1–9

[98] R. Yazami and M. Deschamps, *High reversible capacity carbon-lithium negative electrode in polymer electrolyte*, Journal of Power Sources, 54(1995), 411–415

[99] H. Fukui, N. Nakata, K. Dokko, B. Takemura, H. Ohsuka, T. Hino and K. Kanamura, *Lithiation and Delithiation of Silicon Oxycarbide Single Particles with a Unique Microstructure*, ACS Applied Materials and Interfaces, 3(2011), 2318–2322

[100] M. Winter, J. O. Besenhard, M. E. Spahr and P. Novák, *Insertion Electrode Materials for Rechargeable Lithium Batteries*, Advanced Materials, 10(1998), 725–763

[101] Y. Liu, J. S. Xue, T. Zheng and J. R. Dahn, *Mechanism of lithium insertion in hard carbons prepared by pyrolysis of epoxy resins*, Carbon, 34(1996), 193–200

[102] T. Zheng, Y. Liu, E. Fuller, S. Tseng, U. Vonsacken and J. Dahn, *Lithium Insertion in High-Capacity Carbonaceous Materials*, Journal of the Electrochemical Society, 142(1995), 2581–2590

[103] J. Kaspar, M. Graczyk-Zajac and R. Riedel, *Lithium insertion into carbon-rich SiOC ceramics: Influence of pyrolysis temperature on electrochemical properties*, Journal of Power Sources, 244(2013), 450–455

[104] P. Kroll, *Tracing Reversible and Irreversible Li Insertion in SiCO Ceramics with Modeling and Ab-Initio Simulations*, MRS Online Proceedings Library, 1313(2011)

[105] P. E. Sanchez-Jimenez and R. Raj, *Lithium Insertion in Polymer-Derived Silicon Oxycarbide Ceramics*, Journal of the American Ceramic Society, 93(2010), 1127–1135

[106] V. S. Pradeep, M. Graczyk-Zajac, R. Riedel and G. Soraru, *New Insights in to the Lithium Storage Mechanism in Polymer Derived SiOC Anode Materials*, Electrochimica Acta, 119(2014), 78–85

[107] F. Bonino, S. Brutti, M. Piana, S. Natale, B. Scrosati, L. Gherghel and K. Müllen, *Structural and electrochemical studies of a hexaphenylbenzene pyrolysed soft carbon as anode material in lithium batteries*, Electrochimica Acta, 51(2006), 3407–3412

[108] A. C. Ferrari and J. Robertson, *Resonant Raman spectroscopy of disordered, amorphous, and diamondlike carbon*, Physical Review B, 64(2001), 075414

[109] D. Olego and M. Cardona, *Pressure dependence of Raman phonons of Ge and 3C-SiC*, Physical Review B, 25(1982), 1151–1160

[110] H. Fukui, K. Eguchi, H. Ohsuka, T. Hino and K. Kanamura, *Structures and lithium storage performance of SiOC composite materials depending on pyrolysis temperatures*, Journal of Power Sources, 243(2013), 152 – 158

[111] T. Zheng, J. S. Xue and J. R. Dahn, *Lithium Insertion in Hydrogen-Containing Carbonaceous Materials*, Chemistry of Materials, 8(1996), 389–393

[112] T. Zheng, W. R. McKinnon and J. R. Dahn, *Hysteresis during Lithium Insertion in Hydrogen-Containing Carbons*, Journal of The Electrochemical Society, 143(1996), 2137–2145

[113] A. Claye and J. E. Fischer, *Short-range order in disordered carbons: where does the Li go?*, Electrochimica Acta, 45(1999), 107–120

[114] D. Ahn and R. Raj, *Thermodynamic measurements pertaining to the hysteretic intercalation of lithium in polymer-derived silicon oxycarbide*, Journal of Power Sources, 195(2010), 3900–3906

[115] S. R. Shah and R. Raj, *Mechanical properties of a fully dense polymer derived ceramic made by a novel pressure casting process*, Acta Materialia, 50(2002), 4093–4103

[116] T. Nishimura, R. Haug, J. Bill, G. Thurn and F. Aldinger, *Mechanical and thermal properties of Si-C-N material from polyvinylsilazane*, Journal of Materials Science, 33(1998), 5237–5241

[117] J. Kaspar, M. Graczyk-Zajac and R. Riedel, *Determination of the chemical diffusion coefficient of Li-ions in carbon-rich silicon oxycarbide anodes by electro-analytical methods*, Electrochimica Acta, 115(2014), 665–670

[118] K. Dokko, N. Nakata, Y. Suzuki and K. Kanamura, *High-Rate Lithium Deintercalation from Lithiated Graphite Single-Particle Electrode*, The Journal of Physical Chemistry C, 114(2010), 8646–8650

[119] K. Dokko, N. Nakata and K. Kanamura, *High rate discharge capability of single particle electrode of* $LiCoO_2$, Journal of Power Sources, 189(2009), 783–785

[120] H. Munakata, B. Takemura, T. Saito and K. Kanamura, *Evaluation of real performance of* $LiFePO_4$ *by using single particle technique*, Journal of Power Sources, 217(2012), 444–448

[121] Y. Gao, *Nanodomain Structure and Energetics of Carbon Rich SiCN and SiBCN Polymer-Derived Ceramics*, Ph.D. thesis, Technische Universität Darmstadt, 2014

[122] S. Trassl, M. Puchinger, E. Rössler and G. Ziegler, *Electrical properties of amorphous* $SiC_xN_yH_z$*-ceramics derived from polyvinylsilazane*, Journal of the European Ceramic Society, 23(2003), 781 – 789

[123] C. Haluschka, C. Engel and R. Riedel, *Silicon carbonitride ceramics derived from polysilazanes Part II. Investigation of electrical properties*, Journal of the European Ceramic Society, 20(2000), 1365–1374

[124] S. Trassl, H.-J. Kleebe, H. Störmer, G. Motz, E. Rössler and G. Ziegler, *Characterization of the Free-Carbon Phase in Si-C-N Ceramics: Part II, Comparison of Different Polysilazane Precursors*, Journal of the American Ceramic Society, 85(2002), 1268–1274

[125] E. Ionescu, A. Francis and R. Riedel, *Dispersion assessment and studies on AC percolative conductivity in polymer-derived SiCN / CNT ceramic nanocomposites*, Journal of Materials Science, 44(2009), 2055–2062

[126] G.-A. Nazri and G. Pistoia (editors), *Lithium Batteries: Science and Technology*, Kluwer Academic Publishers, 2003

[127] P. Heitjans and J. Kärger, *Diffusion in Condensed Matter: Methods, Materials, Models*, Springer Berlin, 2005

[128] A. Kuhn, P. Sreeraj, R. Pöttgen, H.-D. Wiemhöfer, M. Wilkening and P. Heitjans, *Li Ion Diffusion in the Anode Material* $Li_{12}Si_7$*: Ultrafast Quasi-1D Diffusion and Two Distinct Fast 3D Jump Processes Separately Revealed by* ^{7}*Li NMR Relaxometry*, Journal of the American Chemical Society, 133(2011), 11018–11021

[129] M. Riccò, M. Belli, M. Mazzani, D. Pontiroli, D. Quintavalle, A. Jánossy and G. Csányi, *Superionic Conductivity in the Li4C60 Fulleride Polymer*, Physical Review Letters, 102(2009), 145901

[130] J. Langer, V. Epp, P. Heitjans, F. A. Mautner and M. Wilkening, *Lithium motion in the anode material* LiC_6 *as seen via time-domain* ^{7}*Li NMR*, Phyical Review B, 88(2013), 094304

[131] N. Bloembergen, E. M. Purcell and R. V. Pound, *Relaxation Effects in Nuclear Magnetic Resonance Absorption*, Physical Review, 73(1948), 679–712

[132] M. Meyer, P. Maass and A. Bunde, *Spin-lattice relaxation: Non-Bloembergen-Purcell-Pound behavior by structural disorder and Coulomb interactions*, Physical Review Letters, 71(1993), 573–576

[133] J. L. Bjorkstam and M. Villa, *Second-order quadrupolar and low-dimensionality effects upon NMR resonance spectra*, Physical Review B, 22(1980), 5025–5032

[134] O. Madelung, *Semiconductors: Data Handbook*, third edition, Springer-Verlag Berlin Heidelberg GmbH, 2004

[135] S. Khachadorian, *Vibrational properties of silicon nanowires*, Ph.D. thesis, Technische Universität Berlin, 2011

[136] J. Ryu, J. Kim, Y. Sung and S. Oh, *Failure modes of silicon powder negative electrode in lithium secondary batteries*, Electrochemical and Solid State Letters, 7(2004), A306–A309

[137] A. Timmons, A. D. W. Todd, S. D. Mead, G. H. Carey, R. J. Sanderson, R. E. Mar and J. R. Dahn, *Studies of $Si_{1-x}C_x$ Electrode Materials Prepared by High-Energy Mechanical Milling and Combinatorial Sputter Deposition*, Journal of the Electrochemical Society, 154(2007), A865–A874

List of Figures

List of Tables

Appendix

A Single Particle Measurements

Single Particle Measurements of HN1-800 at room temperature

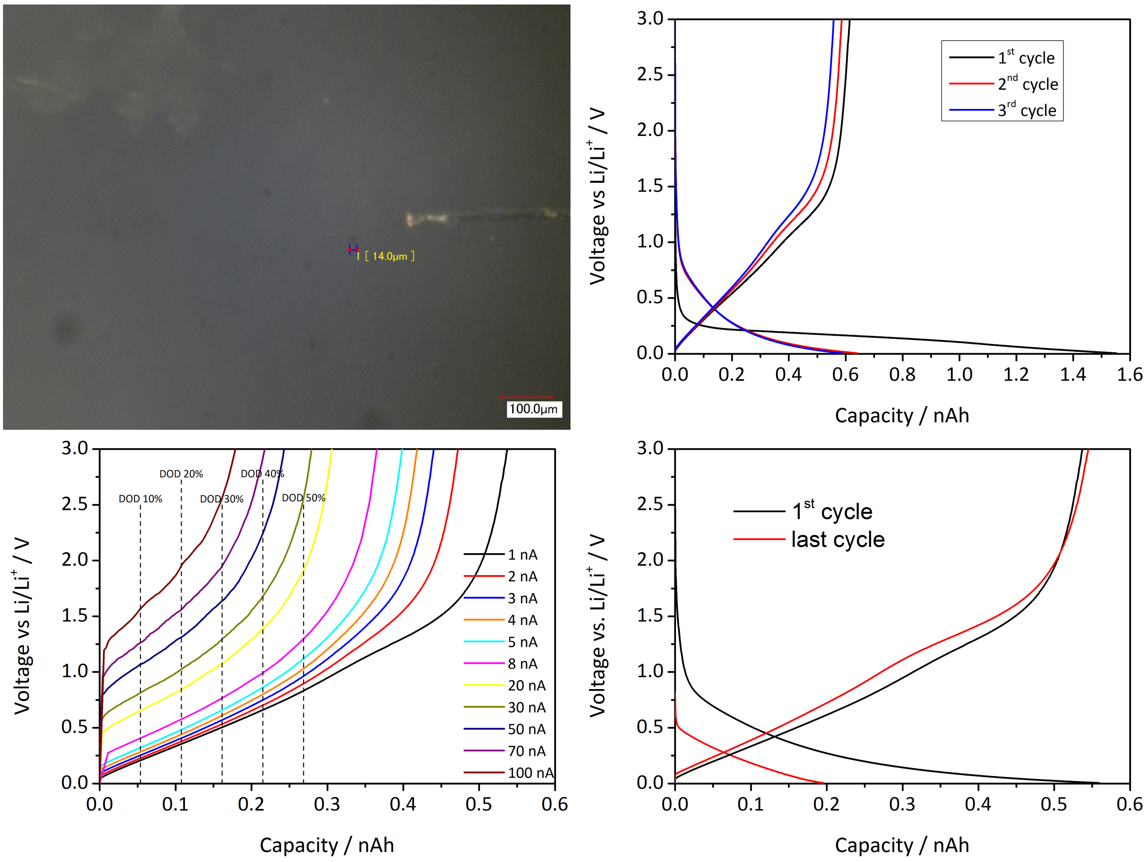

Figure A3: Microscope picture of the measured particle, three initial cycles at 1 nA, delithiation curves of the rate test and the comparison of lithiation-delithiation curve at 1 nA before and after the rate test of HN1-800 at an electrolyte temperature of 25 °C.

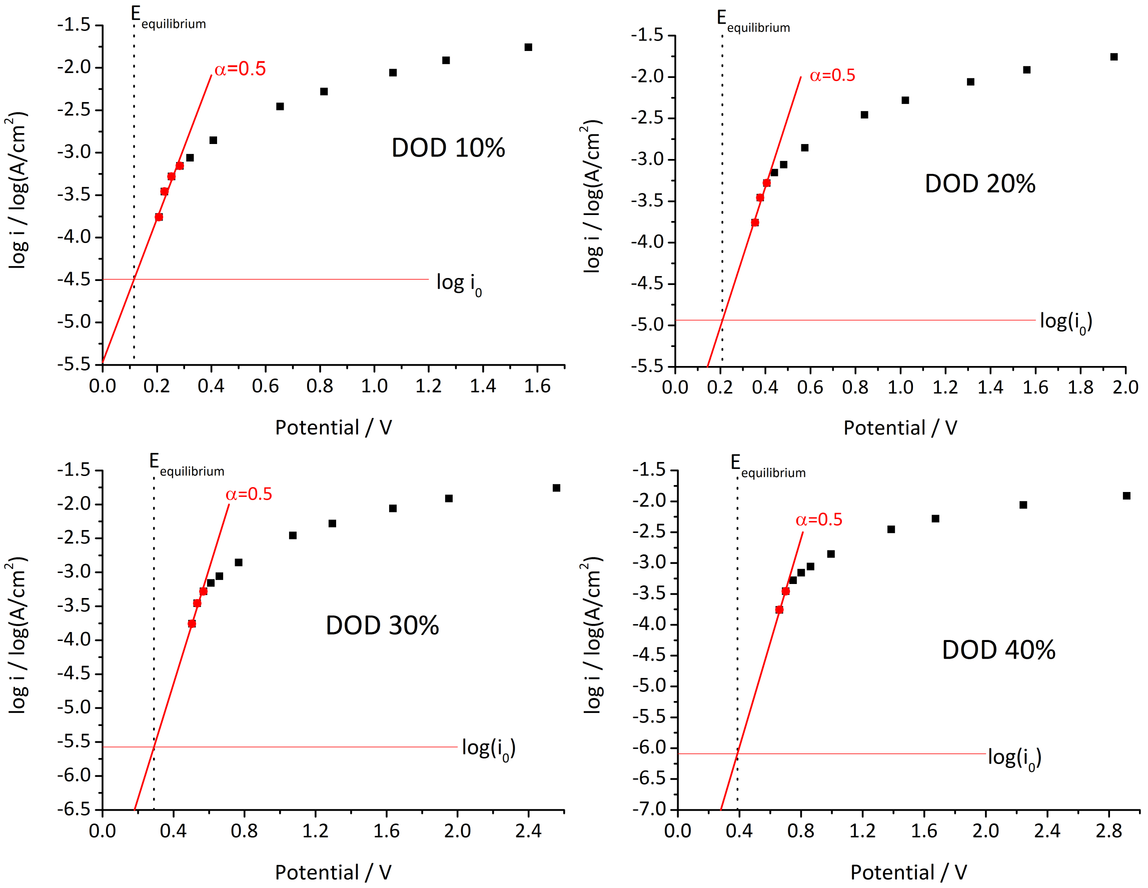

Figure A4: Tafel plots of HN1-800 at an electrolyte temperature of 25 °C at a DOD of 10 %, 20 %, 30 % and 40 % derived from the rate test in Figure A3.

Single Particle Measurements of HN1-1300 at room temperature

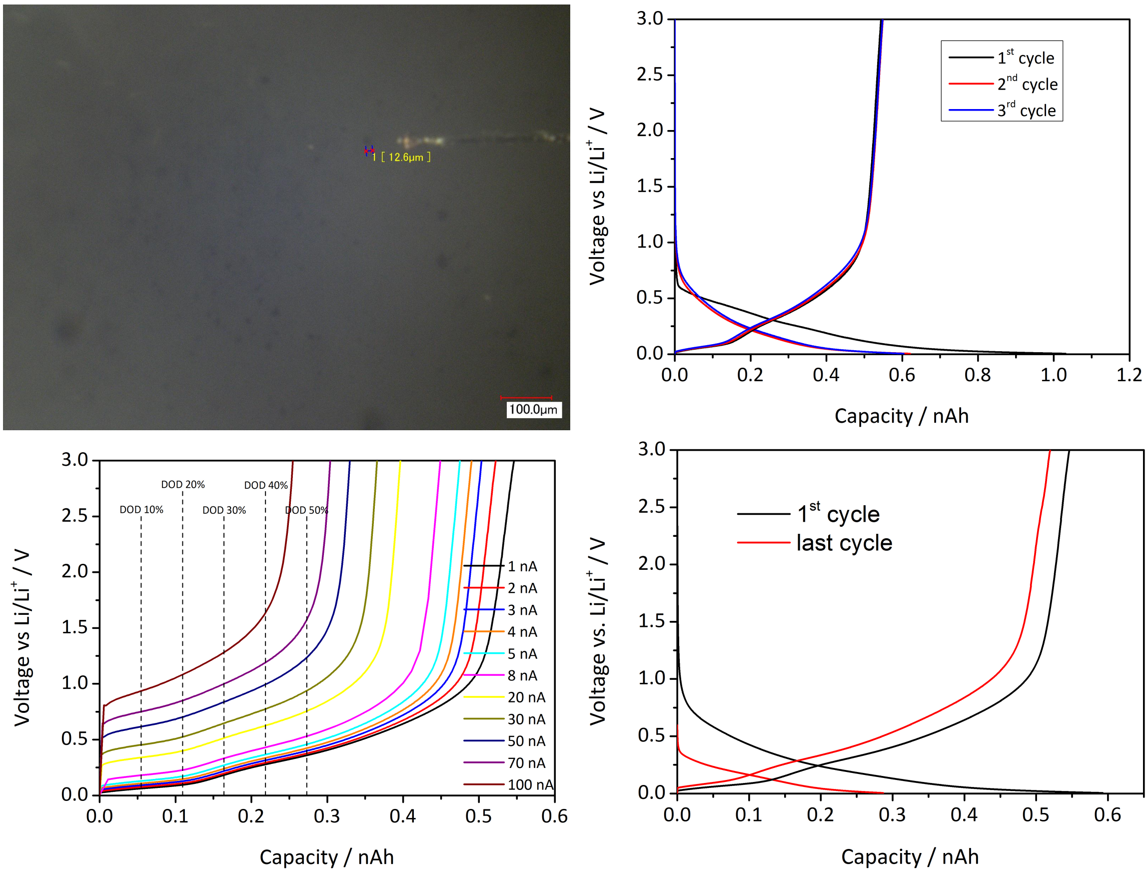

Figure A5: Microscope picture of the measured particle, three initial cycles at 1 nA, delithiation curves of the rate test and the comparison of lithiation-delithiation curve at 1 nA before and after the rate test of HN1-1300 at an electrolyte temperature of 25 °C.

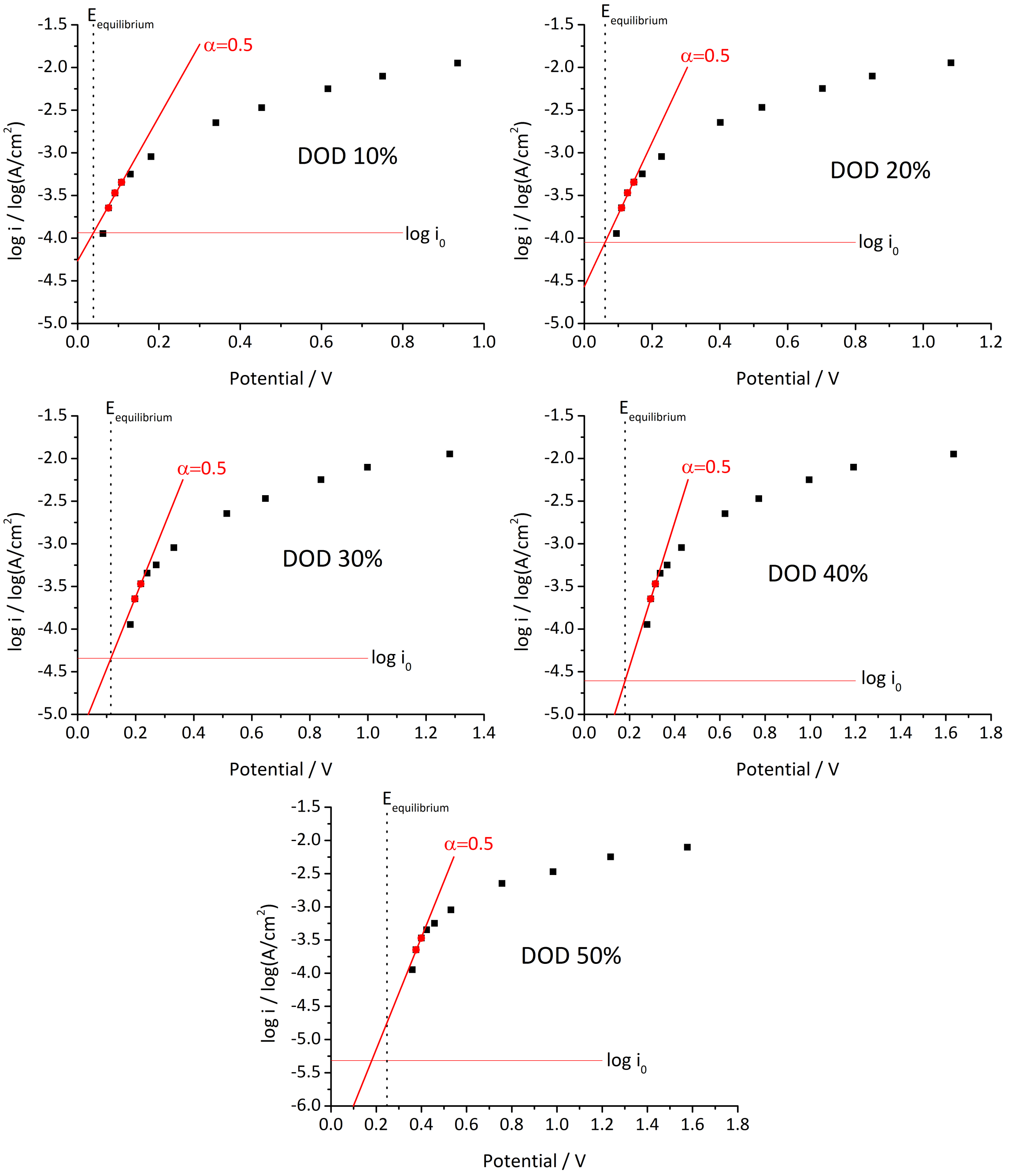

Figure A6: Tafel plots of HN1-1300 at an electrolyte temperature of 25 °C at a DOD of 10 %, 20 %, 30 %, 40 % and 50 % derived from the rate test in Figure A5.

Single Particle Measurements of HN3-800 at room temperature

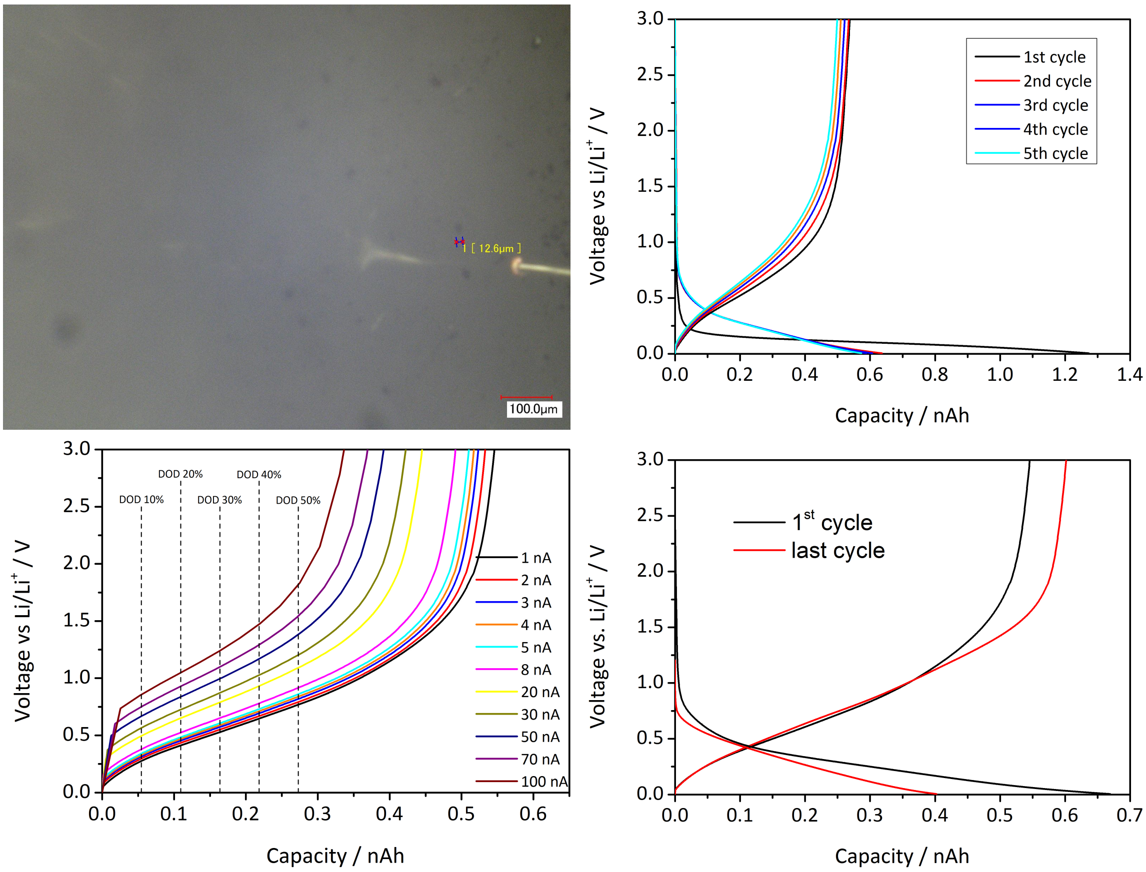

Figure A7: Microscope picture of the measured particle, five initial cycles at 1 nA, delithiation curves of the rate test and the comparison of lithiation-delithiation curve at 1 nA before and after the rate test of HN3-800 at an electrolyte temperature of 25 °C.

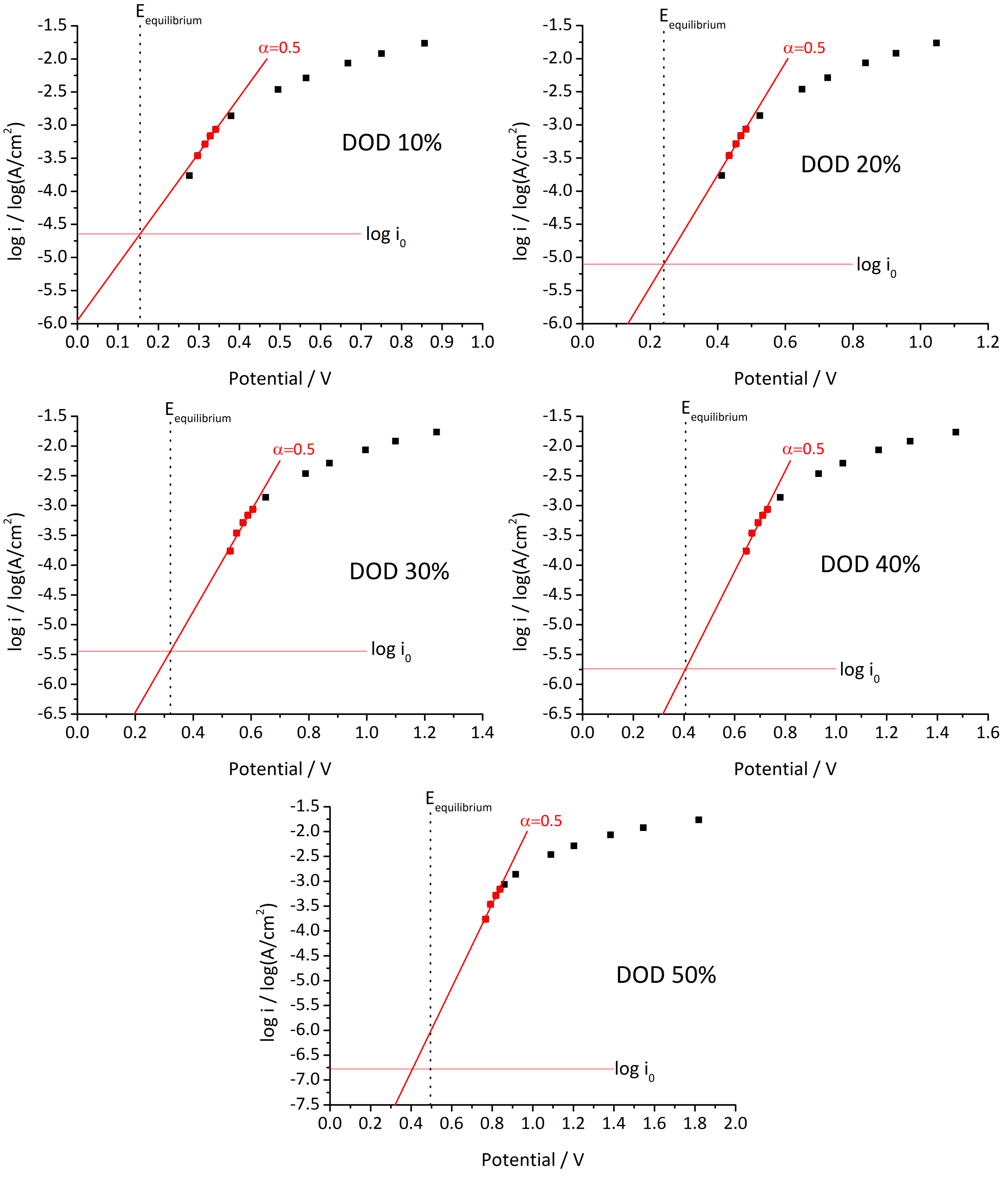

Figure A8: Tafel plots of HN3-800 at an electrolyte temperature of 25 °C at a DOD of 10 %, 20 %, 30 %, 40 % and 50 % derived from the rate test in Figure A7.

Single Particle Measurements of HN3-1300 at room temperature

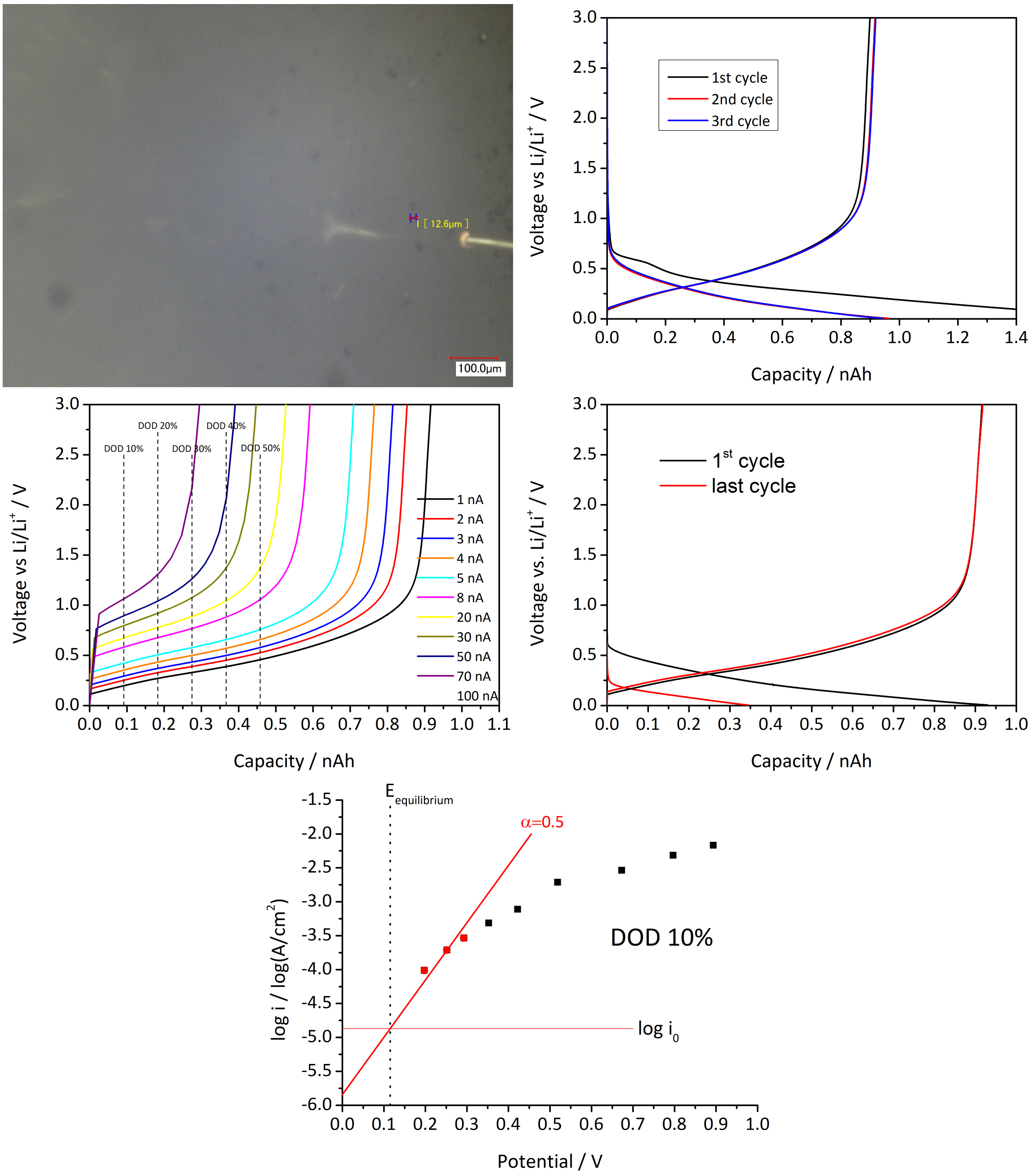

Figure A9: Microscope picture of the measured particle, three initial cycles at 1 nA, delithiation curves of the rate test and the comparison of lithiation-delithiation curve at 1 nA before and after the rate test of HN3-1300 at an electrolyte temperature of 25 °C. Additionally the Tafel plot of HN3-1300 at an electrolyte temperature of 25 °C and a DOD of 10 % is given.

Single Particle Measurements of HN1-800 at 60 °C

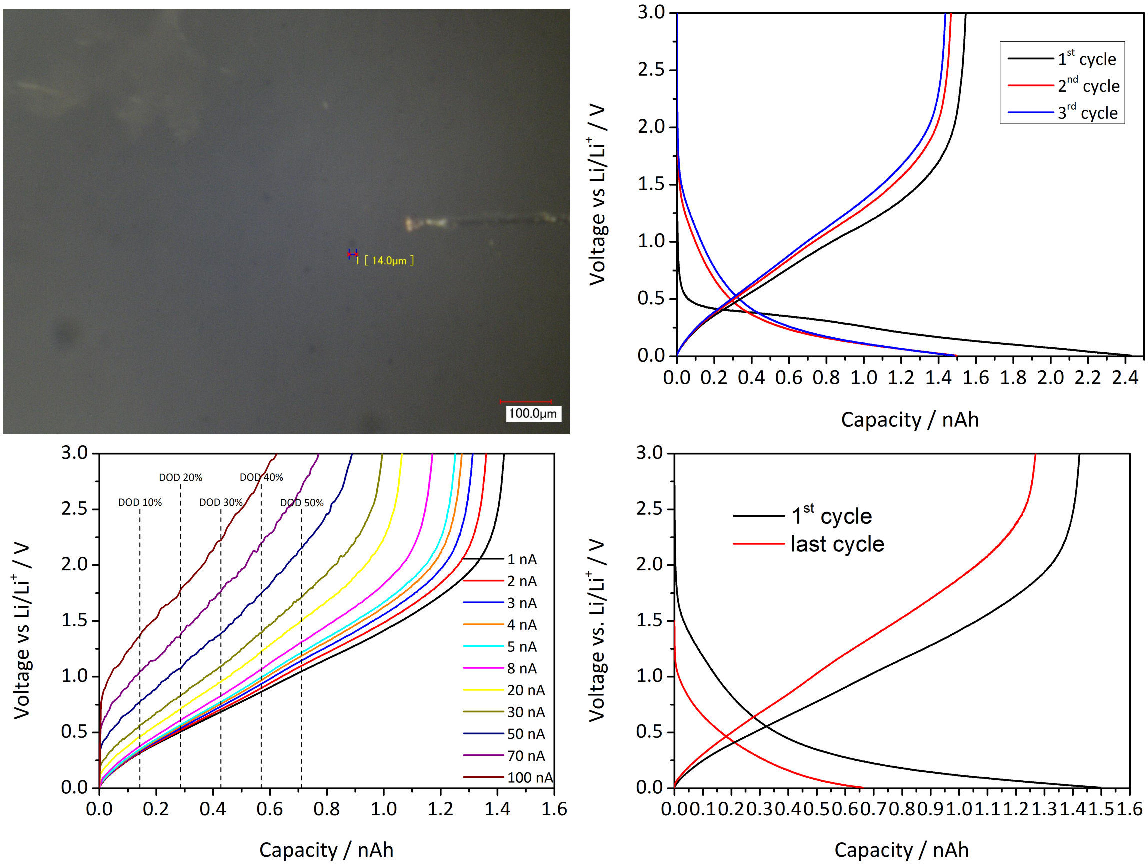

Figure A10: Microscope picture of the measured particle, three initial cycles at 1 nA, delithiation curves of the rate test and the comparison of lithiation-delithiation curve at 1 nA before and after the rate test of HN1-800 at an electrolyte temperature of 60 °C.

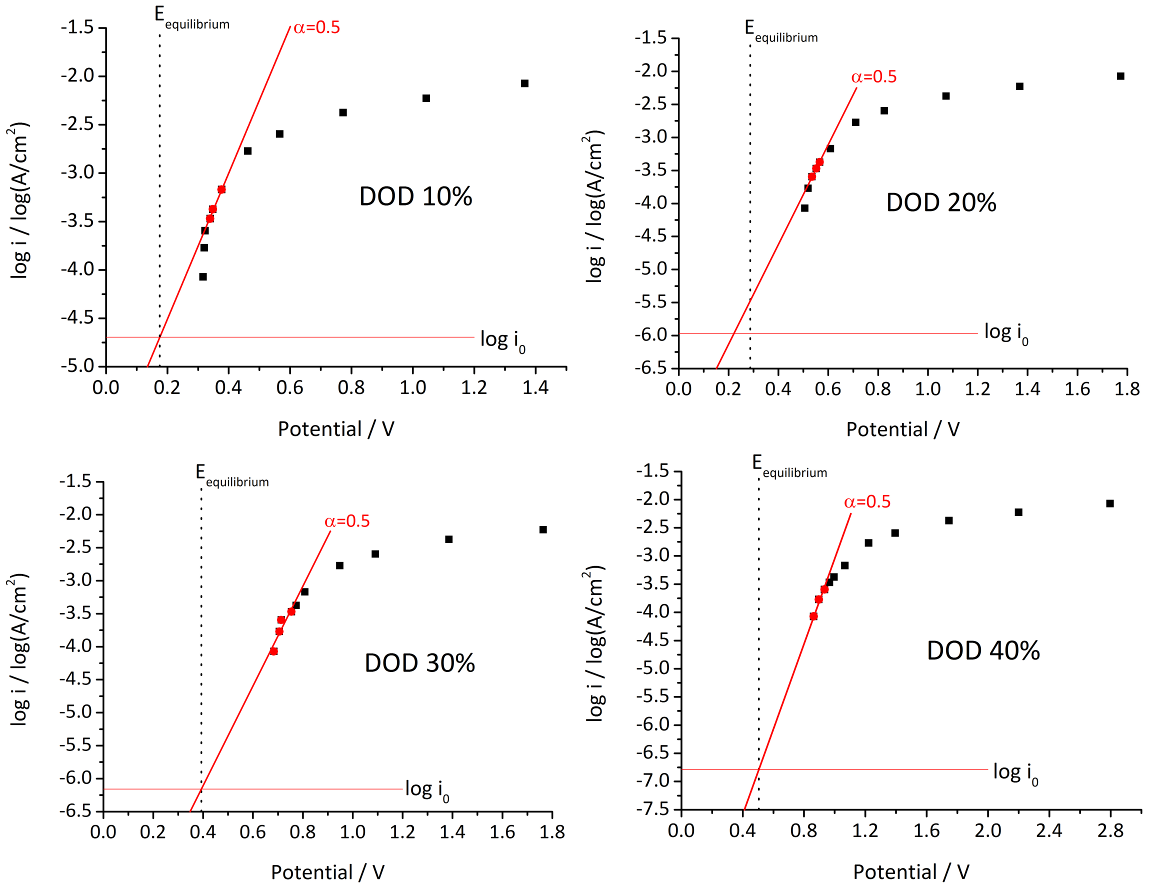

Figure A11: Tafel plots of HN1-800 at an electrolyte temperature of 60 °C at a DOD of 10 %, 20 %, 30 % and 40 % derived from the rate test in Figure A10.

Single Particle Measurements of HN1-1300 at 60 °C

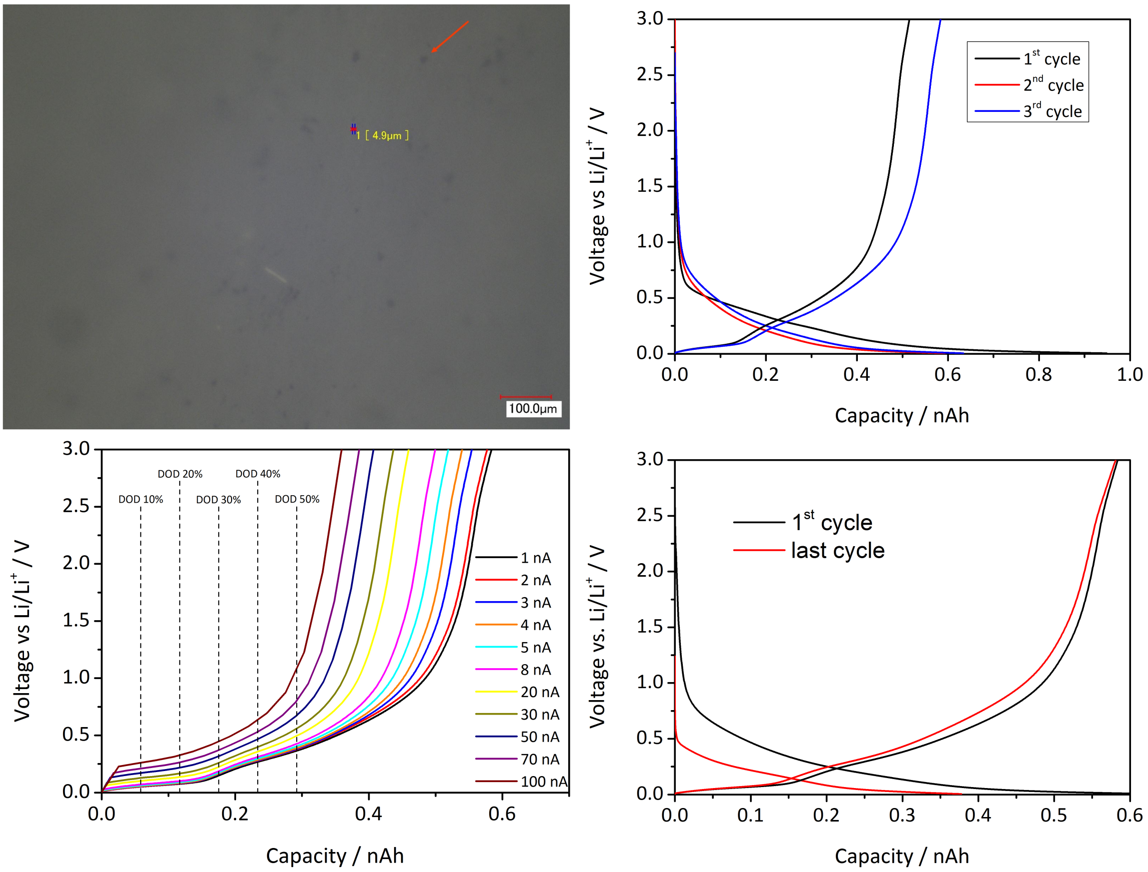

Figure A12: Microscope picture of the measured particle, three initial cycles at 1 nA, delithiation curves of the rate test and the comparison of lithiation-delithiation curve at 1 nA before and after the rate test of HN1-1300 at an electrolyte temperature of 60 °C. The delithiation curve of the the second cycle is not shown as it was interrupted several times to conduct impedance measurements.

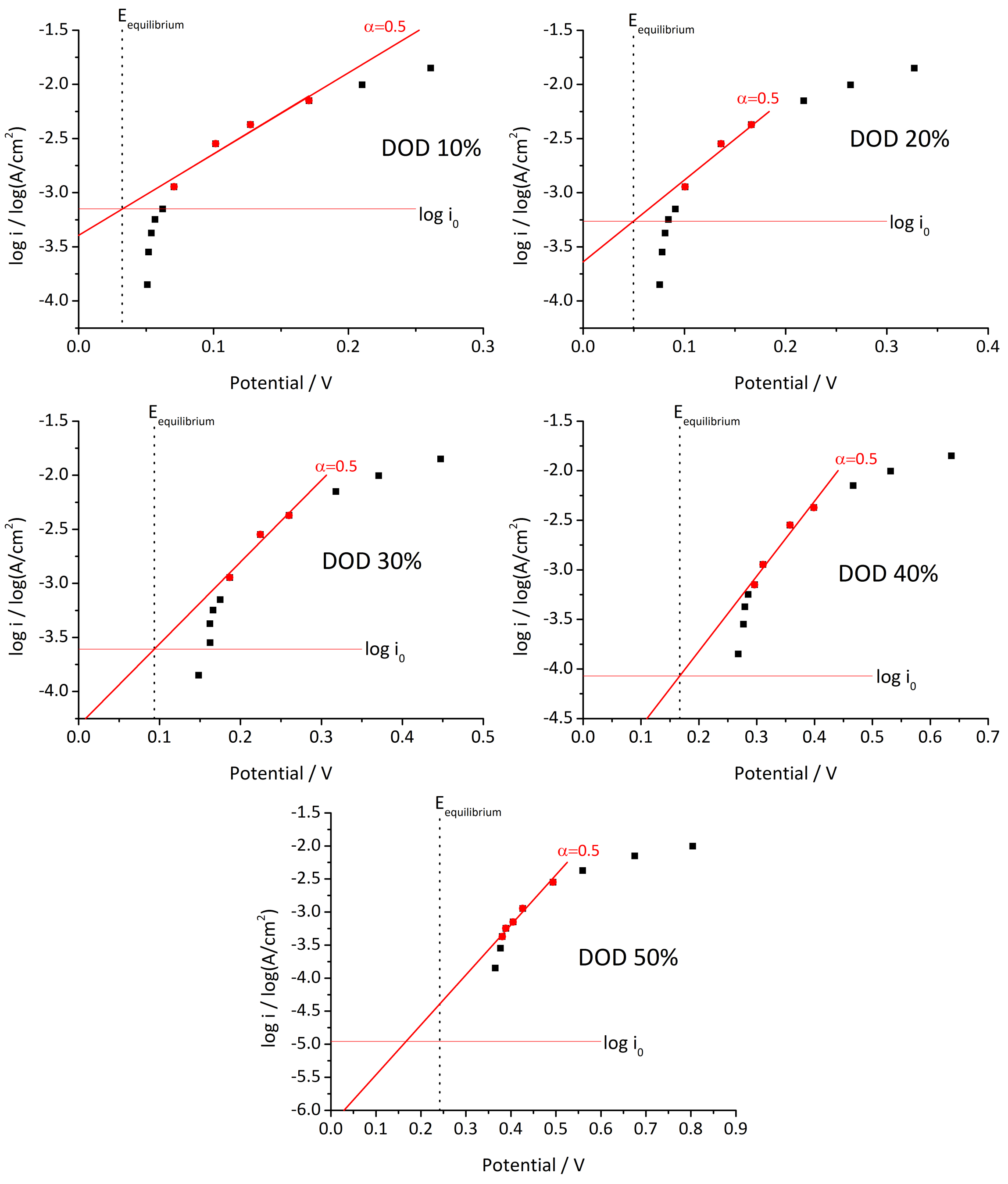

Figure A13: Tafel plots of HN1-1300 at an electrolyte temperature of 60 °C at a DOD of 10 %, 20 %, 30 %, 40 % and 50 % derived from the rate test in Figure A12.

Single Particle Measurements of HN3-800 at 60 °C

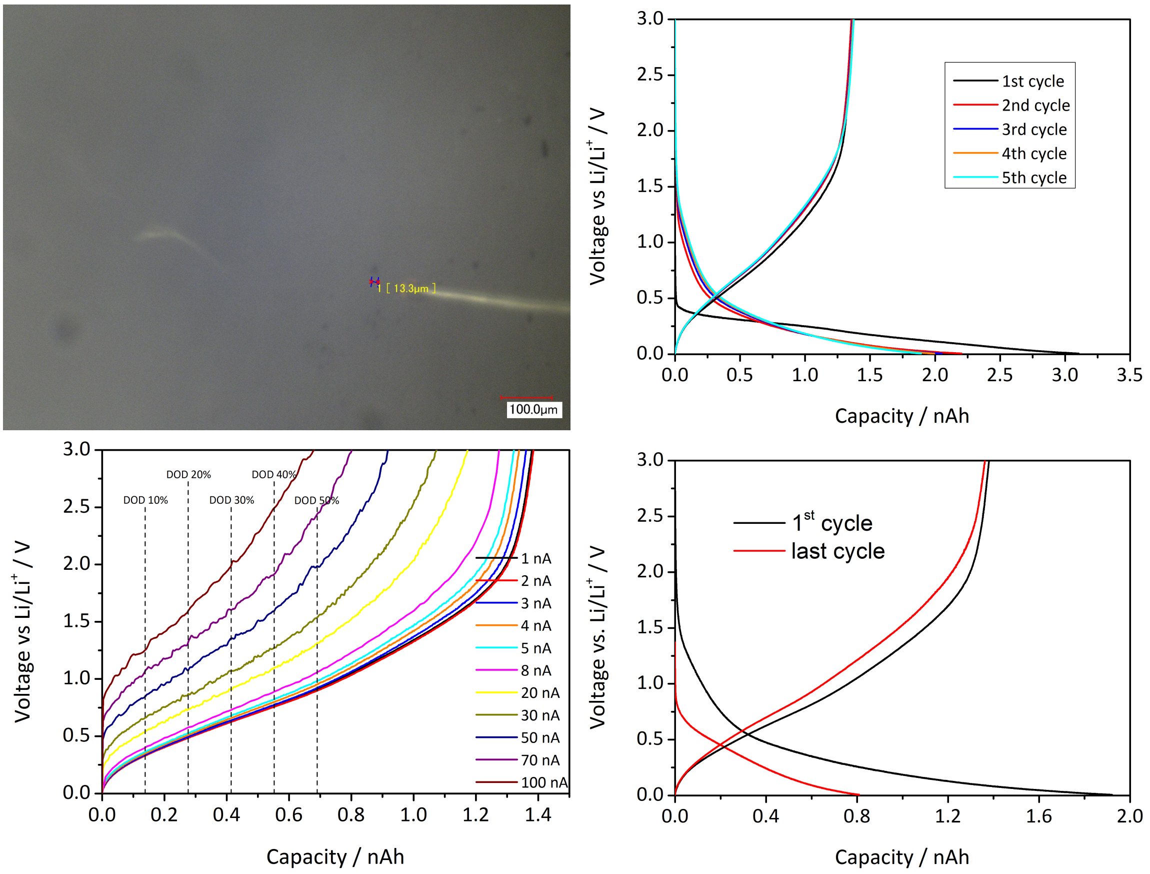

Figure A14: Microscope picture of the measured particle, five initial cycles at 1 nA, delithiation curves of the rate test and the comparison of lithiation-delithiation curve at 1 nA before and after the rate test of HN3-800 at an electrolyte temperature of 60 °C.

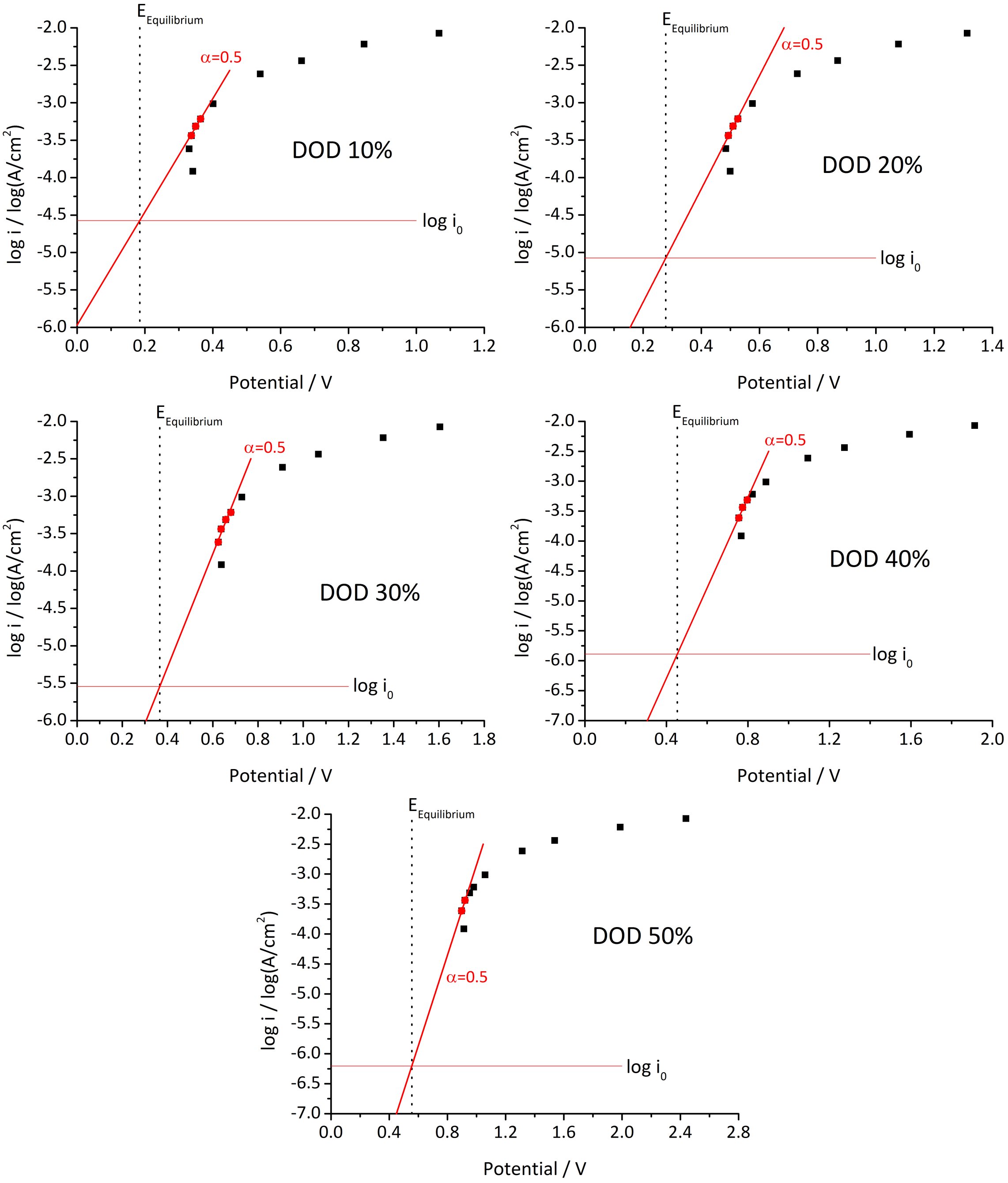

Figure A15: Tafel plots of HN3-800 at an electrolyte temperature of 60 °C at a DOD of 10 %, 20 %, 30 %, 40 % and 50 % derived from the rate test in Figure A14.

Single Particle Measurements of HN3-1300 at 60 °C

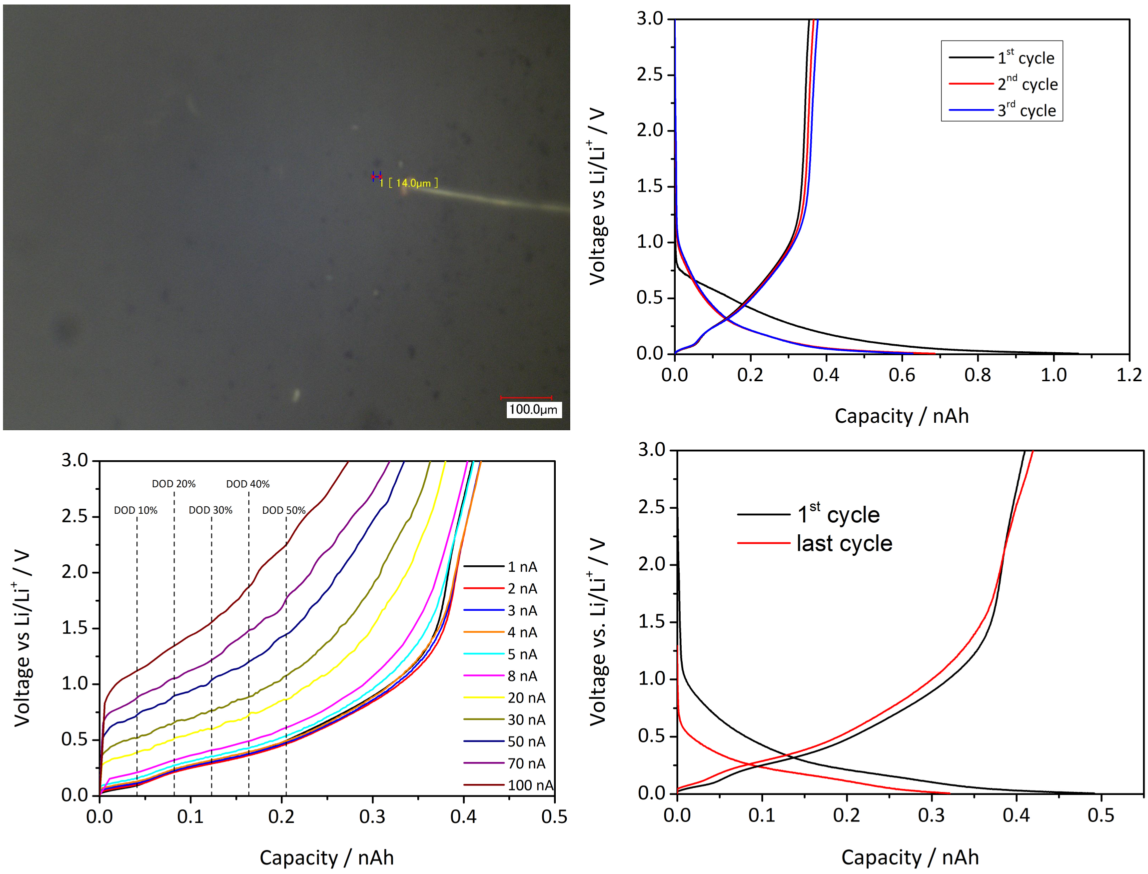

Figure A16: Microscope picture of the measured particle, three initial cycles at 1 nA, delithiation curves of the rate test and the comparison of lithiation-delithiation curve at 1 nA before and after the rate test of HN3-1300 at an electrolyte temperature of 60 °C.

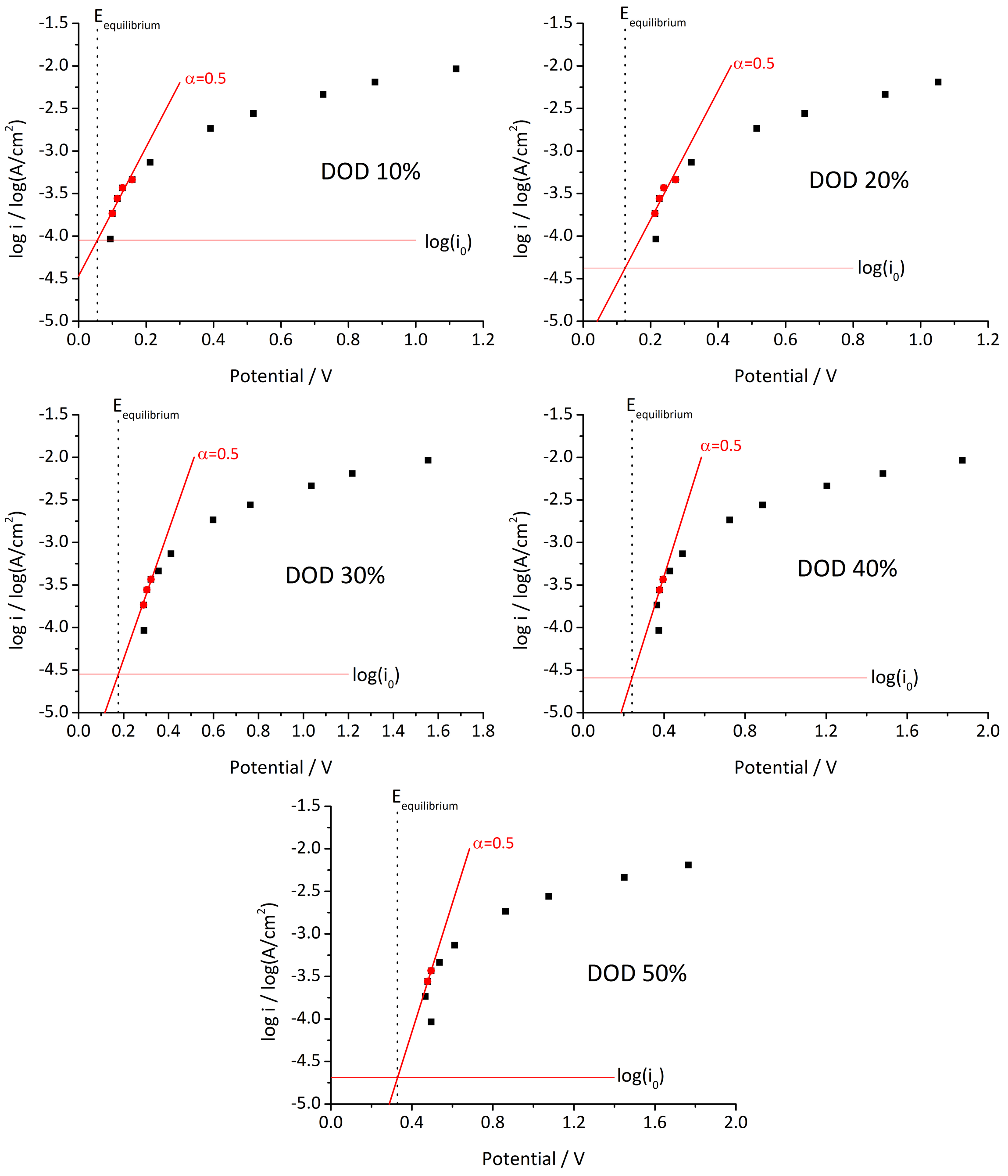

Figure A17: Tafel plots of HN3-1300 at an electrolyte temperature of 60 °C at a DOD of 10 %, 20 %, 30 %, 40 % and 50 % derived from the rate test in Figure A16.

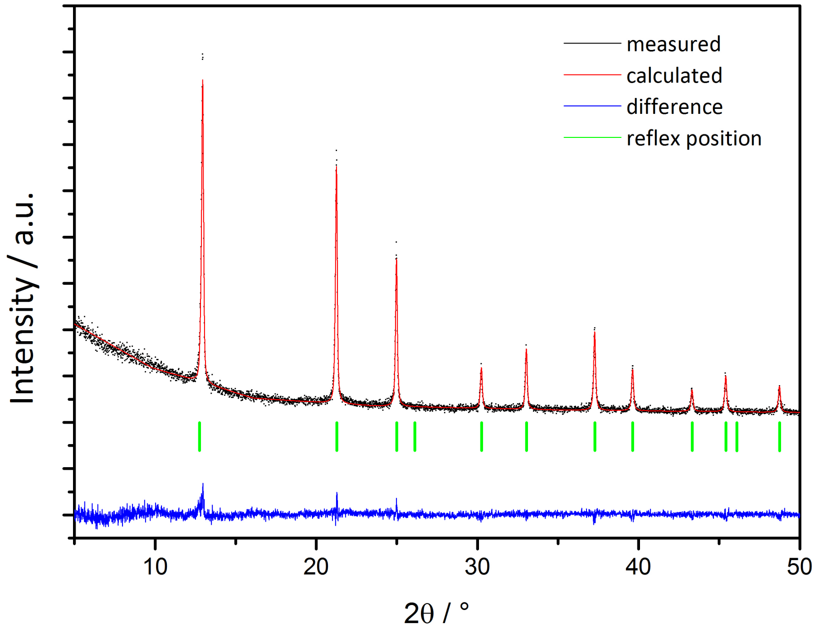

Figure B18: X-ray diffraction pattern and Rietveld refinement of silicon powder as received.

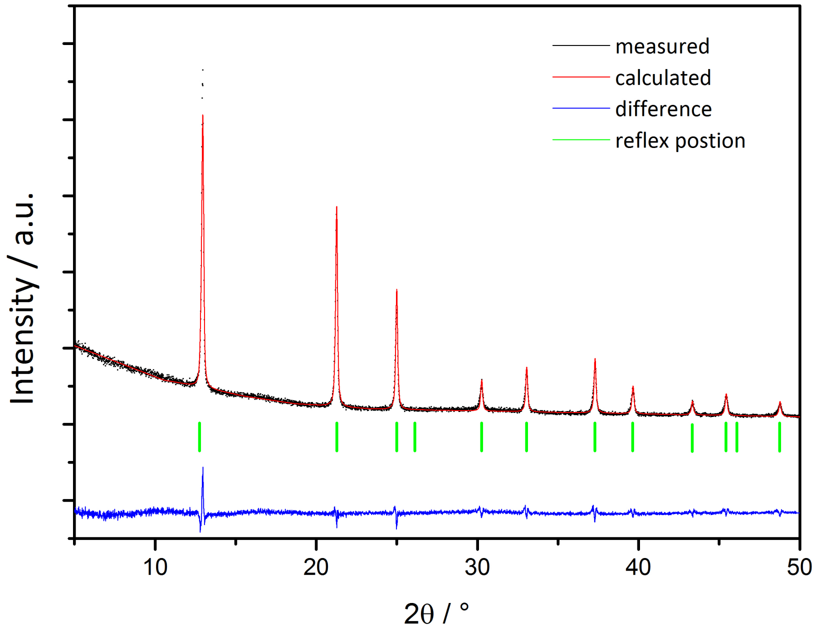

Figure B19: X-ray diffraction pattern and Rietveld of HTT:Si-1:1.

Acknowledgments

I thank Prof. Dr. Ralf Riedel for the possibility to carry out my research on the fields of lithium-ion batteries and polymer-derived ceramics since I started to work in his group for my diploma thesis. In particular I would like to thank him for his help in arranging my stay at the Tokyo Metropolitan University within the group of Professor Kanamura.

Prof. Dr. Christina Roth is acknowledged for the second survey of this thesis.

An important person for the success of the thesis was Dr. Magdalena Graczyk-Zajac who supported me at any time during the last four years.

I want to thank the group of Disperse Feststoffe for the company and support during my PhD thesis. I would like to namely thank Dr. Ravi Mohan Prasad for the SSA measurements, Alexander Uhl for the particle size distribution measurements, Jan Kaspar for elemental analysis, Dr. Guanwei Li for his work on the chemical modification of HTT1800 during his internship, Claudia Fasel for the TGA, Dragoljub Vrankovic for his work during his internship and later on as student research assistant on the composite materials and Dr. Emanuel Ionescu for answering my questions on polymers. I specially thank Dr. Gabriela Mera and Dr. Yan Gao for the collaboration on the carbon-rich SiCN materials which was essential for my research.

I thank Dr. Hans-Joachim Grafe and Dr. Seung-Ho Baek from the IFW Dresden for a very fruitful cooperation on the solid state NMR measurements.

I thank Prof. Kiyoshi Kanamura and his staff for great experiences, scientifically and personally, in his laboratories at Tokyo Metropolitan University. Dr. Hirokazu Munakata and Yuto Yamada thought me a lot about single particle measurements and Dr. Yasuhiro Akita introduced me to Japanese culture.

I gratefully acknowledge the financial support of the Deutsche Forschungsgemeinschaft DFG within the priority program SPP1473 (Grant No. GR3330-3-1) and the Collaborative Research Center SFB 595-A4.

Persönliche Daten

Name	Lukas Mirko Reinold
Adresse	Schaufelder Straße 26 30167 Hannover
Geboren am	24.12.1983 in Wiesbaden

Berufserfahrung

seit 09/2014	Forschung und Entwicklung, Hüttenes-Albertus chemische Werke GmbH
04/2011-06/2014	Wissenschaftlicher Mitarbeiter an der Technischen Universität Darmstadt, Fachgebiet Material- und Geowissenschaften, Fachbereich Disperse Feststoffe
12/2004-08/2005	Zivildienst am Hessischen Landesamt für Umwelt und Geologie, Dezernat Stoffbezogener Schutz oberirdischer Gewässer

Ausbildung

seit 04/2011	Promotion an der Technischen Universität Darmstadt unter der Leitung von Prof. Dr. Prof. h.c. Dr. h. c. R. Riedel
10/2005-02/2011	Studium der Materialwissenschaften an der Technischen Universität Darmstadt Abschluss: Diplom-Ingenieur (mit Auszeichnung)
bis 06/2004	Schulbesuch der Diltheyschule in Wiesbaden Abschluss: Abitur (2,0)

Auslandsaufenthalte

11/2013	Forschungsaufenthalt an der Tokyo Metropolitan University, Kanamura Laboratories, Tokyo, Japan
07/2001-06/2002	Austauschschuljahr mit Besuch des Waiopehu Colleges in Levin, Neuseeland

Darmstadt, den 24 Mai 2016,

Veröffentlichungen

The influence of the pyrolysis temperature on the electrochemical behavior of carbon-rich SiCN polymer-derived ceramics as anode materials in lithium-ion batteries, L.M. Reinold, Y. Yamada, M. Graczyk-Zajac, H. Munakata, K. Kanamura und R. Riedel, *Journal of Power Sources*, 282(2015), 409-415

New Insights into Understanding Irreversible and Reversible Lithium Storage within SiOC and SiCN Ceramics, M. Graczyk-Zajac, L.M. Reinold, J. Kaspar, P.V. Warriam Sasikumar, G.-D. Soraru und R. Riedel, *Journal of Power Sources*, 5(2015), 223-245

Lithium dynamics in carbon-rich polymerderived SiCN ceramics probed by nuclear magnetic resonance, S.-H. Baek, L.M. Reinold, M. Graczyk-Zajac, R. Riedel, F. Hammerath, B. Büchner und H.-J. Grafe, *Journal of Power Sources*, 253(2014), 342-348

Carbon-rich SiCN ceramics as high capacity/high stability anode material for lithium-ion batteries, L.M. Reinold, M. Graczyk-Zajac, Y. Gao, G. Mera und R. Riedel, *Journal of Power Sources*, 236(2013), 224-229

Electrochemical performance of DVB-modified SiOC and SiCN polymer-derived negative electrodes for lithium-ion batteries, G. Liu, J. Kaspar, L.M. Reinold, M. Graczyk-Zajac und R. Riedel, *Electrochimica Acta*, 106(2013), 101-108

Prevention of Solid Electrolyte Interphase Damaging on Silicon by Using Polymer Derived SiCN Ceramics, L.M. Reinold, M. Graczyk-Zajac, C. Fasel und R. Riedel, *ECS Transactions*, 35(2011), 37-44

Vorträge

Materials Science and Engineering 2012
25.-27. September 2012, Darmstadt
Si/SiCN composites as anode material for lithium-ion batteries: Influence of a SiCN matrix on the electrochemical performance of silicon

63rd Annual Meeting of the International Society of Electrochemistry
19.-24. August 2012, Prag, Tschechien
Carbon-rich polymer-derived SiCN ceramics as anode material in lithium-ion batteries

219th Electrochemical Society Meeting
01.-06. Mai 2011, Montreal, Kanada
Nano-silicon dispersed in a SiCN ceramic matrix

Poster

Gesellschaft Deutscher Chemiker - Wissenschaftsforum Chemie 2013

01.-04. September 2013, Darmstadt

Influence of pyrolysis temperature on polymer-derived carbon-rich SiCN anode materials

6th Lithium Battery Discussion

16.-21. Juni 2013, Arcachon, Frankreich

Influence of pyrolysis temperature on polymer-derived carbon-rich SiCN anode materials